Technical Physics, Vol. 49, No. 5, 2004, pp. 521–525. Translated from Zhurnal Tekhnicheskoĭ Fiziki, Vol. 74, No. 5, 2004, pp. 1–5.

THEORETICAL AND MATHEMATICAL PHYSICS

Chaotic Layer of a Pendulum under Low- and Medium-Frequency Perturbations

V. V. Vecheslavov

Budker Institute of Nuclear Physics, Siberian Division, Russian Academy of Sciences, pr. Akademika Lavrent'eva 11, Novosibirsk, 630090 Russia

e-mail: vecheslavov@inp.nsk.su

Received April 22, 2003

Abstract—The amplitude of the separatrix map and the size of a pendulum chaotic layer are studied numerically and analytically as functions of the adiabaticity parameter at low and medium perturbation frequencies. Good agreement between the theory and numerical experiment is found at low frequencies. In the medium-frequency range, the efficiency of using resonance invariants of separatrix mapping is high. Taken together with the known high-frequency asymptotics, the results obtained in this work reconstruct the chaotic layer pattern throughout the perturbation frequency range. © *2004 MAIK "Nauka/Interperiodica".*

INTRODUCTION

Interaction between nonlinear resonances with the formation of dynamic chaos in Hamiltonian systems is a complex problem, which is far from being solved. In a number of cases, this problem may be reduced to studying a pendulum (a fundamental resonance near which initial conditions are chosen) subjected to a quasi-periodic perturbation

$$H(x, p, t) = \frac{p^2}{2} + \omega_0^2\cos(x) + V(x, t), \qquad (1)$$

$$V(x, t) = \varepsilon_1\cos(a_1x - \Omega_1t) + \varepsilon_2\cos(a_2x - \Omega_2t), \quad (2)$$

where harmonic amplitudes ε_1 and ε_2 are assumed to be small ($\varepsilon_1, \varepsilon_2 \ll 1$). Note that either of the harmonics is also of resonant nature and, hence, may be a fundamental resonance in a related region of the phase space.

The set of equations (1) and (2) has been the subject of intensive research (see, e.g., [1–3]). The situation in the vicinity of the separatrices of the fundamental resonance and the formation of a chaotic layer have been studied most frequently. Our goal is to investigate the fundamental chaotic layer throughout the range of perturbation frequencies (it is appropriate here to recall the mechanism of its formation [1]). We will start with describing unperturbed separatrices.

First of all, they always have a saddle, a fixed point, which should be treated as an independent trajectory (an unperturbed pendulum may follow this trajectory for an infinite time). Two trajectories (separatrices) originate from the saddle point and then asymptotically approach it. Either is the boundary between the off-resonance phase rotation and resonant phase oscillation. In the neighborhood of the saddle point in the phase plane, there appears a characteristic cross with two outgoing and two incoming trajectories (Fig. 2.1 in [1]). It is important that actually both unperturbed separatrices consist of two spatially coincident trajectories for forward and backward time, respectively.

In the case of an analytical potential (as in (1)), the presence of at least one (!) perturbing resonance always results in splitting either of the separatrices into two branches ("whiskers" after Arnold). These branches do not return to the saddle point and are no longer coincident with each other. They intersect at so-called homoclinic points.[1] The free ends of these branches form an infinite number of loops with an infinitely increasing length that fill a narrow region near the unperturbed separatrices and create a chaotic layer. This layer can be subdivided into three parts: the top part (the phase x rotates at the top, $p > 0$), the middle part (the phase oscillates), and the bottom part (the phase x rotates at the bottom, $p < 0$). Determination of the sizes of these parts, which may be substantially different for an asymmetrical perturbation like (2), is of great importance from the practical standpoint [8–10].

The formation of a chaotic layer in the case of a symmetrical high-frequency perturbation of the type

$$V(x, t) = \varepsilon\cos\left(\frac{m}{2}x - \Omega t\right) + \varepsilon\cos\left(\frac{m}{2}x + \Omega t\right), \qquad (3)$$

where $\Omega \gg \omega_0$ and m is an integer, was studied in detail by Chirikov [1].

Using the properties of standard mapping and his criterion for resonance overlapping, Chirikov showed

[1] Such a splitting does not always happen in systems with a smooth potential. Striking situations where the separatrices of both fractional and integer resonances remain intact in piecewise linear systems despite the presence of a perturbation and strong local chaos are discussed in [4–6].

1063-7842/04/4905-0521$26.00 © 2004 MAIK "Nauka/Interperiodica"

that, in the high-frequency limit, all three parts of the layer are of equal size:

$$w_{tp} = |w_{md}| = w_{bt} = \lambda W, \quad \lambda \longrightarrow \infty, \tag{4}$$

where $\lambda = \Omega/\omega_0$ is the so-called adiabaticity parameter and $w = H(x, p, t)/\omega_0^2 - 1$ is the relative deviation from the unperturbed separatrix in terms of energy.

The variable W appearing in (4) is the amplitude of the harmonic (with a frequency Ω) of the separatrix map for the set of equations (1) and (3). This map, first introduced in [7], approximately describes the dynamics of a system near the separatrix when it passes through the states of stable equilibrium (see also [1]).

The theoretical value $W = W_T$ is related to the Mel'nikov–Arnold integrals $A_m(\lambda)$ [1] by the relationship

$$W_T(\lambda) = \varepsilon\lambda A_m(\lambda). \tag{5}$$

In this paper, these integrals are also used. According to [1], they are defined as

$$A_m(\lambda > 0) = \frac{2\pi}{(m-1)!}\frac{\exp(\pi\lambda/2)}{\sinh(\pi\lambda)}(2\lambda)^{m-1}[1 + f_m(\lambda)], \tag{6}$$

$$A_m(\lambda < 0) = (-1)^m A_m(|\lambda|)\exp(-\pi|\lambda|), \tag{7}$$

$$f_1 = f_2 = 0, \quad f_{m+1} = f_m - (1 + f_{m-1})\frac{m(m-1)}{4\lambda^2}, \quad m \geq 3. \tag{8}$$

It should be stressed that expressions (6)–(8) were derived in [1] for the general case, i.e., without any assumptions or simplifications. Therefore, they are valid for any λ from the range $0 < \lambda < \infty$.

The pattern drastically and qualitatively changes when a high-frequency perturbation becomes asymmetric, $\Omega_1 \neq \Omega_2$. Even early numerical simulations [8, 9] showed that the separatrix map spectrum of such a system involves (along with the frequencies Ω_1 and Ω_2, appearing in perturbation (2) in explicit form) mixed harmonics ($\sim\varepsilon_1\varepsilon_2$) with the frequencies $\Delta\Omega_+ = \Omega_1 + \Omega_2$ and $\Delta\Omega_- = \Omega_2 - \Omega_1$. Still more surprising is the fact that these harmonics completely determine the size of the chaotic layer under certain conditions. The case when the contribution of the mixed harmonic with $\Delta\Omega_+ = 3$ to the separatrix map amplitude is several hundred times greater than the contributions from the primary harmonics is described in [9]. The impression that weak initial harmonics give rise to an intense secondary harmonic and then do not contribute to the formation of chaos has been conclusively supported by numerical simulation performed in [9].

In Sect. 2, we will show that the specific role of mixed harmonics disappears at low frequencies and their influence becomes insignificant. For this reason, we consider only the fundamental chaotic layer of system (1) subjected to symmetric perturbation (3) at fixed frequencies of the perturbation, $\varepsilon = 0.01$, and weak oscillations, $\omega_0 = 1.0$ (unless otherwise specified). The high-frequency range considered above is complemented by the ranges of medium and low frequencies, which makes it possible to characterize the layer throughout the range $0 < \lambda < \infty$.

1. SEPARATRIX MAP AMPLITUDE

Two basic methods for calculating the sizes of the chaotic layer are known. In the first method, the minimum period $T_{0,\min}$ of motion in a given region of the layer is found (T_0 is the time interval between two successive intersections of the equilibrium phase $x = \pi$). Then, the energy size of this region is determined by the formula [1]

$$w = 32\exp(-\omega_0 T), \tag{9}$$

where T means $T_{0,\min}$.

The second method implies the construction of the separatrix map of the system,

$$\bar{w} = w + W\sin\psi, \quad \bar{\psi} = \psi + \lambda\ln\left(\frac{32}{|\bar{w}|}\right), \quad \psi = \Omega T_0 \bmod(2\pi) \tag{10}$$

and the application of the iteration procedure.

We will briefly recall the numerical algorithm for constructing such a map (for details, see [8]). First, a central homoclinic point p_{pb} as a boundary between the oscillation and rotation of the phase is found with a high accuracy at the line of symmetry $x = \pi$. A narrow interval $p_{pb} + \delta p$ is chosen in the vicinity of this point at $x = \pi$, and a random path is emitted from the interval. This path either executes a prescribed number of cycles of motion or is interrupted because of the transition to another region of the layer. In both cases, a new random path is emitted from the same region until a desired number of cycles N is achieved. The mean energy w is calculated for each of the cycles by formula (9). By determining the energy variation $\delta w = \bar{w} - w$ for each pair of adjacent cycles and assigning it to a time T_0 that is common for a given pair, one can construct separatrix map (10) $(\delta w)_k$ with $T_{0,k}$, where $k = 1, 2, \ldots, N-1$. To be definite, we will investigate the top part of the layer, since its size is equal to that of the bottom part, $w_{tp} = w_{bp}$, in the case of symmetric perturbation. These outer parts are of primary interest, since they are responsible for overlapping adjacent resonances and generating global chaos. As we shall see, map (10) may involve not only one but also several harmonics (see Sect. 3).

Numerical (estimated) results for the separatrix map amplitude W_E should be compared with the theoretical values W_T calculated via the Mel'nikov–Arnold inte-

grals by the formula

$$W_T(\lambda) = \varepsilon\lambda S_m(\lambda), \quad (11)$$

where the sum

$$S_m(\lambda) = A_m(|\lambda|)(1 + (-1)^m \exp(-\pi|\lambda|)) \quad (12)$$

takes into account the influence of both harmonics of the symmetric perturbation. From expressions (6) and (8), it follows that, for $m \geq 3$, these integrals, along with the bracketed factor, vanish at certain $\lambda = \lambda_0$. We use the integrals A_2 and A_4 as examples. The former does not vanish; the latter vanishes at $\lambda_0 = \sqrt{2}$.

2. LOW-FREQUENCY ASYMPTOTICS

Figure 1 compares the normalized separatrix map amplitudes for the top part of the chaotic layer that are found numerically, $W_E^* = |W_E|/\varepsilon$, and calculated using formula (11), $W_T^* = |W_T|/\varepsilon$, for symmetric perturbation (3) as functions of the adiabaticity parameter for $m = 2$ and $m = 4$. As is seen, the theoretical curve W_T^* is in fairly good agreement not only with the high-frequency range $\lambda \gtrsim 5$, which was thoroughly studied by Chirikov, but also with the low-frequency range $\lambda \lesssim 0.1$, where the amplitude is proportional to the adiabaticity parameter: $W_T \sim \lambda$.

This fact is consistent with the theory, since the sum of the integrals appearing in (12) tends to a λ-independent constant $S_m(\lambda) \longrightarrow s_m = \text{const}$,

$$s_1 = 2\pi, \quad s_2 = 8, \quad s_3 = 2\pi, \quad s_4 = 32/3, \quad s_5 = 2\pi, \ldots \quad (13)$$

in the low-frequency limit $\lambda \longrightarrow 0$, while amplitude (11) approaches $W_T \longrightarrow \varepsilon s_m \lambda$. Map (10) takes the form

$$\bar{w} = w + c\lambda \sin\psi, \quad \bar{\psi} = \psi + \lambda \ln\left(\frac{32}{|\bar{w}|}\right),$$

where $c = \varepsilon s_m = \text{const}$.

If $\lambda \ll 1$, the difference equations can be replaced by the differential equations [1]

$$\frac{dw}{dt} = \frac{c\lambda \sin\psi}{T_s}, \quad \frac{d\psi}{dt} = \frac{\lambda \ln(32/|\bar{w}|)}{T_m},$$

where T_m is the mapping period.

This yields

$$\frac{dw}{d\psi} = \frac{c \sin\psi}{\ln(32/|\bar{w}|)}$$

and we see that $w(\psi)$ is independent of the adiabaticity parameter λ. This takes place if the layer size w_{tp} and

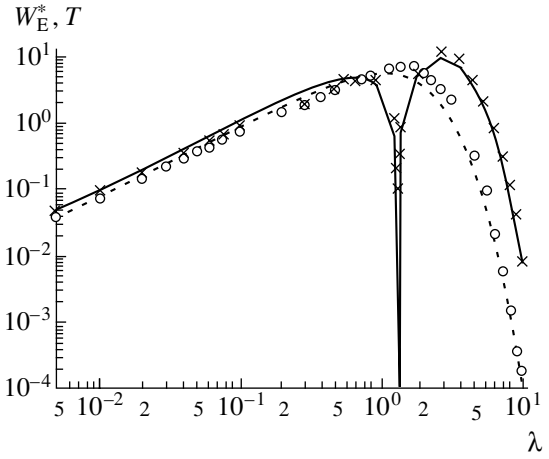

Fig. 1. Symmetric system given by (1) and (3). The normalized separatrix map amplitudes found numerically, W_E^* (symbols), and those calculated by (11), W_T^* (curves), are shown as functions of the adiabaticity parameter λ. The circles and dashed curve correspond to $m = 2$; the crosses and solid curve, to $m = 4$.

separatrix map amplitude W are assumed to be related as

$$w_{tp} \approx b\frac{W}{\lambda} \approx 0.22 s_m = \text{const}, \quad \lambda \longrightarrow 0, \quad (14)$$

at low perturbation frequencies. Here, s_m is the limit of (3) and $b \approx 0.22$ is an empirical factor.

Dependence (14) is supported by numerical simulations (the horizontal portions in Fig. 3).

Thus, in the low-frequency limit, the size of the chaotic layer is independent of the frequency, unlike the high-frequency case, where this dependence is exponential (see (5) and (6)). Above, we noted the special role of mixed (secondary) perturbation harmonics (with frequencies that are combinations of high frequencies of the primary harmonics) in the formation of chaos. The exponential dependence constitutes the basis for this phenomenon, since it allows even very weak but low-frequency harmonics to contribute to chaotic layer formation. In the low-frequency limit, the situation changes drastically: the secondary harmonics turn into small corrections on the order of $\varepsilon_1\varepsilon_2$, and their influence is negligible.

3. MEDIUM-FREQUENCY PERTURBATIONS

The most interesting dynamic effects are observed in the medium-frequency range $0.1 \gtrsim \lambda \gtrsim 5$, where the adiabaticity parameter can be considered neither small nor large. This range is hard to describe theoretically, especially in the vicinity of the zero $\lambda_0 = \sqrt{2}$ of the integral $A_4(\lambda_0) = 0$) (the vertical line in Fig. 1), where $W_T = 0$, whereas the experimental value is finite: $W_{exp}^* \approx$

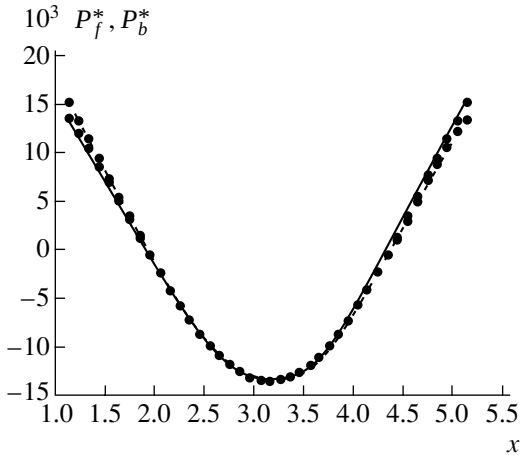

Fig. 2. System given by (1) and (3) with $m = 4$. The intersection of the branches of the fundamental resonance separatrix at $\lambda = 1.3986685\ldots$ is shown. The solid curve shows the relative values of P_f^*; the dashed curve, P_b^*.

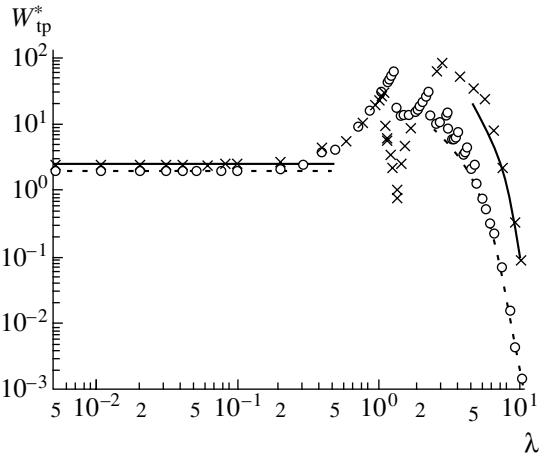

Fig. 3. Symmetric system given by (1) and (3). The numerically found dependence of the normalized size W_{tp}^* of the chaotic layer on the adiabaticity parameter λ. The dashed curves and circles correspond to $m = 2$; the solid curves and crosses, to $m = 4$.

0.103. For this reason, the results discussed below were found numerically.

Systems analysis shows that, in this frequency range, the separatrix map of the system stated by (1) and (3) contains the harmonic at the fundamental frequency Ω and also the harmonic at the doubled frequency 2Ω. Moreover, for $m = 4$, the amplitude $W(\Omega)$ of the fundamental harmonic vanishes at $\lambda = \lambda_1 = 1.4175\ldots > \lambda_0$ and then appears again but with opposite sign. The value of λ_1 varies with the perturbation ε. As λ becomes smaller or larger than λ_1, the influence of the double-frequency harmonics weakens and almost disappears at the boundaries of both asymptotic regions.

The double-frequency harmonic is a secondary one. Its amplitude is proportional to the perturbation squared, $\sim\varepsilon^2$, which is confirmed by the results of numerical experiment, and can be found by the method used in [8] to calculate the amplitudes of secondary harmonics at combined primary frequencies. This method uses variables similar to the coordinate and momentum on an unperturbed separatrix. The expression for this amplitude is omitted here because of its awkwardness; however, it is worth noting that it involves the Mel'nikov–Arnold integrals in the form $A_{m-2}(2\lambda)$ and $A_{m+2}(2\lambda)$.

As is known, valuable information on the behavior of separatrix branches for both integer and fractional resonances can be found by measuring the angle these branches make at the central homoclinic point (see Introduction). This angle is one of a few chaos parameters that can be measured as accurately as desired (for details, see [10]), and its nonzero value is a reliable indication that the separatrices are split. In what follows, we will show that the reverse statement is incorrect.

In the case of perturbation (3) with $m = 2$, the angle between the separatrix branches in the medium-frequency range retains its sign. For $m = 4$, it passes through zero at $\lambda = \lambda_2 = 1.3986685\ldots < \lambda_0$ and then changes sign. The value of λ_2 varies with ε.

In studies of smooth piecewise linear maps, it was assumed that the zero value of this angle always means the retention of the separatrix and the absence of the chaotic layer (see, e.g., [5]). This was also supported by numerical experiments. However, the phase portrait of the system stated by (1) and (3) at $\lambda = \lambda_2$ showed that the separatrix of fundamental resonance is broken making room for an intense chaotic layer. In order to gain insight into this fact, we studied the intersection of the separatrix branches in this case in greater detail.

Let $P_f^* = p_f/p_{s,0} - 1$ be the relative deviation of the separatrix branch from its unperturbed value $p_{s,0} = 2\omega_0\sin(x_s/2)$ [1] for forward time and P_b^* be the same for backward time. Figure 2 shows the intersection of the branches of the upper separatrix at $\lambda = \lambda_2 = 1.3986685\ldots$ in the neighborhood of the central homoclinic point $x = \pi$, which turns out to be an inflection point. That is, the angle between the branches and the slope of the tangent pass through zero simultaneously and then the branches diverge from each other. This example demonstrates that the zero value of the angle between the separatrix branches at the central homoclinic point (and, hence, at any homoclinic point) is not a sufficient condition for separatrix retention, which is contrary to the statement put forward in [5]. Another example of such behavior of the separatrix branches can be found elsewhere [11].

4. CHAOTIC LAYER

Figure 3 shows the normalized sizes $W_{tp}^* = w_{tp}/\varepsilon$ of the top part of the fundamental chaotic layer that were found numerically from the minimum period of motion (see (9)) (each point was calculated for 5×10^6 periods of motion).

The horizontal portions on the left of the plot, which were calculated by (14), correspond to the asymptotic values in the low-frequency limit $\lambda \longrightarrow 0$. The curved portions on the right of the plot, which were calculated by formulas (4) and (5), show the degree of agreement between the theory and experiment for high-frequency perturbations. However, the theory fails in the medium-frequency range, and one has to employ approximate and numerical methods of analysis.

A characteristic feature of the λ dependence of the layer size w_{tp}^* is its discontinuity (although the separatrix map amplitude is smooth, see Fig. 1), which greatly complicates the elaboration of a theory in this frequency range. A number of discontinuities are well seen in Fig. 3 ($m = 2$), and others are observed on an enlarged scale. Such a structure is quite natural and is explained in terms of modern dynamics concepts in the following way. As λ decreases, the invariant curves with irrational rotational numbers give way to so-called Cantori [12]. If such a curve is a boundary between the fundamental chaotic layer and a nearby resonance of separatrix mapping, these objects merge together and the layer size increases stepwise by a finite value, i.e., by the phase volume of the resonance attached. As was noted in [1], the step is maximal when the chaotic layer merges with an integer resonance. The main difficulty here is the need for constructing the pattern of resonances in the vicinity of the chaotic layer boundary and also for finding the separatrix map amplitude corresponding to resonance overlapping.

An efficient method for solving this problem seems to be the one based on so-called resonance invariants, which make it possible to obtain such a pattern without numerically constructing the paths. Invariants of first three orders (resonances 1 : 1, 1 : 2, and 1 : 3) for separatrix mapping have been recently proposed in [13, 14]. In those works, these invariants, along with the well-known Chirikov criterion for resonance overlapping, are used to study the chaotic layer dynamics and calculate stepwise changes in its size in the medium-frequency range at $\lambda = 3$.

Like any analytical algorithm, these invariants are unable to catch a chaotic component of motion; therefore, they "draw" pure separatrices of resonances instead of real chaotic layers [14, Figs. 2–4]. This fact substantially simplifies the estimation of the resonance arrangement.

In [13, 14], good agreement between the resonance patterns constructed from invariant level curves and found by direct numerical iteration of separatrix maps is demonstrated and some technical details are discussed.

CONCLUSIONS

The model of a perturbed pendulum is widely used for studying many real dynamic systems, so that the construction a chaotic layer for such a model throughout the range of perturbation frequencies seems to be necessary. The known results for the high-frequency asymptotics are complemented by those for the low-frequency range; however, the medium-frequency range of perturbation frequencies calls for further investigation.

ACKNOWLEDGMENTS

The author is grateful to B.V. Chirikov for discussion and advice.

This study was supported in part by the Russian Foundation for Basic Research (project no. 01-02-16836) and the Scientific Program "Mathematical Methods in Nonlinear Dynamics" of the Russian Academy of Sciences.

REFERENCES

1. B. V. Chirikov, Phys. Rep. **52**, 263 (1979).
2. A. Lichtenberg and M. Lieberman, *Regular and Chaotic Dynamics* (Springer, New York, 1992).
3. G. M. Zaslavsky and R. Z. Sagdeev, *Introduction to Nonlinear Physics: from Pendulum to Turbulence and Chaos* (Nauka, Moscow, 1988; Harwood, Chur, 1988).
4. S. Bullett, Commun. Math. Phys. **107**, 241 (1986).
5. V. V. Vecheslavov, Preprint No. 2000-27 IYAF (Budker Institute of Nuclear Physics, Siberian Division, Russian Academy of Sciences, Novosibirsk, 2000); nlin.CD/0005048.
6. V. V. Vecheslavov and B. V. Chirikov, Zh. Éksp. Teor. Fiz. **120**, 740 (2001) [JETP **93**, 649 (2001)].
7. G. M. Zaslavsky and N. N. Filonenko, Zh. Éksp. Teor. Fiz. **54**, 1590 (1968) [Sov. Phys. JETP **27**, 851 (1968)].
8. V. V. Vecheslavov, Zh. Éksp. Teor. Fiz. **109**, 2208 (1996) [JETP **82**, 1190 (1996)].
9. V. V. Vecheslavov, Pis'ma Zh. Éksp. Teor. Fiz. **63**, 989 (1996) [JETP Lett. **63**, 1047 (1996)].
10. V. V. Vecheslavov and B. I. Chirikov, Zh. Éksp. Teor. Fiz. **114**, 1516 (1998) [JETP **87**, 823 (1998)].
11. V. V. Vecheslavov, Preprint No. 2002-51 IYAF (Budker Institute of Nuclear Physics, Siberian Division, Russian Academy of Sciences, Novosibirsk, 2002).
12. R. S. MacKay, J. D. Meiss, and I. C. Percival, Physica D **13**, 55 (1984).
13. V. V. Vecheslavov, Physica D **131**, 55 (1999).
14. V. V. Vecheslavov, Zh. Tekh. Fiz. **72** (2), 20 (2002) [Tech. Phys. **47**, 160 (2002)].

Translated by M. Fofanov

Technical Physics, Vol. 49, No. 5, 2004, pp. 526–531. Translated from Zhurnal Tekhnicheskoĭ Fiziki, Vol. 74, No. 5, 2004, pp. 6–11.

THEORETICAL AND MATHEMATICAL PHYSICS

Clustering in Determinate and Stochastic Fields

S. A. Kapliĭ[1], A. V. Prokaznikov[1,2], and N. A. Rud'[1]

[1] *Demidov State University, Sovetskaya ul. 14, Yaroslavl, 150000 Russia*

[2] *Institute of Microelectronics and Informatics, Russian Academy of Sciences, ul. Universitetskaya 21, Yaroslavl, 150007 Russia*

e-mail: rnrgio@yandex.ru

Received July 8, 2003

Abstract—Computer models of gradient-controlled growth are studied. Algorithms used in this class of models allow for the formation of a variety of clusters that have different, including fractal, structures. The problem of formation of nonbranching isolated vertical clusters is solved by using an algorithm that corresponds to a high-gradient long-range potential concentrated in a narrow interval. © *2004 MAIK "Nauka/Interperiodica".*

INTRODUCTION

Investigations into coherent phenomena in stochastic systems are of interest, since their results may find application in various areas of physics. These phenomena are characterized by clustering in stochastic systems under certain conditions. Clustering arises in the frameworks of various models that are in many respects similar to those that describe coherence in dynamic systems. One problem associated with this class of phenomena is impurity clustering in random velocity fields. The basic feature of this problem is the cluster structure of the impurity concentration field. This feature shows up as causticity resulting from focusing and defocusing in a random medium [1].

The problem studied in this work may be stated as follows. In the simplest case, a particle ensemble moving in the random velocity field is described by a set of ordinary first-order differential equations [1]

$$\frac{d\mathbf{r}}{dt} = \mathbf{U}(\mathbf{r}, t), \quad \mathbf{r}(t_0) = \mathbf{r}_0, \tag{1}$$

where $\mathbf{U}(\mathbf{r}, t) = \mathbf{u}_0(\mathbf{r}, t) + \mathbf{u}(\mathbf{r}, t)$, $\mathbf{u}_0(\mathbf{r}, t)$ is the determinate component of the velocity field, and $\mathbf{u}(\mathbf{r}, t)$ is the random component.

Formally, Eq. (1) means that each of the particles moves independently. However, if the random field $\mathbf{u}(\mathbf{r}, t)$ has a finite correlation length l_{cor}, all particles at a distance of less than l_{cor} from each other are under the influence of the random field $\mathbf{u}(\mathbf{r}, t)$ and the dynamics of such an ensemble may exhibit new collective features. For example, in the case of the potential velocity field ($\mathbf{u}(\mathbf{r}, t) = \nabla\psi(\mathbf{r}, t)$), particles regularly arranged within a square at zero time form clusters during evolution [1].

The problem of clustering is also related to the formation of voids in semiconductor crystals, such as porous silicon [2], and in materials prepared by sintering fine-grain powders [3]. Thus, the problem under study is of interest in various fields of contemporary physics.

Computer simulation can solve a wide variety of algorithmic problems whose asymptotic behavior sometimes cannot be derived by any other means. Attempts to study void formation with computer models have been made repeatedly [4]. However, an exhaustive model of void formation has not yet been developed. So, further efforts in this direction are necessary.

PROBLEM DEFINITION AND BASIC RESULTS

In this work, we study clustering on one of the flat sides of a rectangular domain (slab) covered by a square grid. A potential is applied between opposing flat sides. Unlike the problem touched upon in [1], we consider the random walk of particles in a constant potential field of several seeds, while in [1] the dynamics of the system is governed by a stochastic time-dependent field with a certain correlation length. In simulation, we use three specially shaped seeds whose positions are fixed.

Our goal is to find the position of a cluster on the seeds under the action of the seed-induced potential field and the self-field of the cluster. We also seek the conditions under which vertical, weakly branching, and isolated clusters form.

According to Eq. (1), the motion of a particle depends on the determinate, $\mathbf{u}_0(\mathbf{r}, t)$, and stochastic, $\mathbf{u}(\mathbf{r}, t)$, components. The former is defined by the field of needlelike seeds, while the latter, which causes random walk over the square mesh, is described by the Metropolis walk algorithm [5]. The probability of displacement to an adjacent position is specified by a potential gradient in nearby sites so that the probability of a jump to a higher potential state is higher.

1063-7842/04/4905-0526$26.00 © 2004 MAIK "Nauka/Interperiodica"

The simulation of the field distribution is based on the following assumptions. For simplicity, the initial shape of the seeds on the upper side of the slab is approximated by a hyperboloid of revolution [6]. A potential is applied between the upper and lower sides (boundaries) of the slab. The potential is calculated by the Lamé method (for details, see [6]). Calculations [6] show that the field potential φ in this case is a function of a parameter λ and is given by

$$\varphi(\lambda) = \varphi_0 \frac{\ln\left(\frac{b(\lambda)+\lambda}{b(\lambda)-\lambda}\right)}{\ln\left(\frac{b_{\max}+\lambda_{\max}}{b_{\max}-\lambda_{\max}}\right)}, \qquad (2)$$

if the potential difference between the needle and the lower boundary is $\varphi_r = \varepsilon_{Si}\varphi_0$, where ε_{Si} is the permittivity of silicon and φ_0 is the potential difference dimension parameter used in simulation. The quantity $(b^2(\lambda) - \lambda^2)^{1/2}$ was approximated by the linear function $(b^2(\lambda) - \lambda^2)^{1/2} = p\lambda + q$ [6]. Then, $b(\lambda) = (\lambda^2(1 + p^2) + 2pq\lambda + q^2)^{1/2}$ [6], $p = (d_{\min} - d_{\max} + 2D)/(\lambda_{\max} - \lambda_{\min})$, $D = \alpha(\lambda_{\max} - \lambda_{\min})$ is the seed spacing, $q = [\lambda_{\max}(d_{\max} + 2D) - \lambda_{\min}d_{\min}]/(\lambda_{\max} - \lambda_{\min})$ is the thickness of the slab, $b_{\max} = b(\lambda_{\max})$, $d_{\min}$ is the size of the seed, α is a variate, and $d_{\max}$ is the parameter corresponding to the value $\lambda_{\min}$ at which equipotential curves degenerate into a straight line.

In the 2D case with a single needlelike seed, equipotentials are described by the equation of a parabola with the parameters λ^2 and $(b^2 - \lambda^2)$ [6]. By variously approximating the quantity $(b^2 - \lambda^2)^{1/2}$, we could vary the rate of expansion of the parabola with distance from the boundary and thereby simulate both short- and long-range potentials (see below).

A computer algorithm was constructed so as to simulate the formation of a 2D cluster under the action of the potential of three needlelike seeds. Simulation was carried out in the $2(D + d_{\max})(\lambda_{\max} - \lambda_{\min})$ rectangular domain, which was split into squares with sides Δx. To obtain the net (three-seed) potential distribution, we calculated the right-hand side of the field induced by one seed placed in the extreme position. Then, by applying the principle of superposition to the fields and using the symmetry of the problem, the net field of the three equidistant seeds was constructed. Each mesh was assigned a calculated value of the field. Eventually, we obtained the discrete distribution of the potential ϕ_{ij} of the seeds (Fig. 1).

A cluster grew when particles walked over the square grid from the lower to the upper flat boundary, where the three needlelike seeds were located. The random walk algorithm was based on the Metropolis algorithm [5]. The path of a particle that is in a mesh (i, j) was simulated in the vicinity of the four nearest neighbors that have mutual boundaries with the mesh (i, j). Then, the probability of transition from the mesh (i, j)

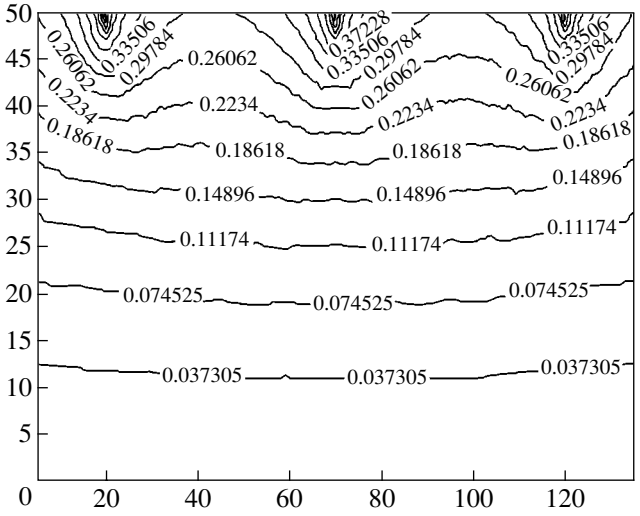

Fig. 1. Distribution of the electric potential from three equidistant seeds. Data shown in the figure are obtained for $(b^2(\lambda) - \lambda^2)^{1/2} = p\lambda + q$, $\varphi_0 = 1$, and $\alpha = 1$.

into a mesh (i', j') in this vicinity was calculated by the formula

$$p[(i, j) \longrightarrow (i', j')] = \frac{\phi_{(i, j)(i', j')}}{\sum_{\Pi} \phi_{(i, j)(i', j')}}, \qquad (3)$$

where

$$\phi_{(i, j)(i', j')} = \frac{1}{n} + \frac{|\varphi_{i, j} - \varphi_{i', j'}|}{|r_{ij} - r_{i', j'}|}; \qquad (4)$$

φ_{ij} and $\varphi_{i'j'}$ are the potentials in the meshes (i, j) and (i', j'), respectively; $n \le 4$ is the number of meshes accessible for the transition; and Π is the vicinity of the mesh (i, j).

The transition of the particle from the state (i, j) to the state (i', j') occurs with related (calculated) probability. The process lasts until the particle reaches the upper boundary or is attached to a forming cluster. For the particle to be attached to the cluster, the ratio of the number of cluster-constituting points within a domain of characteristic radius R_{char} to the number of nearest meshes that have mutual vertices must be larger than a certain value η (the sticking coefficient). This coefficient defines the depth of penetration of a particle into a cluster and, as will be shown later, the inner structure of the cluster. The stopped particle forms the cluster structure. The distance over which a growing cluster influences a particle depends on the radius R_{char}. All points of the cluster falling into the circle of radius R_{char} contribute to the static potential induced in each of the

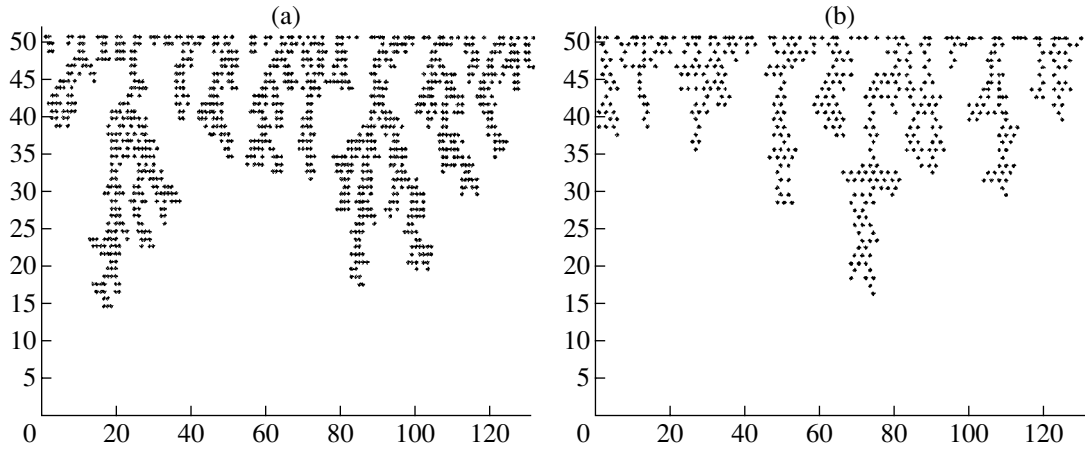

Fig. 2. Results of computer simulation with the standard algorithm of irreversible gradient-controlled growth for $\alpha = 1$, $\varphi_0 = 1$, $\sigma = 0.1$, $\beta = 1.3 \times 10^{-5}$. (a) The sticking coefficient η was calculated by taking into account eight nearest neighbors, the fractal dimension is $D_f = 1.719$–1.802, and the number of points in a cluster is $N = 1100$; (b) the sticking coefficient η was calculated by taking into account 12 nearest neighbors, $D_f = 1.612$–1.682, and $N = 500$.

meshes by its neighborhood according to the formula [7]

$$\psi_{iji'j'}(r_{ij} - r_{i'j'}) = \frac{\sigma_{i'j'}}{|r_{ij} - r_{i'j'}|} e^{-\beta(r_{ij} - r_{i'j'})}, \quad (5)$$

so that

$$\psi_{ij} = \sum_{|r_{ij} - r_{i'j'}| < R_{\text{char}}} \frac{\sigma_{i'j'}}{|r_{ij} - r_{i'j'}|} e^{-\beta(r_{ij} - r_{i'j'})}, \quad (6)$$

where $\sigma_{ij} = \sigma$ is the charge of a mesh, $\beta = 1/r_0$ is the screening constant, and r_0 is the screening length.

The potential ψ is added to the potential φ induced by the seeds (see formula (2)). The contribution to the net field is calculated only for outer points of the cluster, since they screen inner ones.

The application of this algorithm results in the formation of branching clusters with a mutual base (i.e., nonisolated). As the potential decreases, clusters become more extended and more isolated, as well as closer related to the initial seeds. Similar effects were observed in experiments [8, 9]. Our algorithm does not lead to the formations of isolated nonbranching vertically growing clusters (Fig. 2).

The structures shown in Figs. 2a and 2b differ in particle attachment conditions. The structure in Fig. 2a takes into account eight nearest neighbors, while that in Fig. 2b includes 12 neighbors. The fractal dimension was found by plotting the weight of a cluster against the radius of the circumscribed circle in the log–log coordinates [10]. For the clusters in Fig. 2a, the fractal dimension is $D_f = 1.719$–1.802. Similarly, for the clusters in Fig. 2b, $D_f = 1.612$–1.682. It should be noted that, for random walk over a triangular grid, the number of nearest neighbors is 12. As is distinctly seen in Fig. 2b, the structures being formed on the square grid have triangular elements. This is because the number of neighbors taking part at the final stage of clustering is 12. Thus, triangular elements may also form on a square grid under certain conditions. Similar effects were observed when silicon was anodized in a solution of hydrofluoric acid. For example, fractal structures like Serpinsky gaskets were discovered in [11].

It was shown [12] that fractal dimension is not universal; that is, it depends not only on the dimensionality of a grid used in numerical simulation but also on its structure. For example, the fractal dimension is predicted to be 5/3 for a 2D square grid and 7/4 for 2D hexagonal and triangular grids [12]. The results shown in Fig. 2 suggest that the fractal dimension also to a great extent depends on other simulation parameters, such as the growth-controlling sticking coefficient gradient, etc.

To simulate the growth of nonbranching isolated vertical clusters, we applied an algorithm including the statements mentioned above and an algorithm with a moving lower boundary that is similar to that used in [13]. Such a combined algorithm leads to the formation of more extended and less branching clusters, since the initial coordinates of most particles are generated near fast-growing branches of a cluster, favoring their growth. However, the combined algorithm, too, failed to provide the growth of nonbranching isolated vertical clusters (Fig. 3).

To simulate potentials slowly descending at large distances, the parameter $(b^2(\lambda) - \lambda^2)^{1/2}$ was approximated by logarithmic and inversely proportional dependences: $(b^2(\lambda) - \lambda^2)^{1/2} = p\ln(\lambda) + q$ and $p/\lambda + q$. In this case, the hyperbola's branches expand appreciably farther from the upper boundary (Fig. 4), and clusters being formed become more extended. In formula (2), the parameter b may be independent of λ. Qualitatively,

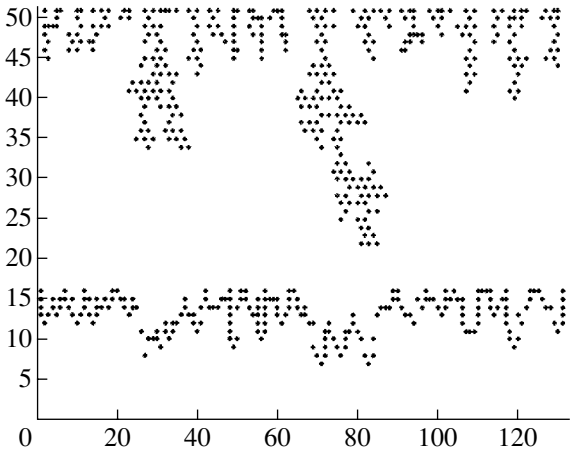

Fig. 3. Typical cluster obtained in terms of the moving-boundary model for $\alpha = 1$, $\varphi_0 = 1$, $\sigma = 0.1$, $\beta = 1.3 \times 10^{-5}$, and $N = 350$. The sticking coefficient was calculated by taking into account 12 nearest neighbors, and the fractal dimension is $D_f = 1.628$.

the picture is similar to that observed when $(b^2(\lambda) - \lambda^2)^{1/2}$ is approximated by the linear function.

Careful examination of the resulting potential and calculated transition probabilities reveals the following effect. On vertical lines strictly under the seeds, the probability of a sideward jump is higher than that of a jump in the vertical direction. These vertical lines are not lines of strong attraction, as was expected from qualitative considerations in view of the fact that the electric field along them is the highest; instead, they behave as lines of local scattering, for which the staying probability is lower than the escape probability. It appears that the potential on the vertical lines is high but varies slowly from mesh to mesh along them. At the same time, in going from the vertical line to a sideward mesh, the potential changes more appreciably. Because of this effect, a walking particle leaves the vertical line, although the potentials vary in a narrow range, and growing clusters are more branched (Fig. 4) than when this effect is suppressed (Fig. 5).

In order to suppress this effect and find conditions for the growth of nonbranching isolated vertical clusters, we proceeded as follows. The probability of jumps from a given mesh was modulated (by introducing a special correction) so as to raise the probability of jumps in the vertical direction; in other words, the anisotropy of the system was increased. Let the probabilities (calculated by the basic algorithm) that a particle jumps leftward, rightward, downward, and upward be p_l, p_r, p_d, and p_u, respectively. Then, the modulated probabilities for leftward, rightward, downward, and upward jumps are expressed as $p_l' = p_l - kp$, $p_r' = p_r - kp$, $p_d' = p_d - 2kp$, and $p_u' = p_u + 4kp$, where kp is the modulating parameter.

This procedure was applied in two versions. In the first version, the jump probability was modulated irrespective of the particle's position; in the second, the probability modulation was carried out only for particles opposite to the seed. In the second case, the problem of nonbranching isolated vertical clusters was solved (Fig. 5): the clusters grew stably and almost without branches. This procedure takes into account the second term in the potential expansion (see expression (7) and relevant comments). In most cases, anisotropy prevents the formation of fractal structures [14].

Note that numerical simulation performed in this work was based on six algorithms.

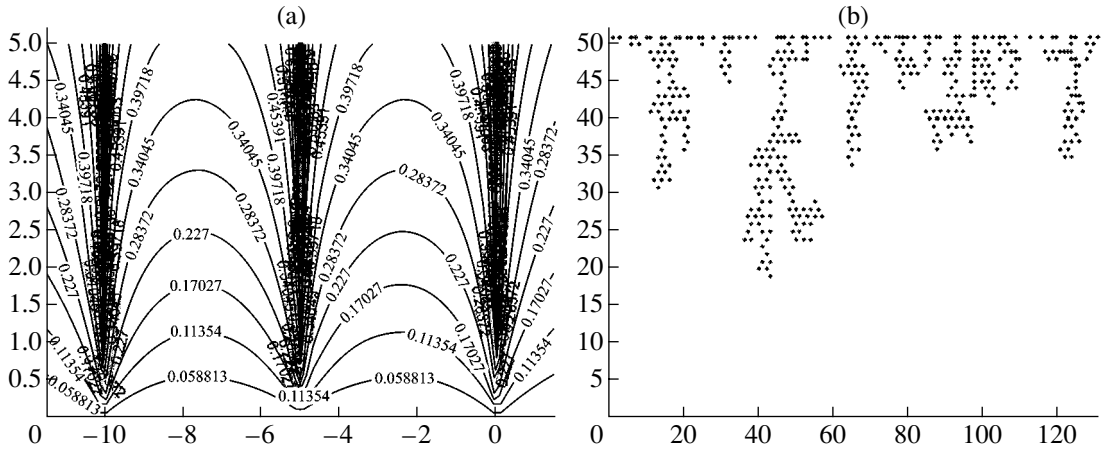

Fig. 4. (a) Distribution of the electric potential from three equidistant seeds. Data shown in the figure are obtained for $(b^2(\lambda) - \lambda^2)^{1/2} = p/\lambda + q$, $\varphi_0 = 1$, and $\alpha = 1$. (b) Typical cluster obtained in terms of the moving-boundary model for $\sigma = 0.1$, $\beta = 1.3 \times 10^{-5}$, and $N = 500$. The sticking coefficient was calculated by taking into account 12 nearest neighbors.

PHYSICAL INTERPRETATION

The problem under study is closely related to void formation in semiconductor crystals, for example, during anodizing of silicon in a solution of hydrofluoric acid. It is known that voids forming during this process contain quantum-size objects. It is expected that the solution of the problem stated will elucidate reasons for sharp anisotropy in void formation, specifically, for the formation of strictly vertical branching pores (trenches).

Let the thickness of a silicon wafer where anodizing causes voids be 500 μm. This corresponds to 50 meshes in the vertical direction. Thus, the size of a square mesh is $10^{-3} \times 10^{-3}$ cm.

For T = 300 K, the impurity concentration n = 10^{15} cm^{-3}, the permittivity of silicon $\varepsilon_{Si} = 11.8$, and the screening length is $\beta = 1.3 \times 10^{-5}$ cm [7].

The parameter σ corresponds to the number of holes in a unit volume $\Delta V = (\Delta x)^3 = 10^{-9}$ cm^3 ($\Delta x = 10^{-3}$ cm). Estimates show that the excess hole concentration at the surface of *n*-Si due to band bending is much lower than the concentration of holes generated by illumination. For typical light fluxes used in our experiment, J = 10^{19} photons/cm^2, the value of σ is no greater than 0.1 absolute electrostatic units. The applied potential was, as a rule, in the range $0 \le \varphi_r \le 120$ V ($\varphi_r = \varphi_0 \varepsilon_{Si}$).

DISCUSSION

We studied computer models of gradient-controlled growth. As follows from the results of computer simulation, taking into account the determinate and stochastic components of the velocity of a particle walking over a square grid generates a wide class of cluster structures. These structures have a wide range of fractal dimensions depending on model parameters.

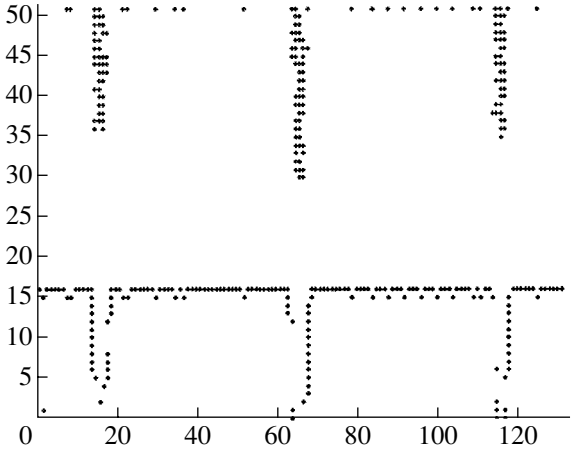

Fig. 5. Typical cluster obtained in terms of the second version of the moving-boundary model for $\alpha = 1$, $\varphi_0 = 1$, σ = 0.1, $\beta = 1.3 \times 10^{-5}$, and N = 394. The sticking coefficient was calculated by taking into account eight nearest neighbors. The probability was modulated in an interval of thickness 3 with a coefficient kp = 0.1.

It was found that isolated nonbranching vertical clusters grow if the electric potential gradient exceeds the normal gradient over the wafer. Formula (4) for the transition probability involves the first term in the expansion of the potential

$$\varphi(\mathbf{r}) \approx \varphi(\mathbf{r}_0) + \frac{\partial \varphi(\mathbf{r}_0)}{\partial \mathbf{r}}(\mathbf{r} - \mathbf{r}_0) + \ldots. \qquad (7)$$

The second term contains the potential gradient and can also contribute to the total probability. If the potential is a slowly varying function, the zeroth-order approximation is valid. Such is long-range potential (2), which is used in our problem (Fig. 1). For potentials of another type, higher order corrections must be considered. Taking into account the second term makes it possible to eliminate the algorithmic effect that imparts scattering properties to the vertical line under the seed. The first term in formula (7) relates the probabilities of the transition between the states to equipotential lines, while the second term relates the probabilities to field lines.

Of special interest are the long-range potentials simulating elastic stresses in the wafer and the strain field of dislocations. The long-range potential simulating elastic stresses is shown in Fig. 4. It is seen that the potential is concentrated in a narrow range. Pore branching is associated to a great extent with the scattering algorithmic effect mentioned above. Suppression of this effect within the range of this potential concentrated in the narrow interval eliminates branching almost completely (Fig. 5). Effects arising when chemical reactions accompanying pore formation proceed only at lattice imperfections also merit attention [16].

It was also discovered in this work that, under certain conditions, triangular elements may form on a square grid. In practice, such effects were observed upon anodizing silicon in dilute hydrofluoric acid. An example is fractal structures like Serpinsky gaskets observed in [11].

The somewhat uncertain relationship between a growing cluster and its generating seed is due to noise inherent in the model [14]. At the initial stage of simulation, the random walk algorithm gives rise to noise-induced instabilities (fluctuation noise), which are comparable to the cluster scale and serve as a specific initial condition for subsequent stages. If any unstable mode starts building up, its growth is of determinate character, although the dependence on the initial conditions can by no means be excluded [14].

Thus, we studied computer models of gradient-controlled growth. Algorithms used in this class of models allow for the formation of a variety of clusters that have different, including fractal, structures. The potential simulating the normal electric field distribution in a silicon wafer generates branching clusters. The problem of growing nonbranching isolated vertical clusters was

solved by using an algorithm that corresponds to a long-range high-gradient potential concentrated in a narrow interval. An example of such potentials is the deformation potential, whose properties were also simulated in this work. Associated results will be reported in subsequent publications.

Our findings may be helpful in analyzing the process of anisotropic etching, which provides vertical walls. Similar effects are observed in anodizing [17] and plasma-chemical etching of silicon [18].

REFERENCES

1. V. I. Klyatskin and D. Gurariĭ, Usp. Fiz. Nauk **169**, 171 (1999) [Phys. Usp. **42**, 165 (1999)].
2. O. Bisi, S. Ossicini, and L. Pavesi, Surf. Sci. Rep. **38**, 1 (2000).
3. V. V. Polyakov and S. V. Kruchinskiĭ, Pis'ma Zh. Tekh. Fiz. **27** (14), 42 (2001) [Tech. Phys. Lett. **27**, 592 (2001)].
4. G. C. John and V. A. Singh, Phys. Rep. **263**, 93 (1995).
5. H. Gould and J. Tobochnik, *An Introduction to Computer Simulation Methods: Applications to Physical Systems* (Addison-Wesley, Reading, 1988; Mir, Moscow, 1990), Vol. 2.
6. N. N. Mirolyubov, M. V. Kostenko, M. L. Levinshteĭn, and N. N. Tikhodeev, *Electrostatic Fields: Methods of Calculation* (Vysshaya Shkola, Moscow, 1963) [in Russian].
7. A. I. Ansel'm, *An Introduction to the Theory of Semiconductors* (Nauka, Moscow, 1978) [in Russian].
8. V. Lehmann, J. Electrochem. Soc. **140**, 2836 (1993).
9. E. Yu. Buchin and A. V. Prokaznikov, Mikroélektronika **27**, 107 (1998).
10. J. Feder, *Fractals* (Plenum, New York, 1988; Mir, Moscow, 1991).
11. C. Levy-Clement, A. Lagoubi, and M. Tomkiewicz, J. Electrohem. Soc. **141**, 958 (1994).
12. L. Turkevich and G. Sher, in *Fractals in Physics*, Ed. by L. Pietronero and E. Tosatti (North-Holland, Amsterdam, 1986; Mir, Moscow, 1988).
13. R. L. Smith, S.-F. Chuang, and S. D. Collins, J. Electron. Mater. **17**, 553 (1988).
14. L. Sander, in *Fractals in Physics*, Ed. by L. Pietronero and E. Tosatti (North-Holland, Amsterdam, 1986; Mir, Moscow, 1988).
15. E. Yu. Buchin, A. V. Prokaznikov, and A. B. Churilov, Appl. Surf. Sci. **102**, 431 (1996).
16. A. V. Prokaznikov and V. B. Svetovoy, Phys. Low-Dimens. Semicond. Struct. **9–10**, 65 (2002).
17. K. Grigoras, A. J. Niskanen, and S. Franssila, J. Micromech. Microeng. **11**, 371 (2001).
18. H. Jansen, J. Micromech. Microeng. **5**, 115 (1995).

Translated by V. Isaakyan

Technical Physics, Vol. 49, No. 5, 2004, pp. 532–539. Translated from Zhurnal Tekhnicheskoĭ Fiziki, Vol. 74, No. 5, 2004, pp. 12–19.

THEORETICAL AND MATHEMATICAL PHYSICS

Fractal Model of Transport: Low-Angle Approximation

V. V. Uchaikin and D. A. Korobko

Ul'yanovsk State University, Ul'yanovsk, 432970 Russia

e-mail: uchaikin@sv.uven.ru

Received October 30, 2003

Abstract—Multiple scattering of particles by a stochastic fractal, a set of point targets (atoms) randomly distributed in a space with a power correlation function, is considered. The energy and angular distributions that generalize the known Landau, Fermi, and Molière distributions are found in the low-angle approximation. The analytical results are checked by Monte Carlo numerical simulation. © *2004 MAIK "Nauka/Interperiodica"*.

INTRODUCTION

In many cases, electromagnetic and corpuscular radiation represents the only source of information about the structure of a material. To interpret information of such a type, one must generally consider radiation–material interaction, which is characterized by angular deviation due to scattering, energy losses during inelastic collisions, etc. Long-range power correlations, showing up in the grouping of atoms to produce bunches and superbunches like the distribution of galaxies in the Universe, are the most important parameter governing interaction with a fractal medium [1, 2]. Under certain conditions, such correlations are also observed in condensed media, the systematic investigation of which has culminated in the emergence of a new field of science, fractal materials science [3]. Single scattering by fractals was considered in [4, 5]; multiple scattering was considered, in [6], where the void distribution in an initially homogeneous medium was assumed to be fractal.

In this work, we are dealing with multiple scattering of particles by point centers ("atoms") whose distribution is characterized by fractal correlations. As in [6], the problem is solved in the low-angle approximation, which is valid both for fast particles and for waves in the absence of interference effects (the wavelength λ is much shorter than the typical spacing between scattering centers) [7]. This work elaborates on studies reported in [8–15].

1. PROBLEM DEFINITION

In the case of multiple scattering of particles, the problem is stated as follows. Let $X(t)$ be a random quantity that characterizes a particle at a depth t. We assume that (i) $X(0) = 0$ at the origin; (ii) in the intervals $0 < T_1 < T_2 < \ldots < T_N < t$ between collisions, $X(t)$ remains constant but discretely changes by a random value X_i after collisions; that is, $X(t) = \sum_{i=1}^{N(t)} X_i$; (iii) the changes (jumps) X_i at collisions are random, mutually independent, and are distributed with the same density $\sigma(x)$.

The distribution $X(N)$ for a particle having experienced N acts of scattering is described by the multiple convolution of the distributions $\sigma(x)$:

$$\sigma^{(N)}(x) = \int \sigma^{(N-1)}(x-\xi)\sigma(\xi)d\xi, \qquad (1)$$

where $\sigma^{(1)}(x) = \sigma(x)$.

Formula (1) is conveniently generalized to the case $N = 0$ by putting $\sigma^{(0)}(x) = \delta(x)$, where $\delta(x)$ is the Dirac function. The distribution over x of the particles traveling a distance t has the form

$$\Psi(x, t) = \sum_{N=0}^{\infty} p(N, t)\sigma^{(N)}(x), \qquad (2)$$

where $p(N, t)$ is the probability that a particle will experience N scattering events over a distance t.

Distribution (2), which characterizes the medium, is related to the density $q(t)$ of the free path distribution as

$$p(N, t) = \int_0^t Q(t-t')q^{(N)}(t')dt', \qquad (3)$$

where

$$Q(t) = \int_t^{\infty} q(t')dt'$$

is the probability that a random path exceeds t and $q^{(N)}(t)$ is the multiple convolution of the densities $q(t)$, which describes the distribution of the coordinate of an Nth scattering event.

As a random quantity X (a random m-dimensional vector), one may take both energy losses ε ($m = 1$) and the deviation of a particle from the initial direction. The latter, in the low-angle approximation, is described by a two-dimensional vector $\boldsymbol{\theta}$ ($m = 2$) (see, e.g., [16]). To solve this problem, it is necessary to find the multiple

1063-7842/04/4905-0532$26.00 © 2004 MAIK "Nauka/Interperiodica"

convolutions $q^{(N)}(t)$ of the spatial distributions of atoms and the convolutions $\sigma^{(N)}(x)$ of distributions that characterize interaction of moving particles with atoms of the media.

2. SELF-AVERAGING IN A REGULAR MEDIUM

In a regular medium, scattering centers (atoms) are assumed to be arranged independent of each other with a constant (if the medium is homogeneous) average density. The free path distribution in this case takes the form

$$q_0(t) = \mu \exp(-\mu t), \quad (4)$$

where μ is the linear scattering coefficient, which is the reciprocal of the mean path.

The probability density that a particle will experience N collisions over a path t is then expressed as

$$p(N, t) = \frac{(\mu t)^N}{N!} \exp(-\mu t),$$

and distribution (2) becomes the generalized Poisson distribution [17]

$$\Psi_0(x, t) = \exp(-\mu t) \sum_{N=0}^{\infty} \frac{(\mu t)^N}{N!} \sigma^{(N)}(x). \quad (5)$$

At $t \longrightarrow \infty$, the mean value of the random number of terms grows as μt and its relative fluctuations decreases as $(\mu t)^{-1/2}$, so that

$$\Psi_0(x, t) \cong \sigma^{(n(t))}(x), \quad t \longrightarrow \infty, \quad (6)$$

where $n(t)$ is the integer part of μt.

In terms of [18], the transition from (5) to (6) means the presence of the self-averaging property: a randomly inhomogeneous medium appears as a determinate homogeneous on small scales. In terms of probability theory, this fact is embodied in the law of large numbers, which is valid if $q(t)$ has a mathematical expectation. This, in turn, means that result (6) remains valid for any distribution with a finite mean value:

$$\int_0^{\infty} q(t) t dt = 1/\mu < \infty.$$

3. RANDOM PATHS IN A FRACTAL MEDIUM

The statistics of point fractal models was carefully studied in [15, 19–22]. It was shown [15] that, when a particle moves along a straight line that accommodates a fractal set of atoms, the distribution of the particle's free paths has an asymptotic power tail with an exponent $\alpha < 1$. To develop a model of radiation passing through a fractal placed in a 3D space, it is necessary to find the desired path distribution and make sure that sequential random paths are mutually independent.

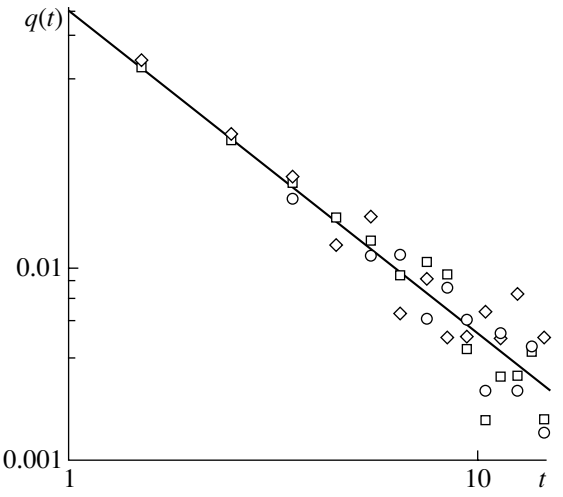

Fig. 1. Simulation of the path distribution in a fractal medium with $D = 1.5$. The continuous curve shows the distribution of the first path length, $q(t) \sim t^{-\alpha-1}$ ($\alpha = 0.65$). The symbols show the distribution of the second path length for different lengths of the first path: (○) first path $l < l_\mu$ (l_μ is the median path, $p\{l < l_\mu\} = 1/2$), (□) $l_\mu < l < 2l_\mu$, and (◇) $2l_\mu < l < 3l_\mu$.

To this end, realizations of a stochastic fractal of given dimensionality were simulated by the Levi–Mandelbrot method of random walk [19–22]. A small-radius sphere was described around each of the points. An arbitrarily directed ray originating at the center of one point was extended until it intersected two spheres. The distance between the origin of the ray and the first sphere was treated as the first path; the distance between the first and second spheres, as the second path. The results of this simulation (Fig. 1) count in favor of the assumption that sequential paths are mutually independent (at least, in the low-angle approximation) and support the power variation of their distribution density:

$$q(t) \propto t^{-\alpha-1}. \quad (7)$$

The exponent α depends on the dimensionality of the point fractal structure.

4. MESOSCOPIC EFFECT

When $\alpha < 1$, the mean value of the path with the distribution density given by (7) is infinite. In this case, one should use the limiting theorem in its generalized form to obtain stable distributions [23, 24]. In summing independent random quantities with infinite variances, these distributions play the same role as the Gaussian law in the case of finite variances. In particular, if the distribution densities of independent random quantities

T_i have power tails $q(t) \cong \alpha B t^{-\alpha-1}$, the normalized sum

$$S_N = \sum_{i=1}^{N} T_i / [NB\Gamma(1-\alpha)]^{1/\alpha}$$

is distributed with a one-sided stable density $g^{(\alpha)}(t)$. In other words, the density $q^{(N)}(t)$ of the sum $\sum_{i=1}^{N} T_i$ in large-N asymptotics has the form

$$q^{(N)}(t) \sim [NB\Gamma(1-\alpha)]^{-1/\alpha} g^{(\alpha)}([NB\Gamma(1-\alpha)]^{-1/\alpha} t). \quad (8)$$

Using the generalized limiting theorem, one can find the distribution of the probability that a particle will experience N collision over a path t:

$$p(N, t) \cong G^{(\alpha)}([NB\Gamma(1-\alpha)]^{-1/\alpha} t) - G^{(\alpha)}([(N+1)B\Gamma(1-\alpha)]^{-1/\alpha} t),$$

where

$$G^{(\alpha)}(t) = \int_0^t g^{(\alpha)}(t')dt'$$

is the stable distribution function.

Straightforward transformations yield

$$p(N, t) \cong \frac{t}{\alpha N}[NB\Gamma(1-\alpha)]^{-1/\alpha} g^{(\alpha)} \times ([NB\Gamma(1-\alpha)]^{-1/\alpha} t), \quad t \longrightarrow \infty. \quad (9)$$

Employing the well-known expression for negative-order moments of distribution $g^{(\alpha)}(t)$ [23],

$$\int_0^\infty g^{(\alpha)}(t) t^{-\nu} dt = \frac{\Gamma(1+\nu/\alpha)}{\Gamma(1+\nu)}, \quad \alpha < 1, \quad (10)$$

we find the moments of a random number of collisions in the interval $(0, t)$:

$$\langle N^k(t) \rangle = \frac{k! t^{k\alpha}}{[B\Gamma(1-\alpha)]^k \Gamma(1+k\alpha)}, \quad \alpha < 1.$$

It is easy to see that the mean value $\langle N(t) \rangle \propto t^\alpha$ and the moments (hence, the distribution) of the normalized random quantity $Z = N/\langle N(t) \rangle$ are independent of the layer thickness t. Because of these properties, which characterize the self-similarity of a stochastic fractal, fluctuations in the medium cannot be neglected at any thickness: self-averaging does not take place. Such a situation was named the mesoscopic effect [25].

5. GENERALIZATION OF THE TRANSPORT THEORY

In this section, we will generalize the known results of the transport theory for media with a fractal distribution of fractal centers. Using (9) and passing from summation over N in expression (2) to integration over the variable $\tau = [NB\Gamma(1-\alpha)]^{-1/\alpha} t$, we arrive at the distribution

$$\Psi(x, t) = \int_0^\infty d\tau g^{(\alpha)}(\tau) \sigma^{n(\tau)}(x), \quad \alpha < 1, \quad (11)$$

where $n(\tau)$ is the integer part of the expression $(t/\tau)^\alpha/[B\Gamma(1-\alpha)]$.

Comparing (11) with (6), we note that the limiting form of the distribution for a path with an infinite mean changes. At $\alpha \longrightarrow 1$, the one-sided stable density $g^{(\alpha)}(\tau) \longrightarrow \delta(\tau - 1)$ and distribution (11) passes into distribution (6), which characterizes a medium with self-averaging. If the mean square of X_i is finite,

$$\langle X_i^2 \rangle = \int_0^\infty x^2 \sigma(x) dx < \infty,$$

the distribution of $\sigma^{(N)}(x)$ at $N \longrightarrow \infty$ tends to the Gaussian distribution (which is two-dimensional for the angular distribution and one-dimensional for the energy loss distribution):

$$\sigma^{(N)}(x) \cong \frac{1}{(2\pi ND)^{m/2}} \times \exp\left(-\frac{(x - N\langle X \rangle t)^2}{2ND}\right); \quad t \longrightarrow \infty; \quad m = 1, 2, \quad (12)$$

$$D = \langle X^2 \rangle - \langle X \rangle^2.$$

In the fractal case ($\alpha < 1$), the distribution over the deviation angle θ we obtain

$$\Psi(\theta, t) = \frac{\psi^{(\alpha)}(\theta/\sqrt{\Delta})}{\Delta}, \quad (13)$$

where

$$\psi^{(\alpha)}(x) = \pi^{-1} \int_0^\infty d\tau \exp(-x^2 \tau^\alpha) \tau^\alpha g^{(\alpha)}(\tau), \quad \alpha < 1. \quad (14)$$

The coefficient Δ and the mean square of the deviation angle over a path t, $\langle \theta^2 \rangle$, are related as

$$\langle \theta^2 \rangle = \frac{\Delta}{\Gamma(1+\alpha)} = \frac{2\langle \theta^2 \rangle t^\alpha}{B\Gamma(1-\alpha)\Gamma(1+\alpha)}. \quad (15)$$

Here, $\langle \theta^2 \rangle$ has the meaning of the mean square of the angle of single scattering. This is the generalization of the Fermi distribution for scatterers distributed in a fractal manner. For the energy loss (ε) distribution, we get

$$\Psi(\varepsilon, t) = (2\pi D)^{-1/2} \int_0^\infty d\tau$$

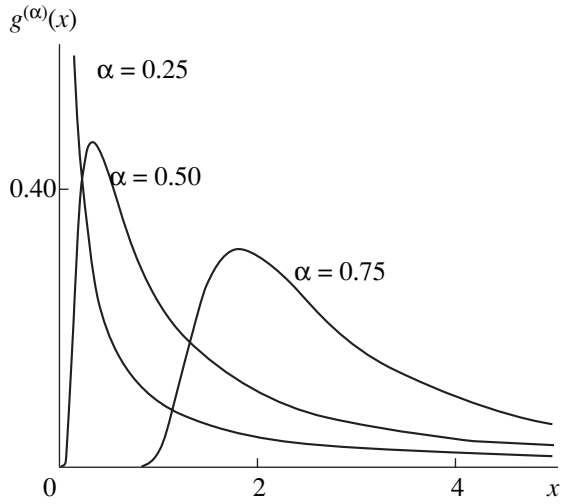

Fig. 2. Densities $g^{(\alpha)}(x)$ of the one-sided stable distributions for α = 0.25, 0.50, and 0.75.

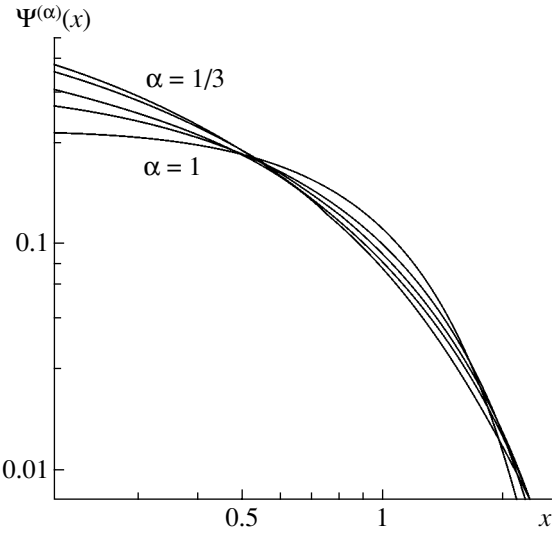

Fig. 3. Distributions $\psi^{(\alpha)}(x)$ for α = 1/3, 1/2, 2/3, 5/6, and 1. The case α = 1 corresponds to the Gaussian distribution.

$$\times \exp\left(-\frac{(\varepsilon - N/(t/\tau)\langle\varepsilon\rangle^2)}{2N(t/\tau)D}\right)\frac{g^{(\alpha)}(\tau)}{\sqrt{N(t/\tau)}}, \qquad (16)$$

$$D = \langle\varepsilon^2\rangle - \langle\varepsilon\rangle^2, \quad N(t/\tau) = (t/\tau)^\alpha/[B\Gamma(1-\alpha)],$$

where $\langle\varepsilon\rangle$ and $\langle\varepsilon^2\rangle$ are the mean energy losses and the mean square of the energy losses, respectively, at single scattering.

In the continuous slowing-down approximation (without energy loss fluctuations), expression (16) takes the form

$$\Psi(\varepsilon, t) = (\alpha\varepsilon)^{-1}\left[\frac{At^\alpha}{\varepsilon}\right]^{1/\alpha} g^{(\alpha)}\left(\left[\frac{At^\alpha}{\varepsilon}\right]^{1/\alpha}\right),$$

$$A = \langle\varepsilon\rangle/B\Gamma(1-\alpha).$$

Using expressions (10) for the moments of the one-sided stable distributions, one can calculate the mean energy losses over a path t:

$$\langle E\rangle = \frac{\langle\varepsilon\rangle t^\alpha}{B\Gamma(1-\alpha)\Gamma(1+\alpha)}. \qquad (17)$$

In both cases (expressions (15) and (17)), we observe the subdiffusion dependence ($\propto t^\alpha$) rather than linear ($\propto t$).

The distributions $g^{(\alpha)}(x)$ and $\psi^{(\alpha)}(x)$ can be expressed via the Fox generalized hypergeometric function [26, 27]. In terms of this function, the one-sided stable density takes the form [28]

$$g^{(\alpha)}(x) = \frac{1}{\alpha x^2}H_{11}^{10}\left(x^{-1}\middle|\begin{matrix}(-1, 1)\\(-1/\alpha, 1/\alpha)\end{matrix}\right).$$

With formula (2.25.2.3) from [29], we obtain

$$\psi^{(\alpha)}(x) = \frac{1}{\pi x^2}H_{12}^{20}\left(x\middle|\begin{matrix}(1, 1)\\(1, 1/\alpha)(1, 1/\alpha)\end{matrix}\right).$$

The distributions $g^{(\alpha)}(x)$ and $\psi^{(\alpha)}(x)$ for different α are plotted in Figs. 2 and 3. In Fig. 3, the limiting distribution at α = 1 corresponds to the Gaussian distribution, i.e., to finite-mean-path scattering. The basic distinction between the distribution $\psi^{(\alpha)}(x)$ and Gaussian distribution is a higher probability density at small and large angles.

Expression (11) is applicable to an arbitrary cross section σ(x) of single scattering, including the case of an infinite variance of X. This problem arises when charged particle scattering is described by the Rutherford formula unless the parameter of maximal energy losses or maximal deviation angle is introduced into the theory. With these parameters, $\sigma^{(N)}(x)$ is described by the Landau distribution (for the energy losses),

$$\sigma^{(N)}(\varepsilon) = \frac{1}{2\pi i}\int_\gamma \exp(p\varepsilon - NA(p))dp,$$

$$A(p) = \int_{\varepsilon_0}^\infty (1 - \exp(-p\varepsilon))\sigma(\varepsilon)d\varepsilon, \quad \sigma(\varepsilon) \cong \varepsilon^{-2}, \qquad (18)$$

$$A(p) \cong p\varepsilon_0 b - p\varepsilon_0 \ln p\varepsilon_0, \quad b = 1 - C_e$$

or the Molière distribution (for the deviation angle),

$$\sigma^{(N)}(\theta) = \frac{1}{2\pi}\int_0^\infty \exp(-NA(p))J_0(p\theta)dp,$$

$$A(p) = \int_{\theta_0}^{\infty}(1 - J_0(-p\theta))\sigma(\theta)\theta d\theta, \quad \sigma(\theta) \cong \theta^{-2}, \quad (19)$$

$$A(p) \cong p^2\theta_0 b - p^2\theta_0 \ln p^2\theta_0, \quad b = 2(1 - C_e).$$

The parameters ε_0 and θ_0 specify the least energy losses (binding energy) and the screening angle, i.e., the applicability domain for the Rutherford formula. In any case, substituting (18) or (19) into (11) yields an expression for the related distributions in a fractal medium that is convenient for numerical calculation.

6. TRANSPORT EQUATION FOR A FRACTAL MEDIUM

Let us derive transport equations in media with exponential and power path distributions. It has been shown above that, in the former case, generalized Poisson distribution (5) describes multiple scattering. By differentiating with respect to t, it is easy to check that it satisfies the kinetic equation

$$\frac{\partial \Psi}{\partial t} + \mu\Psi = \mu\int\sigma(y - x)\Psi(t, y)dy \quad (20)$$

with the initial condition $\Psi(x, 0) = \delta(x)$.

In the limit $t \longrightarrow \infty$, Eq. (20) takes diffusion form (known as the Fokker–Planck approximation)

$$\frac{\partial \Psi}{\partial t} = -\mu\langle X\rangle\frac{\partial \Psi}{\partial x} + \frac{\mu\langle X\rangle^2}{2}\frac{\partial^2\Psi}{\partial x^2}; \quad (21)$$

here, the operator $\partial/\partial\theta$ for the deviation angle is two-dimensional. By virtue of Gaussian asymptotics (12), this asymptotic equation also remains valid for a power path distribution with a finite mean ($\alpha > 1$).

To derive transport equations in a fractal medium, consider relationship (2) for a distribution of paths $q(t)$ that is other than exponential. To do this, it is convenient to use the scattering density $f(x, t)$, which is related to $\Psi(x, t)$ as

$$\Psi(x, t) = \int_0^t Q(t - t')f(x, t')dt'. \quad (22)$$

The distribution

$$f(x, t) = \sum_{N=0}^{\infty} q^{(N)}(t)\sigma^{(N)}(x) \quad (23)$$

satisfies the integral equation

$$f(x, t) = \int_0^t dt' q(t')\int dy\sigma(y)f(x - y, t - t') + \delta(t)\delta(x), \quad (24)$$

which, together with (22), generalizes kinetic equation (20) for a medium with a given distribution of free paths $q(t)$.

In the case of scattering with a finite variance, $\sigma^{(N)}(x)$ is automatically described by Gaussian distribution (12) at $N \longrightarrow \infty$ and satisfies the diffusion equation

$$\frac{\partial \sigma^{(N)}}{\partial N} = \langle X\rangle\frac{\partial \sigma^{(N)}}{\partial x} + \frac{\langle X^2\rangle}{2}\frac{\partial^2\sigma^{(N)}}{\partial x^2}.$$

Substituting this equation into (23) and integrating by parts yields the equation

$$-\langle X\rangle\frac{\partial f}{\partial x} + \frac{\langle X^2\rangle}{2}\frac{\partial^2 f}{\partial x^2} = -\delta(t)\delta(x) - \int_0^{\infty} dN\sigma^{(N)}(x)\frac{\partial q^{(N)}(t)}{\partial N}.$$

Passing on to a power distribution of paths $q(t)$ ($\alpha < 1$), it is necessary to take into account that $q^{(N)}(t)$ behaves according to (8) in the limit $N \longrightarrow \infty$. To cut the notation, we introduce the Riemann–Liouville operator of fractional differentiation [30]

$$\left(\frac{\partial}{\partial t}\right)^{\alpha} f(t) = \frac{1}{\Gamma(-\alpha)}\int_0^t \tau^{-\alpha-1}f(t - \tau)d\tau, \quad \alpha < 1.$$

Using the properties of stable densities, one can show that distributions (8) satisfy the relationship

$$\frac{\partial q^{(N)}(t)}{\partial N} = -\frac{\partial^{\alpha} q^{(N)}(t)}{\partial t^{\alpha}}.$$

Thus, we arrive at a fractional differential equation for the scattering density $f(x, t)$ in the form

$$\left(\frac{\partial}{\partial t}\right)^{\alpha} f + \langle X\rangle\frac{\partial f}{\partial x} - \frac{\langle X^2\rangle}{2}\frac{\partial^2 f}{\partial x^2} = \delta(t)\delta(x), \quad \alpha < 1, \quad t \longrightarrow \infty. \quad (25)$$

By convolving Eq. (25) with $Q(t) = Bt^{-\alpha}$ and changing the order of integration in the term with the fractional derivative by the Dirichlet rule, we arrive at an equation for the distribution function $\Psi(x, t)$:

$$\left(\frac{\partial}{\partial t}\right)^{\alpha}\Psi + A\langle X\rangle\frac{\partial \Psi}{\partial x} - \frac{A\langle X^2\rangle}{2}\frac{\partial^2\Psi}{\partial x^2} = \frac{t^{-\alpha}}{\Gamma(1 - \alpha)}\delta(x), \quad \alpha < 1, \quad t \longrightarrow \infty, \quad A = 1/B\Gamma(1 - \alpha). \quad (26)$$

For $\alpha \longrightarrow 1$, this equation turns into Eq. (21) for normal diffusion. Equations like Eq. (26) appear in [31, 32], where the phenomenon of slow diffusion (subdiffusion) is studied. In these equations, the variable t plays the role of time and the variable x, the role of coordinate (between scattering events, x remains constant; that is, a particle is "trapped").

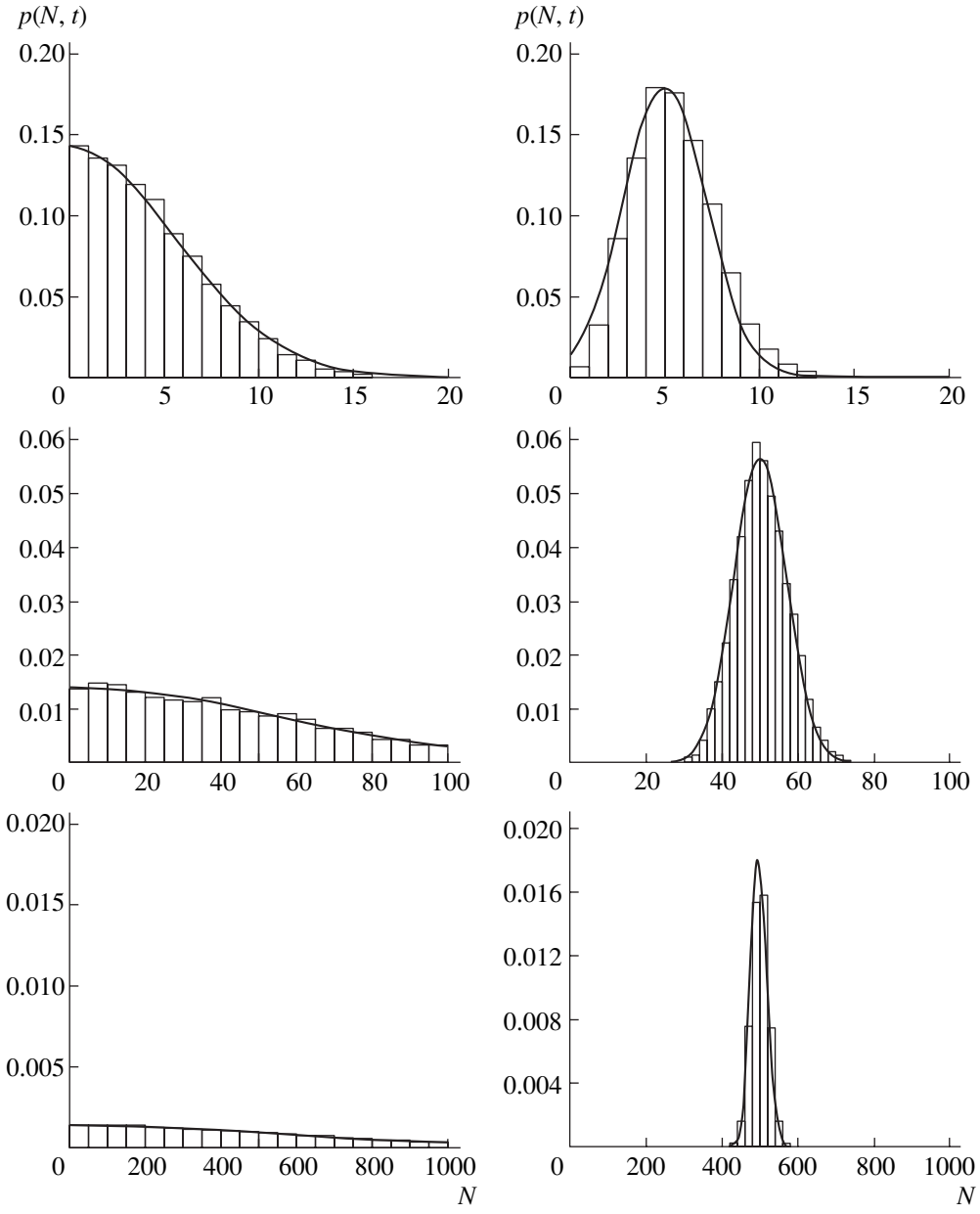

Fig. 4. Distributions $p(N, t)$ over number of interactions at depths t corresponding, on average, to 5, 50, and 500 interactions of a particle scattered by the medium. On the left, results for the fractal medium (the power path distribution: $q(t) \sim t^{-\alpha-1}$, $\alpha = 1/2$); on the right, results for the regular medium (the exponential path distribution).

7. MONTE CARLO SIMULATION OF MULTIPLE SCATTERING IN FRACTAL STRUCTURES

The results obtained above may be checked numerically by applying analog simulation of multiple scattering. In this case, the one-dimensional motion of a particle with a given distribution of paths between interactions is considered. In the initial series of model experiments, the numbers of interactions in the distributions are compared at depths corresponding to equal average numbers $\langle N(t)\rangle$ of interactions. Two path distributions are compared: distribution (4), which corresponds to a homogeneous medium with a linear density μ, and distribution (7) with an exponent $\alpha = 1/2$, which corresponds to a fractal medium. The results of comparison are demonstrated in Fig. 4. The continuous curves show probability distributions (9) for power-law path distribution (7) and the probability distribution that is limiting for the Poisson distribution,

$$p_N(t) = \frac{\exp\left(-\frac{(N - \langle N\rangle)^2}{2\langle N\rangle}\right)}{\sqrt{2\pi\langle N\rangle}},$$

for exponential path distribution (4) ($\langle N\rangle = \mu t$).

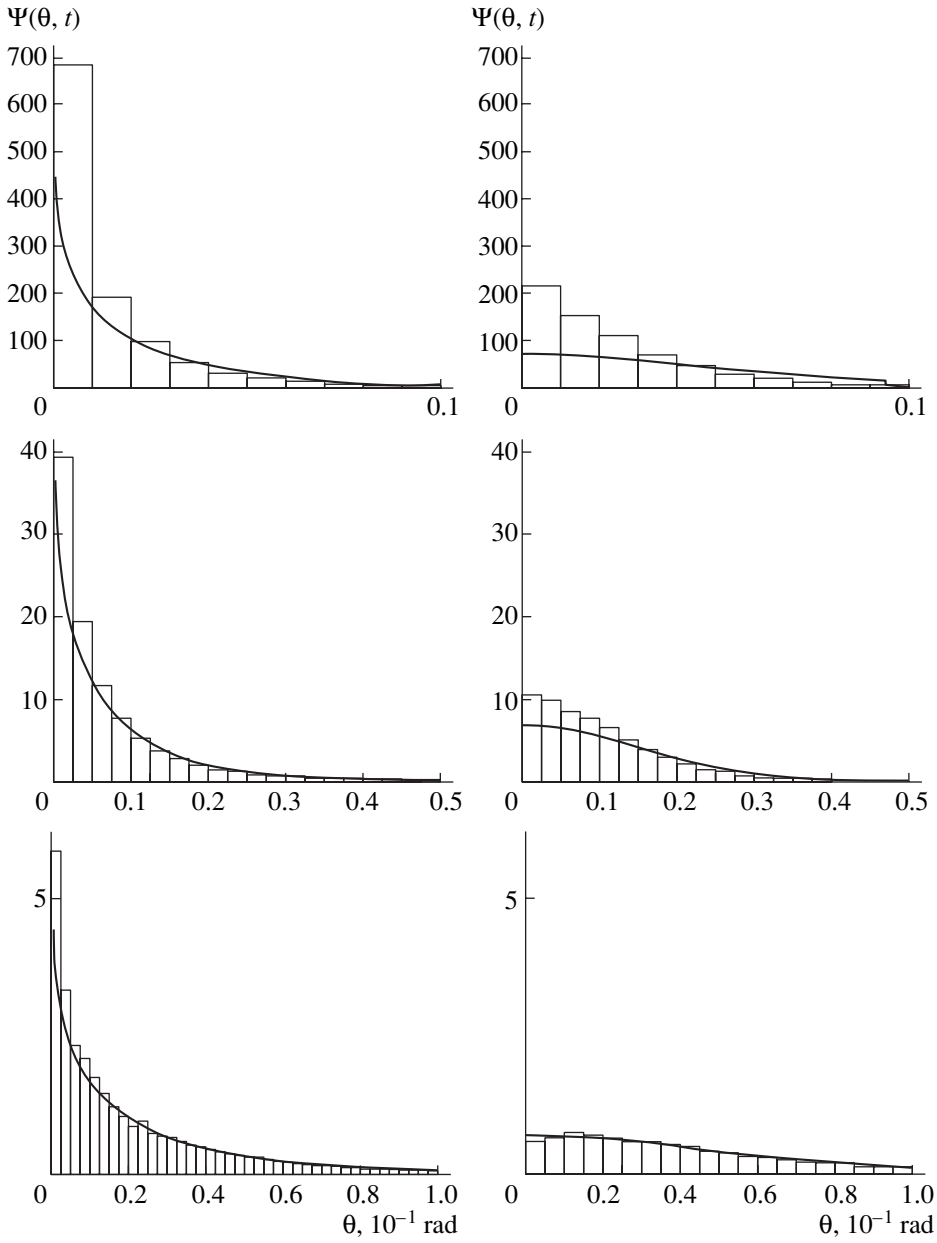

Fig. 5. Distributions $\Psi(\theta, t)$ over multiple scattering angle at depths t corresponding, on average, to 5, 50, and 500 interactions of a particle scattered by the medium. $\langle\Theta^2\rangle = 4 \times 10^{-4}$ rad^2. On the left, results for the fractal medium (the power path distribution: $q(t) \sim t^{-\alpha-1}$, $\alpha = 1/2$); on the right, results for the regular medium (the exponential path distribution).

Then, the multiple scattering angle distribution is considered. A particle that experienced an ith interaction is assigned a random two-dimensional vector Θ_i. Its direction is taken to be azimuth-symmetric, and its magnitude corresponds to the Rutherford distribution $p(\Theta) \sim \Theta^{-4}$ (where the minimal and maximal scattering angles Θ_{min} and Θ_{max} are introduced to avoid the divergence of $\langle\Theta^2\rangle$). For comparison (Fig. 5), for depths corresponding to equal mean values $\langle N(t)\rangle$ of the number of interactions, the multiple scattering angle distributions are shown versus asymptotic solutions (13) and (11). Similar numerical experiments may be carried out for the energy loss distribution.

CONCLUSIONS

We studied the motion of particles through point fractal-like systems [19–22] that simulate a fractal medium. Particles propagating in such media are shown to have a power free path distribution with an exponent α (see (7)). For $\alpha > 1$, the distribution $\Psi(t, x)$ of a multiple scattering random parameter at a depth t depends asymptotically (at $t \longrightarrow \infty$) only on the mean free path

$\langle\tau\rangle$ and does not depend on whether the distribution of τ is exponential or power. In the case $\alpha < 1$, when the mean free path is infinite, we derived expression (9) for the probability distribution of the number of interactions at a depth t and deduced universal rule of transformation (11), which allows one to find the distribution of a multiple scattering random parameter X for any scattering cross section $\sigma(x)$. For a finite variance of X, deviation angle distribution (13) and energy loss distribution (14) are found. The expressions for the mean energy losses and for the mean-square angle of multiple scattering at a depth t exhibit the subdiffusion dependence, $\propto t^{\alpha}$ ($\alpha < 1$), which increases slower than the normal dependence, $\propto t$. The distributions $\Psi(t, x)$ satisfy fractional differential equations (26) of subdiffusion type when the mean free path is infinite. Numerical simulation of multiple scattering with a power free path distribution confirms analytical results.

REFERENCES

1. P. H. Coleman and L. Pietronero, Phys. Rep. **213**, 311 (1992).
2. B. B. Mandelbrot, *The Fractal Geometry of Nature* (Freeman, New York, 1983).
3. V. S. Ivanova, A. S. Balankin, and I. Zh. Bunin, *Synergism and Fractals in Materials Science* (Nauka, Moscow, 1994) [in Russian].
4. F. Ferri, B. J. Frisken, and D. S. Cannell, Phys. Rev. Lett. **67**, 3626 (1991).
5. A. Hasmy, E. Anglaret, M. Foret, *et al.*, Phys. Rev. B **50**, 6006 (1994).
6. S. V. Maleev, Phys. Rev. B **52**, 13163 (1995).
7. S. M. Rytov, Yu. A. Kravtsov, and V. I. Tatarskiĭ, *Introduction to Statistical Radiophysics* (Nauka, Moscow, 1978) [in Russian], Vol. 2.
8. V. V. Uchaikin, in *Proceedings of the 24th International Cosmic Rays Conference (ICRC-95), Rome, 1995*, Vol. 1, pp. 698–701.
9. V. V. Uchaikin, Physica A **255** (12), 65 (1998).
10. V. V. Uchaikin, Zh. Tekh. Fiz. **68**, 138 (1998) [Tech. Phys. **43**, 124 (1998)].
11. V. V. Uchaikin, Teor. Mat. Fiz. **115**, 154 (1998).
12. V. V. Uchaikin and D. A. Korobko, Uch. Zap. Ul'yan. Gos. Univ., Ser. Fiz. **1**, 3 (1998).
13. D. A. Korobko and V. V. Uchaikin, Uch. Zap. Ul'yan. Gos. Univ., Ser. Fiz. **6**, 15 (1999).
14. V. V. Uchaikin, *Critical Technologies and Fundamental Problems in Physics of Condensed Media*, Ed. by S. V. Bulyarskiĭ (Izd. Ul'yan. Gos. Univ, Ul'yanovsk, 1999) [in Russian], pp. 4–25.
15. V. V. Uchaikin and D. A. Korobko, Pis'ma Zh. Tekh. Fiz. **25** (11), 34 (1999) [Tech. Phys. Lett. **25**, 435 (1999)].
16. A. M. Kol'chuzhkin and V. V. Uchaikin, *Introduction into the Theory of Particle Transmission through Materials* (Atomizdat, Moscow, 1978) [in Russian].
17. W. Feller, *An Introduction to Probability Theory and Its Applications*, 3rd ed. (Wiley, New York, 1967; Mir, Moscow, 1984), Vol. 2.
18. I. M. Lifshits, S. A. Gredeskul, and L. A. Pastur, Zh. Éksp. Teor. Fiz. **83**, 2362 (1982) [Sov. Phys. JETP **56**, 1370 (1982)].
19. V. V. Uchaikin, G. G. Gusarov, I. F. Gismjatov, and V. A. Svetuchin, Int. J. Bifurcation Chaos Appl. Sci. Eng. **8**, 977 (1998).
20. V. V. Uchaikin and G. G. Gusarov, J. Math. Phys. **38**, 2453 (1997).
21. V. V. Uchaikin, G. G. Gusarov, and D. A. Korobko, J. Math. Sci. **92**, 3940 (1998).
22. V. V. Uchaikin, D. A. Korobko, and I. V. Gismyatov, Izv. Vyssh. Uchebn. Zaved. Fiz., No. 8, 7 (1997).
23. V. M. Zolotarev, *One-Dimensional Stable Distributions* (Nauka, Moscow, 1983) [in Russian].
24. V. V. Uchaikin and V. M. Zolotarev, in *Chance and Stability: Stable Distributions and Their Applications* (VSP, Utrecht, 1999).
25. M. É. Raĭkh and I. M. Ruzin, Zh. Éksp. Teor. Fiz. **92**, 2257 (1987) [Sov. Phys. JETP **65**, 1273 (1987)].
26. C. Fox, Trans. Am. Math. Soc. **98**, 395 (1961).
27. W. G. Glöckle and T. F. Nonnenmacher, J. Stat. Phys. **71**, 741 (1993).
28. W. R. Schneider, *Lecture Notes in Physics* (Springer, Berlin, 1986).
29. A. P. Prudnikov, Yu. A. Brychkov, and O. I. Marichev, *Integrals and Series*, Vol. 3: *More Special Functions* (Nauka, Moscow, 1986; Taylor & Francis, London, 1990).
30. S. G. Samko, A. A. Kilbas, and O. I. Marichev, *Fractional Integrals and Derivatives: Theory and Applications* (Nauka i Tekhnika, Minsk, 1987; Gordon and Breach, Amsterdam, 1993).
31. J.-P. Bouchaud and A. Georges, Phys. Rep. **195**, 127 (1990).
32. G. M. Zaslavsky, Physica D **76**, 110 (1994).

Translated by V. Isaakyan

Technical Physics, Vol. 49, No. 5, 2004, pp. 540–544. Translated from Zhurnal Tekhnicheskoĭ Fiziki, Vol. 74, No. 5, 2004, pp. 20–23.

THEORETICAL AND MATHEMATICAL PHYSICS

Electrostatic Problem for a Torus Placed in an Infinite Cylinder

G. Ch. Shushkevich

Kupala State University Educational Establishment, Grodno, 230023 Belarus
e-mail: sys@mail.grsu.grodno.by

Received September 15, 2003

Abstract—An analytical solution to the axisymmetric electrostatic problem for a torus placed in an infinite circular cylinder is derived. The capacitance of the torus is calculated for different conductor geometries. © *2004 MAIK "Nauka/Interperiodica".*

In designing various devices, one sometimes runs into the need for analyzing the electrostatic field generated by a set of conductors of different configuration [1, 2]. The solution of the problem stated is reduced to the solution of an infinite set of algebraic equations using formulas that relate cylindrical and toroidal harmonic functions. The capacitance of the torus is calculated for a number of conductor geometries (see Table 2). Earlier, a similar problem was solved by approximate methods alone [3, 4].

STATEMENT AND SOLUTION OF THE PROBLEM

Consider the axisymmetric electrostatic problem for a torus T with a minor radius r and major radius R that is placed in an infinitely long circular cylinder Γ of radius b (see figure). To analytically solve the problem, we take the point 0 as the origin of the cylindrical coordinates $\{\rho, z, \varphi\}$ [5, 6],

$$x = \rho\cos\varphi, \quad y = \rho\sin\varphi, \quad z = z$$

$$(0 \le \rho < \infty,\ 0 \le \varphi \le 2\pi,\ -\infty < z < \infty)$$

and of the toroidal coordinates $\{\alpha, \beta, \varphi\}$ [5, 6],

$$x = \frac{c\sinh\alpha\cos\varphi}{\cosh\alpha - \cos\beta}, \quad y = \frac{c\sinh\alpha\sin\varphi}{\cosh\alpha - \cos\varphi},$$

$$z = \frac{c\sin\beta}{\cosh\alpha - \cos\beta}$$

$$(0 \le \alpha < \infty,\ -\pi < \beta \le \pi,\ 0 \le \varphi \le 2\pi,\ c = \sqrt{R^2 - r^2}).$$

Then, the conductors are described as follows:

$$T = \left\{\alpha = \alpha_0 = \ln\left(\frac{R}{r} + \sqrt{\left(\frac{R}{r}\right)^2 - 1}\right),\right.$$

$$\left.0 \le \beta \le 2\pi,\ 0 \le \varphi \le 2\pi\right\},$$

$$\Gamma = \{\rho = b,\ 0 \le \varphi \le 2\pi,\ -\infty < z < \infty\}.$$

Our goal is to find the electrostatic potential U that satisfies (i) the Laplace equation $\Delta U = 0$ (Δ is the Laplacian) everywhere inside the cylinder except for the torus surface; (ii) the boundary conditions on the torus and cylinder surfaces,

$$U|_T = V_t = \text{const}, \tag{1}$$

$$U|_\Gamma = 0; \tag{2}$$

and (iii) the condition at infinity

$$U(M) \longrightarrow 0 \quad \text{for} \quad M \longrightarrow \infty, \tag{3}$$

where M is an arbitrary point in the space.

Applying the method of separation of variables [5, 6], we represent the electrostatic potential U as the superposition of cylindrical and toroidal harmonics so that condition at infinity (3) is fulfilled automatically:

$$U = U_1(\alpha, \beta) + U_2(\rho, z),$$

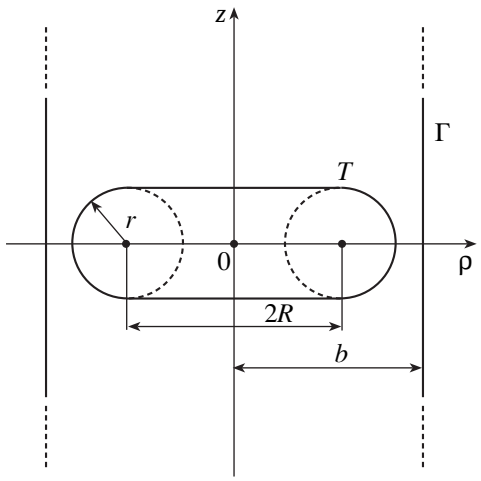

Figure.

1063-7842/04/4905-0540$26.00 © 2004 MAIK "Nauka/Interperiodica"

where

$$U_1(\alpha, \beta) = \sqrt{2(\cosh\alpha - \cos\beta)} \times \sum_{n=-\infty}^{\infty} x_n \frac{P_{n-\frac{1}{2}}(\cosh\alpha)}{P_{n-\frac{1}{2}}(\cosh\alpha_0)} \exp(in\beta), \quad (4)$$

$$U_2(\rho, z) = \int_{-\infty}^{\infty} Z(\lambda) \frac{I_0(\lambda\rho)}{I_0(\lambda b)} \exp(i\lambda z) d\lambda, \quad (5)$$

$P_{n-\frac{1}{2}}(\cosh\alpha)$ is the Legendre function of the first kind or the torus function, $I_0(\lambda\rho)$ is the zeroth-order Bessel function of the first kind [5–8], and $\cosh\alpha_0 = R/r$.

The unknown coefficients x_n and the function $Z(\lambda)$ are determined from boundary conditions (1) and (2).

FULFILLMENT OF THE BOUNDARY CONDITIONS

To satisfy boundary condition (1) on the torus surface, we represent the function $U_2(\rho, z)$ via the toroidal harmonics using the formula [9]

$$I_0(\lambda\rho)\exp(i\lambda z) = \frac{1}{2\pi}\sqrt{2(\cosh\alpha - \cos\beta)} \times \sum_{n=-\infty}^{\infty} a_n(\lambda c) Q_{n-\frac{1}{2}}(\cosh\alpha)\exp(in\beta),$$

where

$$a_n(x) = 2I_0(x) + \sum_{k=1}^{|n|} f_k^{|n|}\left(|n| I_k(x) - k\frac{|n|}{n} I_{k-1}(x)\right)x^k, \quad (6)$$

$$f_k^n = \frac{2^{3k+1} k!(n+k+1)!}{((2k)!)^2 (n-k)!};$$

$Q_{n-\frac{1}{2}}(\cosh\alpha)$ is the Legendre function of the second kind or the torus function [5–8].

Then,

$$U_2(\alpha, \beta) = \sqrt{2(\cosh\alpha - \cos\beta)} \times \sum_{n=-\infty}^{\infty} R_n(\lambda c) Q_{n-\frac{1}{2}}(\cosh\alpha)\exp(in\beta), \quad (7)$$

where

$$R_n(\lambda c) = \frac{1}{2\pi}\int_{-\infty}^{\infty} \frac{Z(\lambda)}{I_0(\lambda b)} a_n(\lambda c) d\lambda. \quad (8)$$

Taking into account representations (4) and (7) and satisfying boundary condition (1), we come to

$$\sqrt{2(\cosh\alpha - \cos\beta)} \sum_{n=-\infty}^{\infty} \left(x_n + R_n(\lambda c) Q_{n-\frac{1}{2}}(\cos\alpha_0)\right) \times \exp(in\beta) = V_t. \quad (9)$$

Dividing both sides of (9) into $\sqrt{2(\cosh\alpha_0 - \cos\beta)}$ and using the representation [5]

$$\frac{1}{\sqrt{2(\cosh\alpha_0 - \cos\beta)}} = \frac{1}{\pi}\sum_{n=-\infty}^{\infty} Q_{n-\frac{1}{2}}(\cosh\alpha_0)\exp(in\beta),$$

we find from (9)

$$\sum_{n=-\infty}^{\infty} \left(x_n + R_n(\lambda c) Q_{n-\frac{1}{2}}(\cosh\alpha_0)\right)\exp(in\beta) = \frac{V_t}{\pi}\sum_{n=-\infty}^{\infty} Q_{n-\frac{1}{2}}(\cosh\alpha_0)\exp(in\beta)$$

or, by virtue of the uniqueness of expansion in Fourier series,

$$x_n + R_n(\lambda c) Q_{n-\frac{1}{2}}(\cosh\alpha_0) = \frac{V_t}{\pi} Q_{n-\frac{1}{2}}(\cosh\alpha_0); \quad n = 0, \pm1, \pm2, \ldots. \quad (10)$$

To satisfy boundary condition (2) on the cylinder surface, we represent the function $U_1(\alpha, \beta)$ via the cylindrical harmonics using the integral formula [9]

$$\sqrt{2(\cosh\alpha - \cos\beta)} P_{n-\frac{1}{2}}(\cosh\alpha)\exp(in\beta) = \frac{c}{\pi}\int_{-\infty}^{\infty} a_n(\lambda c) K_0(|\lambda\rho|)\exp(i\lambda z) d\lambda,$$

where $K_0(x)$ is the Macdonald function [5–8].

Then,

$$U_1(\rho, z) = \int_{-\infty}^{\infty} D(\lambda c) K_0(|\lambda\rho|)\exp(i\lambda z) d\lambda, \quad (11)$$

where

$$D(\lambda c) = \frac{c}{\pi}\sum_{k=-\infty}^{\infty} \frac{x_k}{P_{k-\frac{1}{2}}(\cosh\alpha_0)} a_k(\lambda c). \quad (12)$$

According to representations (5) and (11), boundary condition (2) on the surface of the cylinder takes the form

$$\int_{-\infty}^{\infty} (Z(\lambda) + D(\lambda c) K_0(|\lambda b|))\exp(i\lambda z) d\lambda = 0$$

Table 1

n	C_i
1	−0.5
2	0.0625
3	−0.177083333333
4	0.021809895833
5	−0.12858072917
6	0.01009792752
7	−0.0835903592
8	0.00555534
9	−0.06640809
10	0.0034603
11	−0.055046
12	0.00236
13	−0.047

or

$$Z(\lambda) + D(\lambda c)K_0(|\lambda b|) = 0. \tag{13}$$

Substituting $Z(\lambda)$ from (13) into (8) and taking into account representation (12) yields a relationship between the function $R_n(\lambda c)$ and coefficients x_k:

$$R_n(\lambda c) = -\frac{c}{2\pi^2}\sum_{k=-\infty}^{\infty}\frac{x_k}{P_{k-\frac{1}{2}}(\cosh\alpha_0)} \times \int_{-\infty}^{\infty}\frac{K_0(|\lambda b|)}{I_0(\lambda b)}a_n(\lambda c)a_k(\lambda c)d\lambda. \tag{14}$$

Now, using representation (14), we exclude the function $R_n(\lambda c)$ from (10) to arrive at an infinite set of linear algebraic equations in the unknown coefficients x_k, which enter into the initial representation of the potential:

$$x_n - \sum_{k=-\infty}^{\infty} p_{nk}x_k = \frac{V_t}{\pi}Q_{n-\frac{1}{2}}(\cosh\alpha_0); \quad n = 0, \pm1, \pm2, \ldots, \tag{15}$$

where

$$p_{nk} = \frac{c}{2\pi^2}\frac{Q_{n-\frac{1}{2}}(\cosh\alpha_0)}{P_{k-\frac{1}{2}}(\cosh\alpha_0)} \times \int_{-\infty}^{\infty}\frac{K_0(|\lambda b|)}{I_0(\lambda b)}a_n(\lambda c)a_k(\lambda c)d\lambda. \tag{16}$$

Let us transform improper integral (16) to a form suitable for computer calculation.

In [10], the first 50 values of the improper integral are given:

$$L_k = \frac{2^{k+1}}{\pi k!}\int_0^{\infty}\frac{K_0(t)}{I_0(t)}t^k dt; \quad k = 0, 1, \ldots, 49.$$

The remaining values of the integral L_k ($k > 49$) can be calculated with an accuracy of 10^{-12} by the formula [10]

$$L_k = \sum_{i=1}^{13}\frac{C_i}{\binom{k}{i}},$$

where

$$\binom{k}{i} = \frac{k!}{i!(k-i)!}$$

are binomial coefficients.

The values of the coefficients C_i are listed in Table 1.

Using the expansion of the product of the Bessel functions in a power series [11],

$$I_m(\mu t)I_n(\mu t) = \sum_{p=0}^{\infty}\frac{1}{(n+p)!(m+p)!} \times \binom{m+n+2p}{p}\left(\frac{\mu t}{2}\right)^{n+m+2p},$$

we can show that the integral

$$I_k^{(m,n)}(a) = \int_0^{\infty}\frac{K_0(t)}{I_0(t)}I_m(at)I_n(at)t^k dt \tag{17}$$

is calculated via tabulated integrals L_k by the formula

$$I_k^{(m,n)}(a) = \frac{\pi k!}{2^{k+1}}\sum_{p=0}^{\infty}\binom{m+n+2p}{p}\binom{m+n+k+2p}{k} \times \binom{m+n+2p}{m+p}\left(\frac{a}{4}\right)^{m+n+2p}L_{m+n+k+2p}. \tag{18}$$

Using representations (6) and (17) and carrying out necessary transformations, we express the coefficients p_{nk} of the infinite set of linear algebraic equations (15) via the integral $I_k^{(m,n)}(a)$:

$$p_{00} = \frac{4a}{\pi^2}\frac{Q_{-\frac{1}{2}}(\cosh\alpha_0)}{P_{-\frac{1}{2}}(\cosh\alpha_0)}I_0^{(0,0)}(a),$$

$$p_{0k} = \frac{2a}{\pi^2}\frac{Q_{-\frac{1}{2}}(\cosh\alpha_0)}{P_{k-\frac{1}{2}}(\cosh\alpha_0)}$$

$$\times\left\{2I_0^{(0,0)}(a) + \sum_{p=1}^{|k|} f_p^{|k|}|k|a^p I_p^{(p,0)}(a)\right\};$$

$$k = \pm1, \pm2, \ldots,$$

$$p_{n0} = \frac{2a}{\pi^2}\frac{Q_{n-\frac{1}{2}}(\cosh\alpha_0)}{P_{-\frac{1}{2}}(\cosh\alpha_0)}$$

$$\times\left\{2I_0^{(0,0)}(a) + \sum_{p=1}^{|n|} f_p^{|n|}|n|a^p I_p^{(p,0)}(a)\right\};$$

$$n = \pm1, \pm2, \ldots,$$

$$p_{nk} = \frac{a}{2\pi^2}\frac{Q_{n-\frac{1}{2}}(\cosh\alpha_0)}{P_{k-\frac{1}{2}}(\cosh\alpha_0)}\left\{8I_0^{(0,0)}(a)\right.$$

$$+ 4\sum_{p=1}^{|n|} f_p^{|n|}|n|a^p I_p^{(p,0)}(a) + 4\sum_{p=1}^{|k|} f_p^{|k|}|k|a^p I_p^{(p,0)}(a)$$

$$+ 2\sum_{p=1}^{|n|}\sum_{m=1}^{|k|} f_p^{|n|} f_m^{|k|}|n||k|a^{m+p} I_{m+p}^{(m,p)}(a)$$

$$\left. + 2\sum_{p=1}^{|n|}\sum_{m=1}^{|k|} f_p^{|n|} f_m^{|k|} pm\frac{|n|}{n}\frac{|k|}{k}a^{m+p} I_{m+p}^{(m-1,p-1)}(a)\right\};$$

$$n = \pm1, \pm2, \ldots; \quad k = \pm1, \pm2, \ldots,$$

where $a = c/b < 1$.

CAPACITANCE OF THE TORUS

The charge Q_t of the torus T is calculated through the coefficients x_n by the formula [12]

$$Q_t = 8\pi\varepsilon c\sum_{n=-\infty}^{\infty}\frac{x_n}{P_{n-\frac{1}{2}}(\cosh\alpha_0)},$$

where ε is the permittivity of the medium.

Table 2 lists the normalized capacitance $K_{\text{norm}} = Q_t/4\pi\varepsilon bV_t$ of the torus, which was calculated for different geometries of the conductors. The extreme right column of Table 2 shows the capacitance K of an isolated torus according to [1].

The infinite set of linear algebraic equations (15) was solved by the truncation method [13]. As follows from the computational experiment, a truncation order of 20 will suffice to numerically solve set (15) with an accuracy of 0.001 for the geometrical parameters considered. The coefficients $I_k^{(m,n)}(a)$, which are convergent series (18), were calculated accurate to 10^{-5}.

Table 2

$\frac{r}{R}$	$b/R = 3$	$b/R = 5$	$b/R = 10$	$b/R = 15$	K
0.1	0.921	0.827	0.771	0.753	0.722
0.2	1.174	1.026	0.939	0.915	0.868
0.3	1.412	1.202	1.086	1.053	0.992
0.4	1.658	1.374	1.224	1.182	1.106
0.5	1.921	1.548	1.360	1.308	1.216
0.6	2.208	1.727	1.496	1.434	1.323
0.7	2.527	1.913	1.633	1.559	1.429
0.8	2.883	2.106	1.771	1.684	1.534
0.9	3.286	2.308	1.921	1.811	1.638

The Legendre (torus) functions $P_{n-\frac{1}{2}}(\cosh\alpha_0)$ and $Q_{n-\frac{1}{2}}(\cosh\alpha_0)$ were calculated by the formulas [5, 7]

$$P_{n-\frac{1}{2}}(\cosh\alpha_0) = \frac{1}{\pi}\int_0^{\pi}\frac{d\varphi}{(\cosh\alpha_0 + \sinh\alpha_0\cos\varphi)^{n+0.5}},$$

$$Q_{n-\frac{1}{2}}(\cosh\alpha_0) = \int_0^{\pi}\frac{\cos n\varphi d\varphi}{\sqrt{2(\cosh\alpha_0 - \cos\varphi)}}.$$

The calculations were carried out with the MathCAD 2000 integrated software system [14].

REFERENCES

1. Yu. Ya. Iossel', É. S. Kochanov, and M. L. Strunskiĭ, *Calculation of Electrical Capacitance* (Énergoizdat, Leningrad, 1981) [in Russian].
2. V. P. Il'in, *Numerical Solution of Electrophysics Problems* (Nauka, Moscow, 1985) [in Russian].
3. M. K. Yarmarkin, Izv. Akad. Nauk, Énerg., No. 11, 23 (1979).
4. V. N. Ostreĭko, Radiotekh. Élektron. (Moscow) **26**, 2456 (1981).
5. N. N. Lebedev, *Special Functions and Their Applications* (Fizmatgiz, Moscow, 1963; Prentice-Hall, New York, 1965).
6. G. Ch. Shushkevich, *Calculation of Electrostatic Fields by Methods of Pair and Triple Equations Using Summation Theorems* (Grodnensk. Gos. Univ., Grodno, 1999) [in Russian].
7. M. Abramovitz and I. A. Stegun, *Handbook of Mathematical Functions* (Dover, New York, 1971; Nauka, Moscow, 1979).

8. A. F. Nikiforov and V. B. Uvarov, *Special Functions of Mathematical Physics: A Unified Introduction with Applications* (Nauka, Moscow, 1978; Birkhauser, Basel, 1987).
9. V. T. Erofeenko, Differentsial'nye Uravneniya **19**, 1416 (1983).
10. C. B. Ling and J. Lin, Math. Comput. **26**, 529 (1972).
11. Y. L. Luke, *Mathematical Functions and Their Approximations* (Academic, New York, 1975; Mir, Moscow, 1980).
12. G. Ch. Shushkevich, Zh. Tekh. Fiz. **67** (4), 123 (1997) [Tech. Phys. **42**, 436 (1997)].
13. L. V. Kantorovich and V. I. Krylov, *Approximate Methods of Higher Analysis*, 5th ed. (Fizmatgiz, Moscow, 1962; Wiley, New York, 1964).
14. G. Ch. Shushkevich and S. V. Shushkevich, *Introduction to MathCAD 2000* (Grodnensk. Gos. Univ., Grodno, 2001) [in Russian].

Translated by V. Isaakyan

Technical Physics, Vol. 49, No. 5, 2004, pp. 545–550. Translated from Zhurnal Tekhnicheskoĭ Fiziki, Vol. 74, No. 5, 2004, pp. 24–29.

GAS DISCHARGES, PLASMA

Cold-Hollow-Cathode Arc Discharge in Crossed Electric and Magnetic Fields

P. M. Schanin, N. N. Koval, Yu. Kh. Akhmadeev, and S. V. Grigoriev

Institute of High Current Electronics, Siberian Division, Russian Academy of Sciences, Akademicheskiĭ pr. 4, Tomsk, 634055 Russia

e-mail: schanin@opee.hcei.tsc.ru

Received July 25, 2003

Abstract—A crossed-field cold-hollow-cathode arc is stable at low working gas pressures of 10^{-2}–10^{-1} Pa, magnetic-field- and gas-dependent arcing voltages of 20–50 V, and discharge currents of 20–200 A. This is because electrons come from a cathode spot produced on the inner cathode surface by a discharge over the dielectric surface. The magnetic field influences the arcing voltage and discharge current most significantly. When the plasma conductivity in the cathode region decreases in the electric field direction, the magnetic field increases, causing the discharge current to decline and the discharge voltage to rise. The discharge is quenched when a critical magnetic field depending on the type of gas is reached. Because of the absence of heated elements, the hollow cathode remains efficient for long when an arc is initiated in both inert and chemically active gases. © *2004 MAIK "Nauka/Interperiodica".*

INTRODUCTION

A low-pressure arc finds wide application in various gas-discharge devices owing to low arcing voltages, high discharge currents, and a wide range of pressures at which the arc is initiated and maintained. In ion sources, an arc discharge generates both gas ions and ions of almost all conducting materials [1, 3]. In plasma-assisted processes of surface modification of condensed media, vacuum and gas arcs ensure high energy efficiency of technological equipment, which is otherwise a challenge. A glow discharge, which is today commonly used for ion nitridation, has a high ignition voltage (hundreds of volts) and a high nitrogen pressure (~10^4 Pa) at which the discharge is initiated and maintained. Therefore, it is necessary to introduce hydrogen into this discharge, which binds to oxygen present in the residual atmosphere. The lifetime of an incandescent-cathode arc discharge [4] is limited, because the cathode is damaged by ion bombardment and poisoned in chemically active media. A vacuum arc is sometimes inapplicable because of a large amount of droplets and atoms of the cathode material in the plasma flow, although, as was shown in [5], the percentage of gas ions in a vacuum arc may be increased considerably by modifying the design of related devices. Finally, it was reported [6] that surface nitridation in the ammonia plasma flow generated by a vacuum discharge can be carried out without heating to high temperatures.

A cold-hollow-cathode arc discharge with a cathode spot produced on the inner surface of the hollow cathode [7, 8] makes it possible to reduce or even prevent penetration of the cathode material into the anode region, i.e., into the process chamber, and makes it possible to maintain the arc for a long time in chemically active gases with all the advantages of an arc retained.

DISCHARGE SYSTEM

In the discharge system schematically shown in Fig. 1, an arc initiated by a discharge over the dielectric surface arises between a hollow water-cooled cathode (the diameter D = 110 mm and the length L = 200 mm) and a hollow anode (i.e., a vacuum chamber measuring 600 × 600 × 600 mm). The discharge is maintained

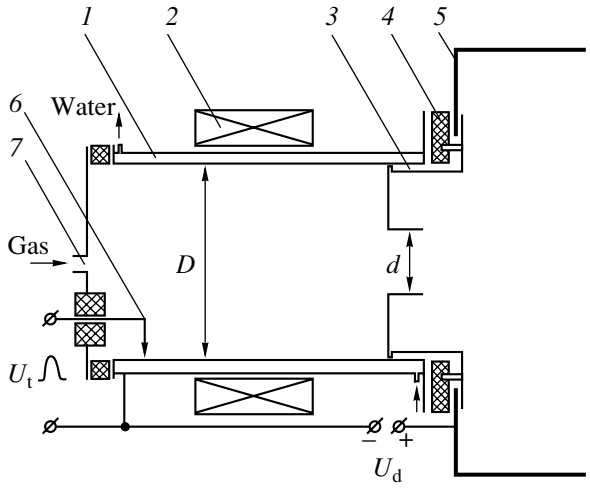

Fig. 1. Schematic view of the hollow-cathode arc discharge system: (*1*) hollow cathode, (*2*) magnetic coil, (*3*) arc arrester, (*4*) insulator, (*5*) vacuum chamber, (*6*) igniter, and (*7*) gas inlet.

1063-7842/04/4905-0545$26.00 © 2004 MAIK "Nauka/Interperiodica"

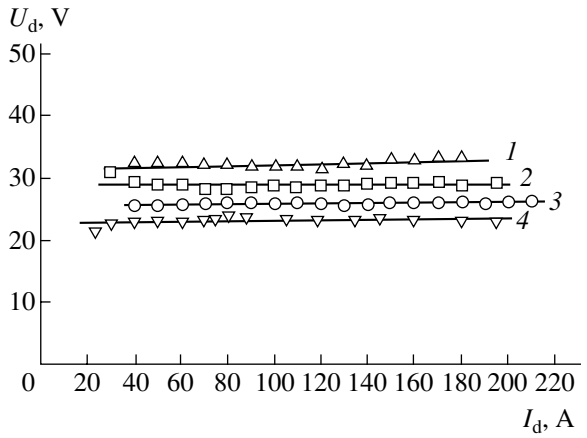

Fig. 2. *I–V* characteristics of the discharge in (*1*) nitrogen, (*2*) oxygen, and (*3*) argon filling the discharge space with the hollow copper cathode. (*4*) Discharge in argon in the case of the stainless steel cathode. The gas pressure is p = 0.44 Pa; B = 3 mT.

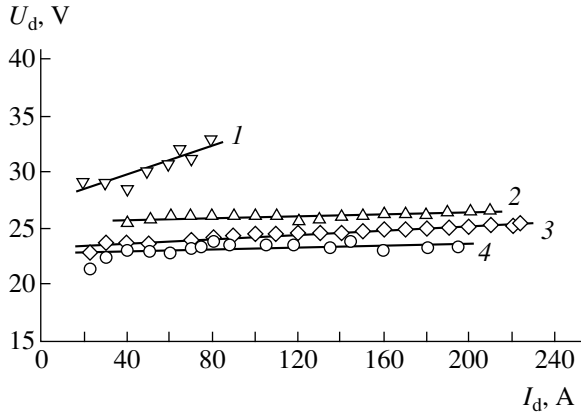

Fig. 3. *I–V* characteristics of the discharge for (*1*) graphite, (*2*) copper, (*3*) aluminum, and (*4*) stainless steel cathodes. The working gas is argon at p = 0.44 Pa; B = 3 mT.

through a diaphragm of diameter d = 15–50 mm in a floating-potential arc arrester mounted on the end face of the hollow cathode.

The arc arrester with the diaphragm prevents the cathode spot from reaching the end face of the hollow cathode. Also, it prevents the transition of the diffusive discharge in the anode region to the pinching discharge with the formation of an anode spot on a nearby part of the anode.

A short magnetic coil wound on the hollow cathode generates an axial magnetic field in the cathode region. According to [8], the cathode spot in crossed fields circles on the inner surface of the hollow cathode, remaining in the maximum of the nonuniform magnetic field, with the spot velocity increasing with increasing magnetic field. The products of cathode sputtering (droplets, atoms, and ions) accumulate mainly on the hollow cathode surface opposite to the cathode spot, thereby reducing the erosion of the cathode and raising its lifetime. A part of the sputtered cathode material that depends on the diameter of the diaphragm in the arc arrester may reach the anode region of the discharge (hereafter, the anode region) in the form of ions, atoms, and droplets.

There are different ways to remove the droplets [9–11]. In this work, we narrowed the diaphragm in the arrester in order to prevent the cathode material from penetrating into the anode region. However, a decrease in the diameter d changes the discharge conditions and, accordingly, the plasma parameters in the anode region.

RESULTS AND DISCUSSION

We experimented with three gases and several hollow cathodes made from stainless steel, copper, aluminum, and graphite. The diameter d = 50 mm of the diaphragm in the arc arrester was fixed, d = 50 mm.

At a constant gas pressure p = 0.44 Pa and a magnetic field B = 0.6–14 mT, the arcing voltage is independent of the discharge current in a wide current range for all the gases. The arcing voltage was the lowest in an argon atmosphere. In the working pressure range p = $(8–80) \times 10^{-2}$ Pa, the arcing voltage varies by no more than 10% for all the gases (Fig. 2).

Since the cathode drops for various materials are close to each other (15–21 V for Cu, 16–20 V for Al, and 17–18 V for Fe [12]), the arcing voltages for the stainless steel and copper cathodes are close to each other (Fig. 3). Surprisingly, the arcing voltage for the graphite cathode is 35–50% higher, although, according to the known data for graphite [13], it was expected to be minimal.

Another intriguing feature of the graphite-cathode arc discharge is an extremely low velocity of the cathode spot on the inner cathode surface: 3 mm/s versus 15 m/s for cathodes made from pure metals in the same magnetic field.

The magnetic field affects the arcing voltage and discharge current most significantly. After the discharge has been ignited in an initial magnetic field, an increase in the field increases the arcing voltage and decreases the discharge current (Fig. 4).

The decrease in the discharge current and arc quenching upon reaching a critical magnetic field are associated with a decrease in the longitudinal plasma conductivity (i.e., the conductivity in the electric field direction) given by

$$\sigma'' = \frac{\sigma_e}{1 + \omega_H^2/\nu_{col}^2}, \qquad (1)$$

where $\sigma_e = e^2 n_e/m\nu_{col}$ is the conductivity in the zero magnetic field, $\omega_H = eB/m$ is the cyclotron frequency, $\nu_{col} = n_n v\sigma$ is the electron–electron collision frequency, v is the electron velocity, n_e is the electron concentration, n_n is the concentration of neutrals, and σ is the

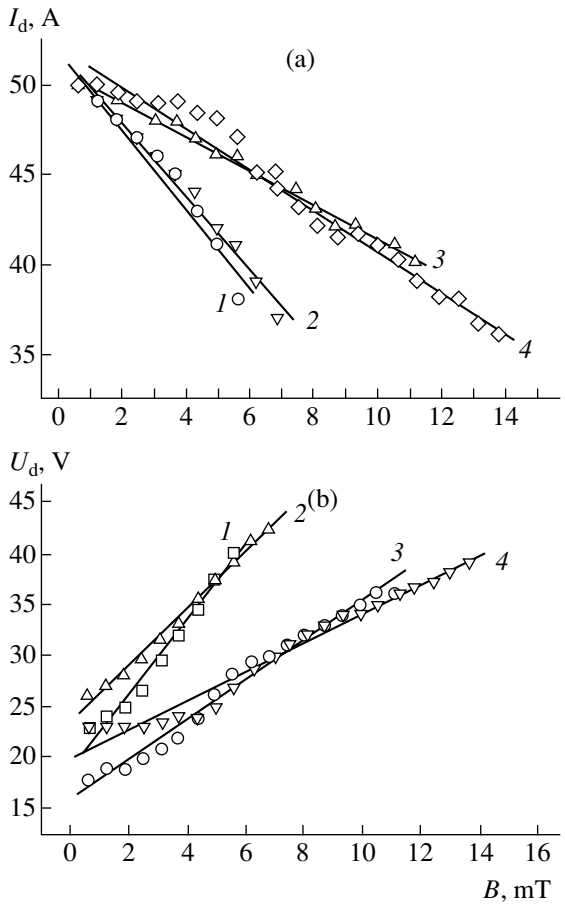

Fig. 4. (a) Discharge current and (b) arcing voltage vs. the magnetic field with (*1*) oxygen, (*2*) nitrogen, and (*3*) argon in the discharge space for the case of the hollow copper cathode and (*4*) with argon for the case of the stainless steel cathode. The gas pressure p = 0.44 Pa.

transport elastic-collision cross section. According to Eq. (1), as the magnetic field (and, accordingly, the cyclotron frequency) increases, the longitudinal conductivity decreases and the current discharge declines. In the magnetic field range studied, the cyclotron frequency varied from 9.0×10^7 to 9.0×10^8 s^{-1}. At an argon pressure $p = 4.4 \times 10^{-1}$ Pa and an average energy electron near the cathode ε =10–20 eV, the collision frequency $\nu_{col} = 1.5 \times 10^8$ s^{-1}. The decrease in the discharge current with increasing magnetic field correlates (at least qualitatively) with the magnetic field dependence of the conductivity. The fact that the rate of variation of the discharge current depends on the magnetic field and the type of gas may be accounted for by different electron–electron collision frequencies. In the range of electron energies near the cathode considered in this work (10–20 eV), the electron–electron collision frequency in argon is about twice as high as that in nitrogen and oxygen. Accordingly, the discharge current in the argon plasma decreases more slowly and the arc is quenched in a magnetic field exceeding that in nitrogen by a factor of 1.5–2.

The effect of magnetic field on the arcing voltage and discharge current depends on the gas pressure. At a lower magnetic field (B = 3 mT), the discharge current does not depend on the pressure in the range 0.25–1.4 Pa (Fig. 5). At a higher magnetic field (B = 9 mT), the arc is initiated and remains stable at higher pressures. As the pressure increases further, the voltage linearly decreases, while the current linearly rises (Fig. 6). The rise in the initial pressure of the stable discharge in the higher magnetic field is associated with the need for increasing the electron–electron collision frequency in order that the longitudinal conductivity of the plasma remain constant (see (1)).

PLASMA PARAMETERS IN THE HOLLOW ANODE

A change in the diameter d of the diaphragm may change the discharge regime and, correspondingly, the

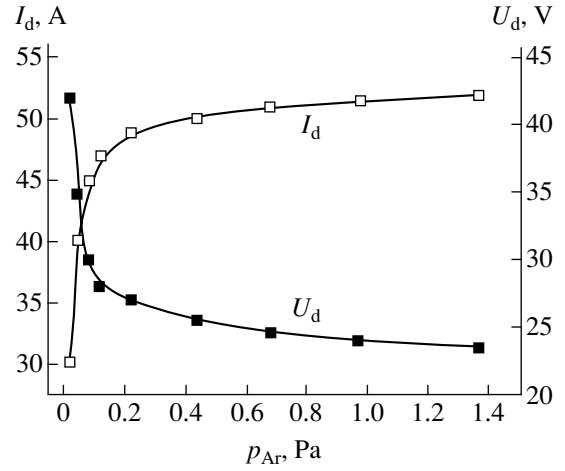

Fig. 5. Discharge current and arcing voltage vs. the argon pressure. The magnetic field is B = 3 mT.

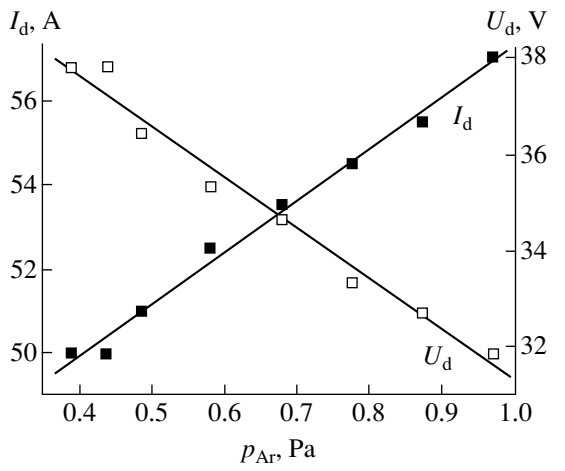

Fig. 6. The same as in Fig. 5 for B = 9 mT.

Table 1. Plasma parameters as a function of the diaphragm diameter

Diameter d, mm	U_d, V	φ_p, V	$n \times 10^9$, cm^{-3}	T_e, eV	φ_f, V	φ_f (calculation), V
50	26.5	4.0	5.3	3.4	–11.5	(–16.2)
20	27.0	3.8	5.2	3.6	–11.5	(–17.1)
15	27.0	3.2	3.9	4.0	–11.5	(–18.6)

Table 2. Plasma parameters versus pressure

Pressure, Pa	$n \times 10^9$, cm^{-3}	φ_f, V	φ_p, V	T_e, eV
0.05	4.4	–16.5	7.2	3.6
0.33	9.2	–13.5	4.4	2.0
0.44	6.8	–12.5	3.6	3.1
0.9	4.0	–11.5	2.7	4.2

plasma parameters in the anode region. For $d = 5$, 2, and 1.5 cm; a discharge current of 50 A; and an argon pressure $p = 4.4 \times 10^{-1}$ Pa, the Ar plasma parameters were measured at a distance of 30 cm from the outer end face of the arc arrester using a plane probe with a guard ring. The results are listed in Table 1.

It is seen from Table 1 that, as the diaphragm narrows, the plasma density n and plasma potential φ_p decrease, while the electron temperature T_e grows provided that the discharge voltage U_d is constant. The floating potential φ_f remains unchanged and is distinct from the value calculated by the formula

$$\varphi_f = T_e \ln\left(\frac{M}{2\pi m}\right)^{1/2}, \quad (2)$$

where T_e is the electron temperature in volts, M is the ionic mass, and m is the mass of an electron.

As follows from visual observations, the narrowing of the diaphragm not only affects the plasma parameters in the anode region but also induces modifications of the discharge structure. At small diameters of the diaphragm, its center glows more brightly. This effect is most probably due to fast electrons present in the diaphragm with the concentration varying as $n_e(r) \sim 1/r$ [4] and also due to the higher plasma density. At an elastic electron–electron scattering cross section in argon $\sigma = 1.2 \times 10^{-15}$ cm^{-2}, pressure $p = 4.4 \times 10^{-1}$ Pa, and mean free path $\lambda \approx 10$ cm, there appears the probability that electrons will oscillate in the hollow cathode plasma and unrelaxed fast electrons will escape into the anode region and ionize the gas.

Table 2 lists the plasma parameters measured in the anode region at a discharge current $I_d = 50$ A and a magnetic field $B = 3$ mT. As the argon pressure changes from 3×10^{-1} to 9×10^{-1} Pa, the electron temperature increases, while the plasma density, the plasma potential relative to the anode, and the floating potential decrease. However, at a low pressure of 5×10^{-2} Pa, the plasma density and temperature behave in a manner other than at high pressures. It is visually observed that the discharge undergoes structural transformation at this pressure: the diffusive discharge turns into the pinching discharge, the pinch being related to the cathode spot rotating in the hollow cathode. This fact is probably associated with the escape of fast electrons from the hollow cathode, which excite and ionize gas molecules in the anode region.

In the case of the graphite-cathode discharge, the plasma parameters in the anode region are, as expected, much different from those considered above. At the discharge current $I_d = 50$ A, arcing voltage $U_d = 40.5$ V, and magnetic field $B = 12$ mT in argon, the plasma potential becomes negative relative to the anode ($\varphi_p = –3.2$ V), the negative floating potential rises to $\varphi_f = –20.5$ V, and the electron temperature increases to $T_e = 8$ eV.

PENETRATION OF THE CATHODE MATERIAL INTO THE ANODE REGION

An arc discharge with a cathode spot causes cathode erosion, which depends on the discharge current. At a discharge current of 60–80 A, the specific erosion (the material lost per unit charge) may be as high as 0.5–1.2×10^{-4} g/C depending on the cathode material [15]. As was mentioned above, the cathode material may enter into the anode region as ions, atoms, or droplets. For the electrode configuration considered, the amount of the material falling into the anode region will depend on the diameter of the diaphragm in the arc arrester, as well as on the ion and atom distribution in the hollow cathode. Let us estimate the distribution of the cathode material particles taking into account elastic collisions between the particles and gas atoms. We suppose that the atoms and ions leave the cathode normally to its surface. Then, the number of the particles traveling a distance x and changing their initial direction as a result of elastic collisions and loss of momentum is described by the expression

$$\Delta N = N_c\left[1 - \exp\left(-\frac{x}{\lambda}\right)\right], \quad (3)$$

where N_c is the number of particles leaving the cathode and $\lambda = 1/n_n\sigma$ is the mean free path of the particles.

Let the elastic collision cross sections for cathode material atoms (Fe, Al, and Cu) be close to that for Ar atoms. Then, at $p = 0.44$ Pa and $\lambda = 1.5$ cm, almost all the atoms will undergo collisions and change their direction over the distance to the axis of the hollow cathode ($x = D/2 = 5$ cm). Due to the effects of charge exchange and polarization of neutrals, ion scattering will be more intense than atom scattering. Therefore,

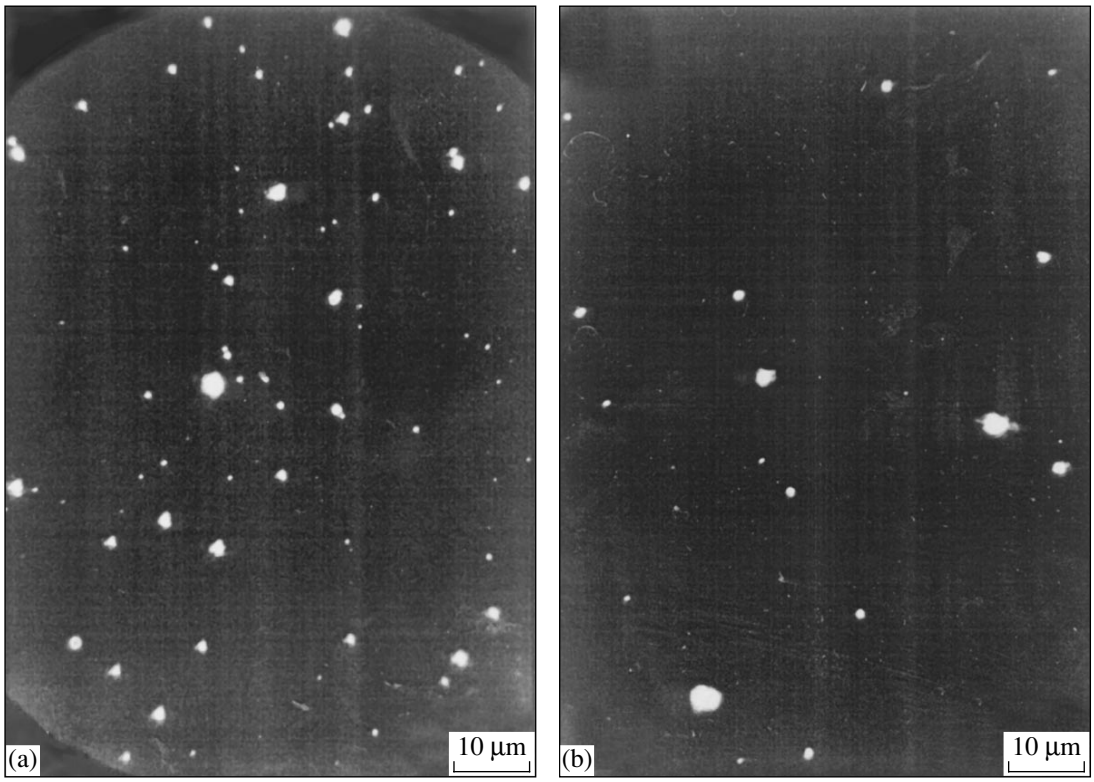

Fig. 7. Image of the target surface exposed to the arc discharge with the hollow copper cathode in the argon atmosphere. The diameter of the diaphragm is (a) 5 and (b) 1.5 cm.

the particle distribution in the hollow cathode may be considered isotropic, in a first approximation. Let us estimate roughly the arrival of ions and atoms at the anode region. If their distribution in the hollow cathode is isotropic, the yield f of cathode material particles is given by the ratio of the diaphragm surface area S to the cathode total surface area S_c, $f = S/S_c$. For example, with a hole diameter $d = 5$ cm, the number N_a of the particles falling into the anode region is $N_a = fN_0 = 1 \times 10^{-2}N_0$; for $d = 1.5$ cm, $N_a = 0.001N_0$ (here, N_0 is the number of particles in the hollow cathode). Note that, in a standard film evaporator, a layer 3 μm thick is applied for 2 h. In our discharge system, the thickness of an impurity layer under similar operating conditions will be within several tens of monolayers when the erosion products contain 80% of ionized and vapor phases.

For experimental detection of droplets entering the anode region, glass and metallic targets were arranged at a distance of 30 cm from the intermediate electrode. For an arc duration of 1 h, droplets from 0.5 to 4 μm in size were revealed. Their concentration varied between 100 and 120 mm^{-2} at a diaphragm diameter of 5 cm and between 10 and 20 mm^{-2} at a diaphragm diameter of 1.5 cm (Fig. 7).

For the stainless steal cathode and the same discharge current, the number of droplets is one order of magnitude smaller. They almost disappear on the metallic target if a negative bias of 100 V is applied to it. This well-known effect [16–18] arises when droplets negatively charged to the floating potential in the discharge plasma are reflected from a negatively biased object.

CONCLUSIONS

In a cold-hollow-cathode crossed-field arc discharge, the cathode spot initiated by a discharge over the dielectric surface moves on the cathode inner surface, remaining in the maximum of the magnetic field. For currents of 20–200 A, a low-pressure gas arc is stable in a narrow range of magnetic fields. At a constant pressure and magnetic field, the arcing voltage is independent of the discharge current (flat I–V characteristic) and amounts to 20–50 V depending on the sort of the working gas and cathode material. Since droplets and atoms of the sputtered cathode material deposit on the surface opposite to the cathode spot, the cathode lifetime increases. Under certain conditions, penetration of the cathode material into the anode region can be prevented. By moving the maximum of the magnetic field produced by a short coil over the hollow cathode, i.e., displacing the cathode spot, one can ensure uniform cathode wear and utilize most of its working surface. To prevent the droplets reflected by the cathode inner surface from penetrating into the anode region, the surface

area of the diaphragm between the cathode and anode regions must be decreased appropriately. Stainless steel is the most promising cathode material for generating a gas plasma. In this case, the fraction of droplets is the lowest among the materials investigated.

A plasma produced by the discharge studied in this work was used for surface modification of steel and alloys.

REFERENCES

1. I. G. Brown, *The Physics and Technology of Ion Sources* (Wiley, New York, 1989; Mir, Moscow, 1988).
2. S. P. Bugaev, A. G. Nikolaev, E. M. Oks, *et al.*, Rev. Sci. Instrum. **63**, 2422 (1992).
3. E. M. Oks and P. M. Schanin, Phys. Plasma **6**, 1649 (1999).
4. D. P. Borisov, N. N. Koval', and P. M. Schanin, Izv. Vyssh. Uchebn. Zaved. Fiz., No. 3, 115 (1994).
5. A. S. Bugaev, V. I. Gushenets, A. G. Nikolaev, *et al.*, *Emerging Application of Vacuum-Arc-Produced Plasma, Ion and Electron Beams* (Kluwer, Dordrecht, 2002), pp. 79–90.
6. Hirokazu Tahara, Yasutaka Ando, and Takao Yoshikawa, IEEE Trans. Plasma Sci. **31**, 281 (2002).
7. N. V. Gavrilov, Yu. E. Kreĭndel, G. A. Mesyats, and F. N. Shvedov, Pis'ma Zh. Tekh. Fiz. **14**, 865 (1988) [Sov. Tech. Phys. Lett. **14**, 383 (1988)].
8. L. G. Vintizenko, S. V. Grigoriev, N. N. Koval, *et al.*, Izv. Vyssh. Uchebn. Zaved. Fiz., No. 9, 28 (2001).
9. I. I. Aksenov, V. A. Belous, V. G. Padalka, *et al.*, Prib. Tekh. Éksp., No. 5, 236 (1978).
10. S. Anders, A. Anders, M. Dickunson, R. MakGill, and I. Brown, in *Proceedings of the 17th International Symposium on Discharges and Electrical Insulation in Vacuum, Berkeley, 1996*, p. 904.
11. A. I. Ryabchikov, S. V. Degtyarev, and I. B. Stepanov, Izv. Vyssh. Uchebn. Zaved. Fiz., No. 4, 193 (1998).
12. Yu. P. Raizer, *Physics of Gas Discharge* (Nauka, Moscow, 1987; Springer-Verlag, Berlin, 1991).
13. J. M. Lafferty, *Vacuum Arcs: Theory and Application* (Wiley, New York, 1980; Mir, Moscow, 1982).
14. A. V. Zharinov and Yu. A. Kovalenko, Izv. Vyssh. Uchebn. Zaved. Fiz., No. 9, 44 (2001).
15. A. M. Dorodnov, Zh. Tekh. Fiz. **48**, 1858 (1978) [Sov. Phys. Tech. Phys. **23**, 1058 (1978)].
16. M. Keidar, R. Aharonov, and I. I. Beilis, J. Vac. Sci. Technol. A **17**, 3067 (1999).
17. P. M. Schanin, N. N. Koval, A. V. Kozyrev, *et al.*, J. Tech. Phys. (Poland) **41**, 177 (2000).
18. P. M. Schanin, N. N. Koval, A. V. Kozyrev, *et al.*, in *Proceedings of the 5th Conference on Modification of Materials with Particle Beams and Plasma Flows, Tomsk, 2000*, pp. 438–441.

Translated by M. Astrov

Technical Physics, Vol. 49, No. 5, 2004, pp. 551–558. Translated from Zhurnal Tekhnicheskoĭ Fiziki, Vol. 74, No. 5, 2004, pp. 30–37.

GAS DISCHARGES, PLASMA

Electron Temperature in a Decaying Krypton Plasma in the Presence of a Low Electric Field

N. A. Gorbunov, N. B. Kolokolov†, F. E. Latyshev, and A. S. Mel'nikov

Research Institute of Physics, St. Petersburg State University, St. Petersburg, 198504 Russia

e-mail: gorbunov@paloma.spbu.ru

Received July 28, 2004

Abstract—The influence of low electric fields on the average electron energy in an afterglow krypton plasma is studied by means of probe diagnostics and theoretical analysis. It is shown that, when the average electron energy is lower than the energy corresponding to the minimum scattering transport cross section, the degree of plasma ionization substantially affects the shape of the electron energy distribution function (EEDF). The nonequilibrium character of the EEDF results in the density dependence of the coefficient of ambipolar diffusion, which leads to a change in the radial profile of the charged particle density, an increase in the drop in the ambipolar potential across the plasma, and an increase in the rate of diffusive plasma decay. These effects substantially enhance the diffusive cooling of electrons, which is probably a decisive factor influencing the electron energy balance in high-*Z* noble gases. © *2004 MAIK "Nauka/Interperiodica".*

INTRODUCTION

The presence of a deep minimum in the energy dependence of the cross sections for electron elastic scattering in high-*Z* noble gases (Ar, Kr, Xe) substantially influences the transport features of the electron gas [1]. This influence is especially pronounced in nonself-sustained discharges at low electric fields when the average electron energy is close to the energy corresponding to the Ramsauer minimum, $\langle\varepsilon\rangle \approx 0.2$–$0.6$ eV. The shape of the electron energy distribution function (EEDF) and, accordingly, the average energy and drift velocity of electrons depend on the degree of ionization [2]. In a number of theoretical studies, the existence of hysteretic effects [3, 4] and bistable states [5] was predicted. An analysis was made of the possibility of the existence of a negative differential conductivity [6] and the absolute negative conductivity in mixtures of high-*Z* noble gases with electronegative gases [7] or in a photoplasma [8]. It should be noted that the EEDF has not yet been studied experimentally under conditions considered in [2–8].

In [2–8], the EEDF and the kinetic coefficients were calculated parametrically for an unbounded plasma, without considering boundary conditions imposed by the electrodes and the wall of a gas-discharge tube. The boundary conditions can substantially influence the domain of existence of the predicted effects. Thus, a transition from one bistable state to another is bound to be accompanied an abrupt change in the current flowing through the plasma, because the electron drift velocity changes jumpwise in the positive column of a discharge. To predict the experimental conditions under which the above effects will occur, it is also necessary to analyze the possibility of jumpwise current density variation in the cathode sheath; such analysis, however, has not yet been performed.

The presence of the wall of a gas-discharge device causes a diffusive cooling of the electron gas [9]. The electrons spend their energy on maintaining the ambipolar field in both the plasma volume and the wall sheath. The rate of diffusive losses depends on the shape of the EEDF. It was shown that depletion of the high-energy part of the EEDF (in comparison to a Maxwellian distribution) due to the diffusive loss of fast electrons escaping to the wall leads to a decrease in the potential jump at the wall [10].

The presence of a heating electric field can lead to an inverse effect, i.e., to an increase in the population of high-energy electrons in comparison to the equilibrium distribution when the value of the average electron energy is below the energy corresponding to the Ramsauer minimum, $\langle\varepsilon\rangle < \varepsilon_R$. The reason is that the electrons gain energy more rapidly when their energy correspond to the minimum frequency of transport collisions with noble-gas atoms. The excess population of electrons that have a high diffusion coefficient increases the electron flux toward the tube wall. To maintain plasma quasineutrality, the ambipolar electric field should increase, since this field suppresses the electron flux toward the wall. This effect should be most pronounced at large distances from the axis of the discharge tube, where the electron density is low. Due to radial variations in the EEDF, the ambipolar diffusion coefficient depends on the charged particle density. The effect of density-dependent diffusion was analyzed in studying the diffusion of ionized impurities in semiconductors [11]. Under the conditions of a low-temper-

† Deceased.

1063-7842/04/4905-0551$26.00 © 2004 MAIK "Nauka/Interperiodica"

ature plasma of high-Z noble gases, such analysis has not yet been performed.

The objective of this paper is an experimental study and theoretical analysis of the formation of the EEDF in the afterglow of a krypton plasma in the presence of low electric field.

EXPERIMENTAL SETUP

The experiments were carried out in a cylindrical glass tube with an inner diameter of $R = 0.6$ cm and a length of $L = 20$ cm. The gas pressure in the tube was $p = 2.2$ torr. A repetitive discharge in the tube was excited with the help of a pulsed power source (PPS). The discharge-pulse duration was $\tau = 5$ μs, the repetition rate was $f = 620$ Hz, the discharge current was $i = 150$ mA, and the reduced electric field at the instants of current measurements was $E/N = 50$ Td. A low electric field was created at a given instant of time by the second PPS. The EEDF and the electric field were measured by cylindrical probes (with a radius of $a = 0.045$ mm and length of $l = 2.5$ mm) located at the axis of the discharge tube. To measure the current–voltage (I–V) characteristics of the probes, we used an electronic circuit connected to a PC. The probe biasing was performed with the help of a 12-bit digital-to-analog converter controlled by the PC. The I–V characteristics were recorded using an expansion board incorporating a 12 bit analog-to-digital converter. The time resolution of the circuit was 10 μs, and the current sensitivity was 1 nA. The EEDFs were determined by numerically differentiating the I–V characteristics of the probes.

The systematic error of the electron-temperature measurements by the method of doubly differentiating the I–V probe characteristic was determined by solving model problems. The method for calculating the error related to the finite ratio of the probe radius to the electron mean free path is described in [12]. The calculations showed that the error in determining the temperature using the energy range $T_e \le \varepsilon \le 6T_e$ did not exceed 10% at $T_e \le \varepsilon_R$.

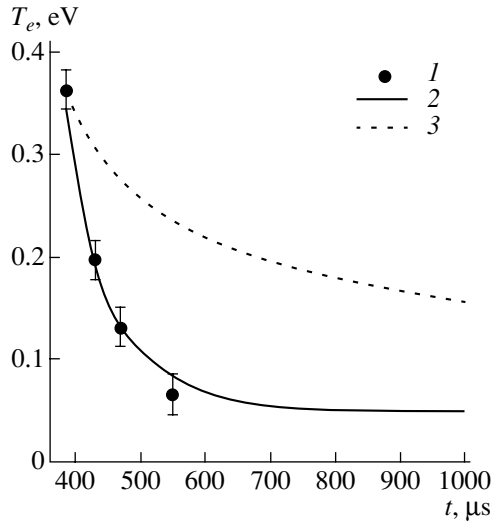

Fig. 1. Relaxation of the electron temperature T_e after the end of the heating pulse: (*1*) experimental results, (*2*) calculation taking into account diffusive losses, and (*3*) calculation assuming $H_{dif} = 0$.

The density of excited Kr atoms ($^3P_0$, $^3P_1$, $^3P_2$, and $^1P_1$) at the discharge axis was measured by the absorption method. As an irradiation source, we used a branch pipe of the discharge tube in which a low-power high-frequency discharge was excited. The presence of this discharge had no effect on the plasma parameters in the tube. Optical signals were measured by a photon-counting system controlled by a PC.

RELAXATION OF THE ELECTRON TEMPERATURE IN THE AFTERGLOW PLASMA

First, we consider the relaxation of the electron temperature in the absence of a heating electric field. Typical measurement results are presented in Fig. 1 (curve *1*). These data were obtained after the end of a 100-μs heating pulse, which provided an initial electron temperature of $T_e \simeq 0.36$ eV. The electron density averaged over the cross section of the discharge tube was determined from the plasma conductivity and amounted to $n_e \simeq 10^{11}$ cm^{-3}. At this n_e value, the electron–electron collisions in the absence of an electric field form a Maxwellian EEDF of the bulk electrons. The fast electrons produced in reactions of chemoionization of two excited (primarily, metastable) krypton atoms and superelasic collisions between electrons and excited atoms determine the high-energy ($\varepsilon > 6$ eV) part of the EEDF. Fast electrons result in an additional heating of the bulk electrons. This is why, under the conditions of quasisteady relaxation of T_e (at $t > 500$ μs), T_e is much higher than the temperature of the neutral component.

Figure 1 also shows the results of calculations of T_e relaxation. The calculations were performed using the balance equation for the average electron energy

$$\frac{\partial \langle \varepsilon \rangle}{\partial t} = -H_{ea} - H_{dif} + H_{eE} + H_{in}, \qquad (1)$$

where H_{ea} and H_{dif} describe the electron energy losses by elastic electron–atom collisions and by diffusive cooling. The electron heating is produced by the electric field H_{eE} and inelastic collisions of electrons with excited krypton atoms H_{in}.

Under afterglow conditions, we have $H_{eE} = 0$ and, for a Maxwellian electron distribution, the electron temperature is $T_e = 2\langle \varepsilon \rangle/3$. The terms H_{ea} and H_{dif} are written as follows:

$$H_{ea} = \delta \nu_{ea}(T_e)(T_e - T_a), \qquad (2)$$

$$H_{\text{dif}} = \frac{1}{\tau_d}(e\Phi_{\text{pl}} + e\Phi_{\text{sh}}), \quad (3)$$

where $\delta = 2m/M$ is the fraction of energy transferred from an electron to an atom in an elastic collision event (here, m and M are the masses of an electron and atom, respectively), $\nu_{ea}(T_e)$ is frequency of elastic electron–atom collisions (in calculating $\nu_{ea}(T_e)$, we used the data on the cross sections for elastic electron–atom collisions from [13]), $\tau_d = \Lambda^2/D_a$ is the characteristic time of ambipolar diffusion, Λ is the diffusion length, D_a is the ambipolar diffusion coefficient, Φ_{pl} is the potential drop across the plasma, and Φ_{sh} is the potential drop across the wall sheath.

A separate analysis showed that the inelastic processes related to the excitation from the ground and metastable states (including a transition from a metastable level to a resonance level [14] and to configurations lying higher this level [15]) are of less importance in comparison to energy losses due to elastic collisions at the measured density of excited atoms $[^3P_2] \simeq 2 \times 10^{10}$ cm^{-3}.

Calculation of the heating of the Maxwellian portion of the EEDF by fast electrons is a rather complicated problem. The main difficulty is to find the relation between the flux of fast electrons escaping onto the wall in the free-diffusion regime and the rate of collisional energy losses of electrons in the plasma volume. This relation depends on the potential of the tube wall. The effective energy transferred to the bulk of the electrons can vary by several orders of magnitude, depending on the relaxation mechanism of fast electrons [16]. This problem was analyzed in detail in [17] using neon afterglow as an example. In our case, we used the energy balance equation to find H_{in} under the conditions of quasi-steady relaxation of the electron temperature ($\partial T_e/\partial t = 0$). Such conditions occur at relatively long times after the end of the discharge current pulse. To calculate H_{in}, we used the measured quasi-steady value of the electron temperature, $T_e = 0.05$ eV. Since at times of $400 \le t \le 550$ μs, at which the measurements of T_e were performed, the relative change in the metastable-atom density was small (less than 10%), we assumed H_{in} to be time-independent.

In calculating H_{dif}, we used the following expressions, which are valid when the electron distribution is Maxwellian [10]: $D_a = D_i(1 + T_e/T_i)$, where D_i is the ion diffusion coefficient and $T_i = 0.026$ eV is the ion temperature; $\Lambda = R/\mu_0$, where $\mu_0 = 2.405$ is the first root of the zeroth-order Bessel function J_0; $\Phi_{\text{pl}} = T_e\ln(\Lambda/\lambda_i)$, where $\lambda_i \simeq 10^{-3}$ cm is the ion mean free path; and $\Phi_{\text{sh}} = T_e\ln\sqrt{(MT_e)/(mT_i)}$.

Under our experimental conditions, the following inequality holds: $\lambda_\varepsilon(\varepsilon) \gg \Lambda$, where $\lambda_\varepsilon(\varepsilon) = \lambda(\varepsilon)/\sqrt{\delta}$ is the electron energy relaxation length. This length is determined by the electron mean free path $\lambda(\varepsilon)$ in elastic collisions of electrons with krypton atoms. Thus, we have $\lambda_\varepsilon(\varepsilon_R) \simeq 400$ cm. Under these conditions, the electron heat conduction equalizes the T_e distribution over the cross section of the tube, so that in calculating the ambipolar flux velocity, thermal diffusion can be ignored [18].

The T_e relaxation was calculated using two approximations. In the first approximation, we took into account energy losses due to elastic collisions and diffusive cooling (Fig. 1, curve *2*). It can be seen that the calculations agree satisfactorily with the experiment. In the second approximation, diffusive cooling was ignored ($H_{\text{dif}} = 0$). It follows from Fig. 1 (curve *3*) that energy losses due to elastic electron–atom collisions cannot provide the experimentally observed decrease in T_e. This result indicates a significant contribution of diffusion processes to the electron energy balance in our case.

ELECTRON TEMPERATURE IN THE HEATING PULSE

Figure 2 shows the results of measurements of the longitudinal reduced electric field E/N (curve *1*) and the electron temperature T_e (curve *2*) in a heating electric-field pulse.

The measured value of T_e at the end of the heating pulse is $T_e = 0.25 \pm 0.05$ eV. The electric field varies only slightly during the second half of the heating pulse. For this reason, when calculating electron heating in the electric field $H_{eE}(T_e) = \mu_e E^2$, where μ_e is the electron mobility), the experimental value of the reduced field was approximated by a constant value

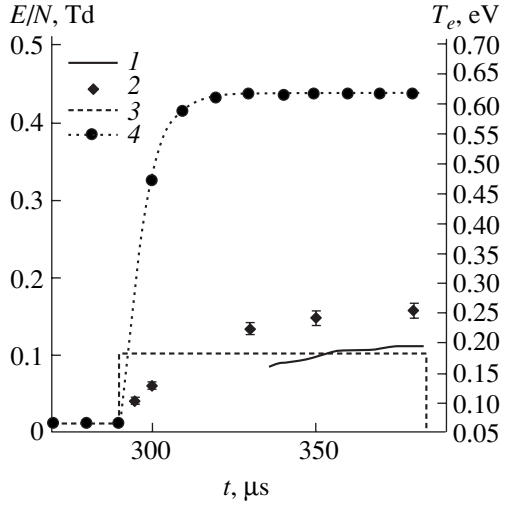

Fig. 2. Time evolution of the electron temperature T_e during the heating pulse: (*1*) longitudinal reduced electric field E/N, (*2*) electron temperature, (*3*) approximation of the reduced electric field E/N used in calculations, and (*4*) T_e calculated assuming a Maxwellian EEDF.

E/N = 0.1 Td. Figure 2 shows the results of calculations of T_e under the assumption that the EEDF is Maxwellian (curve *4*). A comparison of the calculated results with the experiment reveals two specific features. First, both the experiment and calculations demonstrate the weak dependence of T_e on time during the second half of the heating pulse ($340 \le t \le 390$ μs). This fact means that, for an analysis in this time interval, we can use a quasi-steady approximation of the energy balance equation, $\partial T_e/\partial t = 0$. Second, the calculated value of the electron temperature during the second half of the heating pulse is almost three times the experimental value. If the experimental value is substituted into the energy balance equation, then the heating power turns out to be more than one order of magnitude higher than total energy losses due to elastic collisions and diffusive cooling.

In our opinion, the discrepancy between the calculations and experiment can be attributed to the radial nonlocality of the EEDF. Let us consider a model of the formation of the EEDF. The main processes determining the shape of the EEDF under these conditions are the electron–electron and electron–atom collisions, the longitudinal electric field, and the electron diffusion toward the tube wall. Taking into account these processes, the analytical expression for the EEDF has the form [19, 20]

$$f(\varepsilon) = C_n \exp\left(-\int_0^\varepsilon \frac{d\varepsilon}{T(\varepsilon)}\right), \quad (4)$$

where the factor C_n is determined by the EEDF normalization condition

$$\int_0^\infty f(\varepsilon)\sqrt{\varepsilon}\,d\varepsilon = 1 \quad (5)$$

and the characteristic scale of EEDF decay, $T(\varepsilon)$, is defined as follows:

$$T(\varepsilon) = \frac{\dfrac{3e^2E^2}{3m\nu_{ea}(\varepsilon)} + T_a\delta\nu_{ea}(\varepsilon) + T_e\nu_{ee}(\varepsilon)A_0}{\delta\nu_{ea}(\varepsilon) + \nu_{ee}(\varepsilon)A_0}. \quad (6)$$

Here, $\nu_{ee}(\varepsilon) = \pi e^4 n_e \,\mathrm{Ln}/\sqrt{2m}\,\varepsilon^{3/2}$ is the electron–electron collision frequency, Ln is the Coulomb logarithm, $A_0(\varepsilon/T_e) = 0.385\varepsilon/T_e$ at $\varepsilon/T_e \le 2.6$, and $A_0(\varepsilon/T_e) = 1$ at $\varepsilon/T_e \ge 2.6$.

It follows from this expression that $T(\varepsilon)$ depends substantially on the energy range and the degree of ionization. In the thermal energy range ($\varepsilon \ll \varepsilon_R$), for the degree of ionization $\xi \equiv n_e/[\mathrm{Kr}] \ge 10^{-6}$, and at $E/N \le$ 0.1 Td, the dominant process is electron–electron collisions, so that $T(\varepsilon) = T_e$. As the energy increases, the role of electron–electron collisions progressively decreases. In the energy range corresponding to the Ramsauer minimum, the influence of the field term increases and the EEDF can differ markedly from Maxwellian. In calculating the EEDF by formulas (4)–(6), it is necessary to know T_e, which can be calculated using the balance equation for the mean energy or can be determined experimentally. Because of the presence of diffusive losses (the term H_{dif} in Eq. (1)), the value of T_e is always lower than the $\hat{T}_e$ value determined by the local energy balance with allowance for H_{ea} and H_{eE} only. The most pronounced effect of H_{dif} on the T_e in the case of krypton is expected in the range $0.2 < T_e < 0.8$ eV, where the ratio $H_{\mathrm{dif}}/H_{\mathrm{ea}}$ reaches its maximum value [21].

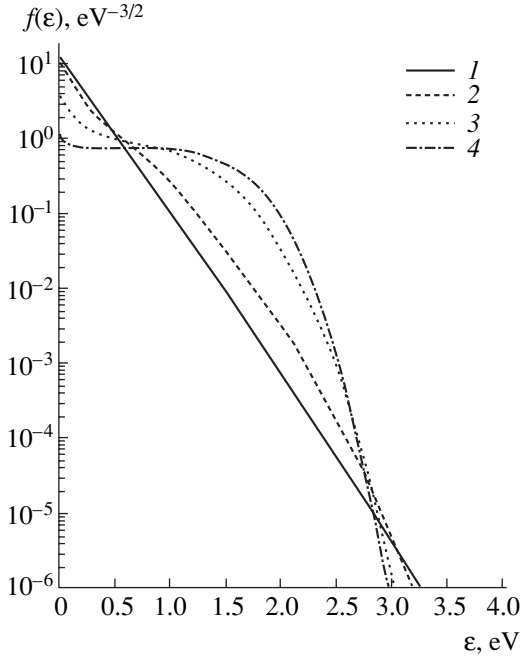

Fig. 3. EEDF calculated by formula (4) at T_e = 0.2 eV, E/N = 0.1 Td, and different degrees of ionization: ξ = (*1*) 10^{-6}, (*2*) 10^{-7}, (*3*) 10^{-8}, and (*4*) 10^{-10}.

Figure 3 shows EEDFs calculated by formula (4) with T_e = 0.2 eV and E/N = 0.1 Td for different degrees of ionization ξ. It can be seen from Fig. 3 that, at $\xi \ge 10^{-6}$, the EEDF is Maxwellian. As ξ decreases, the average electron energy increases sharply. This is because electron–electron collisions fail to retain electrons near the Ramsauer minimum and they are accelerated by the electric field to higher energies, $\varepsilon > \varepsilon_R$.

Under our experimental conditions, the degree of ionization at the tube axis, $\xi_0 \approx 10^{-6}$, was sufficient for a Maxwellian EEDF to be formed. The ratio between the charged particle densities at the plasma edge and in the center of the tube is described by the formula $n_b/n_0 \approx \lambda_i\sqrt{T_e}/\Lambda\sqrt{T_i}$ [9], which, in our case, is equal to $\approx 10^{-3}$. Hence, the electron energy distribution at the periphery of the discharge can be nonequilibrium. Let us consider possible consequences of the radial nonuniformity of the EEDF.

The ambipolar electric field E_a that is established in the plasma to equalize the radial fluxes of oppositely charged particles with the density n is [9]

$$E_a = \frac{D_i - D_e}{\mu_e + \mu_i}\frac{\nabla n}{n} \approx -\frac{\varepsilon_T}{e}\frac{\nabla n}{n}, \quad (7)$$

where D_e is the electron diffusion coefficient, μ_i is the ion mobility, and $\varepsilon_T = D_e/\mu_e$ is the Townsend energy.

It follows from Eq. (7) that E_a depends on the value of ε_T and on the radial profile of the charged particle density in the plasma. For the conditions of Fig. 3, we calculated ε_T as a function of the degree of ionization. The result is presented in Fig. 4a (curve *1*). It can be see that, when the EEDF is Maxwellian and $\xi \geq 10^{-6}$, the Einstein relation $\varepsilon_T = T_e$ holds. As ξ decreases, the value of ε_T in the range $10^{-9} \leq \xi \leq 10^{-7}$ substantially increases, which is related to the increase in $\langle\varepsilon\rangle$.

Let us examine how diffusive depletion of the EEDF influences the dependence of ε on ξ. For this purpose, we will use the "black-wall" approximation: $\tilde{f}(\varepsilon) = f(\varepsilon) + C(e\varphi_{wall})$, assuming $\tilde{f}$ to be zero at kinetic energies higher than the wall potential of the gas-discharge tube $e\varphi_{wall}$. Here, $f(\varepsilon)$ is given by expression (4) at $\varepsilon \leq \varphi_{wall}$, whereas the constant $C(e\varphi_{wall})$ satisfies the condition $C(e\varphi_{wall}) = -f(e\varphi_{wall})$. Figure 4a shows the results of calculations of $\varepsilon_T(\xi)$ for different values of $e\varphi_{wall}$. These results demonstrate that diffusive cooling leads to flatter dependences $\varepsilon_T(\xi)$, which, however, remain qualitatively the same. Thus, a specific feature of the conditions under consideration is that the average electron kinetic energy increases away from the center toward the wall of the gas-discharge tube. When the degree of ionization is low and the effect of electron–electron collisions on the EEDF is negligible, the value of $\langle\varepsilon\rangle$ tends to decrease away from the center of the tube toward the periphery [16, 22–25].

When analyzing the radial profile of the charged particle density, it is necessary to consider the motion of positive ions, because the total plasma diffusion toward the wall is primarily determined by the less mobile component. In the case of a nonlocal EEDF ($\lambda_\varepsilon \gg \Lambda$), the equation describing the ion motion is essentially nonlinear [26]. In constructing a kinetic model for the bulk electrons in a weakly ionized plasma, many authors use a simplified approach consisting in the transition to the total electron energy $w = \varepsilon + e\varphi(r)$, where $\varphi(r)$ is the radial profile of the plasma potential [16, 22, 23, 25]. When an electric field is present in the plasma and, at the same time, electron–electron collisions have a strong effect on the distribution of the bulk electrons, the applicability of this approach should be examined separately. In this paper, we consider the diffusion equation, which, in the absence of volumetric ionization and recombination,

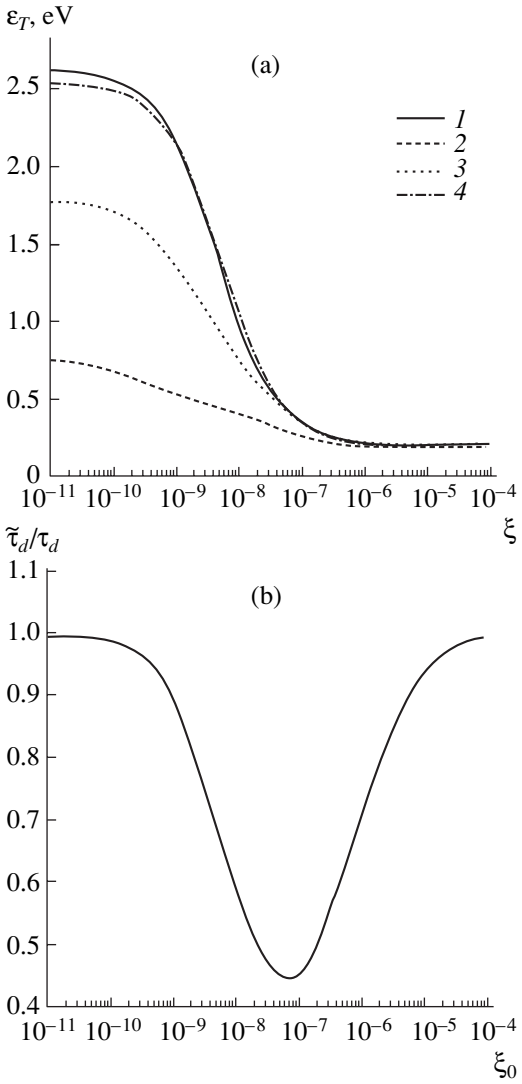

Fig. 4. (a) Dependence ε_T on ξ for $T_e = 0.2$ eV, $E/N = 0.1$ Td, and different values of $e\varphi_{wall}$: (*1*) ∞, (*2*) $5T_e$, (*3*) $7T_e$, and (*4*) $10T_e$. (b) Dependence of the ratio $\tilde{\tau}_d/\tau_d$ on the degree of ionization ξ_0 at the axis of the discharge tube.

takes the form [18]

$$\frac{\partial n}{\partial t} + \nabla \cdot (D_a \nabla n) = 0, \quad (8)$$

where $D_a = D_i(1 + \varepsilon_T/T_i)$ is the coefficient of ambipolar diffusion.

Exact analytic methods for solving this equation are available only for particular dependences $D_a(n)$ [11]. At $D_a = \text{const}$, the solution is solved by the variable separation method [9]. For a cylindrically symmetric plasma and the zero boundary conditions

$$n(R) = 0, \quad \left.\frac{\partial n}{\partial r}\right|_{r=0} = 0 \quad (9)$$

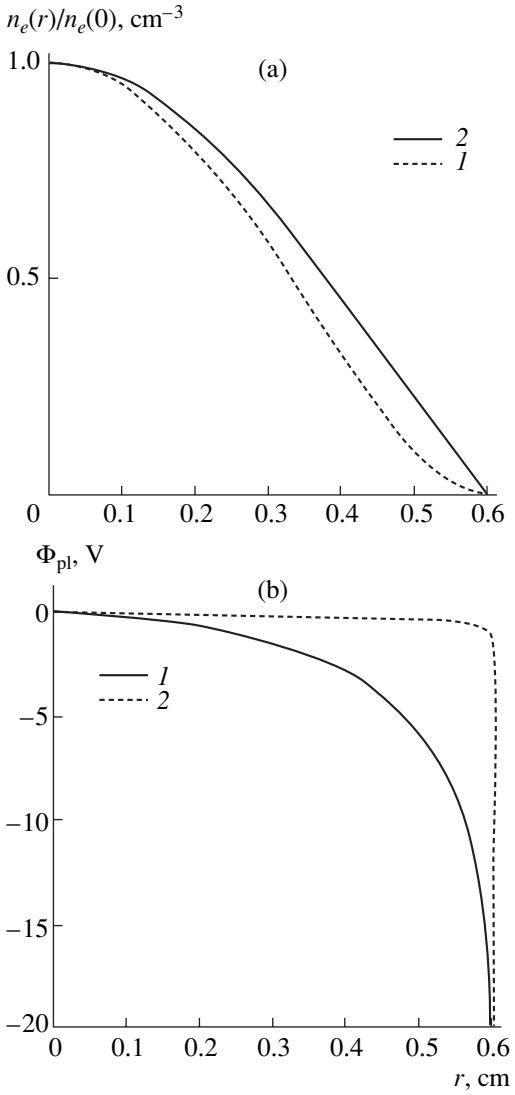

Fig. 5. Radial profiles of the (a) electron density $n_e(r)$ and (b) ambipolar difference of potentials Φ_{pl}: (*1*) for a nonequilibrium EEDF, and (*2*) for a Maxwellian EEDF.

the solution can be represented as a linear combination of the zeroth-order Bessel functions. The profile of the fundamental diffusion mode has the form $n(r) = n_0 J_0(r/\Lambda)$, where n_0 is the charged particle density at the tube axis and the diffusive loss frequency is $\nu_d = \tau_d^{-1}$. If the coefficient of ambipolar diffusion depends on the density, $D_a = D_a(n)$, then the time variations $n(t)$ cause variations in ν_d and in the characteristic diffusion length of the fundamental mode Λ_d. As a result, the radial density profile varies. In this case, the variable separation method can be used to find an approximate solution to Eq. (8) if variations in $D_a(n)$ are relatively small in comparison to variations in $n_0(t)$. The corresponding criterion may be written as $n_0(\partial\nu_d/\partial n_0) \ll \nu_d$. The maximum ratio or the left-hand side of this inequality to the right-hand side is attained at $\xi \approx 10^{-6}$ and does not exceed 30%. This estimate shows that, under these conditions, the variable separation method can be applied to analyze Eq. (8). Using this method, we can qualitatively demonstrate the difference of the density-dependent diffusion from the commonly used approximation D_a = const.

The time-independent equation for the radial profile of charged particles $n(r)$ takes the form

$$D_a\frac{\partial^2 n(r)}{\partial r^2} + \frac{\partial D_a}{\partial n}\left(\frac{\partial n(r)}{\partial r}\right)^2 + D_a\frac{1}{r}\frac{\partial n(r)}{\partial r} = -\frac{n(r)}{\tilde{\tau}_d}, \quad (10)$$

where $\tilde{\tau}_d$ are the eigenvalues of boundary problem (10).

The main difference from the case D_a = const is the presence of the second term in Eq. (10) because of the density dependence of the diffusion coefficient. Equation (10) was solved numerically by using the dependence $\partial D_a/\partial n$ specified by curve *1* in Fig. 4a and ignoring the effect of the diffusive depletion of the EEDF. This calculation provides an upper estimate for the influence of the density dependence of the diffusion coefficient $D_a(n)$ on the radial profiles of the plasma parameters. In solving nonlinear equation (10), the parameter is the degree of ionization at the axis, ξ_0.

Figure 5a (curve *1*) shows as an example the results of calculations of Eq. (10) at $\xi_0 = 10^{-6}$, which corresponds to our experimental conditions. This figure also shows the radial density profile $n(r) = n_0 J_0(r/\Lambda)$ (curve *2*). In both cases, the values of the coefficients of ambipolar diffusion at the axis are same. It can be seen in the figure that, if the diffusion coefficient depends on the density, then the profile of the charged particle density turns out to be narrower as compared to the profile corresponding to the fundamental diffusion mode in the case of D_a = const. The calculated profile $n(r)$ makes it possible to find the $E_a(r)$ profile from Eq. (7) and the profile of the ambipolar potential

$$\Phi_{pl}(r) = \int_0^r E_a(r)dr. \quad (11)$$

Figure 5b (curve *1*) shows the $\Phi_{pl}(r)$ profile calculated using nonlinear equation (10). Curve *2* describes the potential corresponding to the radial electron density profile defined by a Bessel function. It can be seen from Fig. 5b that, for a nonequilibrium distribution, the ambipolar field increases substantially. This is because ε_T increases away from the center of the gas-discharge tube. The ambipolar potential drop increases more than tenfold as compared to a Maxwellian distribution. The increased radial field increases the drift component of the electron flux toward the wall so that to compensate for the increase in the diffusive electron flux toward the wall. At the same time, the increased electric field enhances the ion motion toward the wall. Figure 4b

shows the results of calculations of the ratio $\tilde{\tau}_d/\tau_d$ (the ratio of the diffusion time for the fundamental mode of nonlinear equation (10) to the diffusion time) for the distribution $n(r) = n_0 J_0(r/\Lambda)$ at different values of the degree of ionization at the axis. It can be seen that, in the range where the density dependence is most pronounced ($\xi_0 \approx 10^{-7}$), the regime of enhanced ambipolar diffusion is realized. At the same values of D_a at the axis, the characteristic diffusion time corresponding to nonlinear diffusion halves as compared to a Bessel distribution.

Hence, an increase in Φ_{pl} or a decrease in $\tilde{\tau}_d$ can substantially increase diffusive electron losses. From calculations performed by the method described above for the experimental conditions shown in Fig. 2, it follows that diffusive losses can increase by more than twenty times as compared to a Maxwellian electron energy distribution. The effect is partially due to decreased mobility of the electrons, which in turn results in a decrease in H_{eE}. As a result, after substituting the experimentally measured axial temperature T_e in Eq. (1), diffusive losses predominate over heating. Actually, diffusive depletion of the EEDF in the high-energy range (at $\varepsilon > e\varphi_{wall}$) should increase the H_{dif} value; this probably makes it possible to achieve agreement between calculations and experiment. To take this effect into account correctly, we must determine φ_{wall} by using an equation reflecting the equality of the electron and ion fluxes toward the wall: $\Gamma_e = \Gamma_i$ [22]. Taking into account the density-dependent diffusion, as well as the diffusive depletion of the EEDF, requires the self-consistent determination of T_e, ν_d, and φ_{wall}. Solution of the set of three equations (1), (10), and $\Gamma_e = \Gamma_i$ is a rather complicated computational problem and should be considered separately.

CONCLUSIONS

Experimental measurements of the electron temperature T_e at the axis of the discharge tube have been carried out in a krypton afterglow plasma in the absence and in the presence of a weak longitudinal electric field. The calculation of T_e on the basis of the balance equation for the average electron energy has revealed a decisive role of diffusive cooling under our experimental conditions. Simulations of the relaxation of T_e in the absence of an electric field, assuming the EEDF to be Maxwellian, show that the theory agrees with experiment. In the presence of a heating pulse, the measured values of T_e disagree with calculations based on the balance equation under the assumption of a Maxwellian EEDF. To avoid this disagreement, it is proposed to use a model taking into account the nonequilibrium character of the EEDF at the periphery of the discharge. This model takes into consideration that, when the average electron energy corresponds to the minimum transport cross section for the scattering of electrons by krypton atoms, the shape of the EEDF depends substantially on the electron density and on the strength of the longitudinal electric field. The average electron energy increases away from the axis of the tube toward the wall, resulting in the density dependence of the rate of ambipolar diffusion. This leads to an increase in the difference of the ambipolar potential between the discharge axis and the tube wall, as well as to a higher rate of the diffusive plasma decay. In view of the factors listed above, the diffusive cooling of electrons increases markedly (by more than one order of magnitude), which makes it possible to achieve an agreement between the theory and experiment. To study in detail how the density dependence of the ambipolar diffusion velocity influences the plasma parameters, it is necessary to measure the radial variations in the EEDF, the radial profile of the ambipolar electric field, and the potential of the wall of the gas-discharge tube.

ACKNOWLEDGMENTS

We thank L.D. Tsendin for discussing the results obtained. This work was supported in part by the Russian Foundation for Basic Research, project no. 03-02-16346.

REFERENCES

1. L. G. H. Huxley and R. W. Crompton, *The Diffusion and Drift of Electrons in Gases* (Wiley, New York, 1974; Mir, Moscow, 1977).
2. N. L. Aleksandrov, A. M. Konchakov, and É. E. Son, Zh. Tekh. Fiz. **50**, 481 (1980) [Sov. Phys. Tech. Phys. **25**, 291 (1980)].
3. G. N. Gerasimov, M. N. Maleshin, and S. Ya. Petrov, Opt. Spektrosk. **59**, 930 (1985) [Opt. Spectrosc. **59**, 562 (1985)].
4. V. A. Ivanov and A. S. Prikhod'ko, Zh. Tekh. Fiz. **56**, 2010 (1986) [Sov. Phys. Tech. Phys. **31**, 1202 (1986)].
5. N. A. Dyatko and A. P. Napartovich, in *Proceedings of the 16th Conference on Atomic and Molecular Physics of Ionized Gases, Grenoble, 2002*, p. 215.
6. N. L. Aleksandrov, A. V. Dem'yanov, I. V. Kochetov, and A. P. Napartovich, Fiz. Plazmy **23**, 658 (1997) [Plasma Phys. Rep. **23**, 610 (1997)].
7. N. A. Dyatko, M. Kapitelli, and A. P. Napartovich, Fiz. Plazmy **25**, 274 (1999) [Plasma Phys. Rep. **25**, 246 (1999)].
8. N. A. Gorbunov and A. S. Mel'nikov, Zh. Tekh. Fiz. **69** (4), 14 (1999) [Tech. Phys. **44**, 361 (1999)].
9. V. E. Golant, A. P. Zhilinskii, and S. A. Sakharov, *Fundamentals of Plasma Physics* (Atomizdat, Moscow, 1977; Wiley, New York, 1980).
10. A. P. Zhilinskii, I. F. Liventseva, and L. D. Tsendin, Zh. Tekh. Fiz. **47**, 304 (1977) [Sov. Phys. Tech. Phys. **22**, 177 (1977)].
11. R. Sh. Malkovich, *Mathematical Apparatus of Diffusion in Semiconductors* (Nauka, St. Petersburg, 1999) [in Russian].

12. N. A. Gorbunov, A. N. Kopytov, and F. E. Latyshev, Zh. Tekh. Fiz. **72** (8), 7 (2002) [Tech. Phys. **47**, 940 (2002)].
13. J. L. Pack, R. E. Voshall, A. V. Phelps, *et al.*, J. Appl. Phys. **71**, 5363 (1992).
14. A. P. Morits and O. P. Bochkova, *Metastable States of Atoms and Molecules: Investigation Methods* (Nauka, Cheboksary, 1982) [in Russian], Vol. 5, pp. 140–153.
15. N. B. Kolokolov and O. V. Terekhova, Opt. Spektrosk. **86**, 547 (1999) [Opt. Spectrosc. **86**, 481 (1999)].
16. R. R. Arslanbekov and A. A. Kudryavtsev, Phys. Rev. E **58**, 7785 (1998).
17. N. A. Gorbunov, N. B. Kolokolov, and F. E. Latyshev, Zh. Tekh. Fiz. **71** (4), 28 (2001) [Tech. Phys. **46**, 391 (2001)].
18. V. A. Rozhanskiĭ and L. D. Tsendin, *Collisional Transfer in Partially Ionized Plasmas* (Énergoatomizdat, Moscow, 1988) [in Russian].
19. Yu. B. Golubovskiĭ, Yu. M. Kagan, and R. I. Lyagushchenko, Zh. Éksp. Teor. Fiz. **57**, 2222 (1969) [Sov. Phys. JETP **30**, 1204 (1969)].
20. N. A. Gorbunov, N. B. Kolokolov, and F. E. Latyshev, Fiz. Plazmy **27**, 1143 (2001) [Plasma Phys. Rep. **27**, 1079 (2001)].
21. N. B. Kolokolov, A. A. Kudryavtsev, and O. G. Toronov, Zh. Tekh. Fiz. **55**, 1920 (1985) [Sov. Phys. Tech. Phys. **30**, 1128 (1985)].
22. L. D. Tsendin, Plasma Sources Sci. Technol. **4**, 200 (1995).
23. I. V. Kolobov and V. A. Godyak, IEEE Trans. Plasma Sci. **23**, 503 (1995).
24. D. Uhrlandt and R. Winkler, J. Phys. D **29**, 115 (1996).
25. Yu. B. Golubovskiĭ and I. A. Porokhova, Opt. Spektrosk. **86**, 960 (1999) [Opt. Spectrosc. **86**, 859 (1999)].
26. L. D. Tsendin, Zh. Éksp. Teor. Fiz. **66**, 1638 (1974) [Sov. Phys. JETP **39**, 805 (1974)].

Translated by N. Larionova

Technical Physics, Vol. 49, No. 5, 2004, pp. 559–564. Translated from Zhurnal Tekhnicheskoĭ Fiziki, Vol. 74, No. 5, 2004, pp. 38–43.

GAS DISCHARGES, PLASMA

On Energy Transfer and Generation of an Electric Current in the Vicinity of an Electrode Dipped in an Electrolyte and Strongly Heated by a Current Passing through It

A. I. Grigor'ev

Demidov State University, Sovetskaya ul. 14, Yaroslavl, 150000 Russia

e-mail: grig@uniyar.ac.ru

Received July 16, 2003; in final form, October 4, 2003

Abstract—Processes occurring when a metal electrode dipped in an electrolyte is heated by intense evaporation of the electrolyte are considered in terms of a physically rigorous model. Based on the Onsager principle of least energy dissipation rate in nonequilibrium processes, the fractions of thermal energy that are spent on heating and evaporating the electrolyte and on heating the vapor are found. The energy is released within the vapor–gas sheath when an electric current flows between the electrode and electrolyte surface. It is found that the electrolyte vapor temperature exceeds 1300 K. Analytical expressions are derived for the vapor–gas sheath thickness, the electrolyte vapor pressure, and the velocity of the vapor escaping the discharge zone. It is shown that field evaporation of thermally activated negative ions from the electrolyte surface cannot provide an electric current with densities found in experiments but is responsible for the generation of free electrons near the electrolyte surface. These electrons arise when the ions decay via collisions with excited molecules. © *2004 MAIK "Nauka/Interperiodica".*

(1) The phenomenon of strong heating (up to T = 1000 K) of an electrode in an electrolyte when a potential difference (U = 100–200 V) is applied between the electrode and electrolyte, causing a high electric current (j = 0.1–1.0 A/cm^2) to flow in the system, has been known since late in the 19th century and is now widely used in various devices and instruments (see, for example, [1–5] and Refs. therein). Nevertheless, most qualitative estimates are not sufficiently accurate. Until now, the physical processes attendant on this phenomenon have not been understood in detail and no correct theoretical models of them have been elaborated. In particular, the physical mechanism behind the formation of an electric current between the electrode and electrolyte remains unclear (below, we will consider aqueous solutions of electrolytes for definiteness).

According to the existing concepts [1–4], a vapor–gas sheath between the electrode being heated and the electrolyte is thin ($h \le 100$ μm) and the vapor pressure p exceeds the atmospheric pressure Δp only slightly (by ~$0.1p_*$). So, the possibility of initiating a steady discharge at potential differences U employed is not obvious. Indeed, from experiments with discharges between metal electrodes, it is known [6, 7] that, if the product ph equals several unities (when p is measured in millimeters of mercury and h, in centimeters), as in the case of electrolyte heating, the potential difference U initiating a steady discharge appreciably exceeds 200 V in air and in pure gases of which air consists (for water vapor, relevant data are lacking). However, the phenomenon considered is observed at $U \le 200$ V. A high work function of an electron on the water surface (≈6.2 eV [8]) (which means a low probability of free electrons appearing at the negatively charged electrolyte surface via field emission) casts still more doubt upon the possibility of discharge initiating. These circumstances do not allow one to perform correct calculations of the temperature of the vapor–gas sheath and electrode being heated, although much attention has been given to this issue [2, 9, 10].

Below, we will consider mechanisms behind the formation of an electric current flowing in the system under steady-state conditions and the distribution of the evolving Joule heat. For definiteness, we assume that the electrode being heated and the aqueous electrolyte solution are kept under positive and negative potentials, respectively.

(2) Let a current flowing in the system under steady-state conditions due to the action of a potential difference U have a density j. Negatively charged carriers (electrons and negative ions) that are emitted by the charged electrolyte surface lose the electric field energy eU (e is the electron charge) in the vapor–gas sheath between the electrodes upon colliding with neutral molecules and positively charged ions. As a result, a thermal energy $W = Uj$ per second being released in the volume $V = h \cdot 1$ cm^2 is spent on heating and evaporating the electrolyte and on heating the vapor (we neglect heat removal through the contacts to the metallic electrode). A natural question arises: in what proportion is this thermal energy distributed among the processes mentioned.

1063-7842/04/4905-0559$26.00 © 2004 MAIK "Nauka/Interperiodica"

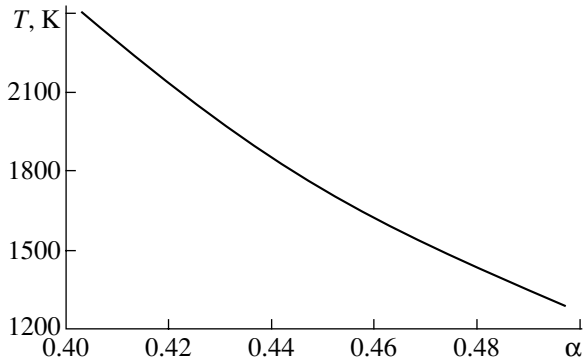

Fig. 1. Temperature T of the overheated vapor as a function of the free parameter α.

Let a one-αth portion of the thermal energy be spent on heating and evaporating an electrolyte and a one-βth portion of α be spent on evaporation. We also assume that β is a function of α, $\beta = \beta(\alpha)$, which seems obvious from physical considerations. Indeed, at small α, most of the energy coming to the volume of the electrolyte is derived from the surface by heat conduction and heats the electrolyte. At large α, conversely, most of the energy is spent on evaporation, since the rate of heat removal into the electrolyte volume is limited because of a small temperature gradient. This gradient may take place in a liquid whose boiling temperature is lower than the temperature of the vapor and electrode being heated. Eventually, the mass

$$m = \alpha\beta(\alpha)W\lambda^{-1} \quad (1)$$

(where λ is the heat of vaporization) will be evaporated from a unit surface of the electrolyte in a second.

The thermal energy spent on heating the vapor is $(1 - \alpha)W$, which is expressed as

$$mc(T)(T - T_0) = (1 - \alpha)W, \quad (2)$$

where $c(T)$ is the temperature-dependent specific heat of the vapor and T_0 is the initial vapor temperature, which is reasonable to equate to the boiling point of the electrolyte.

By substituting (1) into (2), we can express the temperature T of the final state:

$$T = T_0 + \frac{\lambda}{cT}\frac{1-\alpha}{\alpha\beta(\alpha)}. \quad (3)$$

In the process considered, the rate of increase of the entropy is given by

$$\dot{S} \equiv \frac{dS}{dt} = \frac{W}{T}.$$

According to the Onsager principle of entropy production minimum in nonequilibrium processes [11], the quantity $\dot{S}$ must have an extremum in free parameter α. We equate the derivative of $\dot{S}$ with respect to α to zero to find the dependence $\beta = \beta(\alpha)$ that meets this equality in explicit form. Neglecting the weak temperature dependence of the specific heat of the vapor (in the temperature range 400–1400 K, the specific heat of water vapor increases by ≈20% [12]), we obtain a differential equation relating α and β:

$$\frac{d\beta}{d\alpha} = \frac{\beta}{\alpha(\alpha - 1)}$$

with the boundary condition $\beta(0) = 0$. From this equation, it is easy to see that

$$\beta = \frac{\alpha}{1 - \alpha}.$$

Putting $\beta < 1$, one can find that α varies in the range $0 < \alpha \le 1/2$.

Now, from (3) one may evaluate the temperature of the overheated vapor as a function of α, assuming that the vapor pressure exceeds the atmospheric pressure insignificantly (see below), $\lambda \approx 2.25$ kJ/g, and $c_p \approx 2.47$ J/(g K). Numerical calculations show that the vapor temperature strongly depends on α and always exceeds $T = 1284$ K (such a temperature is achieved at $\alpha = 1/2$). Physically, the value $\alpha = 1/2$ is unrealistic; consequently, the true temperature is higher but insignificantly so. It is hard to expect that it may be much higher than 1500 K. The limitation imposed on the temperature limits the range of parameter α. Let us assume that α varies in the range $0.45 \le \alpha < 0.5$. Figure 1 shows the dependence of the vapor temperature on the free parameter α (which varies in a wider range) when the temperature dependence of the specific heat of the vapor is neglected. In estimations that follow, we will take the density of the overheated vapor of the electrolyte at a temperature $T = 1500$ K and at a pressure close to the atmospheric pressure: $\rho \approx 1.5 \times 10^{-4}$ g/cm^{-3} [12].

(3) Now let us estimate the pressure of the overheated vapor in the sheath and the velocity of the vapor relative to the electrolyte surface. We assume that the electrode being heated is a parallelepiped with a section $a \times b$ that is dipped in an electrolyte to a depth c and that the thickness h of the vapor sheath is constant and independent on the coordinates of its position. Then, the electrode's surface area under the current is given by the simple expression $\Sigma = ab + 2(a + b)c$. The area of the near-electrode channel through which the overheated vapor escapes the discharge zone under the action of a pressure drop is $s = 2(a + b)h$. If the velocity with which the vapor leaves the discharge zone is designated by u, the vapor mass balance equation takes the form

$$\rho s u = \alpha^2 W\Sigma/(1 - \alpha)\lambda. \quad (4)$$

The right-hand side of (4) describes the vapor mass produced in a unit time during electrolyte evaporation, while the left-hand side defines the vapor mass leaving the discharge zone in a unit time. From (4), one can express the velocity u through the (unknown) vapor

sheath thickness h and physical parameters that are controlled in experiments:

$$u = \frac{\alpha^2 Uj[ab + 2(a+b)c]}{2(1-\alpha)\rho\lambda h(a+b)}. \quad (5)$$

Now we will relate the vapor pressure p, the sheath thickness h, and the velocity u by means of the Bernoulli equation, assuming that the vapor is an ideal incompressible liquid. Let the physical parameters of the vapor at the center of the base of the electrode be assigned the subscript 0 and the same parameters near the electrolyte surface at the place where the vapor leaves the system be assigned an asterisk. Then, we obtain

$$p_0 + \frac{1}{2}\rho_0 u_0^2 = p_* + \frac{1}{2}\rho_* u_*^2,$$

where p_0 is the vapor pressure at the center of the base of the electrode and p_* is the atmospheric pressure.

Below, we put $u_0 = 0$, $u_* \equiv u$, and $\rho_0 = \rho_* \equiv \rho$. Eventually, we get

$$\Delta p \equiv p_0 - p_* = \frac{1}{2}\rho u^2, \quad (6)$$

where u is defined by relationship (5).

The pressure difference Δp sustains a vapor sheath of thickness h near the electrode and provides a displacement $(c + h)$ of the electrolyte free surface (i.e., the one opposing the electrode) from its natural position in the gravitational field. Consequently,

$$\rho_e g(c+h) = p_0 - p_* = \frac{1}{2}\rho u^2$$

or

$$h = \frac{\rho u^2}{2g\rho_e} - c, \quad (7)$$

where ρ_e is the density of the electrolyte.

From (5)–(7), it is seen that the desired parameters $p_0 - p_*$, h, and u depend on the configuration and depth of immersion of the electrode.

Substituting (5) into (7) yields an expression for the vapor sheath thickness:

$$(c+h)h^2 = \frac{\rho}{2g\rho_e}\left(\frac{\alpha^2 Uj[ab + 2(a+b)c]}{2(1-\alpha)\rho\lambda(a+b)}\right)^2. \quad (8)$$

For $U = 150$ V, $j = 0.2$ A/cm^2, $a = b = 1$ cm, $c = 0.5$ cm, $\rho_e \approx 1$ g/cm^3, $\alpha = 19/40$, and the above values of the remaining physical parameters appearing in (5)–(7), one finds that $T = 1485.8$ K, $h \approx 0.0035$ cm $= 35$ μm, $u \approx 8111$ cm/s, and $p_0 - p_* \approx 4934$ dyn/cm^2.

The pressure difference Δp thus obtained is consistent with the assumption that the vapor pressure is close to the atmospheric value. The high vapor velocity supports the statement [5] that the Kelvin–Helmholtz instability may be observed at the vapor–electrolyte interface. However, this issue, as well as the contribution of the Tonks–Frenkel instability of the charged electrolyte surface to the physical pattern observed, needs special investigation.

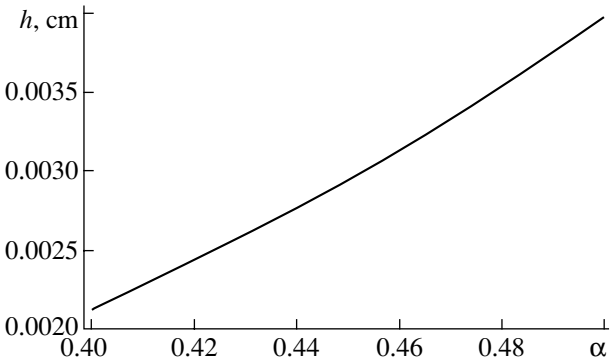

Fig. 2. Thickness h of the vapor sheath between the electrolyte and metal electrode as a function of the free parameter α.

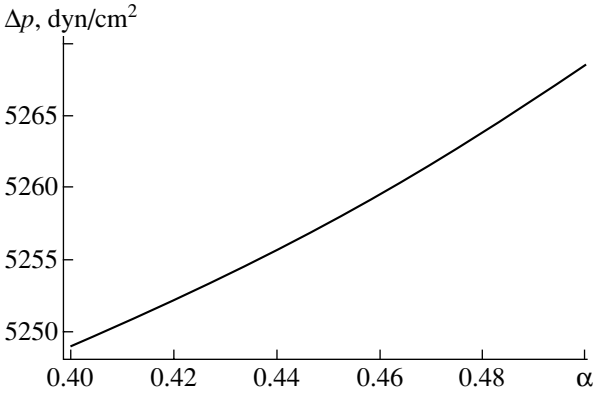

Fig. 3. Excess $\Delta p \equiv (p_0 - p_*)$ of the overheated vapor pressure over the atmospheric value as a function of the free parameter α.

Figures 2–4 plot the characteristics of the process $\Delta p \equiv p_0 - p_*$, h, and u versus the free parameter α for the above values of the physical quantities. It is seen that $p_0 - p_*$, h, and u depend on α only slightly. The most significant dependence is observed for the sheath thickness h; however, even this parameter varies in a sufficiently narrow range (between ≈30 and ≈40 μm) when α increases from 0.45 to 0.5. This circumstance seems to be important, because h, which cannot be found experimentally (it is derived from rough indirect estimates), governs the electric field strength initiating a discharge between the electrolyte surface and the metallic electrode. The pressure difference and the vapor velocity vary with α insignificantly: as α changes from 0.4 to 0.5, these parameters change by no more than a tenth of a percent.

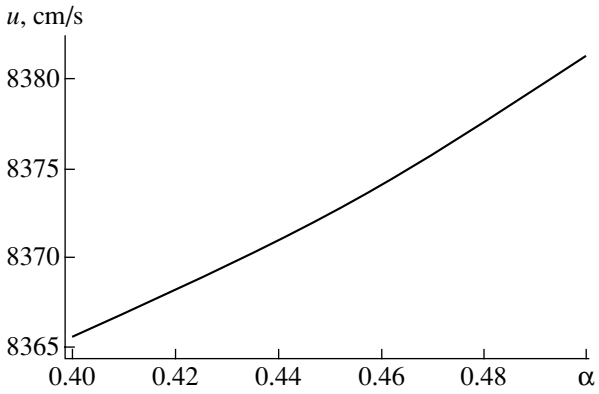

Fig. 4. Velocity u with which the vapor escapes the discharge gap as a function of the free parameter α.

(4) Now, using the above estimate of the vapor sheath thickness h at $\alpha = 19/40$, we will consider possible mechanisms of initiating an electric discharge between the surface of the liquid electrolyte and the electrode. In spite of a large body of relevant experimental data, this issue has escaped the attention of the researchers (some preliminary results have been reported only in [4]). Therefore, we are still in the dark about this type of discharge. At present, one may state with assurance that (i) a discharge between the electrolyte surface and the electrode being heated is self-sustained and is initiated in the vapor at pressures that are much higher than the atmospheric pressure and at relatively low voltages across the discharge gap and (ii) ions emitted by the charged electrolyte surface play a decisive role in the discharge initiation, although they are incapable of providing electric current densities observed in experiments (from 0.1 to 1 A/cm^2).

If an electrolyte heating the electrode is at a negative potential, it is generally assumed that the electric current between the electrolyte surface and the electrode is due to negative ions emitted from the electrolyte surface [3, 9, 10]. Such an approach is valid, since the electron work function on the surface of aqueous solutions of electrolytes is high. Yet, no exact calculation of a negative-ion current density has been performed, because the problem is very complex and only its applied aspects have been of interest to date.

The only physically sound mechanism by which negative ions may pass from the electrolyte surface into the vapor phase is thermally activated field evaporation of ions [5]. In general, the term "field evaporation" implies a substantial contribution of an electric field to the evaporation rate constant. This takes place when the electric field strength near the surface from which an ion evaporates is ≥1 V/nm. According to the estimates obtained above, the electric field strength near the electrolyte surface is $e \approx V/h \approx 43$ kV/cm. It is obvious that such a field cannot provide efficient field evaporation of ions, and one may speak only of thermal evaporation of ions in a weak (in terms of the contribution to the evaporation rate constant) electric field. In this situation, the role of the field is to remove ions evaporating from the electrolyte surface. Thermal evaporation will be efficient if the activation energy of the process is not too high; that is, it must slightly exceed the activation energy of thermal evaporation of a solvent molecule (for aqueous solutions of electrolytes, it is equal to ≈0.42 eV). It appears that it is this parameter that is of crucial importance in selecting an electrolyte for electrolyte heating.

For example, from data in [5, 13], the activation energy of evaporation of a Cl^- ion from a solution of NaCl is evaluated as ≈1.5 eV. In this case, negative ions appear near the electrolyte surface with a rate many orders of magnitude higher than that with which electrons are generated by field emission. The evaporation of ions from an electrolyte solution may also be favored by resonant absorption of UV radiation from the discharge plasma by solvated ions at the electrolyte surface [14, p. 181]. In this case, the energy of an absorbed photon will remain in the solvate for a time on the order of ten solvate oscillation periods, raising the nonequilibrium effective solvate temperature (which may be converted to the energy per atom) by several hundreds of degrees. Such a short-term increase in the temperature near the ion may be high enough for its thermal evaporation within the same time interval.

Summarizing the aforesaid, we may argue that negatively charged ions appear near the charged electrolyte surface mostly due to purely thermal evaporation. However, in electric fields estimated above, thermal evaporation cannot provide electric current densities of $j = 0.1$–1.0 A/cm^2, which are observed in experiments.

Indeed, the constant of thermal evaporation of ions will be much less than unity (or close to unity with account taken of local nonequilibrium heating due to UV radiation absorption) even if the activation energy of their evaporation is about 1 eV. At the same time, the surface concentration of singly charged negative ions at the electrolyte surface will be $U/4\pi he \approx 2 \times 10^{10}$ cm^2. Consequently, the ion current density will be many orders of magnitude lower than detected in experiments. In addition, it is known [7] that ions moving in discharge plasmas at temperatures and electric field strengths estimated are too slow to ionize neutral atoms and vapor molecules, i.e., to generate electron avalanches. Moreover, they cannot even excite neutral atoms. This leads us to conclude that actually the electric field between the electrolyte surface and electrode being heated is produced for the most part by electrons and not by ions. However, it is ions emitted by the charged electrolyte surface that play a decisive part in discharge initiation. The fact is that a discharge of the type considered (and, hence, metallic electrode heating) is observed not in any electrolyte but only in some of them, and the reason for this effect is yet unknown (accordingly, selection criteria for electrolytes are lacking [2]). Most frequently, ammonium perchlorate

$(NH_4)_2SO_4$, ammonium nitrate NH_4NO_3, ammonium chloride NH_4Cl, and sulfuric acid H_2SO_4 are used. So, what may the role of negative ions be?

From the foregoing it follows that the vapor pressure near the surface is sufficiently high, so that negative ions evaporated will inevitably collide with neutral (including excited) vapor molecules and atoms. In the discharge with a current density of 0.1–1.0 A/cm^2, the concentration of the atoms and molecules is bound to be very high (approximately one order of magnitude higher than the concentration of electrons striking the electrode being heated [12]). At the same time, collisions between a negative ion and an excited molecule may generate free electrons [15]. In particular, the following reactions proceed in the plasma of a gas discharge in water vapor [15]:

$$O^- + O = O_2 + e,$$

$$H^- + H = H_2 + e,$$

$$H^- + O_2 = H_2O + e,$$

$$OH^- + H = H_2O + e,$$

$$OH^- + O = HO_2 + e.$$

In the reactions listed, the rate constants vary from 1×10^{-10} to (several tens) $\times 10^{-10}$ cm^3/s and the release of an electron is accompanied by an energy release of about several electron-volts.

Such collisions provide free electrons near the electrolyte surface, which are capable of generating electron avalanches in electric fields mentioned above. The trace of any electron avalanche will contain a large amount of positively charged ions, including H^+ ions, which strike the negatively charged surface of the aqueous solution of the electrolyte, knocking out free electrons from the electrolyte surface due to the Penning effect [7]. Indeed, the ionization energy of a hydrogen atom equals ≈13.5 eV, whereas the electron work function on the water surface does not exceed ≈6.2 eV [8]. In other words, the necessary condition for the Penning effect to take place is fulfilled (the ionization energy of an atom is twice as high as the electron work function on the electrolyte surface). This effect provides one more source of free electrons near the electrolyte surface, which, in turn, will initiate electron avalanches, causing H^+ ions and a large amount of excited atoms to arise.

Thus, negative ions evaporating from the electrolyte surface at a rate lower than 10^{10} cm^2/s release electrons, which, in turn, initiate electron avalanches, provide current passage, and generate a large amount of positive ions contributing to free electron generation near the electrolyte surface due to the Penning effect.

It should be noted that such a pattern of the discharge disregards the possibility of joint occurrence of Kelvin–Helmholtz and Tonks–Frenkel instabilities at the charged electrolyte surface. These effects may be responsible for the emission of highly dispersed and heavily charged droplets into the interelectrode space [5, 16–18], which makes the discharge pattern still more complicated.

The aforesaid refers to the situation when the electrode being heated is kept at a positive potential and the electrolyte is negatively charged. The effect of metal electrode heating may also be observed under reversed polarity; however, the processes in the discharge plasma will be governed by elementary processes at the electrode in this case. Such a situation is the subject of special experimental and theoretical investigation.

CONCLUSIONS

We performed a model theoretical study of physical mechanisms responsible for electric discharge heating of a metal electrode dipped in an electrolyte. The thickness and temperature of the vapor sheath separating the electrolyte from the electrode, the velocity with which the vapor escapes the discharge gap, and the vapor pressure at the base of the electrode being heated are correctly estimated based on physical considerations. Qualitative analysis of an electric discharge between the negatively charged electrolyte surface and positively charged metal electrode revealed the crucial role of negative ion evaporation from the electrolyte surface in the discharge initiation (upon decay, these ions provides the delivery of free electrons to the discharge gap).

REFERENCES

1. O. V. Polyakov and V. V. Bakovets, Khim. Vys. Énerg. **17**, 291 (1983).
2. D. I. Slovetskiĭ, S. D. Terent'ev, and V. D. Plekhanov, Teplofiz. Vys. Temp. **24**, 353 (1986).
3. P. N. Belkin, V. I. Ganchar, and Yu. N. Petrov, Dokl. Akad. Nauk SSSR **291**, 1116 (1986) [Sov. Phys. Dokl. **31**, 1001 (1986)].
4. F. M. Gaĭsin, É. E. Son, and Yu. I. Shakirov, *Volume Discharge in Vapor–Gas Medium between Solid and Liquid Electrodes* (VZPI, Moscow, 1990) [in Russian].
5. S. O. Shiryaeva, A. I. Grigor'ev, and V. V. Morozov, Zh. Tekh. Fiz. **73** (7), 21 (2003) [Tech. Phys. **48**, 822 (2003)].
6. S. C. Brown, *Basic Data of Plasma Physics* (MIT, Cambridge, 1959; Atomizdat, Moscow, 1961).
7. Yu. P. Raizer, *Gas Discharge Physics* (Nauka, Moscow, 1987; Springer-Verlag, Berlin, 1991).
8. V. S. Fomenko, *Emissivity of Materials: A Handbook* (Naukova Dumka, Kiev, 1981) [in Russian].
9. S. Yu. Shadrin and P. N. Belkin, Élektron. Obrab. Mater., No. 3, 24 (2002).

10. P. N. Belkin and A. B. Belikhov, Inzh.-Fiz. Zh. **75** (6), 19 (2002).
11. Ch. C. T. Yang and Ch. C. S. Song, *Encyclopedia of Fluid Mechanics*, Vol. 1: *Flow Phenomena and Measurement* (Gulf, Houston, 1986), pp. 353–399.
12. M. P. Vukalovich, *Thermodynamic Properties of Water and Water Vapor* (Mashgiz, Moscow, 1950) [in Russian].
13. É. D. Lozanskiĭ and O. B. Firsov, *Spark Theory* (Atomizdat, Moscow, 1975) [in Russian].
14. N. A. Izmaĭlov, *Electrochemistry of Solutions* (Khimiya, Moscow, 1976) [in Russian].
15. B. N. Smirnov, *Ions and Excited Atoms in Plasma* (Atomizdat, Moscow, 1974) [in Russian].
16. M. D. Gabovich, Usp. Fiz. Nauk **140**, 137 (1983) [Sov. Phys. Usp. **26**, 447 (1983)].
17. A. I. Grigor'ev, I. D. Grigor'eva, and S. O. Shiryaeva, J. Sci. Explor. **5**, 163 (1991).
18. A. I. Grigor'ev and Yu. B. Kuz'michev, Élektron. Obrab. Mater., No. 3, 30 (2002).

Translated by N. Mende

Technical Physics, Vol. 49, No. 5, 2004, pp. 565–571. Translated from Zhurnal Tekhnicheskoĭ Fiziki, Vol. 74, No. 5, 2004, pp. 44–49.

GAS DISCHARGES, PLASMA

Low-Power RF Plasma Sources for Technological Applications: I. Plasma Sources without a Magnetic Field

K. V. Vavilin*, A. A. Rukhadze, M. Kh. Ri*, and V. Yu. Plaksin***

** Moscow State University, Vorob'evy Gory, Moscow, 119899 Russia*

*** Prokhorov Institute of General Physics, Russian Academy of Sciences, ul. Vavilova 38, Moscow, 119991 Russia*

Received September 10, 2003

Abstract—A general analytical theory is developed and numerical simulations are carried out of cylindrical plasma sources operating at an industrial frequency of $f = 13.56$ MHz ($\omega = 8.52 \times 10^7$ s^{-1}). Purely inductive surface exciters of electromagnetic fields (exciting antennas) are considered; the exciters are positioned either at the side surface of the cylinder or at one of its end surfaces. In the latter case, the plasma flows out of the source through the opposite end of the cylinder. A study is made of both elongated systems in which the length L of the cylinder exceeds its diameter $2R$ and planar disk-shaped systems with $L < 2R$. The electromagnetic fields excited by the antenna in the plasma of the source are determined, and the equivalent plasma resistance, as well as the equivalent rf power deposited in the plasma, is calculated. © *2004 MAIK "Nauka/Interperiodica".*

1. INTRODUCTION: DESIGN OF THE SOURCES AND MAIN PLASMA PARAMETERS

We begin by discussing characteristic features of the geometry of the plasma sources under investigation. We are dealing with elongated cylindrical sources with $L > 2R$ and planar disk-shaped sources with $L < 2R$ (Fig. 1). The sources differ not only in shape but also in the arrangement of antennas at the cylinder surface. In an elongated plasma source, the electromagnetic field is produced by a current-carrying antenna positioned at the side surface of the cylinder (Fig. 1a) and, in a planar source, the antenna is positioned at the closed end opposite to the end through which the plasma flows out of the cylinder (Fig. 1b).

In a planar source, the end surface through which the plasma flows out of the cylinder is a metal grid to which an ion-accelerating potential is applied (in this case, the source serves as an ion implanter). For a source with a metal grid, the boundary conditions at the end surface through which the plasma flows out of the cylinder can be written as

$$E_r|_{z=L} = E_\varphi|_{z=L} = 0. \quad (1.1)$$

For an elongated plasma source with an antenna at its side surface, the same boundary conditions are satisfied at the upper closed end of the cylinder. In a planar disk-shaped source, the current-carrying antenna is positioned at the upper end surface of the cylinder, so that the boundary conditions at this surface are not fixed but instead are derived from the field equations. As for the side surface of a planar source, it is usually metal, so that the boundary conditions at it have the form

$$E_\varphi|_{r=R} = E_z|_{r=R} = 0. \quad (1.2)$$

In contrast, in an elongated plasma source, it is the side surface of the cylinder on which the current-carrying antenna is positioned, so that the boundary conditions at this surface are not fixed but are derived from the field equations.

Let us now discuss the design of the antennas in question. In the most general case, the current density in the antenna positioned at the side surface of the cyl-

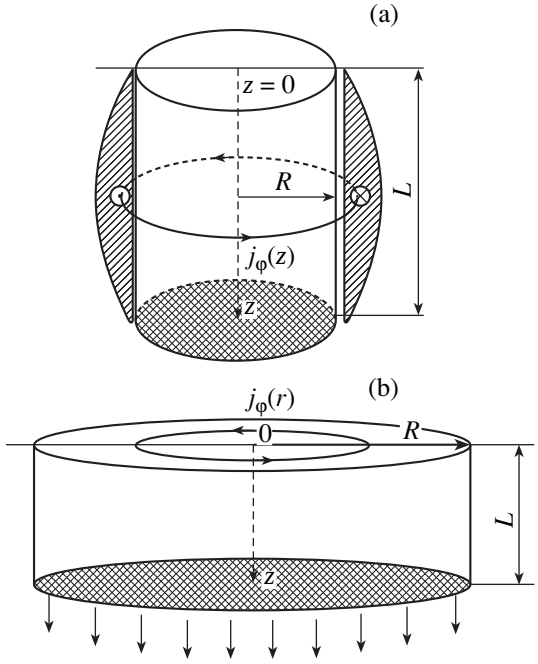

Fig. 1.

1063-7842/04/4905-0565$26.00 © 2004 MAIK "Nauka/Interperiodica"

inder can be represented as

$$\mathbf{j}(r) = \delta(r-R)\mathbf{F}_1(\varphi, z), \quad (1.3)$$

where $F_1(\varphi, z)$ is an arbitrary function that can be expanded in a Fourier series.

Below, the problem of investigating the plasma source will be solved for an individual term of the Fourier series under the assumption that the antenna current is azimuthally symmetric and the arbitrary function has the form

$$\mathbf{F}_1(\varphi, z) \sim \mathbf{i}_\varphi I_0 \sin\frac{\pi z}{L},$$

where I_0 is the net antenna current and $\mathbf{i}_\varphi$ is a unit vector in the azimuthal direction.

The current density in the antenna positioned at the end surface of the cylinder is represented in an analogous form. In the general case, the antenna current density can be written as

$$\mathbf{j}(r) = \delta(z)\mathbf{F}_2(\varphi, r). \quad (1.4)$$

In what follows, however, we will be interested in an azimuthally symmetric antenna current and will use the function

$$\mathbf{F}_2(\varphi, r) \sim \mathbf{i}_\varphi I_0 J_1\left(\frac{\mu r}{R}\right),$$

where I_0 is the net antenna current, $J_1(x)$ is a first-order Bessel function, and $\mu \approx 3.8$ is the first root of the Bessel function ($J_1(\mu) = 0$).

Let us now discuss the mechanisms by which the rf energy is dissipated within the plasma of the source. We are interested in a plasma with the following parameters: the neutral gas pressure is $p_0 < 10^{-3}$ torr (which corresponds to a neutral density of $n_0 \approx 3 \times 10^{13}$ cm^{-3}) and the electron density is $n_e \approx 10^{10}$–10^{11} cm^{-3}. In such a plasma, two dissipation mechanisms—collisionless dissipation due to Cherenkov absorption and collisional field dissipation due to collisions of plasma electrons with plasma ions and with gas atoms and molecules—play an equally important role. In this case, the collision frequency can be represented as

$$\nu_e = \nu_{en} + \nu_{ei} \approx \sqrt{T_e(\text{eV})}\,6 \times 10^9 p_0 + \frac{10^{-4} n_e}{T_e(\text{eV})^{3/2}}, \quad (1.5)$$

where T_e is the electron temperature in eV, p_0 is the gas pressure in torr, and n_0 is the ion density in cm^{-3}. Note that, in source plasmas, the electron temperature satisfies the condition $T_e \gg T_i \sim T_0$, where T_i is the ion temperature and T_0 is the gas temperature (which is usually on the order of room temperature). Such plasma parameters are determined by the large difference between the mass of the electrons and the masses of heavy particles (ions and neutrals), in which case the collisional energy exchange between electrons and heavy particles is hindered. For typical experimental conditions such that $T_e \sim 5$ eV and $V_{Te} \approx 9 \times 10^7$ cm/s, and for $n_e < 10^{12}$ cm^{-3} and $p_0 < 10^{-3}$ torr, we have $\nu_e \sim 1.5 \times 10^7$ s^{-1}. Under these conditions, the collisional dissipation of the rf energy in plasma can be assumed to be weak because $\omega = 8.5 \times 10^7$ s$^{-1} \gg \nu_e \sim 1.5 \times 10^7$ s^{-1}.

For the above plasma parameters, the mean free path of an electron is on the order of $l = V_{Te}/\nu_e \approx 10$ cm. It can be shown that the maximum efficiency of a plasma source operating in a steady mode is achieved when the length of the system does not exceed the electron mean free path l, i.e., when

$$L \le l_e \approx 10 \text{ cm}. \quad (1.6)$$

In what follows, this condition will be assumed to be always satisfied.

The second, purely collisionless, dissipation mechanism is governed by both the electron thermal motion and the geometric dimensions of the system. The contribution of this mechanism to the collision frequency is determined by the parameters $kV_{Te} \approx \pi V_{Te}/L$ and $\pi V_{Te}/R$. The characteristic geometric dimensions of an elongated rf plasma source are $L \ge 10$ cm and $R \le 10$ cm, while those of a planar source are $L \le 10$ cm and $R \ge 10$ cm. As a result, we have $kV_{Te} \approx 1$–2×10^7 s$^{-1} \ll \omega$, so that the collisionless rf energy dissipation in the source is also weak. On the other hand, we have $kV_{Te} \approx \nu_e$, which indicates that the collisionless dissipation is comparable in importance to the collisional dissipation. That is why we will assume that both of the dissipation mechanisms operate simultaneously in the plasma.

The external magnetic field is longitudinal only, $\mathbf{B}_0 \parallel OZ$. It has an important effect on the operating modes of the plasma sources. It is easy to show that, even for relatively weak external magnetic fields ($5 \le B_0 \le 500$ G), the following conditions hold:

$$\omega_{Le} \ge 10^{10} \text{ s}^{-1} \gg \Omega_e = \frac{eB_0}{mc} \le 10^9 \text{ s}^{-1} \gg \omega \approx 8.5 \times 10^7 \text{ s}^{-1}. \quad (1.7)$$

These conditions will be assumed to be satisfied for plasma sources with an external magnetic field. Such sources are the subject of parts II and III of the present paper. The objective of part I is to investigate plasma sources without a magnetic field ($\mathbf{B}_0 = 0$).

Finally, let us discuss the question of what is the rf power that is deposited in the plasma of the source (i.e., the power that ensures the operation of the source). This power depends essentially on the mass of an ion, M, which is assumed to be about 30–40 masses of a hydrogen atom ($M \sim 2 \times 10^{-24}$ g). In this case, the plasma flows out of the source with a velocity on the order of the ion acoustic speed (provided that the plasma ions

are not accelerated by any additional means),

$$v_s = \sqrt{\frac{T_s}{M}} \approx 3 \times 10^5 \text{ cm/s}.$$

For an ion density of $n_i \approx 10^{12}$ cm^{-3}, this formula yields the following estimate for the density of the ion current from the source:

$$j = en_i v_s \approx (5 \times 10^{-10})(10^{12})(3 \times 10^5)\left(\frac{1}{3 \times 10^9}\right)\frac{\text{A}}{\text{cm}^2} \approx 5 \times 10^{-2}\frac{\text{A}}{\text{cm}^2}. \quad (1.8)$$

Since the plasma thermal energy is determined by the electron temperature T_e, which is about 5 eV, the density of the power flux from the source through a unit area of the end surface of the cylinder is equal to

$$P_W \approx n_i v_s T_e + n_i v_s M v_s^2 \approx 2n_i v_s T_e \approx 0.5\frac{\text{W}}{\text{cm}^2} \quad (1.9)$$

so that the net power flux from the source is

$$\mathcal{P}_W = SP_W \approx 0.5S \text{ W}, \quad (1.10)$$

where the total area of the end surface of the cylinder, S, is expressed in cm^2.

For an elongated system with $R < 10$ cm, we have $\mathcal{P}_W < 150$ W, whereas for a planar disk-shaped source with $R > 10$ cm, the net power flux is $\mathcal{P}_W > 150$ W.

It is also an easy matter to estimate the total power that is deposited in the discharge plasma in order to maintain the steady-state operation of the source. To do this, we must take into account not only the electron plasma heating to a temperature of $T_e \sim 5$ eV but also the power lost to ionize neutral gas atoms and, in the absence of magnetic field, the power carried to the side surface of the cylinder by the plasma. Unfortunately, the amount of power expended on ionizing the gas atoms in an rf discharge is very high (most of the field energy is spent on the excitation of atoms, which is followed by the emission of optical photons from the excited atomic states). As a consequence, the net rf power absorbed by the plasma in the source is higher than the net power flowing out of the source by one or even two orders of magnitude, i.e., $\mathcal{P}_W \approx 10^3$–$10^4$ W.

To conclude this section, we will say a few words on additional power losses in the acceleration of ions in ion implanters. The problem concerning the power of an ion accelerator is a separate issue and is not related to the problem of the rf power fed into a plasma source. In what follows, we will not deal with the accelerator-related problem, because it goes beyond the scope of this paper, the primary goal of which is to investigate the steady-state operation of rf plasma sources.

2. ELONGATED CYLINDRICAL PLASMA SOURCE WITHOUT AN EXTERNAL MAGNETIC FIELD

In order to illustrate how the theory of plasma sources is to be constructed, we consider the simplest examples of these devices.[1] We assume that, in an elongated cylindrical plasma source, the electromagnetic field is produced by an antenna that is positioned at the side surface of the cylinder and carries a purely azimuthal current with the density

$$j_\varphi = I_0\frac{k_z}{2}\delta(r - R)e^{-i\omega t}\sin k_z z, \quad (2.1)$$

where I_0 is the net azimuthal current and k_z is the longitudinal wavenumber. For the antenna shown in Fig. 1a, this wavenumber is equal to $k_z = \pi/L$. In such a source, the only nonzero components of the rf electromagnetic field are E_φ, B_r, and B_z. Assuming that these field components depend on time and coordinates as $f(r)e^{ik_z z - i\omega t}$, we can write Maxwell's equations for them in the form

$$ck_z E_\varphi + \omega B_r = 0, \quad \frac{i}{r}\frac{\partial}{\partial r}rE_\varphi + \frac{\omega}{c}B_z = 0, \quad k_z B_r + i\frac{\partial B_z}{\partial r} + \frac{\omega}{c}\varepsilon(\omega)E_\varphi = 0. \quad (2.2)$$

Equations (2.2) contain the plasma dielectric function $\varepsilon(\omega)$, which is to be determined for the conditions of interest to us (those of a confined plasma and low frequencies), when collisional dissipation and collisionless Cherenkov dissipation play an equally important role. Strictly speaking, the plasma dielectric function should be determined from the solution to the electron kinetic equation with the corresponding boundary conditions. However, instead of doing this, we will describe the dielectric function by a familiar relationship that is valid for an unmagnetized plasma in the frequency range

$$\nu_e;\ \omega_{Le}\frac{V_{Te}}{c} \ll \omega \ll \omega_{Le}. \quad (2.3)$$

Under the conditions adopted above, the right-hand inequality is satisfied by a large margin, while the left-hand inequality holds for plasma densities lying in the range $n_e < 2 \times 10^{11}$ cm^{-3}. In what follows, we restrict ourselves to considering the plasma densities for which the function $\varepsilon(\omega)$ can be written in accordance with formulas (17) and (18) in [2]:

$$\varepsilon(\omega) \approx I - \frac{\omega_{Le}^2}{\omega^2}\left(1 - i\frac{\nu_e}{\omega} - i4\sqrt{\frac{2}{\pi}}\frac{\omega_{Le}^3}{\omega^3}\frac{V_{Te}^3}{c^3}\right). \quad (2.4)$$

[1] To the best of our knowledge, the plasma sources under discussion have not yet been systematically analyzed in the literature. To be specific, we can mention the collection of papers [1], which contain review articles on plasma technologies in practically all of the known scientific centers around the world.

Note that expression (2.4) is valid under conditions corresponding to the specular reflection of electrons from the surface of a semi-infinite plasma described in plane geometry (see Appendix),[2] so strictly speaking it can be used only to describe planar disk-shaped plasma sources with $L > c/\omega_{Le} \le 5$ cm. Nonetheless, we will also use expression (2.4) to describe elongated cylindrical sources, because it yields qualitatively correct results for $R > c/\omega_{Le} \le 5$ cm.

Equations (2.2) with dielectric function (2.4) are valid not only for the plasma region ($r \le R$) but also for the region outside the plasma ($r > R$). Therefore, these equations can be solved separately for each of the regions. The solutions obtained can then be joined at the plasma surface with the help of the boundary conditions that are derived from the same equations by integrating them over the radial coordinate r across an infinitely thin transition layer around the plasma surface:

$$\{B_z\}_{r=R} = -\frac{ic}{\omega R}\left\{\frac{\partial}{\partial r}(rE_\varphi)\right\}_{r=R} = -\frac{k_z}{2}\frac{4\pi}{c}I_0. \quad (2.5)$$

Here, I_0 is the net azimuthal current in an antenna positioned at the side surface of the cylinder of a plasma source and $\{\varphi\}_{r=R}$ denotes the jump in the function $\varphi(r)$ at the cylinder surface $r = R$.

It is convenient to reduce Eqs. (2.2) to a single second-order differential equation for the field component E_φ:

$$\frac{\partial^2 E_\varphi}{\partial r^2} + \frac{1}{r}\frac{\partial E_\varphi}{\partial r} - \left(k_z^2 + \frac{1}{r^2} - \frac{\omega^2}{c^2}\varepsilon(\omega)\right)E_\varphi = 0. \quad (2.6)$$

Equation (2.6), which is also valid both inside ($r \le R$) and outside ($r > R$) the plasma, should be supplemented not only with boundary condition (2.5) but also with the continuity condition for E_φ at $r = R$ (this condition follows from the second of Eqs. (2.2)) and the obvious finiteness condition

$$E_\varphi(r = 0) < M, \quad E_\varphi(r \longrightarrow \infty) = 0, \quad (2.7)$$

where M is an arbitrarily large number.

The general solution to field equations (2.2) that satisfies all of the above conditions and, in particular, boundary condition (2.5), can be represented in the form

$$E_\varphi = \begin{cases} C_1 J_1(k_1 r), & r < R \\ C_2 N_1(k_0 r), & r > R. \end{cases} \quad (2.8)$$

Here, the coefficients C_1 and C_2 are related by the relationships

$$C_1 J_1(k_1 R) - C_2 N_1(k_0 R) = 0,$$
$$C_1 k_1 J_1'(k_1 R) - C_2 k_0 N_1'(k_0 R) = -\frac{2\pi k_z \omega}{c^2} I_0, \quad (2.9)$$

where J_1 and N_1 are the Bessel functions, the prime denotes the derivative with respect to the argument, and the quantities k_0 and k_1 are defined as

$$k_1^2 = \frac{\omega^2}{c^2}\varepsilon(\omega) - k_z^2, \quad k_0^2 = \frac{\omega^2}{c^2} - k_z^2. \quad (2.10)$$

The expressions for the coefficients C_1 and C_2 easily follow from relationships (2.9):

$$C_1 = -\frac{2\pi k_z \omega}{c^2} \times I_0 \frac{N_1(k_0 R)}{k_1 J_1'(k_1 R) N_1(k_0 R) - k_0 J_1(k_1 R) N_1'(k_0 R)},$$
$$C_2 = -\frac{2\pi i \omega}{c^2} \times I_0 \frac{J_1(k_1 R)}{k_1 J_1'(k_1 R) N_1(k_0 R) - k_0 J_1(k_1 R) N_1'(k_0 R)}. \quad (2.11)$$

It should be noted that, since $\mathrm{Re}\,k_1^2 < 0$ and $\mathrm{Re}\,k_0^2 < 0$, and since the imaginary parts of k_0 and k_1 are small, the Bessel functions $J_1(k_1 R)$ and $N_1(k_0 R)$ are functions of the almost purely imaginary arguments.

Let us make some estimates. First, note that, for $L \approx 10$ cm, we have $k_z^2 = \pi^2/L^2 \approx 10^{-1}$ cm$^{-2} \gg \omega^2/c^2 \approx 10^{-5}$ cm^{-2}. As a result, we obtain $k_0^2 \approx -(\pi^2/L^2) \approx -0.1$ cm^{-2}, while $k_1^2 \approx -(\omega_{Le}^2/c^2) \approx -0.3$ cm^{-2} at $n_e = 10^{11}$ cm^{-3}. This indicates that the electromagnetic field excited by the antenna is localized near it, both inside and outside the plasma. Outside the plasma, the field is localized on a scale of $|k_0|^{-1} \approx 3$ cm. Inside a plasma with the density $n_e = 10^{11}$ cm^{-3}, the field is localized on a scale of about $|k_1|^{-1} \approx 2$ cm; moreover, the denser the plasma, the shorter the localization scale. Note that it is this localization scale that determines the thickness of the surface region in which the plasma is heated in a cylindrical source. According to the above estimates, this thickness should be on the order of 2–3 cm. For a plasma with the density $n_e = 10^{11}$ cm^{-3}, we have $|k_1|^{-1} < 2$ cm. Therefore, in a source with $R > 5$ cm, almost all of the rf power will be deposited in a thin plasma layer near the surface of the cylinder. At the same time, it is unlikely that elongated cylindrical plasma sources with $R \le 3$ cm find applications in plasma technologies. As

[2] In the case of diffuse reflection of electrons from the plasma surface, the last term in parentheses in expression (2.4) should be replaced by $\sqrt{\frac{2}{\pi}}\frac{\omega_{Le} V_{Te}}{\omega c}$.

for the sources with $R \geq 5$ cm, they do not provide radially uniform parameters of the plasma flow.

Hence, the above analysis shows that, in order for an elongated rf (f = 13.56 MHz) plasma source without a magnetic field to be capable of operating efficiently at a plasma density of $n_e = 5 \times 10^{10}$ cm^{-3}, its length and radius should be $L > 10$ cm and $R < 3$ cm. As the plasma density increases, the operation efficiency of the source decreases and the plasma flow becomes nonuniform over the cross section of the cylinder.[3]

3. PLANAR DISK-SHAPED PLASMA SOURCE

In a planar disk-shaped plasma source, the current-carrying antenna is assumed to be positioned at the upper end of the cylinder (Fig. 1b) and have the form of an Archimedean spiral,

$$\rho = a\varphi, \tag{3.1}$$

where a is the spiral radius.

In the limit $a \ll R$, the azimuthal current density in the antenna can be written, to a good accuracy, as

$$\begin{aligned} j_\varphi &= \frac{I_0 \mu \delta(z)}{R[1 - J_0(\mu)]} J_1\left(\mu \frac{r}{R}\right) e^{-i\omega t} \\ &= \frac{I_0}{R} q \delta(z) J_1\left(\mu \frac{r}{R}\right) e^{-i\omega t}, \end{aligned} \tag{3.2}$$

where I_0 is the net azimuthal current in the antenna, $J_1(x)$ is a first-order Bessel function, $\mu \approx 3.8$ is the first root of the Bessel function ($J_1(\mu) = 0$), and $q = \mu/(1 - J_0(\mu)) \approx 2.7$.

The field equations for a planar disk-shaped source differ from Eqs. (2.2) only slightly. Assigning the dependence $f_r(r) f_z(z) e^{-i\omega t}$ on time and coordinates to the field components, we arrive at the equations

$$\begin{aligned} -ic\frac{\partial E_\varphi}{\partial z} + \omega B_z = 0, \quad \frac{ic}{r}\frac{\partial}{\partial r} r E_\varphi + \omega B_z = 0, \\ i\frac{\partial B_r}{\partial z} - i\frac{\partial B_z}{\partial r} + \frac{\omega}{c}\varepsilon(\omega) E_\varphi = 0, \end{aligned} \tag{3.3}$$

where the dielectric function $\varepsilon(\omega)$ is given by expression (2.4).

As for the boundary conditions for Eqs. (3.3), they are obtained by integrating these equations across a transition layer around the plasma surface in the source:

$$\begin{aligned} E_\varphi|_{z=L} = 0, \quad \{E_\varphi\}_{z=0} = 0, \\ \{B_z\}_{z=0} = \frac{ic}{\omega}\left\{\frac{\partial E_\varphi}{\partial z}\right\}_{z=0} = \frac{4\pi q}{cR} I_0 J_1\left(\mu \frac{r}{R}\right). \end{aligned} \tag{3.4}$$

The right-hand side of the last of conditions (3.4) accounts for the radial dependence of the current in the spiral antenna. According to this dependence, the electric field component should be chosen to have the form

$$E_\varphi(r, z) = \tilde{E}_\varphi(z) J_1\left(\mu \frac{r}{R}\right), \tag{3.5}$$

where $\tilde{E}_\varphi(z)$ satisfies the equation

$$\frac{\partial^2 \tilde{E}_\varphi(z)}{\partial z^2} - \frac{\mu^2}{R^2}\tilde{E}_\varphi(z) + \frac{\omega^2}{c^2}\varepsilon(\omega)\tilde{E}_\varphi(z) = 0. \tag{3.6}$$

The general solution to this equation that approaches zero as $z \longrightarrow -\infty$ has the form

$$\tilde{E}_\varphi(z) = \begin{cases} C_1 e^{k_0 z}, & z \leq 0 \\ C_2 e^{k_1 z} + C_3 e^{-k_1 z}, & 0 \leq z \leq L, \end{cases} \tag{3.7}$$

where we have introduced the notation

$$k_1^2 = \frac{\mu^2}{R^2} - \frac{\omega^2}{c^2}\varepsilon(\omega), \quad k_0^2 = \frac{\mu^2}{R^2} - \frac{\omega^2}{c^2} \approx \frac{\mu^2}{R^2} > 0, \tag{3.8}$$

In deriving solution (3.7), we used approximation (2.3), according to which we have $\mathrm{Re}\, k_1^2 > 0$.

Substituting solution (3.8) into boundary conditions (3.4) yields the following expressions for the coefficients C_1, C_2, and C_3:

$$\begin{aligned} C_1 = C_2(1 - e^{2k_1 L}), \quad C_3 = -C_2 e^{2k_0 L}, \\ C_2 = -\frac{4\pi i \omega}{Rc^2}\frac{qI_0}{(k_0 - k_1) - (k_0 + k_1)e^{2k_1 L}}. \end{aligned} \tag{3.9}$$

Using expressions (3.9), we finally obtain

$$\tilde{E}_\varphi(z) = 2C_2 e^{k_1 L} \sinh[k_1(z - L)]. \tag{3.10}$$

This indicates that the azimuthal electric field component $\tilde{E}_\varphi(z)$ in the plasma is sufficiently large only under the condition

$$k_1 L \approx \frac{\omega_{Le}}{c} L \leq 1. \tag{3.11}$$

For the above values of the plasma parameters (i.e., for $n_e = 5 \times 10^{10}$ cm^{-3}), we arrive at the order-of-magnitude estimate $L \leq 3$ cm. As for the radius of the plasma source, is can be arbitrarily large.

Finally, we estimate the plasma heating power in a planar disk-shaped source under conditions (2.3). To do

[3] Note, however, that, when the transverse particle diffusion is taken into account, the degree of plasma inhomogeneity is lower. As long as R is less than the particle mean free paths (at least, up to $R \approx 5$ cm), it may be that the plasma inhomogeneity will not have any significant effect.

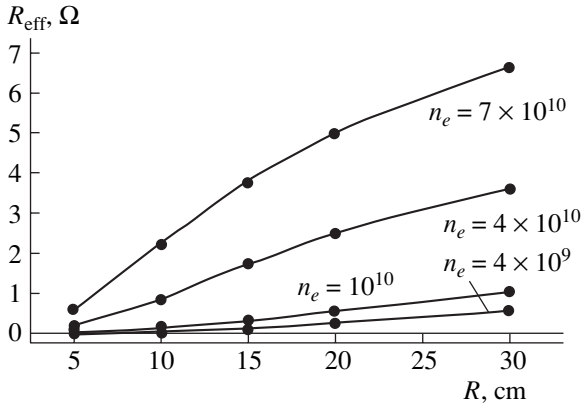

Fig. 2.

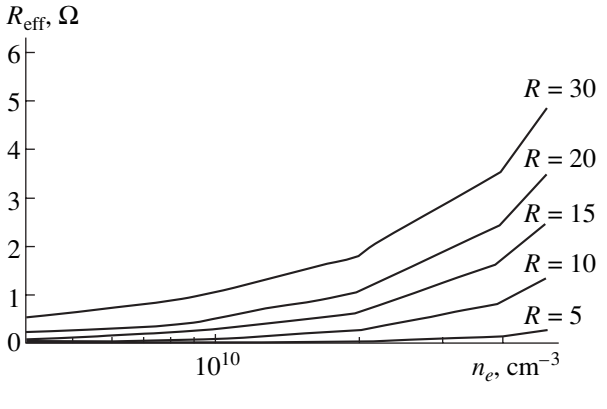

Fig. 3.

this, we set $R = 10$ cm, $L > 3$ cm, $n_e = 5 \times 10^{10}$ cm^{-3}, $T_e = 5$ eV, and $p_0 < 10^3$ torr. We also use the following formula for the rf power deposited in the plasma:

$$\mathcal{P}_W = 2\pi\frac{\omega}{4\pi}\mathrm{Im}\varepsilon(\omega)\int_0^L dz\int_0^R rdr|E_\varphi(z, r)|^2 \approx \frac{\omega}{4}\mathrm{Im}\varepsilon(\omega)\frac{\alpha^2 J_0^2(\mu)}{k_1(k_0 + k_1)^2}I_0^2 \equiv R_{\text{eff}}I_0^2, \tag{3.12}$$

where $\alpha = (4\pi\omega q)/c^2$ and R_{eff} is the equivalent plasma resistance.

According to formula (3.12), the plasma resistance R_{eff} is on the order of 0.5–5 Ω, so that, for $I_0 \approx 3$ A, the deposited power $\mathcal{P}_W$ is no higher than 5–50 W.

Figures 2 and 3 illustrate the results of numerical calculations of the equivalent plasma resistance from formula (3.12) for different values of both n_e and R. The curves plotted in the figures were calculated for plasma densities of up to $n_e = 5 \times 10^{10}$ cm^{-3}, in accordance with conditions (2.3), which are the conditions for applicability of expression (2.4). As is seen in the figures, the plasma resistance increases with plasma density and with radius R. As for the dependence of R_{eff} on L, the plasma resistance increases with cylinder length only on a short spatial scale on the order of $c/\omega_{Le} \sim 1/\sqrt{n_e}$ (it is these values that are presented in the figure) and remains constant on longer scales.

Hence, the above analysis leads to a very important conclusion: under inertial skin effect conditions (2.3), the equivalent resistance of a low-density plasma in a planar disk-shaped source is too low (on the order of 1 Ω) to ensure efficient operation of the source, because most of the rf power will be lost in the antenna (whose resistance is higher than 1 Ω) and only a small fraction of it will be deposited in the plasma. The most promising sources appear to be those operating at plasma densities of 0.5–1.0 × 10^{11} cm^{-3} and having a radius of no less than 20 cm.

APPENDIX

Here, we generalize the problem formulated above to a semi-infinite electron plasma occupying the half-space $z \geq 0$. We take into account the spatial dispersion and restrict ourselves to considering the case of specular reflection of electrons from the surface $z = 0$. A similar problem for a transverse electromagnetic field was solved in [2], so that we can use the solution obtained there. In accordance with formulas (17) and (18) from that paper, we can write

$$\tilde{E}_\varphi(z) = -\frac{\tilde{E}'_\varphi(0)}{\pi}\int_{-\infty}^{\infty}\frac{dke^{ikz}}{k^2 - \frac{\omega^2}{c^2}\varepsilon^{tr}(\omega, k)} = \frac{\alpha I_0}{R\pi}\left[1 + \frac{k_0}{\pi}\int_{-\infty}^{\infty}\frac{dk}{k^2 - \frac{\omega^2}{c^2}\varepsilon^{tr}(\omega, k)}\right]^{-1}\int_{-\infty}^{\infty}\frac{dke^{ikz}}{k^2 - \frac{\omega^2}{c^2}\varepsilon^{tr}(\omega, k)}. \tag{A.1}$$

Here,

$$k_0 = \sqrt{\frac{\mu^2}{R^2} - \frac{\omega^2}{c^2}};$$

the transverse dielectric function of an infinite isotropic plasma, $\varepsilon^{tr}(\omega, k)$, is described by the following expression, which allows for collisions and spatial dispersion [2]:

$$\varepsilon^{tr}(\omega, k) = 1 - \frac{\omega_{Le}^2}{\omega(\omega + i\nu_e)}J_+\left(\frac{\omega + i\nu_e}{kV_{Te}}\right), \tag{A.2}$$

where

$$J_+(x) = xe^{\frac{x^2}{2}}\int e^{\frac{\tau^2}{2}}d\tau.$$

The explicit limiting expressions for the function $J_+(x)$ of the complex argument x are presented in [2]. In deriving solution (A.1), we took into account the profile of $\tilde{E}_\varphi(z)$ at the boundary $z = 0$ and the jump in its derivative, $\tilde{E}'_\varphi$ (see formulas (3.4)), at this boundary.

Under the conditions of weak spatial dispersion, and under inequalities (2.3), the integrals in formula (A.1) can be taken exactly to yield the following solution, which passes over to solution (3.10) in the limit

$$\tilde{E}_\varphi(z) = -\frac{\tilde{E}'_\varphi(0)}{k_1}e^{-k_1 z} = \frac{\alpha I_0}{k_1 + k_0}e^{-k_1 z}, \qquad (A.3)$$

where k_1 is described by expression (3.8), with $\varepsilon(\omega)$ given by formula (2.3).

REFERENCES

1. *High Density Plasma Sources*, Ed. by O. A. Popov (Neges, New Jersey, 1995).
2. V. P. Silin and A. A. Rukhadze, *Electromagnetic Properties of Plasmas and Plasma-Like Media* (Atomizdat, Moscow, 1961) [in Russian].

Translated by O. Khadin

Technical Physics, Vol. 49, No. 5, 2004, pp. 572–576. Translated from Zhurnal Tekhnicheskoĭ Fiziki, Vol. 74, No. 5, 2004, pp. 50–55.

SOLIDS

Self-Organization of Atomic Order and Electronic Structure in LaSrMnO Films

Z. A. Samoilenko*, V. D. Okunev*, T. A. D'yachenko*, E. I. Pushenko*, S. J. Lewandowski, P. Gierlowski**, A. Klimov**, and A. A. Abal'oshev****

** Galkin Physicotechnical Institute, National Academy of Sciences of Ukraine, Donetsk, 83114 Ukraine*
e-mail: okunev@host.dipt.donetsk.ua
*** Institute of Physics, Poland Academy of Sciences, Al. Lotnikov 32/46, Warsaw, 02-668 Poland*
Received June 17, 2003; in final form, October 21, 2003

Abstract—A linear relationship between the critical temperatures T_{max} and T_{min} in the temperature dependences of the resistance of $La_{0.6}Sr_{0.2}Mn_{1.2}O_3$ single-crystal films that have a mesoscopic irregularity (metallic clusters in an insulating matrix) is found. A correlation between the atomic order and electronic structure of the films is studied by taking X-ray diffraction patterns and optical absorption spectra. It is shown that a rise in T_{max} and a simultaneous decrease in T_{min} cause correlated local changes in cluster areas of the structure. Namely, the volume occupied by a family of Mn–O planes with large interplanar spacings (d = 2.04–2.08 Å) shrinks, while the volume occupied by a family of closer spaced (d = 1.90–1.99 Å) planes grows. In the electronic subsystem, the density of states at $\hbar\omega$ = 1.5 and 2.4 eV, which are due to Mn^{3+} and Mn^{4+} ions, increases, and the contribution from Mn^{2+} states at $\hbar\omega$ = 0.9 eV decreases. As the charge states associated with Mn^{3+} and Mn^{4+} ions become dominant, the Mn–O binding energy grows. As a result, the contribution of the structural states with smaller d increases, thereby raising the density of states in the electronic subsystem at energies between 0.5 and 2.7 eV. The effect of self-organization in the multicomponent LaSrMnO system shows up in the transition from the heavily distorted rhombohedral to the less distorted orthorhombic structure. © *2004 MAIK "Nauka/Interperiodica".*

INTRODUCTION

Experimental studies of the temperature dependence of the resistance in $La_{0.6}Sr_{0.2}Mn_{1.2}O_3$ magnetoresistive films have shown [1–3] that the curves $R(T)$ frequently run nonmonotonically and have a minimum and maximum (see inset to Fig. 1). It has also been noted that different samples have unequal critical temperatures T_{max} and T_{min} that correspond to the maximal and minimal resistance values. These temperatures have been found to vary over wide limits. However, the relationship between these two temperatures has been explored inadequately. However, in spite of a large difference in the resistance, one may expect such a relationship, since the same atomic system (with specific features for each test sample) is studied both at high and low temperatures. The features of the atomic and electronic configurations of metallic oxides are highlighted in clustering, which causes mesoscopic-scale nonuniformities in the mass and electronic density distributions [4–8].

In view of the aforesaid, we studied a correlation between the atomic and electronic configurations for a number of $La_{0.6}Sr_{0.2}Mn_{1.2}O_3$ films (grown on $SrLaGaO_4$ substrates) with greatly differing T_{max} and T_{min}. This difference was controlled by varying the synthesis temperature T_s in the range 600–730°C when the films were deposited by pulsed laser sputtering of the target. To enhance clustering, which has an effect on the electric and magnetic properties of manganites, the target had an excessive content of manganese. To synthesize the films, we used a KrF excimer laser with a pulse dura-

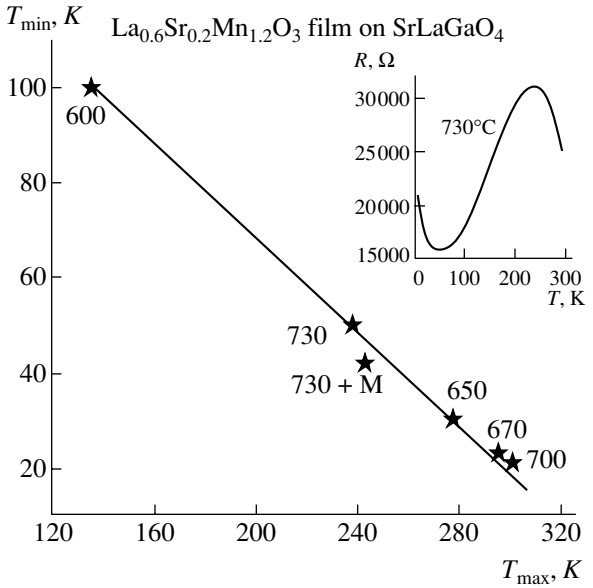

Fig. 1. Relation between T_{min} and T_{max} in the curve $R(T)$ (a typical curve $R(T)$ is shown in the inset) for $La_{0.6}Sr_{0.2}Mn_{1.2}O_3$ films on $SrLaGaO_4$ substrates.

1063-7842/04/4905-0572$26.00 © 2004 MAIK "Nauka/Interperiodica"

tion τ = 25 ns and an energy density on the target of 3.0 J/cm^2. The oxygen pressure in the working chamber was kept at 300 mTorr. The structure of the films was examined by the photometry method using long-wave CrK_α radiation. This method makes it easy to detect X rays diffusely scattered by cluster solid solutions [6], which our objects are. Electrical measurements were accomplished in the interval 4.2–300 K by the standard technique. Optical absorption spectra were taken at room temperature in the energy range $\hbar\omega$ = 0.5–5.0 eV with an SP 700C spectrophotometer.

RESULTS AND DISCUSSION

For all the films studied in this work, the temperature dependence of the resistance had two extrema $R_{max}(T)$ and $R_{min}(T)$ (see inset to Fig. 1). The maximal value R_{max} in the curves $R(T)$ is related to the onset of magnetic ordering. The temperature T_{max} is usually close to the Curie temperature. The reasons for the occurrence of the minimum value R_{min} are still unclear. According to the results [9–11] for lightly doped lanthanum manganites, where the concentration of Mn^{4+} ions is considerably lower than that of Mn^{3+} ions, the temperature T_{min} is coincident with the temperature of charge ordering. Thus, in the interval $\Delta T = T_{max} - T_{min}$, the atomic, electronic, and magnetic subsystems intensely interact between each other and the resistance of the film in this temperature interval drops with increasing temperature. However, the metallic conductivity is not reached and the films remain in the dielectric state throughout the interval ΔT [4].

When films of the $La_{0.6}Sr_{0.2}Mn_{1.2}O_3$ solid solution are formed from a plasma flux at different synthesis temperatures T_s, all other growth parameters being equal, interaction between chemical elements in the multicomponent system is bound to result in various types of atomic order. A group of $La_{0.6}Sr_{0.2}Mn_{1.2}O_3$ films were deposited on $SrLaGaO_4$ substrates at T_s = 600, 650, 670, and 700°C. They have the critical temperatures T_{max} = 135, 277, 285, and 300°C and T_{min} = 100, 30.7, 23, and 21°C, respectively. These temperatures are shown in Fig. 1 together with the critical temperatures for the films grown on other substrates and also for the film grown at 730°C and measured in a magnetic film (730 + M). The films grown at higher (>730°C) temperatures degraded because of interaction between the growing film and substrate. X-ray diffraction reflections from the films grown at T_s = 600–700°C are shown in Fig. 2. Here, the synthesis temperature (and T_{max}) rises from top to bottom, while T_{min} rises in the opposite direction.

From Fig. 1, it follows that $T_{min} = aT_{max} + b$, where a = –0.46 and b = 154.3. Such a definite relationship between T_{min} and T_{max} for the $La_{0.6}Sr_{0.2}Mn_{1.2}O_3$ films is expected to be reflected in the atomic order of the films grown in the temperature range T_s = 600–700°C (the interval $\Delta T = T_{max} - T_{min}$ depends on the synthesis temperature). The structure of the films were examined by taking X-ray diffraction pattern. The diffraction patterns shown for the angular interval $29° \le \theta_{Cr} \le 40°$ in Fig. 2 characterize the most significant features of the crystal structure, namely, families (clusters) of Mn–O planes belonging to the rhombohedral and orthorhombic phases. These clusters are sources of free holes and are responsible for local metallic conduction, thereby controlling the mean conductivity of the films. As the synthesis temperature grows, so does T_{max}, while T_{min} diminishes. As a result, the interval where the resistance decreases, manifesting the transition to the magnetically ordered state, widens [4, 12].

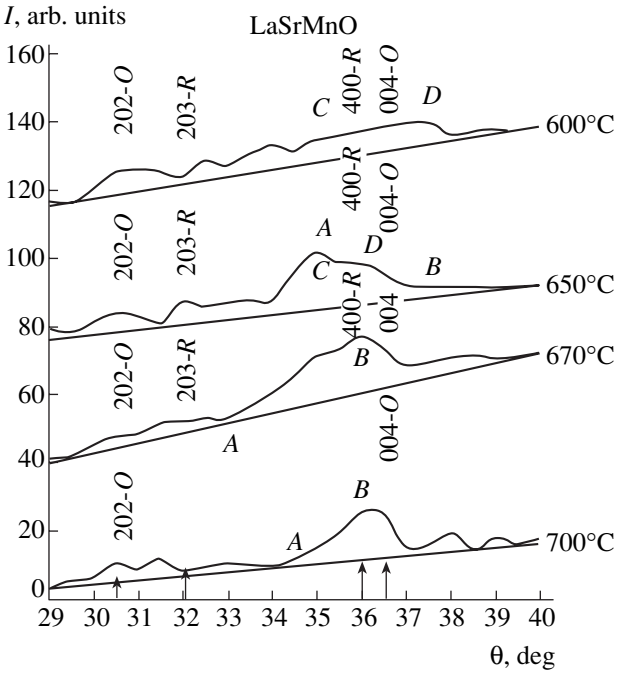

Fig. 2. X-ray diffraction patterns in the angular interval $29° < \theta_{Cr} < 40°$ taken from the $La_{0.6}Sr_{0.2}Mn_{1.2}O_3$ films differing in synthesis temperature T_s.

The "metallicity" of the planes in the clusters shows up as either flat-top maxima or extended tails (portions *CD* and *AB* in Fig. 2) in the diffraction pattern, as indicated in [13, 14]. Most significant changes are observed in the structure of metallic clusters represented by diffuse peaks from {004} planes of the orthorhombic phase. Here, not only do the maxima shift along the θ axis, indicating that other interplanar spacings prevail in the clusters (according to the Bragg equation $2d\sin\theta = n\lambda$), but their configuration also changes (Fig. 2). For example, in going from T_s = 650 to 670°C, the asymmetry of the (004) diffuse maxima in Fig. 2 changes: the tail at the right (*AB*) at 650°C changes to the tail + plateau (*CD*) at the left at 670°C.

PLANE DISTRIBUTION IN THE CLUSTER AREA OF THE STRUCTURE

Let us see how the intensity of X-ray scattering from different families of planes (in the angular range shown in Fig. 2) varies with growing synthesis temperature T_s (recall that a rise in T_s causes a rise in T_{max} and a fall of T_{min}). We will trace the variation of the scattering intensity in the angular range $\theta_{Cr} = 29.5°–40°$ by taking diffraction patterns in steps $\Delta\theta = 0.5°$. The related interplanar spacings are given by the curves in Fig. 3. It is seen that the intensities of diffuse X-ray scattering are redistributed among adjacent planes with close interplanar spacings. The variation of $I(T_s)$ is the most pronounced for two families of planes: with d ranging from 2.16 to 2.25 Å (including the (202) plane of the orthorhombic phase with $d = 2.24$ Å; the (203) plane of the rhombohedral phase with $d = 2.16$ Å; and the calculated MnO(2) bond length, $d = 2.17$ Å) and with d varying from 1.92 to 2.04 Å (including the (400) plane of the rhombohedral phase with $d = 1.942$ Å; the (004) plane of the orthorhombic phase with $d = 1.93$ Å; and the calculated MnO(2) and MnO(1) bond lengths, $d = 1.97$ and 1.907 Å [15]).

In the given case, the scattering intensity redistribution means the change in the fraction of planes with a specific interplanar spacing; therefore, one can argue that, as the synthesis temperature of LaSrMnO films rises from 600 to 700°C, the fractions of the planes with $d = 2.22–2.25$ Å and those with $d = 2.09–2.16$ Å change. At 650°C, this change is characterized by the curve with a minimum for the first family of planes and by the curve with a maximum for the other (Fig. 3).

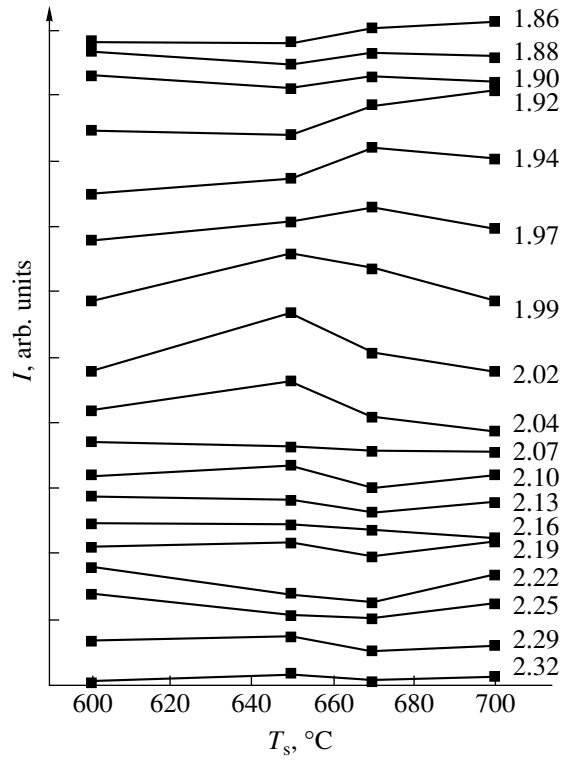

Fig. 3. Intensities of X-ray coherent scattering from different samples in the angular interval $\theta_{Cr} = 29°–40°$ (measured in 0.5° steps). The figures at the right indicate the interplanar spacings d in Å.

The scattering intensities from the family of planes with $d = 1.92–2.04$ Å, which is placed above the curve with $d = 2.07$ Å (the run of this curve is independent of T_s), vary in a different way (Fig. 3). Here, as the synthesis temperature of LaSrMnO films rises from 600 to 700°C, first (<650°C) the fraction of planes with large spacings ($d = 1.99–2.04$ Å), which form the region of extension, increases and then (>650°C) the fraction of planes with smaller d ($d = 1.86–1.97$ Å, the region of contraction) prevails (Fig. 3). These findings allow us to conclude that the volume occupied by smaller d planes continuously grows in the cluster structure starting from $T_s = 650$°C.

Since the interplanar spacings considered are comparable to Mn–O interatomic spacings, the atomic order reconstruction observed with an increase in the LaSrMnO synthesis temperature suggests that the planes with $d < 2$ Å start dominating over the planes with $d > 2$ Å. In other words, one may state that Mn–O interatomic interaction is enhanced with increasing T_s. Correspondingly, the overlap of the wave functions and, hence, the density of states responsible for the electronic and optical properties increase.

EVOLUTION OF THE ELECTRONIC SUBSYSTEM

The effect of atomic order on the electronic structure of LaSrMnO films is indicated by the optical absorption spectra shown in Fig. 4. The transmission of all the samples is low (in Fig. 4, the absorption coefficient α exceeds 2×10^4 cm^{-1}). The absence of a distinct optical absorption edge, which is typical of normal semiconductors and insulators, is noteworthy. For the film with $T_s = 600$°C (the rhombohedral phase), three absorption maxima are observed: at (*A*) 0.9, (*B*) 1.5, and (*C*) 2.0 eV. These maxima correlate with the maxima (at the same energies) of the density of electronic states participating in optical transitions.

In the electronic structure of manganites, splitting of d states by the crystal field plays an essential role, causing the formation of energy gaps. The energy gap Δ_{cf} between the e_g and t_{2g} states in the crystal field of manganites depends on the charge state of manganese ions and decreases with increasing spacing between Mn and O ions [2]. For oxides, the typical values of Δ_{cf} for Mn^{4+}, Mn^{3+}, and Mn^{2+} ions are, respectively, 2.5, 1.8, and 1.0 eV. For Mn^{4+} and Mn^{3+} ions in the spectra of perovskite-like manganites, these values are 2.4 and 1.5 eV. These findings agree with the positions of maxima in the optical absorption spectra (Fig. 4). The lower

concentration of Mn^{3+} ions in the rhombohedral phase compared with their concentration in the orthorhombic phase is embodied in the fact that the optical absorption coefficient α (hence, the density of states participating in optical transitions) is one order of magnitude higher in the films with the orthorhombic structure at $\hbar\omega \approx 1.5$ eV. At $\hbar\omega > 2.1$ eV, the difference between the absorption coefficients for the orthorhombic and rhombohedral phases is small (less than 40%).

The increase in the density of states in the orthorhombic phase in the energy interval 0.5–2.7 eV is consistent with the increase in the fraction of more close-packed structural features (i.e., of those with small d) in the clusters. This shows up in the enhanced intensity of diffuse scattering from clusters that involve Mn–O bonds with a high charge state of manganese ions (Mn^{3+} and Mn^{4+}). In these clusters, the energy of interaction is higher and, accordingly, the Mn–O spacings are smaller [2] (the curves with d = 1.92–1.99 Å in Fig. 3). As manganese and oxygen ions in the orthorhombic phase approach each other, the density of states increase noticeably, as follows from Figs. 3 and 4.

The changes in the atomic order and electronic structure of the films have a decisive effect on the conductivity. The rhombohedral films with $T_s \le 600$°C have a high resistivity ($\rho \approx 5 \times 10^5$ Ω cm at 300 K). However, the presence of the orthorhombic phase in a small amount (several percent) in the film with T_s = 600°C decreases the resistivity to $\rho \sim 10^{-2}$ Ω cm. In the films with the orthorhombic structure, the resistivity is much (by three or four orders of magnitude).

The absorption spectrum of the rhombohedral phase (T_s = 600°C) depends not only on the split of the e_g and t_{2g} states of Mn in the crystal field but also on the presence of metallic-conduction clusters in the insulating matrix. Because of built-in electric fields induced by the clusters, typical of heavily inhomogeneous optical media [16, 17], the absorption edge has a near-Uhrbach shape: $\ln\alpha \sim \hbar\omega$ [18] (Fig. 4, dotted lines).

The samples with $T_s > 600$°C are less transparent. The spectra taken from the films grown at 650, 670, and 700°C differ only slightly. They have a peak at $\hbar\omega \approx 1.5$ eV and peak C at $\hbar\omega \approx 2.0$ eV. The weak feature of the spectra at ≈2.0 eV (peak C, which is observed almost in all the films shown in Fig. 4 except for the stoichiometric films) may be associated with the off-stoichiometric composition of the films and the formation of MnO_2-like clusters, which are coherently embedded in the host crystal. If so, we are dealing with one-phase heterogeneity.

The spectra for the orthorhombic and rhombohedral phases differ not only in density of states but also in the presence of additional peak A at $\hbar\omega \approx 0.9$ eV in the spectra for the rhombohedral phase. This peak is presumably related to the energy gap between the t_{2g} and e_g states in the presence of Mn^{2+} ions.

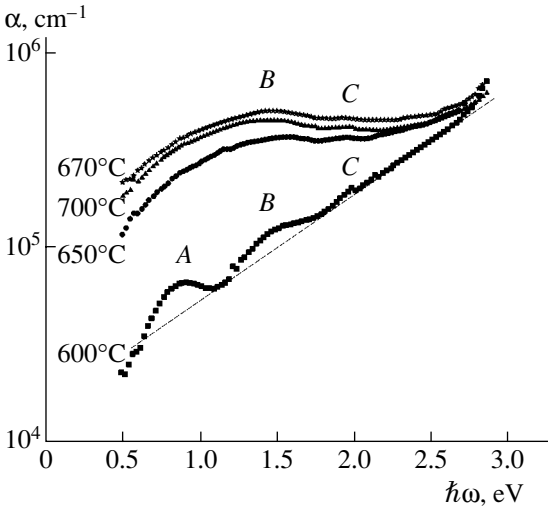

Fig. 4. Optical absorption spectra for the $La_{0.6}Sr_{0.2}Mn_{1.2}O_3$ films differing in synthesis temperature T_s.

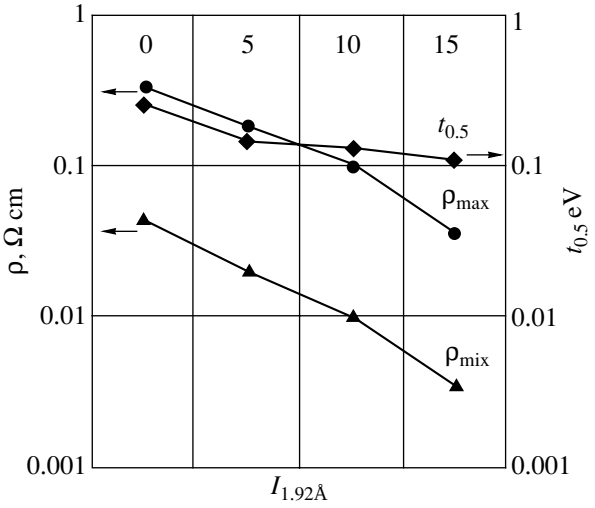

Fig. 5. Relation between the optical transmission (t at 0.5 eV), resistivity extremes ρ_{min} and ρ_{max}, and intensity $I_{1.92\,Å}$ of diffuse scattering from closely spaced (d = 1.92 Å) planes.

For the films with the orthorhombic structure (T_s = 650, 670, and 700°C), the approximation of the experimental data by the formula $\alpha(\hbar\omega) \sim (\hbar\omega - E_{g0})^2/\hbar\omega)$ (where $\hbar\omega$ is the photon energy and E_{g0} is the optical energy gap) [19] when $[\alpha(\hbar\omega)]^{1/2}$ tends to zero yields $E_{g0} \approx 0$, which the case for manganites [20]. In the short-wave range ($\hbar\omega > 3$ eV), where the slope of the curve $\alpha(\hbar\omega)$ in Fig. 4 increases, we obtain $E_g = 2.4 \pm 0.05$ eV by the same approximation for all the samples. This value of E_g agrees with the split Δ_{cf} between the t_{2g} and e_g states of Mn^{4+} ions.

Figure 5 shows the correlation between the intensity $I_{1.92\,Å}$ of diffuse X-ray scattering from closely spaced

(d = 1.92 Å) Mn–O planes with the extreme resistivity values (ρ_{max} and ρ_{min}) of the LaSrMnO films and the optical transmission t in the energy range where the contribution from free charge carriers to intraband optical transitions is appreciable ($\hbar\omega$ = 0.5 eV).

These parameters are contrasted at T_s = 600, 650, 670, and 700°C = const. The synthesis temperature grows along the abscissa from left to right. It is seen that both the resistivity and the optical transmission decrease as the fraction of the closely spaced Mn–O planes in the cluster structure grows. This supports the experimentally found fact that the metallicity of LaSrMnO films becomes more pronounced when manganese and oxygen atoms approach each other as a result of increasing the degree of Mn ionization. The ionization favors the crystallographic phase transition [4] (Mn^{2+} + Mn^{3+} + Mn^{4+}) rhombohedral phase $\longrightarrow$ (Mn^{3+} + Mn^{4+}) orthorhombic phase.

CONCLUSIONS

The results of studying $La_{0.6}Sr_{0.2}Mn_{1.2}O_3$ films differing in interval $\Delta T = T_{max} - T_{min}$ between the extreme values in the temperature dependence of the resistance may be summarized as follows.

(i) The extension of the metallicity interval (a rise in T_{max} and a simultaneous decrease in T_{min}) is favored by the redistribution of atoms within a family of correlated planes (with the total amount of scatterers remaining the same): the fraction of widely spaced (d = 2.02–2.04 Å) planes drops, while that of closely spaced (d = 1.90–1.99 Å) planes grows. This enhances Mn–O interatomic interaction.

(ii) Enhanced Mn–O interaction raises the density of states responsible for optical transitions at energies $\hbar\omega$ = 1.5 and 2.4 eV, which are typical of Mn^{3+} and Mn^{4+} ions. Simultaneously, the density of states at $\hbar\omega$ = 0.9 eV associated with Mn^{2+} ions decreases.

Thus, the reason for the extension of the metallicity interval $\Delta T = T_{max} - T_{min}$ is an increase in the density of states as a result of enhanced Mn–O interatomic interaction and in the local mass density of clusters in LaSrMnO films.

ACKNOWLEDGMENTS

This work was partially supported by the Government of Poland (grant no. PBZ-KBN-0.13/TO8/19).

REFERENCES

1. É. L. Nagaev, Usp. Fiz. Nauk **166**, 833 (1996) [Phys. Usp. **39**, 781 (1996)].
2. J. M. D. Coey, M. Viret, and S. von Molnar, Adv. Phys. **48**, 167 (1999).
3. Salamon Myron B. and Jaime Marcelo, Rev. Mod. Phys. **73**, 583 (2001).
4. Z. A. Samoĭlenko, V. D. Okunev, E. I. Pushenko, *et al.*, Zh. Tekh. Fiz. **73** (2), 118 (2003) [Tech. Phys. **48**, 250 (2003)].
5. V. D. Okunev, Z. A. Samoilenko, A. Abal'oshev, *et al.*, Appl. Phys. Lett. **75**, 1949 (1999).
6. V. D. Okunev, Z. A. Samoilenko, V. A. Isaev, *et al.*, Pis'ma Zh. Tekh. Fiz. **28** (2), 12 (2002) [Tech. Phys. Lett. **28**, 44 (2002)].
7. V. D. Okunev, Z. A. Samoilenko, V. M. Svistunov, *et al.*, J. Appl. Phys. **85**, 7282 (1999).
8. M. A. Krivoglaz, *Electronic Structure and Electronic Properties of Metals and Alloys: Collection of Scientific Works* (Naukova Dumka, Kiev, 1988), pp. 3–39 [in Russian].
9. S. F. Dubinin, V. E. Arkhipov, Ya. M. Mukovskiĭ, *et al.*, Fiz. Met. Metalloved. **93** (3), 60 (2002).
10. É. A. Neĭfel'd, V. E. Arkhipov, N. A. Tumalevich, and Ya. M. Mukovskiĭ, Pis'ma Zh. Éksp. Teor. Fiz. **74**, 630 (2001) [JETP Lett. **74**, 556 (2001)].
11. U. Staub, G. I. Meijer, F. Fauth, *et al.*, Phys. Rev. Lett. **88**, 126402/1 (2002).
12. N. G. Bebenin, R. I. Zaĭnullina, V. V. Mashkautsan, *et al.*, Zh. Éksp. Teor. Fiz. **117**, 1181 (2000) [JETP **90**, 1027 (2000)].
13. *Physical Properties of High-Temperature Superconductors*, Ed. by D. M. Ginsberg (World Sci., Singapore, 1989; Mir, Moscow, 1990).
14. C. Thomsen and M. Cardona, in *Raman Scattering in High-Temperature Superconductors* (Mir, Moscow, 1990), pp. 411–504.
15. Q. Huang, A. Santoro, J. W. Lynn, *et al.*, Phys. Rev. B **55**, 14987 (1997).
16. V. D. Okunev, Fiz. Tverd. Tela (St. Petersburg) **34**, 1263 (1992) [Sov. Phys. Solid State **34**, 667 (1992)].
17. V. D. Okunev, Z. A. Samoilenko, A. Abal'oshev, *et al.*, Phys. Rev. B **62**, 696 (2000).
18. V. L. Bonch-Bruevich, Usp. Fiz. Nauk **140**, 583 (1983) [Sov. Phys. Usp. **26**, 664 (1983)].
19. R. A. Smith, *Semiconductors* (Cambridge Univ. Press, Cambridge, 1978; Mir, Moscow, 1982).
20. A. S. Moskvin, E. V. Zenkov, Yu. D. Panov, *et al.*, Fiz. Tverd. Tela (St. Petersburg) **44**, 1452 (2002) [Phys. Solid State **44**, 1519 (2002)].

Translated by V. Isaakyan

Technical Physics, Vol. 49, No. 5, 2004, pp. 577–582. Translated from Zhurnal Tekhnicheskoĭ Fiziki, Vol. 74, No. 5, 2004, pp. 56–61.

SOLIDS

Frequency Spectrum of the Nonlinear Magnetoimpedance of Multilayer Film Structures

N. A. Buznikov, A. S. Antonov, A. L. D'yachkov, and A. A. Rakhmanov

Institute for Theoretical and Applied Electrodynamics, Russian Academy of Sciences, Moscow, 125412 Russia

e-mail: n_buznikov@mail.ru

Received August 11, 2003; in final form, October 22, 2003

Abstract—Magnetization reversal by high-frequency current in FeCuNbSiB/Al/FeCuNbSiB three-layer film structures is studied. The frequency spectrum of the voltage arising in a coil wound on the sample as a function of a permanent magnetic field (nonlinear magnetoimpedance) is taken. It is shown that the frequency spectra of the voltage are qualitatively different for the longitudinal and transverse orientations of the field with respect to the direction of the current. Frequency spectrum harmonics are demonstrated to be highly sensitive to a magnetic field. A simple electrodynamic model to describe experimental data is suggested. © *2004 MAIK "Nauka/Interperiodica".*

INTRODUCTION

The giant magnetoimpedance effect (a drastic increase in the complex resistance of a conductor in a weak magnetic field) is of great interest because of its possible applications in various fields of technology [1–3]. To date, the giant magnetoimpedance effect has been studied in detail in amorphous wires and cobalt stripes (see, e.g., [4, 5]), where it was first discovered. Subsequently, this effect was observed in multilayer film structures consisting of magnetically soft or nanocrystalline films separated by a high-conductivity metallic spacer [6–12]. A potentially high sensitivity of these multilayer structures to an external magnetic field makes them promising for small-size detectors of weak magnetic fields.

The giant magnetoimpedance effect is observed at relatively low amplitudes of a time-varying current, when the signal measured is proportional to the conductor impedance. Recently, nonlinear effects in magnetically soft wires have attracted considerable attention [13–19]. They appear when a relationship between the magnetization and current amplitude becomes nonlinear. In this case, magnetization reversal takes place in a part of the sample volume and the spectrum of the voltage across the ends of the wire or in a pickup coil wound on the sample consists of harmonics with frequencies that are multiples of the current frequency. From the applied point of view, a nonlinear voltage response may turn out to be even more promising than the giant magnetoimpedance effect [13, 15, 19]. Such a response is often called the nonlinear magnetoimpedance effect [15, 16, 19]. Strictly speaking, the term "impedance" is applicable to only the linear case; however, because of apparent similarity to the giant magnetoimpedance effect, this term is in frequent use in the relevant literature for brevity. It should be noted that measurement of the magnetic field based on higher harmonics is a well-known procedure, which is applied, for example, in ferroprobes (see, e.g., [20, 21]). However, in magnetically soft amorphous conductors exhibiting the giant magnetoimpedance effect, the output signal spectra have a number of intriguing features, which make it possible to considerably improve the sensitivity to low (on the order of 1 Oe) magnetic fields.

Calculations [22] showed that technologically the nonlinear effects offer a number of advantages over the giant magnetoimpedance effect. It is known [8, 9, 23] that pronounced transverse (relative to the current vector in the sample) magnetic anisotropy is a necessary condition for the impedance of a film to change considerably. However, providing for uniform and stable transverse anisotropy is a technological challenge due to the influence of the sample shape. Obtaining a highly sensitive response based on the nonlinear magnetoimpedance effect does not require transverse magnetic anisotropy [22], which greatly simplifies the fabrication of the film structures. In addition, unlike the case of magnetically soft wires, the frequency spectrum of the nonlinear voltage signal picked up from the film is highly sensitive to two components of an external magnetic field [22], allowing for the design of a two-component field detector.

In this work, we study the nonlinear magnetoimpedance of a three-layer film structure consisting of magnetically soft amorphous films separated by a high-conductivity nonmagnetic spacer. The frequency spectra of the voltage arising in a coil wound on the sample are taken for both transverse and longitudinal orientations (relative to the direction of the time-varying current) of an external magnetic field. It is shown that the amplitudes of odd and even harmonics depend on the transverse and longitudinal field strength in a considerably

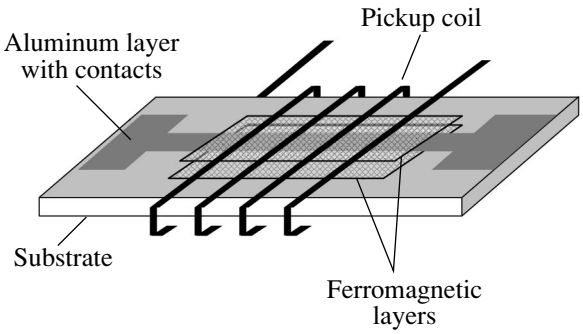

Fig. 1. Sandwich used in the experiment.

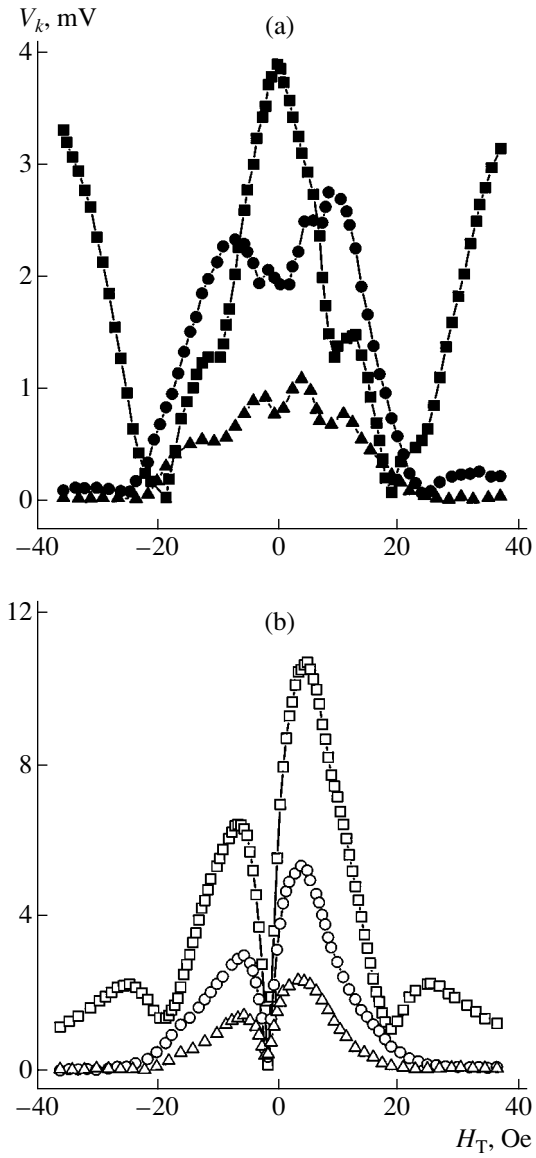

Fig. 2. Measured harmonic amplitudes V_k against the transverse magnetic field H_T (I_0 = 50 mA, f = 1 MHz). (a) Odd harmonics: k = (■) 1, (●) 3, and (▲) 5; (b) even harmonics: k = (□) 2, (○) 4, and (△) 6.

different manner. Experimental data are analyzed in terms of a quasi-static approximation.

EXPERIMENTAL

Experiments were performed with $Fe_{73.5}Cu_1Nb_3Si_{16.5}B_6$/Al/$Fe_{73.5}Cu_1Nb_3Si_{16.5}B_6$ three-layer film structures (sandwiches). The films were prepared by electron-beam vacuum evaporation. Ferromagnetic films were l = 5 mm long, w = 3 mm wide, and d = 0.6 μm thick. The thickness of the aluminum layer was 2 μm. At the ends of the aluminum layer, 3 × 3-mm copper contact pads were formed. No special measures to induce magnetic anisotropy were taken. Stresses at the layer–layer and layer–substrate (Sitall) interfaces were relieved by annealing at 250°C.

The nonlinear magnetoimpedance was measured by passing a time-variable current along the longer side of the sandwich. The peak amplitude of the current was I_0 = 75 mA, and its frequency f was varied between 0.1 and 2.0 MHz. The test sample was placed in a permanent solenoidal magnetic field whose strength was varied from –37 to 37 Oe. The magnetic field could be oriented both longitudinally and transversely relative to the longer side of the sandwich. A 45-turn pickup coil was wound on the test sample (Fig. 1). The amplitudes of voltage harmonics generated in the coil were measured with an HP4395A spectrum analyzer.

RESULTS AND DISCUSSION

Figure 2 plots the amplitudes of voltage harmonics V_k (k is the harmonic number) arising in the coil against the transverse magnetic field strength H_T. The amplitude V_1 of the first harmonic peaks in the absence of the field. As the field magnitude grows, V_1 decreases, exhibits a low peak at $|H_T| \cong 10$ Oe, goes to zero at $|H_T| \cong 20$ Oe, and increases at $|H_T| > 20$ Oe (Fig. 2a). The third-harmonic amplitude is minimal in the absence of the field, grows with increasing field magnitude, and reaches a maximum at $|H_T| \cong 10$ Oe. The maximum of the third harmonic exceeds that of the first harmonic at $|H_T| < 20$ Oe. The behavior of the fifth harmonic in low fields is qualitatively similar to that of the first one, but the amplitude of the latter is higher.

In the transverse magnetic field, even harmonics behave in a radically different manner (Fig. 2b). Their amplitudes equal zero at $H_T \cong –1.5$ Oe and then sharply grow with increasing magnetic field, being considerably dependent on the sense of the transverse field. For example, the second harmonic has peaks at $H_T \cong –6.5$ and ≅5 Oe and its amplitudes in these peaks differ by a factor of more than 1.5 (Fig. 2b). As the magnitude of the field increases, the amplitudes of even harmonics decline. The amplitude V_2 has an additional small peak at $|H_T| \cong 25$ Oe. Note that V_2 far exceeds V_1 and is more sensitive to the transverse magnetic field H_T. In positive

fields, the field sensitivity of V_2 is about 2 mV/Oe, as follows from Fig. 2b.

For the coil placed in the longitudinal field H_L, the voltage harmonic amplitudes are shown in Fig. 3. The first harmonic amplitude V_1 has a maximum at $|H_L| \cong 1.5$ Oe and remains virtually the same in high fields (Fig. 3a). The amplitudes of other odd harmonics are much smaller than V_1 and also vary insignificantly with the longitudinal field.

The amplitudes of odd harmonics grow with increasing H_L, reach a peak, and then slowly decrease (Fig. 3b). From Figs. 2b and 3b, it follows that the dependence of the even harmonic amplitudes on the sense of the field in the case the longitudinal configuration is lower. The second-harmonic amplitude V_2 reaches a peak at $H_L \cong \pm 3.5$ Oe, and the peak values of V_2 differ by no more than 10%. In addition, the dependence $V_2(H_L)$ has no extra peaks in high fields. Figure 3 shows that the even harmonic amplitudes are much more sensitive to the longitudinal field H_L than the amplitudes of odd harmonics. The sensitivity of the second harmonic to the longitudinal field is roughly 4 mV/Oe. It should be noted that the behavior of even harmonics in the longitudinal field are qualitatively similar to that observed when the nonlinear magnetoimpedance was studied in amorphous cobalt microwires [13, 24] and in composite wires consisting of a high-conductivity core and a magnetically soft cladding [14, 17].

The field dependences of the signal spectra taken from the pickup coil may be qualitatively explained in terms of a simple model of a sandwich consisting of two ferromagnetic layers separated by a nonmagnetic spacer. We assume that the domain structure in both ferromagnets is absent. As was shown [22], the one-domain approximation is valid for not too wide sandwiches with a low constant of induced anisotropy. In the absence of an external magnetic field, the magnetization distribution is found from the minimum condition for the sum of the induced anisotropy energy and the energy of interaction between ferromagnetic layers through stray fields. For simplicity, we will assume that anisotropy in the films is uniaxial and the effective anisotropy field is the superposition of the induced anisotropy field and stray fields.

Let the current flow only through the middle high-conductivity layer and its associated variable field be uniformly distributed across the ferromagnetic films. The variable field amplitude H_0 is related to the current amplitude I_0 as

$$H_0 = 2\pi I_0/cw. \quad (1)$$

When the current $I(t) = I_0\sin(2\pi ft)$ passes through the sandwich, its magnetic field makes the transverse magnetization components M_{xi} time-dependent (hereafter, the subscripts $i = 1$ and 2 refer to the ferromagnetic layers, and the x and y axes run along the shorter and longer sides of the sandwich, respectively). The time variation of the transverse magnetization components causes the longitudinal components M_{yi} to vary with time. Then, according to the Faraday law, a voltage V arises in the coil wound on the sample. If I_0 is low, the voltage varies linearly with the current amplitude [23]. Large current amplitudes reverse the magnetization of the sandwich, and the voltage generated in the coil becomes high and nonlinearly dependent on I_0. The voltage in the coil is given by

$$V = -(V_0/M)\left[\frac{dM_{y1}}{d\tau} + \frac{dM_{y2}}{d\tau}\right]. \quad (2)$$

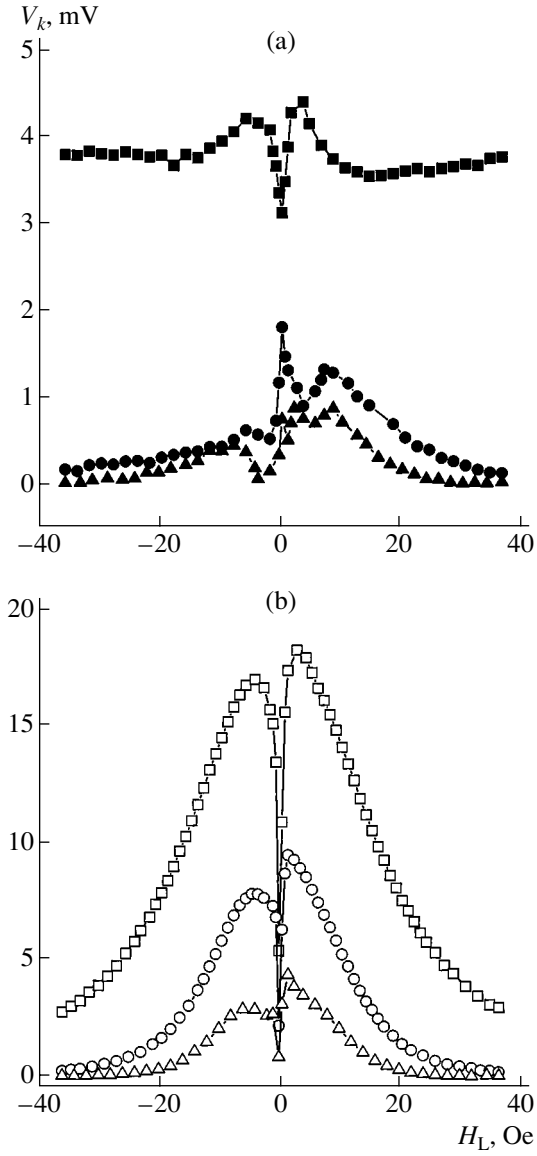

Fig. 3. Measured harmonic amplitudes V_k against the longitudinal magnetic field H_L ($I_0 = 50$ mA, $f = 1$ MHz). (a) Odd harmonics: $k =$ (■) 1, (●) 3, and (▲) 5; (b) even harmonics: $k =$ (□) 2, (○) 4, and (△) 6.

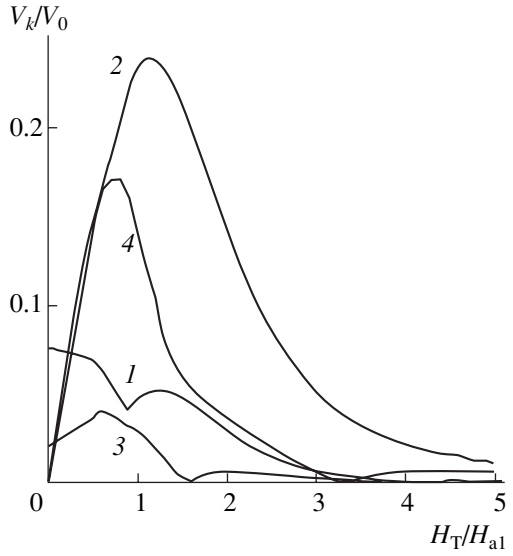

Fig. 4. Calculated harmonic amplitudes V_k against the transverse magnetic field H_T for $H_0/H_{a1} = 1.1$, $H_{a1} = H_{a2}$, $\psi_1 = 0.15\pi$, and $\psi_2 = 0.2\pi$. k = (*1*) 1, (*2*) 2, (*3*) 3, and (*4*) 4.

Here, $V_0 = 8\pi^2 NMfwd/c$, N is the number of turns in the pickup coil, M is the saturation magnetization, and $\tau = 2\pi ft$ is dimensionless time. Since in experiments the frequency of the current is not too high, the magnetization reversal process can be described in a quasi-static approximation. Under the assumptions made above, the free energy U of the sandwich can be represented as the magnetic anisotropy energy and the Zeeman energy in the field of the current and in an external magnetic field:

$$\begin{aligned} U/lwd &= (MH_{a1}/2)\sin^2(\theta_1 - \psi_1) \\ &+ (MH_{a2}/2)\sin^2(\theta_2 - \psi_2) - MH_0\sin(\tau)(\sin\theta_1 - \sin\theta_2) \\ &- MH_T(\sin\theta_1 + \sin\theta_2) - MH_L(\cos\theta_1 + \cos\theta_2). \end{aligned} \tag{3}$$

Here, θ_i are the angles between the magnetization vector and y axis in the ferromagnetic films, H_{ai} is the effective anisotropy fields in the films, and ψ_i are the angles the anisotropy axis makes with the y axis in the films. Note that the anisotropy fields in the films may differ substantially [9]. The magnetization components in the ferromagnetic layers satisfy the minimum condition for the free energy U.

Let us consider the frequency spectrum of the voltage in the coil for the transverse field ($H_T \neq 0$, $H_L = 0$). The minimization of the free energy yields the following equations for the magnetization components in the ferromagnetic layers:

$$\begin{aligned} H_{ai}^2\cos^2(2\psi_i)M_{yi}^2(M^2 - M_{yi}^2) \\ = M^2[\{H_T - (-1)^i H_0\sin\tau\}MM_{yi} \\ + H_{ai}\sin(2\psi_i)(M_{yi}^2 - M^2/2)]^2, \end{aligned}$$

$$\begin{aligned} \partial^2 U/\partial\theta_i^2 &= \{H_T - (-1)^i H_0\sin\tau\}MM_{xi} \\ &+ H_{ai}\cos(2\psi_i)(M_{yi}^2 - M_{xi}^2) \\ &+ 2H_{ai}\sin(2\psi_i)M_{xi}M_{yi} > 0, \\ M_{xi}^2 &= M^2 - M_{yi}^2. \end{aligned} \tag{4}$$

At low amplitudes of the variable current, the curves $M_{xi}(\tau)$ and $M_{yi}(\tau)$ are smooth. If the amplitude of the current-induced field exceeds a certain threshold value, the magnetization components change sign stepwise, causing irreversible magnetization switching in the films. Near the steps, the quasi-static approximation is inapplicable, and one would have to use the Landau–Lifshitz equation to describe the magnetization reversal process. However, at low frequencies ($f \ll 1/\Delta t$, where Δt is the characteristic time of step change in magnetization), one need not know the behavior of the curves $M_{xi}(\tau)$ and $M_{yi}(\tau)$ near the steps in detail to analyze the frequency spectrum of the voltage [13]. Ignoring the steps and using Eqs. (2) and (4), we get for the voltage in the pickup coil

$$V = V_0 H_0 \cos\tau\left[\frac{M_{x1}M_{y1}}{\partial^2 U/\partial\theta_1^2} - \frac{M_{x2}M_{y2}}{\partial^2 U/\partial\theta_2^2}\right], \tag{5}$$

where M_{xi}, M_{yi}, and $\partial^2 U/\partial\theta_i^2$ satisfy Eqs. (4).

The frequency spectrum in the pickup coil can be found by applying Fourier transformation to expression (5). The calculated dependences of the voltage harmonic amplitudes V_k on the transverse magnetic field H_T are shown in Fig. 4. Here, the results are given only for positive values of the field ($H_T > 0$), since the harmonic amplitudes in the model considered are symmetric under change of sign of the field. From Fig. 4, it follows that, for low fields, the calculation qualitatively agrees with the measured dependences of the harmonic amplitudes on the transverse field. However, the model cannot account for the increase in the amplitudes of the first and second harmonics in the high field range (Fig. 2) because of the above assumptions. In real sandwiches, the anisotropy field is distributed over the ferromagnetic films nonuniformly. Magnetization reversal takes place also nonuniformly, which may lead to an increase in the amplitude of some harmonics in high magnetic fields.

Consider now the nonlinear impedance in the longitudinal magnetic field ($H_L \neq 0$, $H_T = 0$). The minimization of free energy (3) yields the following equations for the magnetization components:

$$\begin{aligned} (M^2 - M_{yi}^2)[H_L M + H_{ai}\cos(2\psi_i)M_{yi}]^2 \\ = M^2[H_0 MM_{yi}\sin\tau + H_{ai}\sin(2\psi_i)(M_{yi}^2 - M^2/2)]^2, \\ \partial^2 U/\partial\theta_i^2 = H_L MM_{yi} - (-1)^i H_0 MM_{xi}\sin\tau \\ + H_{ai}\cos(2\psi_i)(M_{yi}^2 - M_{xi}^2) \end{aligned} \tag{6}$$

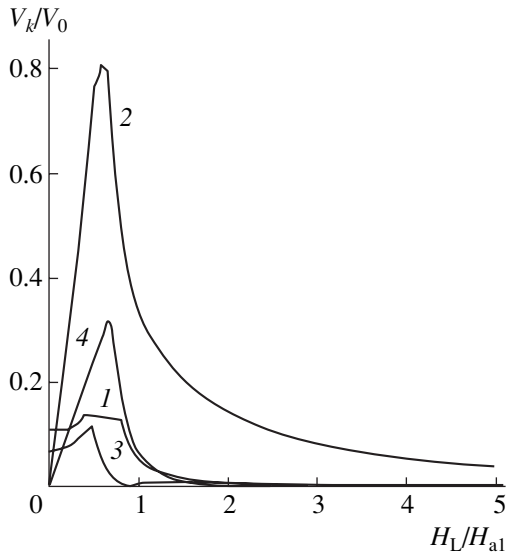

Fig. 5. Calculated harmonic amplitudes V_k against the longitudinal magnetic field H_L for $H_0/H_{a1} = 1.1$, $H_{a1} = H_{a2}$, $\psi_1 = 0.15\pi$, and $\psi_2 = 0.2\pi$. k = (*1*) 1, (*2*) 2, (*3*) 3, and (*4*) 4.

$$+ 2H_{ai}\sin(2\psi_i)M_{xi}M_{yi} > 0,$$

$$M_{xi}^2 = M^2 - M_{yi}^2.$$

In Fig. 5, the voltage harmonic amplitudes V_k are plotted against the longitudinal magnetic field. The curves are calculated by applying Fourier transformation to expressions (5) and (6). As in the case of the transverse field, the model assumes that the harmonic amplitudes are symmetric with respect to sign of the field. The measured and calculated amplitude versus field curves are qualitatively similar to each other, but the calculated even-harmonic amplitudes fall faster.

Thus, our simple model makes it possible to describe the basic features of the experimental frequency spectrum of the voltage arising in the pickup coil. However, it fails in explaining the harmonic amplitude asymmetry under change of sign of the field and the increase in the first and second harmonic amplitudes in high transverse magnetic fields. In addition, the decrease in the even-harmonic amplitudes with increasing field, which was observed in the experiment, is slower than predicted. These discrepancies between the theory and experiment are due to the assumptions of the model. For a more detailed analysis of experimental curves, it is necessary to take into account the nonuniform distribution of the variable magnetic field and anisotropy field over the ferromagnetic layers and edge effects.

CONCLUSIONS

We studied the nonlinear impedance of $Fe_{73.5}Cu_1Nb_3Si_{16.5}B_6$/Al/$Fe_{73.5}Cu_1Nb_3Si_{16.5}B_6$ sandwiches. The frequency spectra of the voltage arising in a pickup coil were taken for external magnetic fields oriented both transversely and longitudinally relative to the direction of the time-varying current. The frequency spectrum of the voltage is found to be appreciably sensitive to the field orientation. In the transverse configuration, the first several harmonics have high amplitudes, and even harmonics are more sensitive to the field. In the longitudinal configuration, odd harmonic amplitudes depend on the field only slightly, and even harmonics remain highly sensitive to the field. For both orientations, the field sensitivity of the second harmonic is on the order of 1 mV/Oe at a current frequency of 1 MHz. This value is comparable in order of magnitude to the sensitivity obtained in [6, 8, 10], where the giant magnetoimpedance effect in film structures was investigated, and can be improved by optimizing the sandwich geometry and using a variable current of higher amplitude and frequency. Since the effect is observed in both longitudinal and transverse magnetic fields, it may provide a basis for designing two-component low-magnetic-field detectors.

ACKNOWLEDGMENTS

This work was supported by the Russian Foundation for Basic Research (grant no. 02-02-16707) and by grant no. NSh-1694.2003.2 of the President of the Russian Federation.

N.A.B. thanks the Foundation in Support of Russian Science.

The authors are indebted to A.L. Rakhmanov for the valuable discussion.

REFERENCES

1. K. Mohri, T. Uchiyama, and L. V. Panina, Sens. Actuators A **59**, 1 (1997).
2. M. Vazquez, M. Knobel, M. L. Sanchez, *et al.*, Sens. Actuators A **59**, 20 (1997).
3. K. Mohri, T. Uchiyama, L. P. Shen, *et al.*, J. Magn. Magn. Mater. **249**, 351 (2002).
4. M. Vazquez, J. Magn. Magn. Mater. **226–230**, 693 (2001).
5. M. Knobel and K. R. Pirota, J. Magn. Magn. Mater. **242–245**, 33 (2002).
6. M. Senda, O. Ishii, Y. Koshimoto, and T. Tashima, IEEE Trans. Magn. **30**, 4611 (1994).
7. K. Hika, L. V. Panina, and K. Mohri, IEEE Trans. Magn. **32**, 4594 (1996).
8. T. Morikawa, Y. Nishibe, H. Yamadera, *et al.*, IEEE Trans. Magn. **32**, 4965 (1996).
9. A. S. Antonov, S. N. Gadetskiĭ, A. B. Granovskiĭ, *et al.*, Fiz. Met. Metalloved. **83** (6), 60 (1997).
10. S. Q. Xiao, Y. H. Liu, S. S. Yan, *et al.*, Phys. Rev. B **61**, 5734 (2000).
11. Y. Zhou, J. Xu, X. Zhao, and B. Cai, J. Appl. Phys. **89**, 1816 (2001).
12. G. V. Kurlyandskaya, J. L. Munoz, J. M. Barandiaran, *et al.*, J. Magn. Magn. Mater. **242–245**, 291 (2002).

13. A. S. Antonov, N. A. Buznikov, I. T. Iakubov, *et al.*, J. Phys. D **34**, 752 (2001).
14. A. S. Antonov, N. A. Buznikov, A. F. Prokoshin, *et al.*, Pis'ma Zh. Tekh. Fiz. **27** (8), 12 (2001) [Tech. Phys. Lett. **27**, 313 (2001)].
15. C. Gomez-Polo, M. Knobel, K. R. Pirota, and M. Vazquez, Physica B **299**, 322 (2001).
16. G. V. Kurlyandskaya, H. Yakabchuk, E. Kisker, *et al.*, J. Appl. Phys. **90**, 6280 (2001).
17. A. S. Antonov, N. A. Buznikov, A. B. Granovsky, *et al.*, J. Magn. Magn. Mater. **249**, 315 (2002).
18. J. G. S. Duque, A. E. P. de Araujo, M. Knobel, *et al.*, Appl. Phys. Lett. **83**, 99 (2003).
19. G. V. Kurlyandskaya, A. Garcia-Arribas, and J. M. Barandiaran, Sens. Actuators A **106**, 239 (2003).
20. Yu. V. Afanas'ev, *Ferroprobes* (Énergiya, Leningrad, 1969) [in Russian].
21. N. N. Zatsepin and V. G. Gorbash, *Ferroprobe Transducers with Transverse Excitation* (Nauka i Tekhnika, Minsk, 1988) [in Russian].
22. A. S. Antonov, N. A. Buznikov, and A. L. Rakhmanov, Fiz. Met. Metalloved. **94** (4), 5 (2002).
23. A. S. Antonov and I. T. Yakubov, Fiz. Met. Metalloved. **87** (5), 29 (1999).
24. A. S. Antonov, N. A. Buznikov, A. B. Granovsky, *et al.*, Sens. Actuators A **106**, 213 (2003).

Translated by V. Isaakyan

Technical Physics, Vol. 49, No. 5, 2004, pp. 583–586. Translated from Zhurnal Tekhnicheskoĭ Fiziki, Vol. 74, No. 5, 2004, pp. 62–65.

SOLIDS

High-Rate Penetration of a Striker into SiC Ceramic with Different Void Content

A. S. Vlasov*, E. L. Zil'berbrand*, A. A. Kozhushko*, A. I. Kozachuk*, A. B. Sinani*, A. I. Slutsker*, V. I. Betekhtin*, and S. S. Ordan'yan**

** Ioffe Physicotechnical Institute, Russian Academy of Sciences, Politekhnicheskaya ul. 26, St. Petersburg, 194021 Russia*

e-mail: alex@mdlab.ioffe. ru

*** St. Petersburg State Technological Institute (Technical University), Moskovskiĭ pr. 26, St. Petersburg, 198013 Russia*

Received October 2, 2003

Abstract—The kinetics of penetration of deformable striking rods into SiC ceramics with different void content is studied. The penetration may be viewed as a two-stage process. At the first stage, the penetration rate is minimal and the rate of contraction of the rod is maximal. At this stage, the penetration resistance of the ceramic is the highest. At the second (quasi-steady-state) stage, the penetration kinetics is similar to the kinetics of penetration into a zero-strength medium and resistance to penetration is largely inertial. At the first stage, the penetration resistance is shown to correlate with the hardness of the ceramic and depend strongly on the void content. © *2004 MAIK "Nauka/Interperiodica".*

INTRODUCTION

It has been shown [1–3] that high-rate penetration of deformable strikers into ceramic materials is a two-stage process in the general case. At the first stage, the penetration rate is minimal and the rate of contraction of the striking rod is maximal. At this stage, the penetration parameters vary significantly as the ceramic material is crushed, turning into a zero-strength free-flowing bulk medium. At the second stage, the penetration rate is almost constant, being equal to the rate of penetration into a zero-strength material. This means that the penetration resistance is specified mainly by inertial forces at this stage.

Obviously, the ballistic efficiency of ceramic materials for the first place depends on the parameters of the first stage, where the penetration resistance is maximal.

As was shown in [2, 3], the failure kinetics of ceramics and their impact behavior depend on both the impact intensity (the impact velocity and the density of the rod) and the physicomechanical properties of the material. It remains to answer the question as to which properties of ceramic materials are responsible for their ballistic efficiency.

The purpose of this work was to study the kinetics of penetration into ceramics of the same composition that have different physicomechanical properties because of different void content, since the effect of voidage on the ballistic efficiency of ceramics is of great interest.

EXPERIMENTAL

We studied the penetration of deformable striking rods made from tungsten alloy into SiC-based ceramics. The voidage of the ceramics was varied over wide ranges. The ceramics were prepared by sintering fine-grained (a grain size of about 0.2 μm) SiC powders with admixtures of aluminum and yttrium oxides. Boron and carbon were also added in small amounts (about 0.5 wt %). The sintering temperature was varied from 1920 to 2150°C. The samples were 30-mm-long cylinders 40 mm in diameter.

The physicomechanical properties of five ceramic samples (hereafter, SiC *1*, SiC *2*, SiC *3*, SiC *4*, and SiC *5*) are listed in the table. The voidage π was determined from the formula $\pi = 1 - \rho/\rho_0$, where ρ is the measured material density and ρ_0 is the calculated density of the pore-free material. The voidage of the ceramic materials under study was considered in detail elsewhere [4].

The rods (30 mm long and 3 mm in diameter) were made from tungsten alloy with a density of 17.3 g/cm^3 and a dynamic yield strength of 2 GPa. The impact velocity was measured in each of the tests and was equal to ≈1600 m/s.

The positions of the rod at different times were visualized with a four-shot X-ray pulsed unit. A set of bench marks and a high accuracy of measuring the time between X-ray pulses provide high temporal and spatial resolutions of the penetration process (±0.1 μs and ±0.2 mm, respectively).

Figure 1 shows typical X-ray images of the rod that were taken at different times for sample SiC *1*.

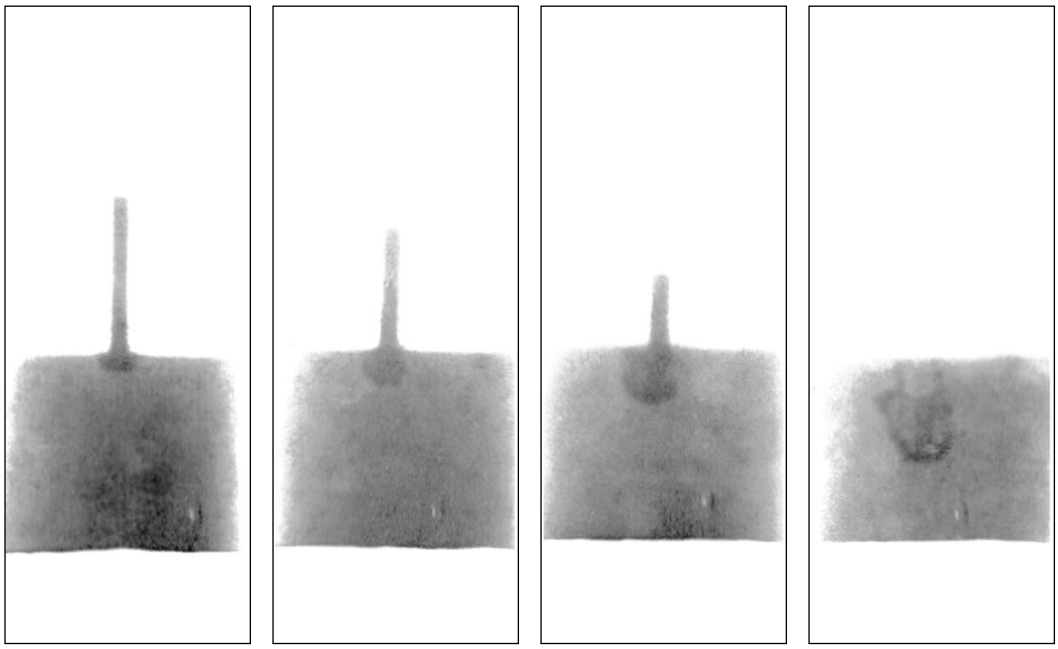

Fig. 1. Phases of penetration of the striking rod made from W alloy into SiC *1* ceramic. The impact velocity is $V_i \approx 1600$ m/s.

Three to five runs with each of the samples provide sufficient information for the process of penetration. Figure 2 shows typical distance–time curves for the leading and rare ends of the rod penetrating into SiC *1*. Using the X-ray images, we can directly measure $P(t)$ and $L(t)$ (where P is the penetration depth of the rod, L is the current length of the rod, and t is the time) and calculate the basic parameters of the process: the penetration rate $U(t) = dP/dt$, the rate of contraction of the rod as a function of time (dL/dt), and the rate of contraction as a function of the penetration depth (dL/dP).

RESULTS AND DISCUSSION

Figure 3 plots the ratio between the penetration rate U and the current rod speed V versus time at the impact velocity $V_i = 1600$ m/s for all the samples. The curves support the earlier conclusions [1–3] that the process is two-stage. In our case, the penetration rate at the first stage, which specifies the ballistic efficiency of ceramic materials, depends strongly on the material properties, in particular, on the voidage.

Table

Material	ρ, g/cm^3	π, %	*E*, GPa	*G*, GPa	μ	σ_R, MPa	*HV*, GPa	R_{T0}, GPa
SiC *1*	3.28	0.9	380	160	0.22	430	31	11.0
SiC *2*	3.26	1.8	375	155	0.21	330	25	9.0
SiC *3*	3.22	2.4	360	150	0.21	310	23	6.9
SiC *4*	3.05	5.0	360	150	0.21	230	22	5.3
SiC *5*	2.93	10.0	255	105	0.21	180	19	5.1

Note: ρ is the density; π, the voidage; E, Young's modulus; G, the shear modulus; μ, Poisson's ratio; σ_R, the bending strength; *HV*, the Vickers hardness; and R_{T0}, the initial penetration resistance (initial strength) of the ceramics.

As the ceramics are crushed, the penetration kinetics become much alike. The U/V versus t curves converge, tending toward the "hydrodynamic" value

$$U/V = \frac{1}{1 + \sqrt{\rho_T/\rho_R}} = 0.7,$$

which is obtained in terms of the model of ideal incompressible liquid (here, ρ_T and ρ_R are the densities of the target and rod, respectively) [5]. Moreover, late in the penetration, the experimental values of U/V exceed the hydrodynamic one. This fact can be explained by stress relieving in the relatively small targets when stress waves reflect from their free surfaces, which decreases the density ρ_T. However, in the case of lower resistance targets, the strength of the striker, which is ignored in the model of ideal incompressible liquid, becomes significant.

More information about the process can be extracted by considering the contraction of the striking rod. In this case, the penetration resistance of the target can be estimated from the rate of contraction of the rod versus time (dL/dt) or penetration depth (dL/dP). As is

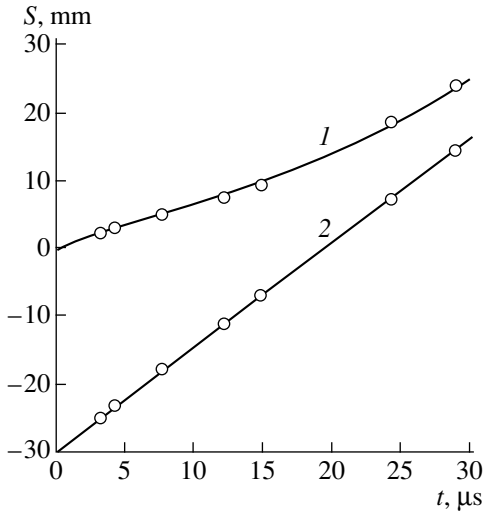

Fig. 2. Distance–time curves for the (*1*) leading and (*2*) rare ends of the striker penetrating into SiC *1*.

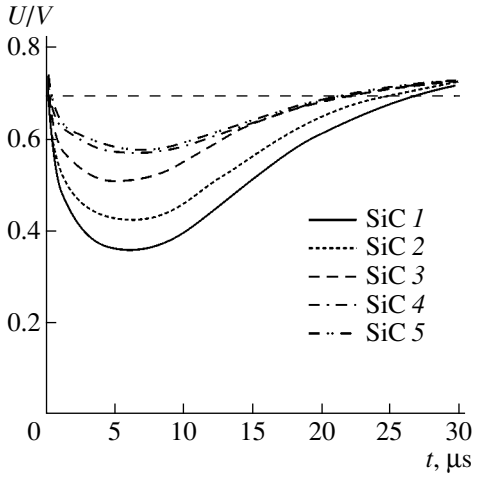

Fig. 3. Time dependence of the relative penetration rate U/V for the SiC ceramics with different voidage. The value $U/V \approx 0.7$ (straight line) is calculated in terms of the hydrodynamic model.

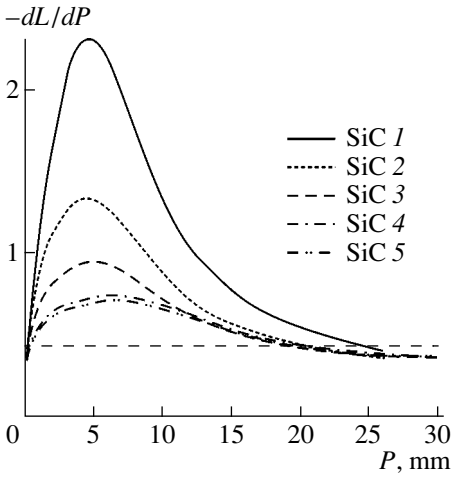

Fig. 4. Contraction of the striker as a function of the penetration depth in the SiC ceramics. The value $-dL/dP \approx 0.42$ (straight line) is calculated in terms of the hydrodynamic model.

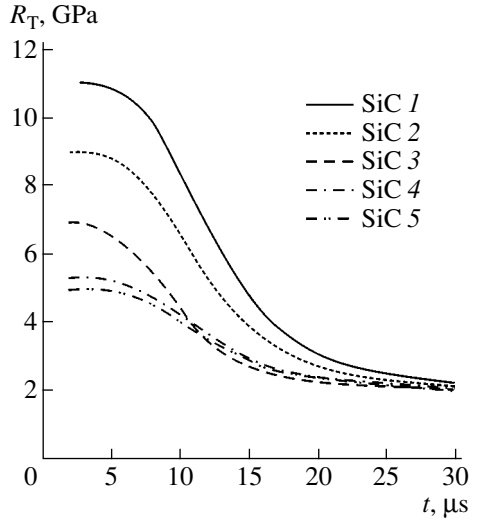

Fig. 5. Penetration resistance of the SiC ceramics vs. the time of interaction with the striking rod.

seen from Fig. 4, at the early stage of penetration, the rate of contraction significantly exceeds the value

$$-\frac{dL}{dP} = \sqrt{\rho_R/\rho_T} \approx 0.42,$$

which is obtained from the model of ideal incompressible liquid.

As noted above, the effective penetration resistance of the target can be estimated from the experimental values of the kinematic parameters, in particular, from the rate U and speed V. The penetration resistance is estimated with the Alekseevskiĭ–Tate equation [6, 7]

$$\frac{1}{2}\rho_T U^2 + R_T = \frac{1}{2}\rho_R (V-U)^2 + R_R, \qquad (1)$$

where R_T and R_R characterize the strength properties of the target and striker under experimental conditions.

Taking R_R to be equal to the yield strength Y_R of the rod, i.e., $R_R = Y_R = 2$ GPa, we can easily calculate R_T from Eq. (1).

The time dependences of R_T for all the samples are given in Fig. 5. It is seen that R_T significantly varies with time, remaining constant only within initial 3 to 5 μs of the process in all the cases. This constant value may be taken as the initial resistance R_{T0} of the target material to high-rate penetration. In the course of penetration, the resistance decreases sharply because of failure of the ceramics. By the 30th microsecond, the

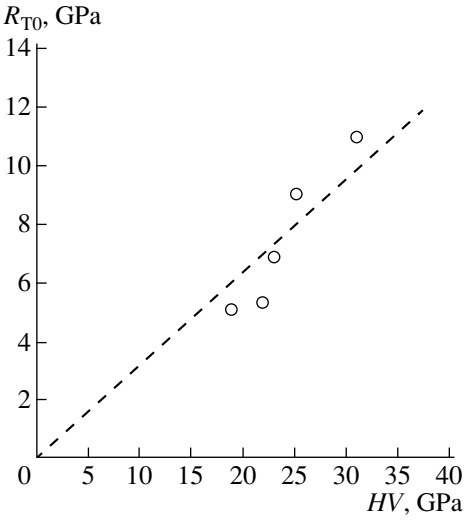

Fig. 6. Initial penetration resistance (initial strength) vs. the hardness for SiC ceramics.

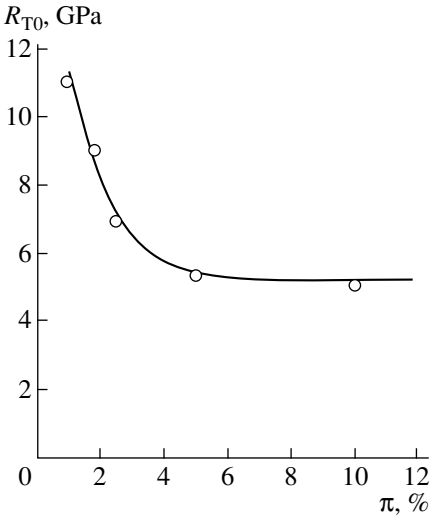

Fig. 7. Initial penetration resistance vs. the voidage for SiC ceramics.

strength of the ceramics drops to an extent that they can be considered as a zero-strength medium.

It seems that the parameter R_{T0} may be viewed as a basic property of ceramics, such as strength, elastic modulus, and hardness. As follows from the table, R_{T0}, like other physicomechanical properties, regularly decreases with increasing voidage. Physically, R_{T0} is very close to the Vickers hardness *HV* (these parameters correlate, as is seen from Fig. 6). The fact that $HV/R_{T0} \approx 3$ can be accounted for as follows. On the one hand, this may reflect the fact that material damage around a 1- to 3-mm-deep crater (used in determining R_{T0}) is heavier than around a 10- to 30-μm-deep indentation, which is characteristic of *HV* measurements. In other words, the failure of the material in *HV* measurements is not as intense as in R_{T0} measurements. On the other hand, the difference between R_{T0} and *HV* may be due to the same reason as the difference in superhard material hardness when it is determined from recovered ($HV_d \equiv HV$) and actual (HV_h) indentations [6, 7]. In our case, R_{T0} was calculated using the kinematic characteristics of penetration and, thus, is closer to HV_h, which is measured from the actual depth of a continuously penetrating indenter. As follows from [6, 7], $HV_d/HV_h \approx 2$.

To conclude, emphasis should be placed upon the strong voidage dependence of R_{T0} in the low-voidage ceramic materials: R_{T0} is almost half as much in the voidage range 1–5% (Fig. 7).

CONCLUSIONS

High-rate penetration into porous ceramics follows the mechanism established earlier for a variety of brittle materials. In essence, penetration into porous ceramics can be viewed as two-stage failure.

The penetration resistance is maximal at the early stage, where the resistance depends strongly on the voidage. The penetration resistance drops when the voidage increases to 5%.

At the next stage, the penetration resistance is defined mainly by inertial forces and depends on the voidage only slightly.

The strength of the ceramics observed at the very beginning of the process (R_{T0}) correlates with the hardness *HV*. The strength R_{T0} can be considered as a basic property of ceramics that specifies their penetration resistance and, hence, ballistic efficiency.

ACKNOWLEDGMENTS

We thank the QinetiQ (formerly DERA) research organization (Great Britain) for assistance.

REFERENCES

1. E. L. Zil'berbrand, N. A. Zlatin, A. A. Kozhushko, *et al.*, Zh. Tekh. Fiz. **59** (10), 54 (1989) [Sov. Phys. Tech. Phys. **34**, 1123 (1989)].
2. A. S. Vlasov, Yu. A. Emel'yanov, E. L. Zil'berbrand, *et al.*, Pis'ma Zh. Tekh. Fiz. **23** (3), 68 (1997) [Tech. Phys. Lett. **23**, 117 (1997)].
3. A. S. Vlasov, Yu. A. Emel'yanov, E. L. Zil'berbrand, *et al.*, Fiz. Tverd. Tela (St. Petersburg) **41**, 1785 (1999) [Phys. Solid State **41**, 1638 (1999)].
4. A. I. Slutsker, V. I. Betekhtin, A. B. Sinani, *et al.*, Sci. Sin. **34**, 143 (2002).
5. M. A. Lavrent'ev, Usp. Mat. Nauk **12** (4), 41 (1957).
6. O. N. Grigor'ev, Yu. V. Mil'man, V. N. Skvortsov, *et al.*, Poroshk. Metall., No. 8 (176), 72 (1977).
7. B. A. Galanov, O. N. Grigor'ev, Yu. V. Mil'man, and I. P. Ragozin, Probl. Prochn., No. 11, 93 (1983).

Translated by K. Shakhlevich

Technical Physics, Vol. 49, No. 5, 2004, pp. 587–591. Translated from Zhurnal Tekhnicheskoĭ Fiziki, Vol. 74, No. 5, 2004, pp. 66–70.

OPTICS, QUANTUM ELECTRONICS

Localization of the Femtosecond Pulse Train Energy in a One-Dimensional Nonlinear Photonic Crystal

V. A. Trofimov, E. B. Tereshin, and M. V. Fedotov

Moscow State University, Vorob'evy gory, Moscow, 119899 Russia

Received March 5, 2003; in final form, October 27, 2003

Abstract—Computer simulation demonstrates the feasibility of pumping a one-dimensional nonlinear photonic crystal (layered one-dimensional periodic structure) by optical energy localizing in the crystal when it is irradiated by a femtosecond pulse train. Simulation is based of the recently suggested approach to similar problems. It is shown that the pumping effect can be employed in 3D optical storages. © *2004 MAIK "Nauka/Interperiodica".*

INTRODUCTION

Interaction of femtosecond pulses with photonic crystals is of great practical interest, in particular, for data transfer through fiber-optic communication lines. Various photonic-crystal-related nonlinear optical effects are known (see, e.g., [1, 2]), such as soliton formation, optical switching, etc., which are promising for designing optical processors and 3D optical storages. In view of the latter application, it is instructive to see whether the pumping a nonlinear photonic crystal (PC) by radiation energy localized inside the crystal is feasible. With this in mind, we performed a computer simulation of this problem for a one-dimensional photonic crystal, using the approach recently suggested [3, 4] for problems of this class. This approach assumes that light wave propagation is isotropic (a preferred direction is absent) and, according to our analysis [4], yields qualitatively more adequate and quantitatively more accurate results compared with those obtained by the conventional methods. It should be noted that the same problem was also analyzed as applied to discrete lattices [5], i.e., in terms of a discrete model.

STATEMENT OF THE PROBLEM

Propagation of an electromagnetic pulse in a one-dimensional photonic crystal with cubic nonlinearity is described by the nonlinear wave equation

$$\frac{\partial^2 E(z,t)}{\partial z^2} - \frac{n^2(z)}{c^2}\frac{\partial^2 E(z,t)}{\partial t^2} = \frac{4\pi}{c^2}\frac{\partial^2}{\partial t^2}P_{\text{nl}},$$
$$P_{\text{nl}} = \varepsilon_{\text{nl}}|E|^2 E, \quad 0 < t < L_{\text{t}}, \quad 0 < z < L_z. \tag{1}$$

Here, $E(z, t)$ is the electric field strength; z is the coordinate along the pulse propagation direction; L_z and $n(z)$ are the length and refractive index of the medium, respectively; t is time; L_{t} is the time interval within which optical pulse propagation is analyzed; c is the velocity of light; and ε_{nl} is a nonlinear correction to the permittivity.

In order to derive an equation for the complex amplitude $A(z, t)$, slowly varying with time, let us represent the electric field strength and the correction to the permittivity in the form

$$E(z,t) = 0.5(A(z,t)e^{-i\omega t} + \text{c.c.}),$$
$$P_{\text{nl}} = 0.5\varepsilon_{\text{nl}}|A|^2(A(z,t)e^{-i\omega t} + \text{c.c.}),$$

where c.c. means the complex conjugate.

Assuming a linear relationship between the wavenumber k and frequency of light ω, as is customary for this class of problems [2], and using the same coordinate notation for convenience, we transform the wave equation for femtosecond pulse propagation in a nonlinear periodic medium into the Schrödinger equation [3], which in dimensionless form appears as

$$\varepsilon(z)\frac{\partial A}{\partial t} + iD\frac{\partial^2 A}{\partial z^2} + i\beta(\varepsilon(z) + \alpha(z)|A|^2)A = 0. \tag{2}$$

Here,

$$D = -\frac{1}{4\pi\Omega}, \quad \beta = -\pi\Omega, \quad \Omega = \frac{\omega}{\omega_{\text{str}}}, \quad L = \frac{L_z}{\lambda_0}, \tag{3}$$

$$\varepsilon(z) = \begin{cases} 1, & 0 \le z \le L_0 \\ \varepsilon_1, & L_0 + (d_1 + d_2)(j-1) \le z \le L_0 + d_1 \\ + (d_1 + d_2)(j-1), & 1 < j < N_{\text{str}} + 1 \\ \varepsilon_2, & L_0 + d_1 + (d_1 + d_2)(j-1) \le z \le L_0 \\ + (d_1 + d_2)j, & 1 < j < N_{\text{str}} \\ \varepsilon_3, & L_0 + (d_1 + d_2)N_{\text{str}} + d_1 \le z \le L, \end{cases} \tag{4}$$

1063-7842/04/4905-0587$26.00

$$\alpha(z) = \begin{cases} 0, \quad 0 \le z \le L_0 \\ \alpha_1, \quad L_0 + (d_1 + d_2)(j-1) \le z \le L_0 + d_1 \\ + (d_1 + d_2)(j-1), \quad 1 < j < N_{\text{str}} + 1 \\ \alpha_2, \quad L_0 + d_1 + (d_1 + d_2)(j-1) \le z \le L_0 \\ + (d_1 + d_2)j, \quad 1 < j < N_{\text{str}} \\ 0, \quad L_0 + (d_1 + d_2)N_{\text{str}} + d_1 \le z \le L. \end{cases} \quad (5)$$

Thus, the first and last layers of the photonic crystal have the same permittivity ε_1. Next is the substrate with a permittivity ε_3. It should be noted that the case $\varepsilon = 1$ corresponds to one of two cases: either the substrate is air or the permittivities of other layers are measured in units of the permittivity of the substrate. Above, ω_{str} is the frequency of the periodic structure: $\omega_{\text{str}} = 2\pi c/\lambda_0$, where $\lambda_0 = d_1\sqrt{\varepsilon_1} + d_2\sqrt{\varepsilon_2}$; d_1, d_2 and ε_1, ε_2 are the thicknesses and permittivities of the respective layers; N_{str} is the number of the layers; ε_3 is the permittivity of the substrate under the layered structure; L_0 is the dimensionless distance from a radiation source to the PC; L is the normalized length of the region considered (it includes the distance to the PC, the length of the layered structure, and the length of the substrate); and α_1 and α_2 characterize the cubic nonlinearity of the layers.

We consider a time interval that is too short for a pulse propagating along the z axis to reach the boundary of the region of interest. Therefore, the initial and boundary conditions for Eq. (2) have the form

$$A|_{t=0} = A_0(z)e^{i2\pi\Omega z}, \quad A|_{z=0,\,L} = 0. \quad (6)$$

For a Gaussian pulse, the complex amplitude $A_0(z)$ in the space before the PC is given by

$$A_0(z) = \exp\left(-\frac{(z - L_c)^2}{a^2}\right), \quad (7)$$

where L_c is the position of the center of a pulse and a is the spatial size of the beam (coincident with the pulse length in our case).

The problem stated by (2) and (6) has invariants [3], which were used to construct conservative difference schemes that retain difference analogues of these invariants during calculation. Such an approach excludes calculation errors that may arise because of an inappropriately chosen scheme. However, in view of the complex character of pulse–PC interaction, one should perform calculations on grids with successively decreasing steps to control the results obtained. If the pulse shape does not depend on the step, the spectral distribution of the grid solution is valid.

To conclude this section, we note that the results that follow were obtained for the layers with the dimensionless lengths

$$d_1 = 0.2, \quad d_2 = 0.6, \quad (8)$$

which are close to the physical values presented in [2, 6] for an optical radiation wavelength of 780 nm.

It should be mentioned that fixed values of d_1 and d_2 do not restrict the generality of the results. With these lengths changed, the phenomena considered below will be observed for other values of the related parameters, as follows from the numerical simulation discussed here. The value of L_0 was chosen such that the pulse does not reach the first layer of the PC at zero time.

REFLECTION AND TRANSMISSION BANDS VERSUS NONLINEARITY PARAMETER AND PULSE DURATION

Since many mechanisms may be responsible for the effect of energy localization within a PC (pulse self-focusing in a definite layer, a frequency shift of the transmission band, etc.), let us consider the variation of the transmission and reflection bands with the pulse duration and the nonlinearity factor. The solid curve in Fig. 1 shows the percentage R of the energy reflected from a linear ($\alpha_1 = \alpha_2 = 0$) PC for a long ($a = 20$) incident pulse. It is seen that total internal reflection takes place in the range $1.85 \le \Omega \le 1.91$, while the transmission band lies in the range $2.11 \le \Omega \le 2.16$. The parameters $\varepsilon_1 = (2.3)^2$, $\varepsilon_2 = \varepsilon_3 = 1$, and $N_{\text{str}} = 10$ were fixed. Note that the value of ε_1 coincides with the permittivity of ZnS [6]. It is important that the simulation [6] of this curve gave the result that is totally coincident with the experiment, indicating a high accuracy of the simulation.

The dashed curve shows the same dependence for a shorter pulse ($a = 10$). In the range $1.85 \le \Omega \le 1.91$, the reflected energy fraction reaches only 86.9%; at the same time, it does not drop below 3.8% in the range $2.11 \le \Omega \le 2.16$. Hence, neither the band of total reflection nor the band of total transmission exist in this case. This is because the pulse begins to interact with each layer of the PC rather than with the PC as a whole.

The dash-and-dot curve corresponds to a long ($a = 20$) pulse incident on a slightly nonlinear PC ($\alpha_1 = 0$, $\alpha_2 = 0.25$). Here, the minimal fraction of the reflected energy is even higher, 9%. This is associated with the fact that self-focusing breaks a pulse into short subpulses, for which the fraction of the energy transmitted in the transmission band of the long pulse diminishes. It should be emphasized that the localization effect is absent in this case.

With an increase in the incident intensity, for example, at $\alpha_1 = 0$ and $\alpha_2 = 2$ (triangles in Fig. 1), this curve becomes difficult to construct because of the light energy localization effect. Since this effect is frequency-dependent, the localized energy fraction varies with Ω. Moreover, the localized energy fraction affects

in various ways the reflected and transmitted fractions of the energy at different Ω. Yet one can see that the reflected energy fraction is appreciably lower than in the three previous cases.

SINGLE PULSE ENERGY LOCALIZATION

To detect the phenomenon of energy localization experimentally, we studied the light intensity localized in the PC versus the pulse duration when either the input intensity or the energy of the pulse is kept constant. As follows from our numerical simulation performed under the latter conditions, the shorter the pulse (the higher its intensity), the higher the localization efficiency. Table 1 presents the peak intensities of subpulses localized in the PC as a function of the input parameters of an incident pulse. For a short pulse (a = 25), subpulses are localized in the sixth and eighth layers (their peak intensities equal 1.4 and 1.0, respectively). For a pulse of duration a = 39, localization is observed only in the eighth layer with a subpulse peak intensity of 0.7. Finally, for a = 100, the localization effect is absent.

Thus, the higher the incident pulse intensity, the higher the fraction of the energy localized in PC layers. Another conclusion that can be drawn from Table 1 is that, for every nonlinear layer, there exists a lower energy threshold above which the energy localizes in this layer. If the energy delivered to a nonlinear layer is insufficient, localization does not occur (as in the case with an intensity of 0.25).

Table 2 shows the calculated fraction of the energy localized in PC layers as a function of the incident pulse duration. These data support the conclusion that the effect of localization depends on the amount of energy delivered to a nonlinear layer. For example, when the initial pulse duration equals four, the energy delivered to the layer is insufficient for a subpulse to be localized although the light intensity in this layer grows to 1.5.

It is significant that localization takes place even in the transmission band of a linear PC irradiated by a long pulse. Computer simulation performed for Ω = 2.14, α_1 = 0.01, and α_2 = 5 revealed the localization effect in the second, fourth, and sixth layers. The respective fractions of the localized energy equals 16, 11, and 4% of the initial pulse energy. The fraction $\theta_j(t)$ of the localized energy was calculated as the ratio of the energy at a given time instant to the total incident pulse energy:

$$\theta_j(t) = \frac{\int_{\frac{L_0 + (d_1 + d_2)j - d_2}{L_0}}^{L_0 + (d_1 + d_2)j} \varepsilon(z)|A|^2 dz}{I_1(t) = \int_0 \varepsilon(z)|A|^2 dz}, \quad (9)$$

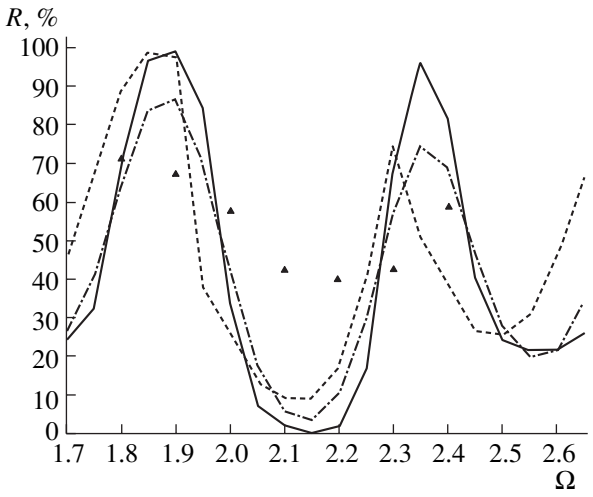

Fig. 1. Percentage of the energy reflected from a linear PC exposed to a pulse of duration a = 20 (solid curve) and 10 (dashed curve) vs. the parameter Ω. The same dependences for slightly nonlinear (α_1 = 0, α_2 = 0.25) and highly nonlinear (α_1 = 0, α_2 = 2) PCs are shown by the dot-and-dash line and triangles, respectively.

where j is the number of an even layer and $I_1(0)$ is the energy of a pulse before the PC.

Note that, in the nonlinear case, 25% of the incident energy reflect from the crystal because of a shift in the transmission band. It is also essential that, in the nonlinear case, the energy may localize in several top layers even in the total reflection band of a linear PC.

Table 1. Localized subpulse intensity vs. the incident pulse duration with the incident energy fixed. $\varepsilon_1 = (2.3)^2$, $\varepsilon_2 = 1$, $\varepsilon_3 = (1.3)^2$, $N_{str} = 7$, $\Omega = 2.14$, $\beta = -6.73$, $D = -0.037$, $\alpha_1 = -5$, and $\alpha_2 = 5$

Incident pulse parameters		Localized subpulse intensity (number of PC layer)
a	max $\lvert A(z, 0)\rvert^2$	
25	1	1.4 (sixth) and 1 (eighth)
39	0.54	0.7 (eighth)
100	0.25	No localization

Table 2. Localized subpulse intensity vs. the incident pulse duration for the peak input intensity $|A(z, 0)|^2 = 1$. $\varepsilon_1 = (2.3)^2$, $\varepsilon_2 = 1$, $\varepsilon_3 = (1.3)^2$, $N_{str} = 7$, $\Omega = 2.14$, $\beta = -6.73$, $D = -0.037$, $\alpha_1 = -5$, and $\alpha_2 = 5$

Incident pulse duration a	Localized subpulse intensity (number of PC layer; fraction of the initial pulse energy)
10	3 (eighth layer; 20%)
6	1.5 (eighth layer; 22%)
4	No localization

LOCALIZATION OF THE PULSE TRAIN ENERGY

Computer simulation was performed for a wide range of dimensionless parameters, specifically, for $\varepsilon_1 = (2.3)^2$, $\varepsilon_2 = 1$, $\varepsilon_3 = (1.3)^2$, $N_{str} = 7$, $\Omega = 1.88$, $\beta = -5.92$, $D = -0.042$, $\alpha_1 = -5$, and $\alpha_2 = 5$. The pulse repetition period Δt (in our case, $\Delta t = 20$) is taken such that the reflected and transmitted parts of the energy of a previous pulse have traveled a considerable distance before the next pulse arrives at the crystal. Under these conditions, the influence of the previous pulse on the process is negligible. At this time, the complex amplitude in the regions before and behind the PC are set equal to zero and a next pulse defined by (6) and (7) is specified. For clearness, the inset to Fig. 2 shows the initial distribution of the pulse intensity over the region before the PC, which was set discretely at time instants $t = p\Delta t$, where p is an integer and $0 \le p \le 3$.

The effect is demonstrated in Fig. 2, which plots the time evolution of the fraction of the energy localized in the second, fourth, sixth, and eighth layers. It is seen that a part of the energy of the first pulse localizes in the second and fourth layers (19 and 9% of its total energy, respectively). In odd layers (with defocusing nonlinearity), localization is absent and the radiation leaves them after a time. Note that the early sign of energy localization in a layer is the appearance of an intense subpulse (with a peak intensity higher than 1), which propagates in the layer via reflections from adjacent layers. Figure 2 also supports the above conclusion that there is a threshold energy above which this subpulse may appear and, hence, energy localization may take place. In the fourth and sixth layers, localization starts from 9% of the initial energy and one subpulse appears in the layer. In the second layer, 19% of the first-pulse energy are localized and two subpulses arise with their peak intensities differing by a factor of five (3 and 0.6, respectively).

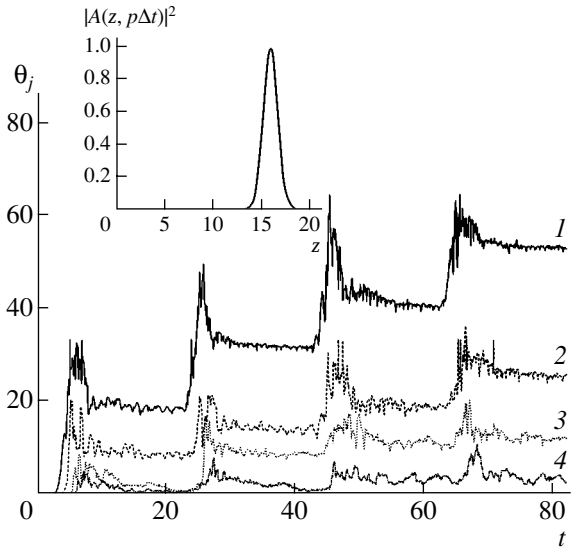

Fig. 2. Time evolution of the energy fraction localized in the (*1*) second, (*2*) fourth, (*3*) sixth, and (*4*) eighth layers. The inset shows the initial intensity distribution for one of four successive pulses separated by Δt dimensionless units.

In the case of the second pulse, which arrives at the PC within the time Δt, 13, 5, and 9% of its energy are localized in the second, fourth, and sixth layers, respectively. Generally speaking, the following pulses may either increase the number of subpulses inside the layers (the subpulses usually differ in both peak intensity and propagation velocity in the layer) or enhance the intensity of already existing subpulses. For example, after the second pulse has been incident on the PC, two subpulses remain in the second layer but their amplitudes become almost the same ($\max|A|^2 \approx 4.5$); in the forth layer, the second subpulse arises with its intensity more than half as much as that of the first one (1.8 and 0.8, respectively); and in the sixth layer, the first subpulse appears, which concentrates 9% of the initial energy of the second incident pulse.

The third pulse incident on the PC still further increases the peak intensity of subpulses in the second layer (to 10 and 5, respectively) and in the fourth layer (to 2 for both subpulses). Finally, the fourth incident pulse gives rise to one more subpulse in the second layer. As a result, the intensities of the three subpulses in the second layer become equal to 11, 5, and 2.5, respectively. The intensities of subpulses in the fourth layer grow to 3.5 and 2, respectively, and the intensity of the subpulse in the sixth layer rises to 2.5. Note that, for a certain intensity of the incident pulse, the subpulse intensity in a nonlinear layer may increase by more than one order of magnitude, causing the "breakdown" (fracture) of the PC. Such conditions can be realized in experiments.

In some of the energy-localizing layers (in our case, in the second one), two subpulses propagating with close velocities merge into one with a higher intensity and proportionally lower velocity. This phenomenon is observed when the subpulses approach the next layer almost simultaneously.

It is worth noting that the energy localization in remote layers (in our case, the fourth, sixth, eighth, etc.) depends not only on the incident pulse energy but also on the time the pulse is incident on the PC. The energy of an incident pulse reaches, e.g., the second layer if it falls on the left-hand boundary of the second layer at the time any subpulse localized within this layer either approaches this boundary or has just reflected from it. This subpulse interacts with incident radiation before it reaches the right-hand boundary. Therefore, the incident pulse and the subpulse must propagate in the same direction. Otherwise, when the incident pulse and the subpulse counterpropagate, the latter will capture the incident pulse if its energy in this layer exceeds the threshold. In other words, the incident energy will

either be partially distributed among the existing subpulses or give rise to a new subpulse.

CONCLUSIONS

We described the phenomenon of energy localization in a one-dimensional nonlinear photonic crystal irradiated by a train of femtosecond pulses and studied energy localization conditions. It is shown that this effect is of complex character and depends on the time a pulse acts on a given PC layer. Localization either gives rise to new subpulses or rises the intensity of those already localized in the PC.

Note that difference schemes used for simulating these effects must meet stringent demands. To obtain conservative estimates, the mesh must not only be fine in the spatial coordinate (in order that short high-intensity subpulses in the layers be simulated correctly) but also have small time steps. Furthermore, more stringent requirements should be imposed upon the iteration procedure, which is also associated with high pulse intensities.

Experimentally, the localization effect may be detected several ways, e.g., by measuring the transmitted and reflected energies as functions of the incident pulse duration or intensity. From the dependences thus obtained, one can find the localized energy fraction. Another possibility is to detect PC fracture caused by successively applied pulses with an intensity one order of magnitude lower than the breakdown threshold. As was mentioned above, the intensity of localized subpulses may increase by a factor of 10 or more.

In our opinion, the effect of energy localization within a layer (or layers) of a nonlinear photonic crystal opens up possibilities of creating 3D optical memories. For example, a 3D optical disk may be made of a layered structure where layers with given optical properties (for example, linear and nonlinear layers) alternate in the direction of pulse propagation. In the transverse direction, the active part of the disk may contain alternating nonlinear (active) pits and pits whose optical properties are the same as those of preceding and following inactive layers. The resulting 3D structure will consist of "columns" of a layered periodical structure (one-dimensional photonic crystal). As follows from this paper, by applying a train of pulses, one may increase the localized energy to a desired degree, for example, to initiate chemical reactions. However, this issue calls for further investigation.

ACKNOWLEDGMENTS

This work is supported in part by the Russian Foundation for Basic Research (grant no. 02-01-727).

REFERENCES

1. Yu. S. Kivshar and D. E. Pelinovsky, Phys. Rep. **331**, 117 (2000).
2. M. Scalora, F. P. Dowling, G. M. Bowden, and M. J. Blomer, Phys. Rev. Lett. **73**, 1368 (1994).
3. V. A. Trofimov, Zh. Vychisl. Mat. Mat. Fiz. **41**, 1458 (2001).
4. V. A. Trofimov, E. B. Tereshin, and M. V. Fedotov, Zh. Vychisl. Mat. Mat. Fiz. **43**, 1550 (2003).
5. Yu. S. Kivshar, P. G. Kervekidis, and S. Takeno, Phys. Lett. A **307**, 281 (2003).
6. A. V. Balakin, B. V. Bushuev, B. I. Mantzyzov, *et al.*, Phys. Rev. E **63**, 046609 (2001).

Translated by A. Sidorova

Technical Physics, Vol. 49, No. 5, 2004, pp. 592–597. Translated from Zhurnal Tekhnicheskoĭ Fiziki, Vol. 74, No. 5, 2004, pp. 71–76.

OPTICS, QUANTUM ELECTRONICS

Terahertz Oscillator with Vertical Radiation Extraction

Yu. A. Morozov*, I. S. Nefedov*, and V. Ya. Aleshkin**

** Institute of Radio Engineering and Electronics (Saratov Branch), Russian Academy of Sciences, Saratov, 410019 Russia*

e-mail: mor@ire.san.ru

*** Institute of Physics of Microstructures, Russian Academy of Sciences, Nizhni Novgorod, 603600 Russia*

e-mail: aleshkin@ipm.sci-nnov.ru

Received June 10, 2003

Abstract—A model of a laser that uses the GaAs/$Al_yGa_{1-y}As$ lattice nonlinearity to lase in the terahertz range is proposed. The laser mixes two-frequency near-IR oscillations in a vertical (i.e., arranged across the structure layers) Bragg cavity. The cw output at a wavelength of 10 μm may reach 0.5 to 5 μW. © *2004 MAIK "Nauka/Interperiodica".*

INTRODUCTION

Quantum-well cascade lasers (QCLs) are today prominent among optical oscillators operating in middle and far infrareds [1–4]. Of the most important achievements in this field, a QCL with a peak output of about 0.5 W at a wavelength of about 9 μm at room temperature stands out [1]. In the cw mode, this laser operates at temperatures below 140 K. In [2], a QCL that, when cooled, operates at a wavelength of 17 μm and has a peak power on the order of 10 mW was studied. Köhler *et al.* [3] penetrated deeper into the IR range toward longer wavelengths with their QCL, which offers a peak power of about 1 mW at 4.5 THz under helium temperatures. Finally, a QCL with an output of 10 mW in the cw mode at room temperature was studied in [4].

Although the potentialities of the known lasing mechanisms, which have provided a great step forward in developing IR QCLs, have by no means been exhausted, researchers are looking for new approaches that would allow them to devise new sources of radiation in this as yet poorly understood frequency range. Research in this field is dictated by the need for compact semiconductor sources of coherence radiation with a wavelength from 5 to 50 μm, which may find application in spectroscopy, astronomy, and medicine. Among alternatives to the mechanisms underlying the QCL operation (amplification due to intersubband transitions and carrier tunneling under a high electric field), we may point out nonlinear frequency conversion in semiconductor structures that is due to lattice [5] or electron nonlinearity. The latter effect appears in the three-level model of quantum well [6]. It was also suggested that two-frequency lasing be used in devices such as a coupled-cavity laser with vertical extraction of radiation [7, 8]. Such a design implies that mid- or far-IR radiation is generated via external nonlinear conversion.

In our opinion, a still more promising approach is one where two-frequency lasing and nonlinear frequency conversion, which provide the difference-frequency harmonic, are integrated in one cavity [5, 6]. Unlike QCLs, whose quantum-well structure is very complex in order to match the wave functions of carriers in each of the cascades, nonlinear conversion requires simple and inexpensive hardware. Since the electric field amplitude in the cavity may be as high as 10^4–5×10^4 V/cm and the nonlinear susceptibility tensor components, for example, for GaAs are $\approx 2 \times 10^{-8}$ cm/V, the nonlinear polarization in the cavity becomes significant and, according to [5], sufficient for terahertz lasing with an output feasible for applications. Additionally [6], unlike the lasing mechanism in QCLs, lasing due to nonlinear frequency conversion is thresholdless, which is particularly important for advancing into the long-wavelength infrared range, where Drude free-carrier absorption makes a major contribution to wave attenuation. This means that absorption losses during nonlinear conversion reduce the output power but do not quench lasing as in QCLs.

In this paper, we analyze the possibility of mid-IR lasing in a vertical-cavity semiconductor laser via mixing of two-frequency radiation on lattice nonlinearity. To date, attempts have been made to create a vertical-cavity laser where lattice nonlinearity was used to generate the second harmonic in the visible range (see, e.g., [9]). However, as far as we know, generation of the difference-frequency terahertz harmonic in such devices has not been discussed in the literature.

LASER MODEL, EIGENVALUES, AND EIGENFUNCTIONS

A model of a laser cavity with vertical extraction of the difference-frequency mode and high-frequency modes is shown in Fig. 1. Quantum-size

1063-7842/04/4905-0592$26.00 © 2004 MAIK "Nauka/Interperiodica"

$In_xGa_{1-x}As/GaAs$ active layers, which lase at wavelengths of about 1 μm, are separated by an $Al_yGa_{1-y}As$ spacer of thickness d_3 roughly equal to $\lambda_{mid}/4n_3(\lambda_{mid})$, where λ_{mid} is the middle wavelength between the wavelengths λ_1 and λ_2 of high-frequency laser modes. It is clear that each of the active layers is at the node of the "foreign" field, i.e., the field amplified by another active layer. Such a configuration is bound to reduce competition between the modes at wavelengths λ_1 and λ_2 as much as possible. The upper and lower Bragg reflectors (BRs) are made of alternate GaAs and AlAs layers with thicknesses intended for operation at a mid-wavelength λ_{mid}. An oxide window limits the pump current and optical fields across the laser structure. The layers with the thicknesses d_1, d_2, and d_3 and also the Bragg reflectors, which constitute the cavity and contribute mostly to the nonlinear polarization, will be referred to as nonlinear conversion layers.

Preliminary study has shown that the output of the difference harmonic is reasonable when the diameter of the oxide window is much greater than the related wavelength. Therefore, the characteristics of the laser can be analyzed with a good accuracy in the approximation of a plane uniform wave propagating normally to the layers of the structure; i.e., the boundedness of optical fields in the transverse direction is ignored.

The parameters of the cavity were determined as follows.

First, given the wavelength λ_1, the geometry of the lower and upper BRs, and the thicknesses of both active layers and of the oxide layer, we calculated the "eigenthickness" d_1 of that nonlinear conversion layer adjacent to the lower reflector. That is, the electromagnetic problem was solved for eigenvalues under given conditions at the cavity boundaries. The thickness d_2 of the nonlinear conversion layer between the second active layer and upper BR was calculated as $d_2 = d_1 - (d_3 + d_a)$. This condition places the lower active layer at the geometric center of the cavity (d_a is the thickness of the active layers). With these geometrical dimensions of the structure, the mode with wavelength λ_1 belongs to the cavity eigenmode spectrum.

By solving the eigenvalue problem again for the cavity geometry found at the previous stage, we determined the resonant wavelength λ_{2_0} in the vicinity of the wavelength λ_2 specified initially (note that the modes with the wavelengths λ_1 and λ_{2_0} must belong to the BR reflection band). The cavity eigenfunction corresponding to the eigenvalue λ_{2_0} has a maximum in the plane of the second active layer.

The eigenfunctions calculated as a function of the longitudinal coordinate are shown in Fig. 2. Here, $\lambda_1 = 0.96$ μm and $\lambda_{2_0} = 1.0367$ μm; hence, $\lambda_{cav} = \lambda_1\lambda_{2_0}/(\lambda_{2_0} - \lambda_1) = 12.976$ μm. The cavity length (the spacing between the BRs) is about $3\lambda_1/n(\lambda_1)$ or $2.5\lambda_{2_0}/n(\lambda_{2_0})$. The material dispersion in the nonlinear conversion layers and BRs was found from formulas given in [10]. The upper and lower reflectors consist of 30 pairs of layers. The abscissa axis originates at the middle of the upper active layer. As was noted above, the maximum of the field at the wavelength l_1 is roughly coincident with the plane of the first active layer, while the maximum of the electric field at the wavelength λ_{2_0} is in the middle of the second layer.

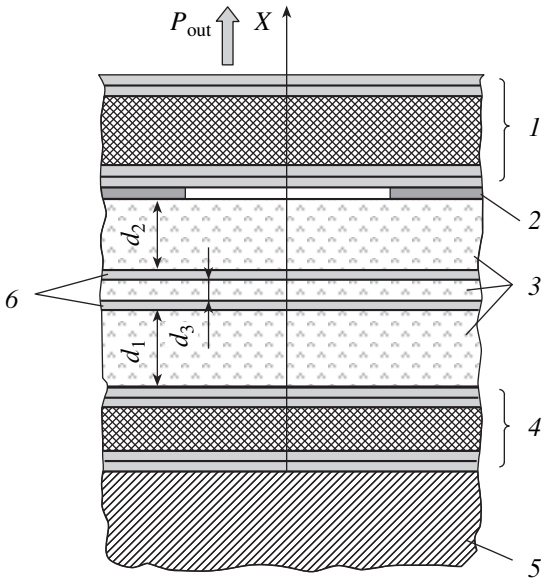

Fig. 1. Model of the laser structure: (*1*, *4*) upper and lower BRs, respectively; (*2*) oxide aperture; (*3*) nonlinear conversion layers; (*5*) substrate; and (*6*) active layers.

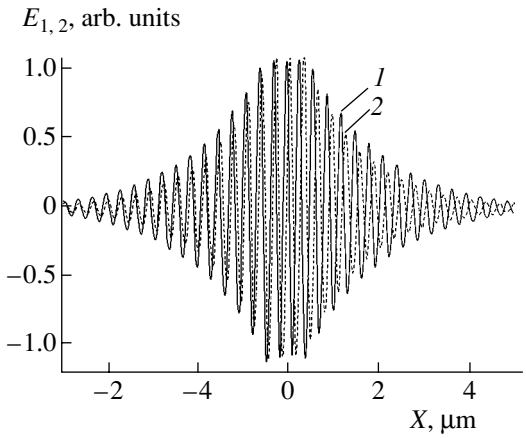

Fig. 2. Eigenfunctions of the modes with the wavelength (*1*) λ_1 and (*2*) λ_{2_0}.

BASIC RELATIONSHIPS

It is known that the zinc blende structure is such that films grown on its (100) crystallographic plane are

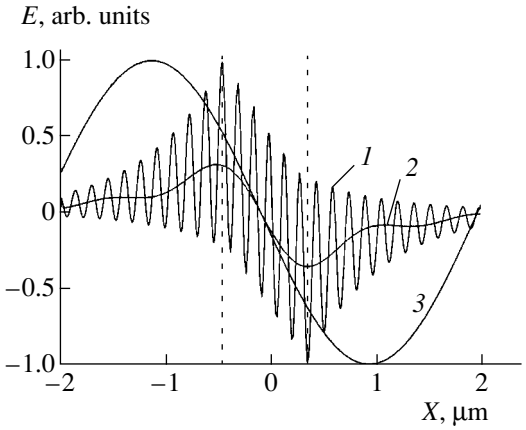

Fig. 3. Distribution of (*1*) the nonlinear polarization and (*2*) its envelope over the length of the cavity. Curve *3* shows the "frozen" pattern of the difference-frequency electric field for comparing the longitudinal scales. The dotted lines indicate the BR inner boundaries.

inappropriate for nonlinear lattice conversion when waves propagate normally to the growth plane. Theoretically, the (211) plane would provide a maximum conversion (see, e.g., [9]). However, publications are scarce in which good vertical-cavity lasing structures grown on the (211) substrate were reported. Generation of the second harmonic in the visible part of the spectrum by vertically emitting lasers grown on the oblique (311) substrate was studied in [9, 11]. Therefore, we will assume that the lasing structure considered here is grown on the (311) substrate.

It is easy to check that the nonlinear polarization modulus for copolarized high-frequency components in semiconductors is $\mathfrak{p} = 2\chi\varepsilon_0 d_{14} E^{(1)} E^{(2)}$. Here, $E^{(1)}$ and $E^{(2)}$ are the amplitudes of high-frequency components (i.e., the modes with the wavelengths λ_1 and λ_{2_0}, respectively), d_{14} is the element of the nonlinear susceptibility tensor (about 2×10^{-8} cm/V for GaAs), $\chi = 27/(11\sqrt{22}) \approx 0.523$, and ε_0 is the permittivity. The polarization vector $\vec{\mathfrak{p}}$ is coplanar with the polarizations of the high-frequency optical fields.

The theory of wave-guiding structures excited by impressed currents [12] yields the following expression for the power density at the difference frequency:

$$\frac{P_{\text{out}}}{S} = \frac{1}{8\rho_0 n(\lambda_{\text{cav}})} \times \left[\frac{4\pi\chi}{\lambda_{\text{cav}}} E_0^{(1)} E_0^{(2)} \left| \int_l d_{14}\psi_1\psi_2 e^{-j\beta_{\text{cav}}x} dx \right| \right]^2. \quad (1)$$

Here, the high-frequency fields are represented as $\mathbf{E}^{(1,2)} = \mathbf{E}_0^{(1,2)} \psi_{1,2}(x)$ are the field amplitudes in the first and second quantum wells, respectively), $n(\lambda_{\text{cav}})$ and β_{cav} are the cavity-averaged refractive index and propagation constant at the difference frequency, $\rho_0 = 120\pi$, and Ω is the wave impedance of free space.

As follows from Eq. (1), the output depends largely on the overlap integral of the normalized nonlinear polarization $\psi_1(x)\psi_2(x)$ and electric field intensity at the difference frequency, which varies as $\exp(-j\beta_{\text{cav}}x)$. The variation of these functions along the longitudinal coordinate is illustrated in Fig. 3. From general considerations, it follows that the standing wave of nonlinear polarization (curve *1*) may excite waves both at the difference and the summary frequencies. The summary-frequency mode is associated with the rapidly varying component of the polarization; the difference-frequency one, with the polarization envelope. The envelope, derived by filtering out the rapidly oscillating polarization component, is shown in Fig. 3 (curve *2*). For the lasing structure considered, the maxima of the envelope lie near the BR inner boundaries (shown by the dotted lines in Fig. 3). Curve *3* describes the intensity of the difference-frequency field. Clearly, the interaction conditions in such a cavity are not optimal for maximizing the overlap integral. Theoretically, this integral reaches a maximum value when the BR spacing is increased to about half the wavelength of the nonlinear polarization envelope. However, such an extension of the cavity raises total losses due to absorption by free carriers. More detailed analysis of the contributions of these mechanisms to the lasing efficiency at the difference frequency will be the subject of subsequent investigation.

The field amplitudes in the active layers are related to the laser parameters through the rate equation for carrier concentration (see, e.g., [13]):

$$\frac{J}{ed_{\text{a}}} = \frac{N_{\text{th}_i}}{\tau_{\text{N}}} + BN_{\text{th}_i}^2 + CN_{\text{th}_i}^3 + g(N_{\text{th}_i})c\frac{n_{\text{a}}\varepsilon_0 \left|\mathbf{E}_0^{(i)}\right|^2}{2hf_i}; \quad i = 1, 2.$$

Here, J is the density of the pump current; e is the elementary charge; N_{th_i}, $g(N_{\text{th}_i}) = g_0 \ln(N_{\text{th}_i}/N_0)$, and hf_i are the threshold carrier concentration, gain, and photon energy, respectively in an ith layer; c is the velocity of light; n_{a} is the refractive index of the layer; τ_{N} is the lifetime at nonradiative recombination; B and C are the coefficients of radiative and Auger recombination, respectively; and N_0 is the antireflection carrier concentration.

In the framework of our approximation, it is natural to assume that the current is uniformly distributed over the cross section and neglect carrier diffusion. We introduce normalized quantities $\nu_{\text{th}} = N_{\text{th}}/N_0$ and $G_{\text{th}} =$

$g(N_{th})/g_0$ for the squared field amplitudes in the wells to obtain

$$\left|\mathbf{E}_0^{(i)}\right|^2 = D(\nu_{th_i} + \gamma\nu_{th_i}^2 + \delta\nu_{th_i}^3)\frac{1}{G_{th_i}n_a\lambda_i}\left(\frac{J}{J_{th_i}} - 1\right), \quad (2).$$

where $D = 2hcN_0\rho_0/(g_0\tau_N)$, $\gamma = BN_0\tau_N$, $\delta = CN_0^2\tau_N$, and J_{th_i} is the threshold current in an *i*th active layer.

Expression (1) can thus be recast in the form more convenient for calculations:

$$\frac{P_{out}}{S} = \frac{1}{8\rho_0 n(\lambda_{cav})}\left[\frac{4\pi\chi}{\lambda_{cav}n_a}D\left|\int_l d_{14}\psi_1\psi_2 e^{-j\beta_{cav}x}dx\right|\right]^2$$
$$\times\frac{(\nu_{th_1} + \gamma\nu_{th_1}^2 + \delta\nu_{th_1}^3)}{G_{th_1}\lambda_1}\frac{(\nu_{th_2} + \gamma\nu_{th_2}^2 + \delta\nu_{th_2}^3)}{G_{th_2}\lambda_{2_0}} \quad (3)$$
$$\times\left(\frac{J}{J_{th_1}} - 1\right)\left(\frac{J}{J_{th_2}} - 1\right).$$

To calculate the threshold gains G_{th_i}, we specified radiation conditions (reflection coefficients) at the BR–air interfaces and the damping constant in each of the layers. In this case, a solution to an eigenvalue problem that is similar to those discussed above takes a complex value, with one of its parts (real or imaginary) being a solution in the absence of losses, while the other allows one to find the gain at the lasing threshold. We assumed that the frequency dependence of the gain in an *i*th active layer is similar to that in a Lorentzian contour:

$$G_i(\lambda) = G_{i_0}\left[1 + \left(2\frac{\lambda - \lambda_i}{\Delta\lambda_{g_i}}\right)^2\right]^{-1},$$

where G_{i_0} is the maximum gain and $\Delta\lambda_{g_i}$ is the amplification bandwidth.

Using the relationship between the electric field and output at the upper BR–air interface, we obtain the following expression for the output power density at the high-frequency modes:

$$\frac{P_i}{S} = D'(\nu_{th_i} + \gamma\nu_{th_i}^2 + \delta\nu_{th_i}^3)$$
$$\times\frac{1}{G_{th_i}n_a\lambda_i}(e_b^{(i)})^2\left(\frac{J}{J_{th_i}} - 1\right). \quad (4)$$

In this expression, $D' = hcN_0/(g_0\tau_N)$ and $e_b^{(i)} = |\mathbf{E}_b^{(i)}|/|\mathbf{E}_0^{(i)}|$ is the ratio of the electric field amplitudes at the emitting boundary and in an *i*th active layer.

RESULTS OF CALCULATION

The analysis of the oscillator was performed for the parameter values listed in Table 1. Thermal effects due to the current passing through the structure were neglected.

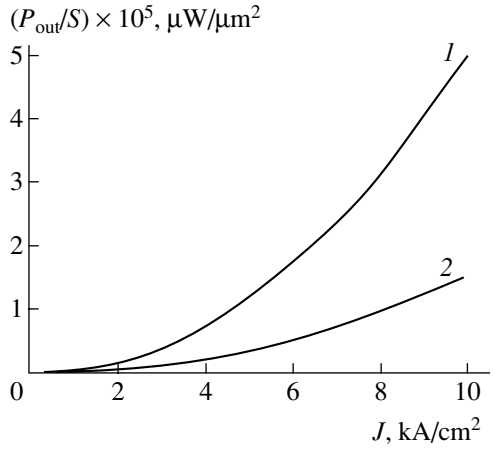

Fig. 4. Output density at the difference frequency for the damping constant α_{mid} = (*1*) 5 and (*2*) 10 cm^{-1}.

Figure 4 illustrates the dependence of the power density at the difference-frequency mode on the pump current. The cavity-length-averaged damping constant for high-frequency modes, $\alpha_{mid} \approx \alpha_{1,2}$, is taken as a parameter. From the experimentally found parameters of the materials used in the laser structure [9, 10, 14], it follows that the value $\alpha_{mid} \approx 5$ cm^{-1} is reached when the upper (lower) BR has an acceptor (donor) concentration of up to 1×10^{18} cm^{-3} and the nonlinear conversion layers (NCLs) are doped to 3×10^{17} cm^{-3}. When the degree of doping in all the layers increases twofold, α_{mid} changes in proportion. In the mid-IR range, the attenuation of a wave passing through a doped semiconductor is known to be associated mainly with losses due to free-carrier absorption [10, 14, 15]. These losses can be estimated using the expression for the permittiv-

Table 1. Structure parameters

Parameter	Value
Midwavelength λ_{mid}, μm	1
active layer thickness d_a, μm	0.03
Element d_{14} of nonlinear susceptibility tensor, cm/V	1.7×10^{-8} (GaAs [9]) 0.39×10^{-8} (AlAs [9])
Carrier lifetime τ_N, ns	5
Gain g_0, cm^{-1}	2000
"Transparent" carrier concentration N_0, cm^{-3}	1.5×10^{18}
Radiative recombination coefficient B, cm^3/s	10^{-10}
Auger recombination coefficient C, cm^6/s	3.5×10^{-30}
Amplification bandwidth $\Delta\lambda_g$, μm	0.1

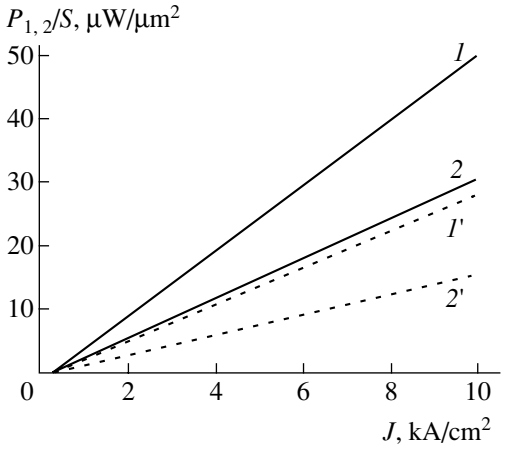

Fig. 5. Effect of the distributed losses on the output density of the high-frequency components. α_{mid} = (*1*, *1*') 5 and (*2*, *2*') 10 cm^{-1}.

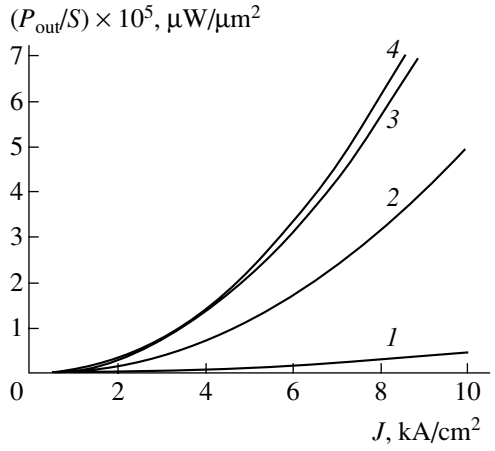

Fig. 6. Effect of the BR reflection coefficient (number of periods) on the output density at the difference frequency: (*1*) 20, (*2*) 30, (*3*) 40, and (*4*) 50 periods.

ity (see, e.g., [14]). The wave damping constants $\alpha_{cav} = 2\mathrm{Im}(\beta_{cav})$ at the difference frequency that were calculated as a function of the carrier concentration in the layers are summarized in Table 2.

Figure 4 shows that, at moderate losses in the cavity, the power nonlinearly converted to the difference-frequency mode ranges from 0.5 to 5 μW for a cross-sectional area of the laser structure of 10^4–10^5 μm². Note that the attenuation affects the difference-frequency harmonic power twofold. First, for a given laser geometry, a decrease in the attenuation factor at wavelengths λ_1 and λ_{2_0} reduces the threshold currents and thereby enhances the electric field in the Bragg cavity. Additionally, as α_{cav} decreases, the overlap integral for the eigenfunctions of the cavity and the difference-frequency mode grows (see expression (3)). These two mechanisms in combination cause the power emitted at the difference frequency to rise.

Table 2. Damping constant for the difference-frequency wave in the laser structure

Material	Carrier concentration, 10^{18} cm^{-3}	α_{cav}, cm^{-1}
p-GaAs	1	100
(BR)	2	230
p-AlAs	1	120
(BR)	2	290
p-$Al_{0.2}Ga_{0.8}As$	0.3	20
(NCL)	0.6	50
n-$Al_{0.2}Ga_{0.8}As$	0.3	130
(NCL)	0.6	330
n-GaAs	1	200
(BR)	2	570
n-AlAs	1	650
(BR)	2	1400

Figure 5 compares the powers of the high-frequency modes (high-frequency sources) with the power obtained as a result of their nonlinear mixing. The output of the high-frequency modes is seen to be roughly six orders of magnitude greater than the power of the difference-frequency mode (the calculations were performed for a cavity bounded by BRs each consisting of 30 pairs of alternating layers). The solid lines show the power density at the wavelength λ_1; the dashed lines, at the wavelength λ_{2_0}. The difference between the curves taken at the same damping constant results from the difference between the BR reflection coefficients for these waves. This is because λ_1 and λ_{2_0} lie asymmetrically about the center frequency of the reflection band.

The effect of the number of BR periods on the power density at the difference frequency is illustrated in Fig. 6 (α_{mid} = 5 cm^{-1}). The output of the difference-frequency mode saturates when the BRs contain more than 40 pairs of layers, since the losses in the cavity saturate in this case. On the one hand, the external (radiation) losses decline with increasing reflection coefficient. On the other hand, extra layers in the BRs enhance the dissipation of the high-frequency mode power inside the cavity. The net effect is the saturation of the threshold currents, which limits the electric fields giving rise to nonlinear polarization.

CONCLUSIONS

A model of a vertical-cavity laser that lases in the terahertz range via mixing of two-frequency near-IR radiation on lattice nonlinearity is proposed.

The eigenvalues and eigenfunctions of a Bragg cavity for high-frequency modes are calculated under the assumption that the structure is infinite in the transverse

direction. Relationships for the power density of the modes at the frequencies being mixed and at the difference frequency are obtained.

The output at the difference frequency is studied as a function of the number of layers (of the reflection coefficient) constituting the BR structure. It is shown that, as the BR reflection coefficient increases, the output first grows and then saturates. When the damping constant of the high-frequency modes is $\alpha_{mid} = 5$ cm^{-1}, saturation is observed for the cavity bounded by reflectors consisting of about 40 pairs of layers.

The effect of losses due to free-carrier absorption and to high-frequency radiation on the output of the laser is analyzed. For an emitting surface area of 10^4–10^5 μm^2, it is shown that the power emitted at the difference frequency may reach 0.5–5.0 μW. According to our estimates, this value may be significantly (several tens of times) increased if a resonant structure for the difference-frequency mode is provided. This is a subject of further investigation.

ACKNOWLEDGMENTS

This work was supported by the Russian Foundation for Basic Research (project no. F02R-095), the Belarussian Foundation for Basic Research (grant no. 02-02-81036), the program "Low-Dimensional Quantum Structures" of the Presidium of the Russian Academy of Sciences, the program "Semiconductor Lasers" of the Russian Academy of Sciences, and ISTC (project no. 2293).

REFERENCES

1. A. Matlis, S. Sivken, A. Tahraoui, *et al.*, Appl. Phys. Lett. **77**, 1741 (2000).
2. A. Tredicucci, C. Gmachl, F. Capasso, *et al.*, Appl. Phys. Lett. **76**, 2164 (2000).
3. R. Köhler, A. Tredicucci, F. Beltram, *et al.*, Nature **417**, 156 (2002).
4. J. Faist, D. Hofstetter, M. Beck, *et al.*, IEEE J. Quantum Electron. **38**, 533 (2002).
5. V. Ya. Aleshkin, A. A. Afonenko, and N. B. Zvonkov, Fiz. Tekh. Poluprovodn. (St. Petersburg) **35**, 1256 (2001) [Semiconductors **35**, 1203 (2001)].
6. A. Belyanin, F. Capasso, V. Kocharovsky, *et al.*, Phys. Rev. A **63**, 53803 (2001).
7. L. Chusseau, G. Almuneau, L. Coldren, *et al.*, IEE Proc.: Optoelectron., Special Issue **149**, 88 (2002).
8. M. Brunner, K. Gulden, R. Hovel, *et al.*, IEEE Photonics Technol. Lett. **12**, 1316 (2000).
9. Y. Kaneko, S. Nakagawa, Y. Ichimura, *et al.*, J. Appl. Phys. **87**, 1597 (2000).
10. S. Adachi, J. Appl. Phys. **58**, R1 (1985).
11. N. Yamada, Y. Kaneko, S. Nakagawa, *et al.*, Appl. Phys. Lett. **68**, 1895 (1996).
12. B. Z. Katsenelenbaum, *High-Frequency Electrodynamics* (Nauka, Moscow, 1966) [in Russian].
13. G. Hadley, K. Lear, M. Warren, *et al.*, IEEE J. Quantum Electron. **32**, 607 (1996).
14. J. Blakemore, J. Appl. Phys. **53**, R123 (1982).
15. *Guided-Wave Optoelectronics*, Ed. by T. Tamir (Springer-Verlag, Berlin, 1990; Mir, Moscow, 1991).

Translated by A. Khzmalyan

Technical Physics, Vol. 49, No. 5, 2004, pp. 598–602. Translated from Zhurnal Tekhnicheskoĭ Fiziki, Vol. 74, No. 5, 2004, pp. 77–82.

OPTICS, QUANTUM ELECTRONICS

Multilayer Structures with Magnetically Controlled Light Transmission

D. G. Makarov, V. V. Danilov, and V. F. Kovalenko

Shevchenko National University, ul. Glushkova 6, Kiev, 01033 Ukraine

e-mail: lab124@univ.kiev.ua

Received June 30, 2003

Abstract—Taking into account the gyromagnetic properties of multilayer two-component structures of which one or both components are magnetoactive materials shows that their optical properties can be controlled by an external magnetic field. In particular, when applied to multilayer structures with a phase shift (defect), the magnetic field changes (decreases or increases) the width of the spectral resonance curve of the transmission coefficient. The application of longitudinal and transverse (relative to the light propagation direction) magnetic fields gives different results. Analysis shows that the effects observed may find application, for example, in fiber optics. © *2004 MAIK "Nauka/Interperiodica".*

INTRODUCTION

Control of optical properties of various media has attracted considerable attention in recent years. These investigations have led to the development of materials that suppress light propagation or transmit radiation of a certain wavelength. One example of such materials is the multilayer structures described in [1, 2].

Periodic structures of this type may be used as distributed Bragg gratings to produce feedback in semiconductor lasers [3] and also as photonic, phononic, or magnonic crystals [2, 4–8] that have an energy band forbidden for transmission of light with a particular wavelength. These multilayer structures may consist of several magnetic layers or of alternating magnetic and nonmagnetic layers. Among the former are structures exhibiting the giant magnetoresistance effect [9] and magnetic reflectors based on the Kerr magnetooptic effect [10]. The introduction of an additional magnetic (or nonmagnetic) layer (defect) into the structure that disturbs the layer sequence makes resonance transmission at a certain wavelength possible. The parameters of such a transmission depend on the position, dimension, and material of the defect [5–7].

The spectrum of radiation transmitted through these multilayer structures is characterized by forbidden energy bands. It should be noted that light transmission through such materials may be accompanied by the Faraday, Cotton–Mouton, and Kerr magnetooptic effects [11, 12]. The multilayer structures studied and used in practice are usually several tens of micrometers in size; therefore, radiation damping may be disregarded.

It is common practice [2, 4–6] to study multilayer structures with magnetic layers by exposing them to a permanent magnetic field. This field switches the magnetization of the magnetic layer (layers) or carries it (them) to the state of saturation.

The aim of our study is to trace the variation of the transmission spectrum taken from multilayer two-component structures with a phase shift that are placed in a variable magnetic field.

The study was performed with regard to the gyromagnetic properties of the magnetic component of the structure. Such an approach is correct in a certain material-dependent wavelength range. For example, it is correct if iron garnet (IG) is taken as a magnetic component of the multilayer structure and the radiation wavelength is $\lambda = 1.5$ μm (this wavelength is at the transmission edge of most IGs). At the transmission edge in the near infrared, IGs are bigyrotropic media, where the off-diagonal components of the permittivity and permeability tensors almost equally contribute to the rotation of plane of polarization [11, 12]. For large λ ($\lambda \geq 5$ μm), IGs feature purely gyromagnetic properties. When measuring the permeability of IGs at optical frequencies [13–15], we took into consideration the fact that the gyroelectric contribution to magnetooptic effects may be minimized in the transmission range of IGs, i.e., far away from the absorption line of Fe^{3+} or rare-earth ions (the magnetooptic effects become wavelength-independent in this case).

Thus, the effect of magnetic field on both the permittivity and permeability tensors must be taken into account in order to describe properly the properties of multilayer structures with bigyrotropic magnetic layers. Changes associated with the permittivity tensor alone do not provide the adequate pattern of what is actually taking place. Therefore, studies [4–7], where the forbidden bands in magnetic photonic crystals were examined for specific materials and wavelengths, cannot be regarded as complete, since the gyromagnetic

1063-7842/04/4905-0598$26.00

properties of the materials were not considered. It seems therefore reasonable to combine the results obtained in [4–6] and in this work (where the effect of a magnetic field on the permeability tensor of the ferromagnetic components entering into the multilayer structure is taken into account) in order to provide a better insight into the optical performance of a multilayer two-component structure incorporating magnetic and nonmagnetic insulating layers when it is subjected to an external magnetic field.

THEORY

The schematic of the structure is shown in Fig. 1a. Because of the periodic variation of the refractive index, radiation at a wavelength $\lambda \approx \lambda_0$ (λ_0 is the Bragg wavelength for a given structure) may arise if counterpropagating waves are coupled. Therefore, further analysis will be performed based on a solution to coupled wave equations. An important parameter in such a description is the coupling coefficient χ. When the refractive index varies periodically, the analytic expression for the coupling coefficient has the form

$$\chi = \frac{k_0^2}{2\beta N^2}\int \Delta n^2(x, z)E_y^2(x)dx,$$

where $E_y(z)$ is the distribution of the light wave electric field along the $0X$ direction and $k_0 = 2\pi/\lambda_0$. The integral is defined in the domain of periodic variation of the refractive index, and the normalizing factor (radiation intensity) is given by

$$N^2 = \int_{-\infty}^{\infty} E_y^2(x)dx.$$

Comparing the results for the coupling coefficient obtained when the refractive index varies harmonically and discretely (by a rectangular law), one can infer [3] that sufficiently accurate estimates can be made under the assumption that the refractive index varies harmonically:

$$n(z) = n_0 + \Delta n\cos(2\beta_0 z + \Omega), \quad (1)$$

where

$$\Delta n = \frac{n_2(H) - n_1(H)}{2}, \quad \beta_0 = \frac{m\pi}{\Lambda},$$

m is the grating order (we put $m = 1$), Λ is the period of variation of the refractive index, and Ω is the phase of the refractive index in the plane $z = 0$.

In this case, the coupling coefficient can be determined from the expression $\chi = \pi\Delta n/\lambda_0$. In a homogeneous Bragg waveguide, the reflection coefficient is known to have a maximum at $\lambda = \lambda_0$. In the case of transmission, one therefore should use a Bragg waveguide at the center of which the spatially modulated refractive coefficient experiences a phase shift

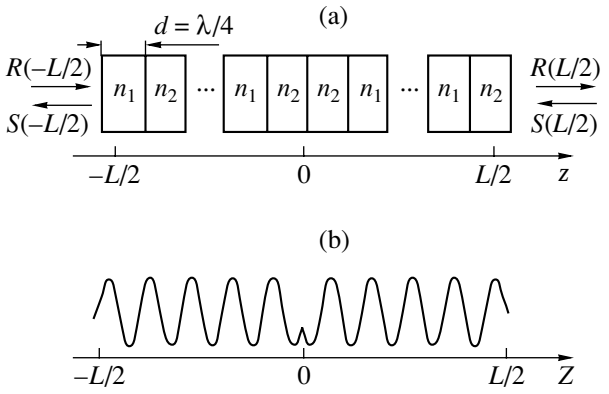

Fig. 1. (a) Multilayer two-component structure and (b) the refractive index profile of the structure with a phase shift.

(Fig. 1b). For $z < 0$ and $z \geq 0$, the refractive index varies according to (1).

As was noted above, because of the periodic variation of the refractive index, forward and backward waves of amplitudes $R(z)$ and $S(z)$, respectively, that propagate in the structure become coupled at $\lambda \approx \lambda_0$. These waves are described by the coupled wave equations

$$\begin{aligned} -\frac{dR}{dz} + (\alpha - j\delta\beta)R &= j\chi e^{-j\Omega}S, \\ \frac{dS}{dz} + (\alpha - j\delta\beta)S &= j\chi e^{-j\Omega}R, \end{aligned} \quad (2)$$

where χ is the coupling coefficient, α is the gain (attenuation), and $\delta\beta = \beta - \beta_0$.

Let us consider a solution to set (2) under the assumption that radiation of amplitude R_0 is incident on the left wall of the structure, $z = -L/2$. If reflection on both ends of the system is absent and the boundary conditions are $R(-L/2) = R_0$ and $S(L/2) = 0$, the solution to set (2) takes the form [3]

$$\begin{aligned} R(z) &= \frac{-\Gamma_1 e^{\gamma(z-L/2)} + \Gamma_2 e^{-\gamma(z-L/2)}}{\Gamma_2 e^{\gamma L} - \Gamma_1 e^{-\gamma L}}R_0, \\ S(z) &= \frac{-e^{\gamma(z-L/2)} + e^{-\gamma(z-L/2)}}{\Gamma_2 e^{\gamma L} - \Gamma_1 e^{-\gamma L}}j\chi R_0, \end{aligned} \quad (3)$$

where $\gamma = \sqrt{\chi^2 + (\alpha - j\delta\beta)^2}$, $\Gamma_1 = \gamma + \alpha - j\delta\beta$, and $\Gamma_2 = -\gamma + \alpha - j\delta\beta$.

Now it is easy to find desired relationships for a Bragg waveguide with a phase shift. Its properties are described with the coupled wave equations for the left-hand and right-hand parts in view of the boundary conditions

$$R(+0) = e^{-j\Omega}R(-0); \quad S(-0) = e^{-j\Omega}S(+0)$$

at $z = \pm 0$.

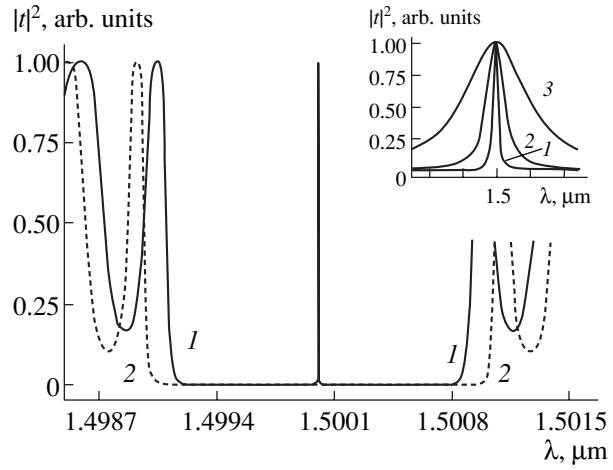

Fig. 2. Transmission coefficient vs. the wavelength of radiation incident on the multilayer structure. The depth of modulation δn_0 = (*1*) 0.0012, (*2*) 0.0010, and (*3*) 0.0008. The inset shows the enlarged vicinity the central peak for the same depths of modulation.

Then, the relative amplitude transmission coefficient for a wave passing through the multilayer structure [3] is given by

$$t \equiv \frac{R(L/2)}{R_0} = \frac{4\gamma^2 e^{-j\Omega}}{(\Gamma_1 e^{-\gamma L/2} - \Gamma_2 e^{\gamma L/2})^2 + \chi^2 e^{-j2\Omega}(e^{-\gamma L/2} - e^{\gamma L/2})^2}. \quad (4)$$

Figure 2 shows the wavelength dependence of the intensity transmission coefficient (hereafter, the transmission coefficient) or the spectral curve of transmission coefficient (hereafter, curve) $|t|^2 = f(\lambda)$. The depth of modulation of the refractive index $\delta n = (n_2 - n_1)/(n_2 + n_1)$ serves as a parameter. The curve $|t|^2 = f(\lambda)$ has a central peak and two side transmission bands. The inset to Fig. 2 shows the central maximum on an enlarged scale for several depths of modulation δn. A small change in δn is seen to greatly change the width $\delta\lambda$ of the central maximum. Hence, by varying the refractive index of one or both components of the structure, one can vary the curve $|t|^2 = f(\lambda)$.

It is known [11, 12] that the relative refractive index of a magnetoactive material changes when the material is placed in a magnetic field. In a gyromagnetic medium, the magnetic field dependence of the refractive index depends on the diagonal, μ_1, and off-diagonal, μ_a, components of the permeability tensor for a gyrotropic medium. They obey the relationships

$$\mu_1 = \frac{\omega_H(\omega_H + \omega_M) - \omega^2}{\omega_H^2 - \omega^2}, \quad \mu_a = \frac{\omega\omega_M}{\omega_H^2 - \omega^2},$$

where $\omega_M = \gamma_0 4\pi M(H)$, $\omega_H = \gamma_0 H$, $\omega = 2\pi c/\lambda$, $\gamma_0 = 2.8$ MHz/Oe, and H is the external field strength.

To simplify the final analytical relationship, we neglect second-order terms in an expansion in powers of $\omega_{M,H}/\omega$. This is valid for the optical range, where $\omega_{M,H}/\omega \ll 1$.

In this approximation, the variation of the relative refractive index with applied magnetic field H (the Faraday effect geometry) can be described as [16]

$$n^{\mathrm{F}} = \sqrt{\mu_1 \pm \mu_a} \approx 1 \pm \omega_M/(2\omega)$$

(the plus and minus signs refer to different senses of rotation of polarization of incident radiation). When the field is applied in the transverse direction (the Cotton–Mouton geometry), for the linearly polarized component that is normal to the field, we have

$$n_{\mathrm{tr}}^{\mathrm{CM}} = \sqrt{\mu_1 - \mu_1^{-1}\mu_a^2} \approx 1 - \frac{\omega_M(\omega_M + \omega_H)}{2\omega^2}.$$

If both components of a two-component structure are magnetoactive and characterized by the zero-field refractive index and parameter ω_M, the depth of modulation of the refractive index over the layers may be expressed as

$$\delta n = \frac{\Delta n(H)}{n_0} = \frac{n_2(H) - n_1(H)}{n_2(H) + n_1(H)} = \delta n_0[1 + (a_i\lambda)^i], \quad (5)$$

where $i = 1$ or 2 for the Faraday effect and Cotton–Mouton effect, respectively, and

$$\delta n_0 = \frac{n_2(H=0) - n_1(H=0)}{n_2(H=0) + n_1(H=0)}$$

is the depth of modulation of the zero-field refractive index Hereafter, we will use the designations $n_1(H = 0) = n_{10}$ and $n_2(H = 0) = n_{20}$).

The parameter a_i is a measure of interaction of the structure with the magnetic field configured in a particular way and is determined as follows:

for the Faraday effect,

$$a_1(H) = \frac{\pm\omega_{M1}n_{10} \mp \omega_{M2}n_{20}}{4\pi c(n_{20} - n_{10})};$$

for the Cotton–Mouton effect,

$$a_2^2(H) = \frac{\omega_{M1}n_{10}(\omega_{M1} + \omega_H) - \omega_{M2}n_{20}(\omega_{M2} + \omega_H)}{8\pi^2 c^2(n_{20} - n_{10})}. \quad (6)$$

Since δn depends on the applied magnetic field, magnetization of the layers, and incident radiation wavelength, one can expect that the parameters of the curve $|t|^2 = f(\lambda)$ (such as the amplitude, width, and the position of the peak) will also depend on the quantities listed.

The application of a magnetic field to the multilayer structure alters the width $\delta\lambda$ of the narrow central peak of the curve near λ_0. This change depends on the polar-

ization of incident radiation. The value of $\delta\lambda$ may be found from the transcendental equation

$$\frac{[4(\lambda_0/\lambda-1)^2-\delta n^2][\delta n^2-4(\lambda_0/\lambda-1)^2 ch\gamma(H)L]}{[\delta n^2-4(\lambda_0/\lambda-1)^2 ch\gamma(H)L]^2+4(\lambda_0/\lambda-1)^2[(\delta n^2-4(\lambda_0/\lambda-1)^2)sh^2\gamma(H)L]} = \pm\frac{1}{\sqrt{2}}. \quad (7)$$

The solution to Eq. (7) has two roots (λ_1 and λ_2), which define the width $\delta\lambda = |\lambda_2 - \lambda_1|$ of the central peak of the curve $|t|^2 = f(\lambda)$. As follows from Fig. 2, the actual value of $\delta\lambda$ is typically much smaller than that resulting from the calculation of the reflection coefficient for a homogeneous Bragg waveguide ($\Omega = 0$).

The orientation of the magnetic field relative to the radiation propagation direction may be chosen arbitrarily. It is therefore reasonable to see how the parameters of a multilayer structure with a phase shift ($\Omega = \pi/2$) vary when the field is applied longitudinally and transversely. Calculations were carried out for $\delta n_0 = 0.001$ and 0.0012, the number of layers $p = 10^4$, and $\lambda_0 = 1.5$ μm.

LONGITUDINAL APPLICATION OF THE MAGNETIC FIELD

When the field is applied in the longitudinal direction, one can judge the variation of the curve $|t|^2 = f(\lambda)$ using the magnetization $M(H)$ rather than the field strength H. This is because in this case the depth of modulation of the relative refractive index as a function of the wavelength and applied magnetic field has the form of (5),

$$\frac{\Delta n}{n_0}(H) = \delta n_0[1 + a_1(H)\lambda],$$

and dependence (6) for $a_1(H)$ implies that the controlling effect of the field on $a_1(H)$ shows up via the dependence $M(H)$ alone. It is this dependence that makes it possible to vary ω_M of the magnetoactive layer over certain limits and thus influence the parameters of the curve $|t|^2 = f(\lambda, H)$.

Let us analyze the variation of the width of the curve $|t|^2 = f(\lambda, H)$ with magnetization (Fig. 3) using the numerical solution to Eq. (7). If radiation passing through the structure has clockwise circular polarization, the resonance curve $|t|^2 = f(\lambda, H)$ narrows. If the radiation is polarized counterclockwise, the width $\delta\lambda$ of the curve $|t|^2 = f(\lambda, H)$ grows with increasing magnetization. It is seen that high values of $M(H)$ are necessary for $\delta\lambda$ to change significantly in the optical range.

It should be noted that the change in the width $\delta\lambda$ of the transmission curve goes in parallel with the change in the width of the basic band of the reflection curve (near the central peak of the curve $|t|^2 = f(\lambda, H)$). For example, in the case of radiation with clockwise circular polarization, the transmission curve narrows, while the reflection curve widens, as the magnetization increases and vice versa.

Taking into account the wavelength dependence of the relative refractive index, one could expect a change in the position of the central peak in the curve $|t|^2 = f(\lambda, H)$ when the multilayer structure is magnetized. However, since the dependence $\delta n = f(\lambda)$ is weak, the position of the central peak changes insignificantly in the magnetization range studied ($\leq 10^3$ G). Analytic relationships and transcendental equations that prove this statement are too awkward and are omitted here. Related plots may be obtained by numerically analyzing relationships (7).

TRANSVERSE APPLICATION OF THE MAGNETIC FIELD

In this case, the depth of modulation of the refractive index varies with magnetic field as (see (5))

$$\frac{\Delta n}{n_0}(H) = \delta n_0\{1 + [a_2(H)\lambda]^2\}.$$

From (6), it follows that the variation of $a_2(H)$ is due to the variation both of the magnetization $M(H)$ of the magnetoactive layer and of the external field H itself. Suppose that the magnetization $M(H)$ far exceeds the field H (for ferromagnets, such a supposition is valid). In this case, we can ignore the linear field dependence of a_2 and will consider only magnetization-related changes in the structure parameters.

When the field is applied in the transverse direction, the magnetization dependence of the width $\delta\lambda$ of the curve $|t|^2 = f(\lambda, H)$ (Fig. 4) obtained by numerically solving Eq. (7) shows that $\delta\lambda$ decreases as the magneti-

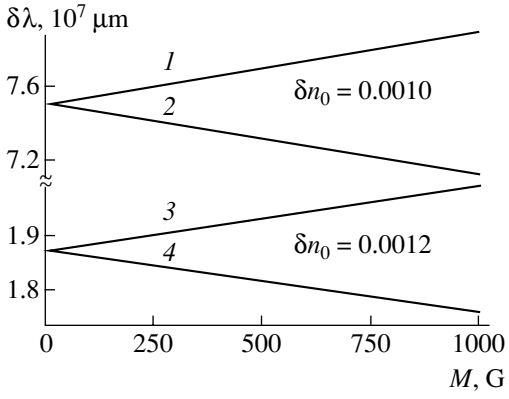

Fig. 3. Width $\delta\lambda$ of the curve $|t|^2 = f(\lambda, H)$ vs. the magnetization of the multilayer structure for two depths of modulation δn_0 with the magnetic field applied in the longitudinal direction. (*1*, *3*) Clockwise and (*2*, *4*) counterclockwise circular polarization.

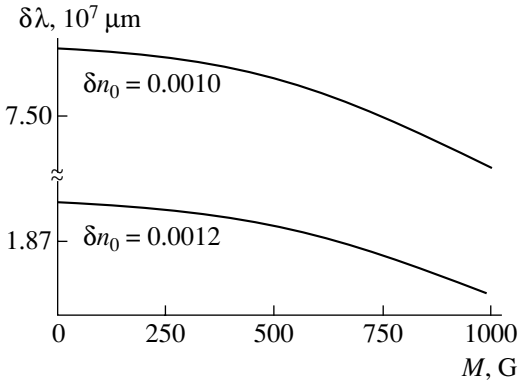

Fig. 4. Width δλ of the curve $|t|^2 = f(\lambda, H)$ vs. the magnetization of the multilayer structure for two depths of modulation δn_0 with the magnetic field applied in the transverse direction. Linearly polarized radiation.

zation grows in the range $M(H) \in [0; 10^3]$ G. For the structure parameter values adopted in our model, δλ is maximal at $M = 0$. For $\delta n_0 = 0.001$ and 0.0012, the maximal value of δλ is 7.497071×10^{-7} and 1.86985×10^{-7} μm, respectively. For the other extreme M = 1000 G, δλ = 7.49706×10^{-7} and 1.86984×10^{-7} μm, respectively.

As in the case of the longitudinal field, no effect of magnetization on the position of the central peak in the curve $|t|^2 = f(\lambda, H)$ was detected when the field ranging from 0 to 1000 G was applied in the transverse direction. However, the shift of the peak is absent due to the above assumption (all the estimates made in this section are based on the assumption that $a_i(H)\lambda \ll 1$, which is valid for the optical wavelength range). It may be expected that a more detailed consideration will reveal a shift, but it is bound to be much smaller than the change δλ in the width of the curve $|t|^2 = f(\lambda, H)$ Practical use of this effect seems problematic.

In the range $M(H)$ = 0–1000 G, the transmission coefficient in the central peak remains unchanged for both the longitudinal and transverse configurations: $|t|^2_{\max} = 1$.

CONCLUSIONS

The effect of a magnetic field on the transmission coefficient of two-component multilayer structures of which one or both components are magnetoactive materials shows up in a change (decrease or increase depending on the sense of circular polarization) in the width of the curve $|t|^2 = f(\lambda)$. Calculations carried out for periodic structures placed in a longitudinal and transverse magnetic field show that the width of the curve $|t|^2 = f(\lambda, H)$ varies with increasing magnetization: it linearly increases or decreases in the longitudinal configuration and decreases by a quadratic law when the field is applied in the transverse direction.

In the magnetization range 0–1000 G used in this study, the shift of the central peak in the curve $|t|^2 = f(\lambda, H)$ is negligible. A magnetic field applied to the multilayer structure does not affect the transmission coefficient amplitude.

REFERENCES

1. M. Herman, *Semiconductor Superlattices* (Akademie-Verlag, Berlin, 1986; Mir, Moscow, 1989).
2. M. Inoue, K. Arai, T. Fujii, and M. Abe, J. Appl. Phys. **85**, 5768 (1999).
3. S. Akiba and K. Utaka, in *Dynamically Unifrequent Semiconductor Lasers* (Mir, Moscow, 1989).
4. M. J. Steel, M. Levy, and R. M. Osgood, J. Lightwave Technol. **18**, 1297 (2000).
5. M. J. Steel, M. Levy, and R. M. Osgood, J. Lightwave Technol. **18**, 1289 (2000).
6. M. J. Steel, M. Levy, and R. M. Osgood, IEEE Photonics Technol. Lett. **12**, 1171 (2000).
7. S. A. Nikitov and Ph. Tailhades, Opt. Commun. **199**, 389 (2001).
8. N. V. Britun and V. V. Danilov, Pis'ma Zh. Tekh. Fiz. **29** (7), 27 (2003) [Tech. Phys. Lett. **29**, 277 (2003)].
9. G. A. Prinz, Science **282**, 1660 (1998).
10. I. A. Andronova, M. Yu. Gusev, Yu. N. Konoplev, *et al.*, Izv. Vyssh. Uchebn. Zaved. Radiofiz. **28**, 388 (1985).
11. G. S. Krinchik, *Physics of Magnetic Phenomena* (Mosk. Gos. Univ., Moscow, 1985) [in Russian].
12. R. V. Pisarev, *Magnetic Ordering and Optical Phenomena in Crystals: Physics of Magnetic Dielectrics*, Ed. by G. A. Smolenskiĭ (Nauka, Leningrad, 1974) [in Russian].
13. G. S. Krinchik and M. V. Chetkin, Zh. Éksp. Teor. Fiz. **38**, 1643 (1960) [Sov. Phys. JETP **11**, 1184 (1960)].
14. G. S. Krinchik and M. V. Chetkin, Zh. Éksp. Teor. Fiz. **40**, 729 (1961) [Sov. Phys. JETP **13**, 509 (1961)].
15. G. S. Krinchik and M. V. Chetkin, Zh. Éksp. Teor. Fiz. **41**, 673 (1961) [Sov. Phys. JETP **14**, 485 (1961)].
16. M. I. Lyubchanskiĭ, Candidate's Dissertation (Donetsk, 2001).

Translated by V. Isaakyan

Technical Physics, Vol. 49, No. 5, 2004, pp. 603–608. Translated from Zhurnal Tekhnicheskoĭ Fiziki, Vol. 74, No. 5, 2004, pp. 83–88.

OPTICS, QUANTUM ELECTRONICS

Effect of Spontaneous Frequency Fluctuations on the Emission Line of a Semiconductor Laser with Pseudorandom Modulation of the Pump Current

Yu. A. Morozov

Institute of Radio Engineering and Electronics (Saratov Branch), Russian Academy of Sciences, Saratov, 410019 Russia

e-mail: mor@ire.san.ru

Received July 7, 2003

Abstract—The effect of random frequency fluctuations due to spontaneous emission and generation–recombination noise on the shape of the emission line of a semiconductor laser with pseudorandom modulation of the pump current is studied numerically. The roles of spontaneous emission and chirp modulation in forming the lasing spectrum are separated out. The dependence of the output spectral characteristics of the laser on the parameters and type of modulation is analyzed. © *2004 MAIK "Nauka/Interperiodica".*

INTRODUCTION

Optimal characteristics of long-range fiber-optic communications (FOCs) can be achieved only if they are fed by dynamically single-mode semiconductor lasers, such as distributed feedback lasers or lasers with a distributed Bragg reflector. Another candidate for radiation sources in high-rate communications is a vertical-cavity laser, which has recently been the subject of extensive development [1]. At present, it is generally recognized that the main factors that retard further development of FOCs are time jitter (random variation of the pulse length) and emission line widening due to chirp modulation [2–11]. Much research has been devoted to analyzing these phenomena with the aim of removing or at least reducing their effect on lasing. In particular, it has been found that jitter depends on the type of a pseudorandom pulse train and on the contribution of spontaneous emission to lasing intensity fluctuations [2–6].

Chirp modulation is the other basic and, presumably, physically unavoidable feature of stimulated emission from a semiconductor laser with pulse modulation of the pump current [7–11]. Chirp usually arises when current modulation causes variation of the refractive index of the lasing medium. Clearly, in a fiber with chromatic dispersion, chirp modulation distorts the pulse shape and, ultimately, causes transmission errors. It should be noted that these distortions are dynamic; i.e., they depend, in particular, on the length of a pulse being transmitted. The effect of chirp on the FOC characteristics was studied, for example, by Yamamoto *et al*. [9]. However, they considered only Gaussian pulses and linear chirp modulation. In other words, it was assumed that the lasing frequency varies in proportion to time within a pulse, which does not correspond to the actual situation in most cases. Moreover, Yamamoto *et al.* [9] disregarded the effect of spontaneous fluctuations on the shape of the emission line in the case of pseudopulse frequency modulation. A more comprehensive analysis of the emission spectrum of a semiconductor laser transmitting a pseudorandom pulse train was performed by Balle *et al.* [11], who solved the well-known stochastic rate equations of semiconductor laser dynamics with allowance for random Langevin sources, which take into account the contribution of spontaneous fluctuations of the carrier and photon concentrations to lasing. However, they did not separate out the effects of pseudorandom chirp and spontaneous-emission-induced noise on the emission line shape. At the same time, both effects are of random nature and, consequently, produce continuous-spectrum radiation; i.e., it is impossible to distinguish the contributions to the shape of the emission line from spontaneous emission and from pseudorandom pulse modulation. It, therefore, appears that numerical simulation of lasing is the only way to analyze these two factors separately. Also, it is known that the integral measure of the fraction of spontaneous emission in the lasing mode (spontaneous emission coefficient β) may vary over a wide range from 10^{-5} to 10^{-1} depending on the active region size and the properties of the cavity [12, 13]. Therefore, the effect of spontaneous emission on the shape of the semiconductor laser emission line under pseudorandom pulse modulation of the pump current is of great applied interest, especially for fiber-optics communications.

In this work, we consider the role of spontaneous emission in forming the spectral line of a semiconductor laser when the pump current is modulated by a pseudorandom pulse train in the nonreturn-to-zero (NRZ) format. The effect of modulation parameters, such as

1063-7842/04/4905-0603$26.00 © 2004 MAIK "Nauka/Interperiodica"

the bit rate and the reference bias current, on the emission line shape is analyzed. The emission spectra of a semiconductor laser modulated by a pseudorandom and periodic pulse train are compared. We apply a new approach where the stochastic rate equations for semiconductor laser dynamics are replaced by a set of ordinary differential equations. The latter are derived from the Einstein–Fokker–Planck equations for the probability density functions of the carrier and photon concentrations in the lasing region. Earlier, this approach was successfully used to analyze the lasing intensity [14], its spectral density [15], and its transformation in an optical fiber [16].

MODEL AND BASIC RELATIONSHIPS

The dynamics and noise properties of a single-mode semiconductor laser are usually analyzed in terms of the set of stochastic differential equations [13, 17]

$$\begin{aligned}\dot{\nu} &= C(T) - S_0(1 - \varepsilon S_0) + \chi_1,\\ \dot{S}_0 &= \eta[(\nu - \varepsilon S_0)S_0 + \beta N_{th}] + \chi_2,\\ \dot{\varphi} &= \frac{\alpha}{2}\eta\nu + \chi_3.\end{aligned} \tag{1}$$

Here, $\nu = (n - n_{th})g\tau_p$ is the normalized deviation of the carrier concentration n in the active layer from the lasing threshold concentration nth; $S_0 = s_0 g\tau_e$ is the dimensionless photon flux density in the lasing mode; φ is the phase of the complex amplitude of the emission electric field; g is the linear component of the gain in the active medium; τ_e and τ_p are the electron and photon lifetimes, respectively; e is the elementary charge; d is the thickness of the active region; β is the spontaneous emission coefficient (i.e., the fraction of spontaneous emission in the lasing mode); α is the line broadening parameter in the cw lasing mode; $N_{th} = n_{th}g\tau_p$; and $\eta = \tau_e/\tau_p$. The quantity $C(T) = (j(T) - j_{th})g\tau_e\tau_p/ed$ stands for the excess of the effective current $j(T)$ over its threshold value jth. The Langevin noise sources, which simulate random processes of photon generation and generation–recombination processes, are characterized by the functions $\chi_{1,2,3}$. Differentiation in (1) is performed with respect to dimensionless time $T = t/\tau_e$, and the derivatives on the left-hand sides of the equations are marked by overcircles. The effect of gain saturation is taken into account by the normalized coefficient $\varepsilon = \varepsilon_0/g\tau_e$. The pump current was specified by a pseudorandom pulse train (in the NRZ format) superimposed on the reference bias current j_0.

From the Einstein–Fokker–Planck equation [14–16], which may be written for the probability density of the simultaneous distribution of carriers and photons (see set (1)), we come to the following set of ordinary differential equations for the statistical moments of the random variables ν, S_0, and φ:

$$\begin{aligned}\dot{y}_1 &= C(T) - y_2 + \varepsilon(y_2^2 + y_5),\\ \dot{y}_2 &= \eta[(y_1y_2 + y_7) - \varepsilon(y_2^2 + y_5) + 1.5\beta N_{th}],\\ \dot{y}_3 &= \frac{\alpha}{2}\eta y_1,\\ \dot{y}_4 &= D_{11} - 2y_7(1 - 2\varepsilon y_2),\\ \dot{y}_5 &= D_{22} + 2\eta[(y_1y_5 + y_2y_7) - 2\varepsilon y_2y_5],\\ \dot{y}_6 &= D_{33} + \alpha\eta y_8,\\ \dot{y}_7 &= D_{12} - y_5(1 - 2\varepsilon y_2) + \eta[(y_1y_7 + y_2y_4) - 2\varepsilon y_2y_7],\\ \dot{y}_8 &= D_{13} + \frac{\alpha}{2}\eta y_4 - y_9(1 - 2\varepsilon y_2),\\ \dot{y}_9 &= D_{23} + \frac{\alpha}{2}\eta y_7 + \eta[(y_2y_8 + y_1y_9) - 2\varepsilon y_2y_9].\end{aligned} \tag{2}$$

Here, $y_1 = \langle\nu\rangle$, $y_2 = \langle S_0\rangle$, and $y_3 = \langle\varphi\rangle$ are the first moments (mathematical expectations); $y_4 = \langle\nu^2\rangle - \langle\nu\rangle^2 = \sigma_\nu^2$, $y_5 = \sigma_{S_0}^2$, and $y_6 = \sigma_\varphi^2$ are the variances; and $y_7 = \langle\nu S_0\rangle - \langle\nu\rangle\langle S_0\rangle$, $y_8 = \langle\nu\varphi\rangle - \langle\nu\rangle\langle\varphi\rangle$, and $y_9 = \langle S_0\varphi\rangle - \langle S_0\rangle\langle\varphi\rangle$ are the covariances of carriers, photons, and the slowly varying emission phase.

The expectations of the diffusion coefficients D_{ij} can be calculated by formulas given, for example, in [17]. It should be emphasized that the diffusion coefficients, being a measure of the Langevin source intensity, are proportional to the spontaneous emission coefficient β.

Keeping in mind that, according to the Wiener–Khinchin theorem, the energy spectrum $G(\Omega)$ shifted toward lower frequencies is related to the correlation function of the radiation electric field $\langle U(T)U(T + \tau)\rangle$ via the Fourier transform

$$G(\Omega) = \lim_{T\to\infty}\frac{4}{T}\int_0^T d\xi \int_0^{T-\xi}\langle U(\xi)U(\xi + \tau)\rangle \times \cos(\omega_0 + \Omega)\tau d\tau, \tag{3}$$

we will first find this correlation function, neglecting the terms at the double carrier frequency ω_0:

$$\langle UU_\tau\rangle = \frac{1}{2}AA_\tau\mathrm{Re}[e^{j[\omega_0\tau + \delta\varphi(T,\tau)]}\langle e^{j\Delta\varphi(T,\tau)}\rangle]. \tag{4}$$

As before, the angular brackets mean averaging over an ensemble; U is the instantaneous electric field of optical radiation; A and ω_0 are the amplitude and angular frequency of the carrier, respectively; and $\delta\varphi(T, \tau)$ and $\Delta\varphi(T, \tau)$ are the nonstationary (random) phase advances over the time τ due to chirp and spontaneous emission, respectively (the new variables are normalized so that $S_0 = A^2$). The variables indicated by the sub-

script τ refer to the time instant $(T + \tau)$. Note that Eq. (4) has been obtained under the assumption that the effect of random amplitude fluctuations on the line shape can be neglected. Supposing that the random phase advance $\Delta\varphi$ obeys the Gaussian law, we have $\langle e^{i\Delta\varphi}\rangle = e^{-\frac{\alpha_{\Delta\varphi}^2}{2}}$, where

$$\sigma_{\Delta\varphi}^2(T, \tau) = (2\pi)^2 \int_T^{T+\tau} \int_T^{T+\tau} Z_{ff}(T', T'')dT'dT'' \quad (5)$$

is the nonstationary variance of the phase advance at times separated by intervals of τ.

The last expression contains the time-dependent frequency correlation function Z_{ff}. As follows from the third equation in set (1), Z_{ff} can be expressed via the correlation functions of the carrier concentrations and the correlation function χ_3 of Langevin sources:

$$Z_{ff}(T, \tau) = \left(\frac{\alpha\eta}{4\pi}\right)^2 Z_{vv}(T, \tau) + \frac{1}{(2\pi)^2} D_{33}(T)\delta(\tau), \quad (6)$$

where $Z_{vv}(T, \tau) = \langle v(T)v(T + \tau)\rangle - y_1(T)y_1(T + \tau)$ and δ is the Dirac function.

Introducing a new variable $\xi = T'' - T'$, we get the expression for the variance

$$\sigma_{\Delta\varphi}^2(T, \tau) = \int_T^{T+\tau} dv \left[D_{33}(v) + \frac{(\alpha\eta)^2}{2} \int_0^{T+\tau-v} Z_{vv}(v, v + \xi)d\xi \right]. \quad (7)$$

Using the approach detailed in [15], we may derive a set of ordinary differential equations for the nonstationary correlation function Z_{vv} of the carrier concentration in the active layer:

$$\begin{aligned} \dot{Z}_{vv}(T, \tau) &= -(1 - 2\varepsilon y_{2\tau})Z_{vS}(T, \tau), \\ \dot{Z}_{vS}(T, \tau) &= \eta[(y_{1\tau} - 2\varepsilon y_{2\tau})Z_{vS} + y_{2\tau}Z_{vv}(T, \tau)]. \end{aligned} \quad (8)$$

Here, $Z_{vS}(T, \tau) = \langle v(T)S_0(T + \tau)\rangle - y_1(T)y_2(T + \tau)$ is the mutual correlation function for the concentrations of carriers and photons. Differentiation is performed with respect to the variable τ. The necessary initial conditions

$$\begin{aligned} Z_{vv}(T, 0) &= y_4(T), \\ Z_{vS}(T, 0) &= y_7(T) \end{aligned} \quad (9)$$

are determined from solving the set of equations (2) for the moments.

RESULTS OF NUMERICAL SIMULATION

The most important parameters of the lasing regions that were used in calculations are summarized in the table. We assumed that the modulation amplitude j_m always equals the threshold current density j_{th} and that the rise time of the current pulse to a level of $0.9j_m$ equals $0.1(BR)^{-1}$ (BR is the bit rate of modulation in the NRZ format).

Laser parameters

Parameter	Laser structure *A*	Laser structure *B*
τ_e, ns	2	2
τ_p, ps	1	2
g, cm^3/s	2×10^{-6}	1×10^{-6}
d, cm	1×10^{-5}	2×10^{-5}
V, cm^3	2×10^{-11}	2×10^{-10}
n_{th}, cm^{-3}	10^{18}	10^{18}
ε_0, cm^3	2×10^{-17}	2×10^{-17}
α	5	5
β	4×10^{-4}	2×10^{-5}

Theoretical curves *1* in Fig. 1 illustrate the effect of frequency fluctuations induced by spontaneous emission on the shape of the emission line of a single-mode semiconductor laser when the pumping current is pseudorandomly modulated with a $BR = 5$ Gbit/s in the NRZ format. Chirp modulation was also taken into account. For comparison, curves *2* in Fig. 1 show the emission spectra of the laser in the absence of spontaneous frequency fluctuations (i.e., for $\sigma_{\Delta\varphi}^2(T, \tau) = 0$) and dashed lines *3* demonstrate the spectra without chirp (i.e., at $\alpha = 0$). It is seen that chirp renders the emission line highly asymmetric with a plateau in the high-frequency part of the spectrum. It should be noted that such behavior of the emission intensity subject to pseudorandom modulation of the pump current has also been observed in experiments [10]. The effect of spontaneous emission shows up, first, in smoothing out of the curves. Also, when the spontaneous emission coefficient reaches 4×10^{-4}, random frequency fluctuations begin to considerably affect the shape of the emission line and the spectral density exceeds its value in the absence of the fluctuations by roughly 3 to 5 dB. Simultaneously, the linewidth increases and the asymmetry becomes less pronounced (Fig. 1a). For laser diode *B* with a lower spontaneous emission coefficient, the effect of random frequency fluctuations on the emission line shape is negligible (Fig. 1b). In this case, the shape and width of the line are governed primarily by chirp due to the pseudorandom modulation of the current.

Figure 2, which shows isolevel sections of the surface of the nonstationary correlation function $\langle U(T)U(t + \tau)\rangle$, gives a better visualization of the mechanism underlying the effect of spontaneous frequency fluctuations on the shape of the semiconductor laser emission line (the factor $\exp[j(\omega_0\tau + \delta\varphi)]$, which is responsible for the high-frequency oscillations of the correlation function is omitted for clarity). Calculations

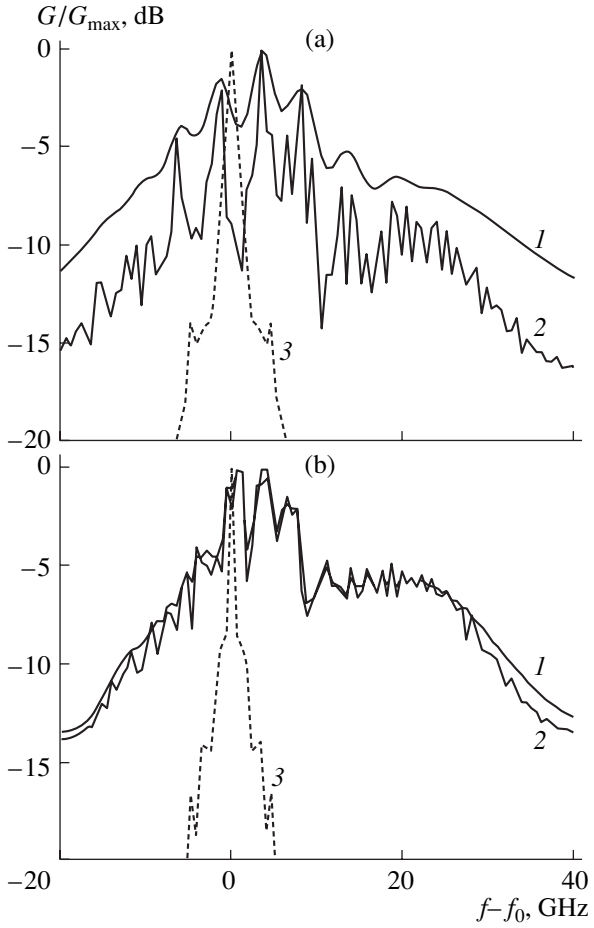

Fig. 1. Effect of the parameter β on the emission spectrum of a semiconductor laser (*1*, *3*) with and (*2*) without allowance for random frequency fluctuations. The current is modulated relative to $j_0 = j_{th}$. β = (a) 4×10^{-4} and (b) 2×10^{-5}.

were performed for the segment (0–0–1–1–1–0–1–0–1–0–0–0–0–0–1–1–0–1) of a pseudorandom pulse train realization for the cases when spontaneous frequency fluctuations (a) are not and (b, c) are taken into account. In the regions where the correlation function increases, the isolevel lines come closer together and these regions appear darker. In the absence of random frequency fluctuations (Fig. 2a), the intensities of the optical radiation electric field correlate throughout the pulse train segment analyzed. Random frequency fluctuations violate correlation in the pulse train: as the parameter β increases, the number of pulses adjacent to a given pulse that show radiation field correlation decreases. In particular, for $\beta = 2 \times 10^{-5}$, the pulse in the interval $0.4 \le t \le 1$, which consists of three consecutive binary unities, correlates, in essence, only with its neighbor appearing in the interval $1.2 \le t \le 1.4$ (Fig. 2b). For laser *A* with a higher β, only the radiation fields within the same pulse remain statistically related (Fig. 2c). Obviously, such behavior of the correlation function is reflected in the shape of the emission line.

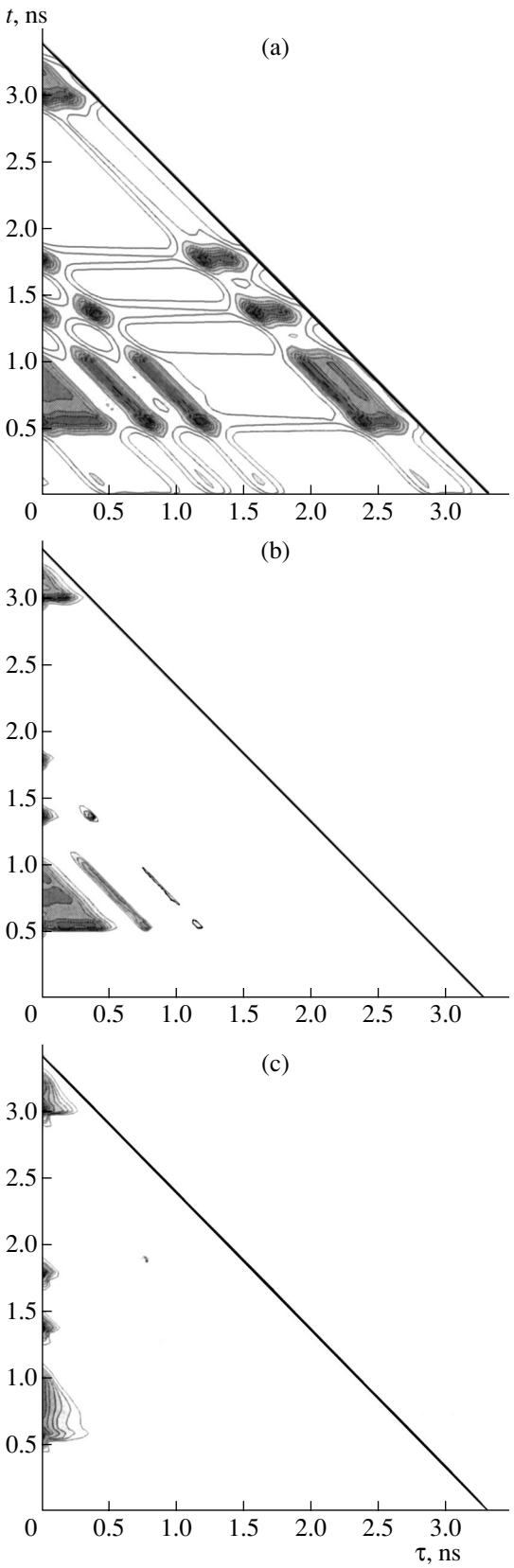

Fig. 2. Isolevel lines of the correlation function $\langle U(T)U(t+\tau)\rangle$ (a) without ($\sigma^2_{\Delta\varphi} = 0$) and (b, c) with spontaneous frequency fluctuations. β = (b) 2×10^{-5} and (c) 4×10^{-4}.

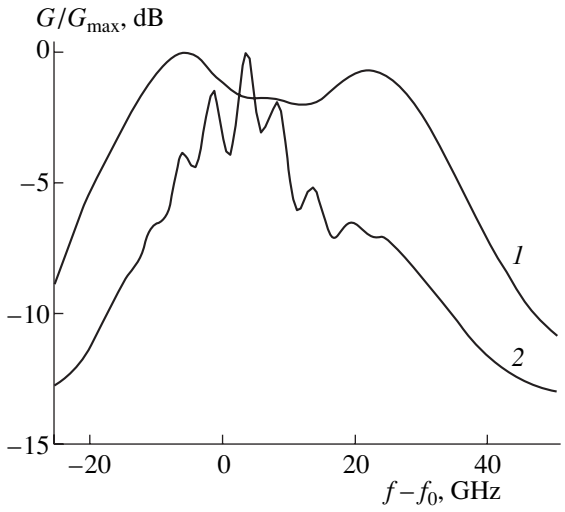

Fig. 3. Emission spectrum of laser *A* modulated by (*1*) regular and (*2*) pseudorandom pulse train at the bit rate *BR* = 5 Gbit/s.

For applications, in particular, for FOCs, it is of interest to see how the parameters and type of modulation influence the emission spectrum (calculations that follow refer to laser *A*, in which the effect of spontaneous emission on the lasing spectrum is the most noticeable). Figure 3 demonstrates the dependence of the emission line on format of modulation: curve *1* refers to the current modulated by a regular pulse train and curve *2* illustrates modulation in the NRZ format. In the former case, the emission line is much wider than in the case of the pseudorandomly modulated current. This unexpected (at first sight) result may be explained as follows. In the NRZ format, the pseudorandom pulse train contains not only solitary binary unities (i.e., unities surrounded by binary zeros) but also many pulses consisting of several consecutive binary unities. For such extended pulses, the process of emission is nearly stationary, i.e., similar to the process observed at a constant current. In the stationary mode, the emission line is clearly much narrower. As a consequence, for a pseudorandom pulse train in the NRZ format, the width of the emission spectrum must be smaller than in the case of a regular sequence of solitary binary unities.

The shape of the emission line varies significantly with the parameters of modulation. In particular, an increase in the bit rate of the pseudorandom pulse train widens the emission spectrum (Fig. 4) apparently because the average correlation interval for the pulse train at *BR* = 10 Gbit/s shrinks. Indeed, as follows from Fig. 2c, for laser *A* this time is no longer than the duration of a binary unity (i.e., BR^{-1}). Therefore, the larger the parameter *BR*, the shorter the correlation time and the wider the emission line.

Figure 5 illustrates the effect of the constant component of the pumping current (bias current) on the shape of the emission line. At least two features here are noteworthy. First, as the constant component increases, the maximum of the spectrum shifts toward the blue (high-frequency) range, since the refractive index of the active region decreases because of an increase in the average concentration of nonequilibrium carriers. Second, the linewidth narrows and the asymmetry of the line becomes less pronounced. This is because binary zeros in the pulse train start playing a greater part in emission (when the constant bias is set above the threshold value, zeros of the pulse train generate a nonzero output). These features of the emission spectrum are qualitatively corroborated by experiments [10].

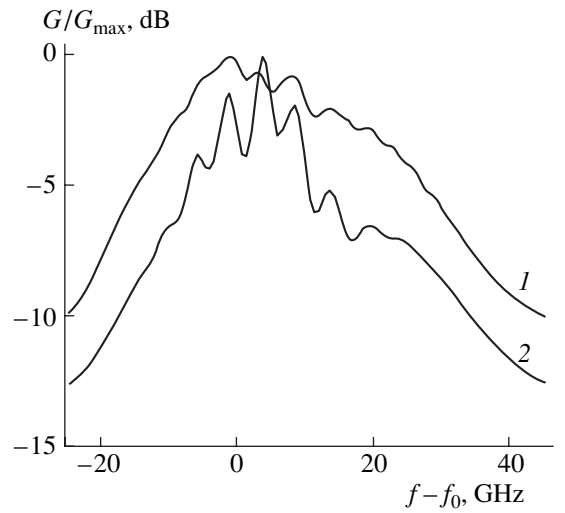

Fig. 4. Effect of the bit rate of modulation on the shape of the semiconductor laser emission line. *BR* = (*1*) 10 and (*2*) 5 Gbit/s.

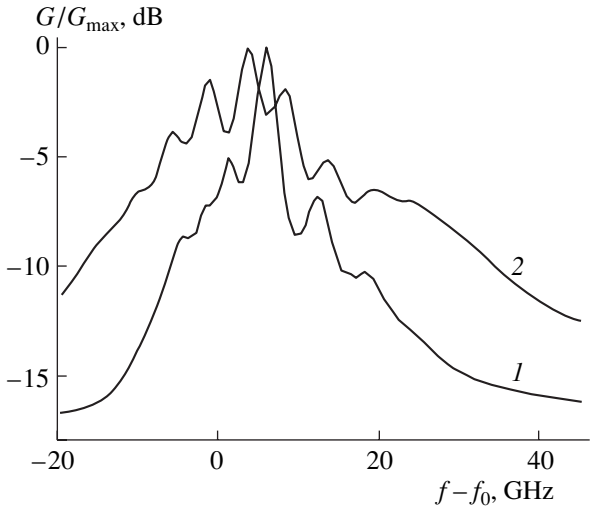

Fig. 5. Emission spectrum of the laser for the bias current $j_0 = 1.5j_{th}$ and (*2*) jth.

CONCLUSIONS

The dynamics of a single-mode semiconductor laser when the pump current is modulated by a regular or pseudorandom pulse train in the NRZ format is simulated numerically. The effect of random frequency fluctuations caused by spontaneous emission and generation–recombination noise, as well as the effect of the type and parameters of modulation on the emission line shape, is analyzed. It is found that, if the spontaneous emission coefficient reaches 4×10^{-4}, frequency fluctuations to a large degree determine the width and shape of the emission line: its spectral density becomes 3 to 5 dB higher than in the case when these fluctuations are disregarded. When the pump current is modulated by a regular pulse train, the emission spectrum is significantly wider than when the train is pseudorandom. The parameters of modulation also affect the shape of the emission line. The higher the bit rate of modulation, the wider the spectrum. If binary zeros in a pseudorandom pulse train generate an above-threshold pump current, the width and asymmetry of the emission line become smaller and its maximum shifts towards high frequencies.

The results obtained should be taken into account in analysis of the noise characteristics of semiconductor lasers used in FOCs with chromatic dispersion and in evaluating fluctuations in microlasers and so-called thresholdless lasers, where the spontaneous emission coefficient is high [12].

REFERENCES

1. A. Karim, J. Björlin, J. Piprek, and J. Bowers, IEEE J. Sel. Top. Quantum Electron. **6**, 1244 (2000).
2. P. Liu and M. Choy, IEEE J. Quantum Electron. **25**, 1767 (1989).
3. M. Choy, P. Liu, and S. Sasaki, Appl. Phys. Lett. **52**, 1762 (1988).
4. T. Shen, J. Lightwave Technol. **7**, 1394 (1989).
5. M. Mirasso, P. Colet, and M. San Miguel, IEEE J. Quantum Electron. **29**, 23 (1993).
6. A. Weber, W. Rongham, E. Böttcher, *et al.*, IEEE J. Quantum Electron. **31**, 441 (1995).
7. Y. Kum, H. Lee, J. Lee, *et al.*, IEEE J. Quantum Electron. **36**, 900 (2000).
8. P. Anderson and K. Akermak, Electron. Lett. **28**, 471 (1992).
9. S. Yamamoto, M. Kuwazuru, H. Wakabayashi, *et al.*, J. Lightwave Technol. **5**, 1518 (1987).
10. N. Henmi, S. Fujita, M. Yamaguchi, *et al.*, J. Lightwave Technol. **8**, 936 (1990).
11. S. Balle, M. Homar, and M. San Miguel, IEEE J. Quantum Electron. **31**, 1401 (1995).
12. T. Baba, T. Hamano, F. Koyama, and K. Iga, IEEE J. Quantum Electron. **27**, 1347 (1991).
13. *Guided-Wave Optoelectronics*, Ed. by T. Tamir (Springer-Verlag, Berlin, 1990; Mir, Moscow, 1991).
14. Yu. Morozov, IEEE J. Quantum Electron. **34**, 1209 (1998).
15. Yu. Morozov, IEEE J. Quantum Electron. **35**, 783 (1999).
16. Yu. A. Morozov, Zh. Tekh. Fiz. **70** (5), 61 (2000) [Tech. Phys. **45**, 584 (2000)].
17. J. Cartledge, IEEE J. Quantum Electron. **26**, 2046 (1990).

Translated by A. Khzmalyan

Technical Physics, Vol. 49, No. 5, 2004, pp. 609–612. Translated from Zhurnal Tekhnicheskoĭ Fiziki, Vol. 74, No. 5, 2004, pp. 89–93.

OPTICS, QUANTUM ELECTRONICS

Analysis of Oscillatory Processes in Lasers Using the Method of Generalized Eigenfunctions

V. Yu. Petrunkin and B. V. Lvov

St. Petersburg State Polytechnical University, ul. Politekhnicheskaya 29, St. Petersburg, 195251 Russia
e-mail: borislvov@hotmail.ru

Received October 13, 2003

Abstract—The method of generalized eigenfunctions, which is used in the theory of diffraction, is applied to analyze stationary and narrow-band nonstationary processes in lasers. Using this method, one can avoid difficulties associated with integration of the eigenfunctions of an emitting system over the continuous spectrum, difficulties typical of the conventional frequency method. The method employs expansion in modes that are orthogonal inside the lasing medium. The problem of exponential growth of modes at infinity is eliminated. In addition, the field distribution inside the lasing medium is better described using the generalized eigenfunctions in a number of important cases. © *2004 MAIK "Nauka/Interperiodica".*

The method of generalized eigenfunctions has been developed to solve steady-state diffraction problems [1]. Preliminary results of applying this method in the theory of lasers can be found in [2, 3]. The method was also used to study dynamic processes in antennas [4, 5]. Its main advantage is the possibility of analyzing emitting systems without integration over the continuous radiation spectrum. Using the values of a certain intrinsic parameter of the system as eigenvalues, one can expand the electromagnetic field in eigenfunctions that are orthogonal inside the lasing medium. This makes it possible to eliminate the problem of increase of eigenfunctions at infinity, which is typical of active-amplification systems with radiation losses. Recently, we have used this method to analyze oscillatory processes in dielectric-resonator antennas [6]. In this work, the method of generalized eigenfunctions is applied to find the field distribution in the laser cavity with the active medium in the form of a plane-parallel layer. Examples of such systems are semiconductor lasers, active waveguides in integrated optics, and some of solid-state (glass and crystalline) lasers. In addition, we will deal with the mode formation dynamics in the laser cavity.

Consider in brief the statement of the problem. (For applications of the method of the generalized eigenfunctions in analysis of stationary and nonstationary problems, see [1] and [2], respectively.)

We assume that the active layer of a laser has the form of a plane-parallel plate arranged as shown in Fig. 1. The radiation propagates along the z axis. The coordinates of two mirrors that are perpendicular to the z axis are $z = 0$ (a totally reflecting mirror) and $z = L$ (a mirror with an amplitude reflection coefficient Γ). The thickness of the layer along the x axis is $2a$, $a \ll L$. In the vertical direction (the y axis), the size of the plate is taken to be much greater than L and a. In other words, we assume that the vertical size equals infinity and actually consider a plane problem. The permittivities ε_1 and ε_2 of the plate and environment, respectively, can be complex quantities. The permeability μ everywhere is set equal to unity. In calculations, the radiation wavelength λ in free space is taken to be equal to 1 μm.

The electromagnetic field distribution in such a system can be characterized by *TE* and *TM* waves (see, for example [7, 8]). We will consider only *TE* waves, since solutions for these two types of waves are similar. In this case, the magnetic field H has x and z components, whereas the electric field E is directed along the y axis. Let

$$H_x(x, z, t) = H_x(x, z)\exp(j\omega t),$$
$$H_z(x, z, t) = H_z(x, z)\exp(j\omega t),$$
$$E_y(x, z, t) = E_y(x, z)\exp(j\omega t).$$

Equations for the field components have the form

$$\frac{\partial^2 E_y}{\partial x^2} + (k^2(x) - \gamma^2)E_y = 0,$$

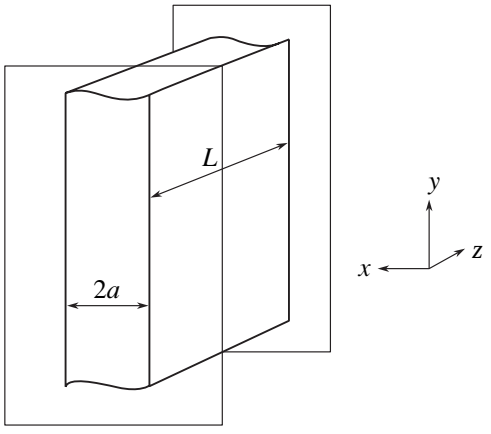

Fig. 1.

1063-7842/04/4905-0609$26.00 © 2004 MAIK "Nauka/Interperiodica"

$$H_z = -\left(\frac{1}{j\omega\mu_0}\right)\frac{\partial E_y}{\partial x}; \quad (1)$$

$$H_x = \left(\frac{1}{j\omega\mu_0}\right)\frac{\partial E_y}{\partial z},$$

where γ is the complex propagation constant in the z direction (to be found) and $\mu_0 = 4\pi \times 10^{-7}$ H/m.

Below, we follow the procedure proposed in [1–3] and search for the electric field in the form of the sum

$$E_y = \sum b_n E_{yn}$$

over modes, each satisfying Eqs. (1) and the boundary conditions that follow. We assume that the tangential components of the electric and magnetic fields are continuous in the interval $x = \pm a$. The wave propagates along the z axis from $z = 0$ to $z = L$, varying as $\exp(-i\gamma z)$; reflects from the mirror with the amplitude reflection coefficient $|\Gamma| < 1$; and returns to $z = 0$, varying as $\exp(i\gamma z)$. At $z = 0$, the electric field is $E = 0$. At infinity, the fields satisfy the limitedness conditions. Assume that

$$k(x) = k\sqrt{\varepsilon_n}$$

inside the active medium [1] and

$$k(x) = k\sqrt{\varepsilon_2},$$

outside the active medium, where $k = 2\pi/\lambda = \omega/c$ is the wavenumber and ε_n are the eigenvalues (i.e., those values of ε_1 for which Eqs. (1) and boundary conditions are satisfied).

In the method of generalized eigenfunctions, ε_n is assumed to be the complex eigenvalue for a given mode number n and the frequency, a real quantity.

In view of the boundary conditions, the solution to the set of equations (1) for the electric field is given by [8]

$$E_y(x, z) = AE_n(x)[\exp(i\gamma z) - \exp(-i\gamma z)],$$

$$\exp(2i\gamma L) = -\Gamma,$$

$$E_n(x) = \cos(ux/a), \quad -a < x < a, \quad (2)$$

$$E_n(x) = \cos(u)\exp[-q(x-a)/a], \quad x > a,$$

$$E_n(x) = \cos(u)\exp[q(x+a)/a], \quad x < -a.$$

The quantities u/a and q/a are the propagation constants along the x axis inside and outside the active medium, respectively. They can be found from the continuity conditions for the electric and magnetic fields at $x = a$ and $x = -a$. It follows from [8] that the following relationships are valid:

$$q = utgu,$$

$$\gamma^2 = k^2\varepsilon_n - (u/a)^2 = k^2\varepsilon_2 + (q/a)^2. \quad (3)$$

Representing γ as $\gamma = \beta + i\alpha$, we find from the boundary conditions that $\beta = \pi n/L$ and $\alpha = -\ln|\Gamma|/2L$ ($\Gamma < 0$), where n is the mode number. Thus, the impedance boundary condition at $z = L$ in combination with the mode number completely determine the complex propagation constant γ.

Subsequent steps are described in detail elsewhere [2, 3], so that below we summarize the results. Representing Eqs. (3) as

$$u^2 + q^2 = k^2a^2\varepsilon_n,$$

$$(u/a)^2 = k^2\varepsilon_n - \gamma^2, \quad (4)$$

$$(q/a)^2 = \gamma^2 - k^2\varepsilon_2,$$

we numerically solve the set of equations (4) and find the complex quantities u and q and the complex eigenvalues

$$\varepsilon_n = \varepsilon_n' + i\varepsilon_n''.$$

In laser systems, lasing at the amplification frequency ω of the active medium is usually considered; therefore, $\varepsilon_n' \approx \varepsilon_1$. This condition makes it possible to find the number n of the longitudinal mode. Solutions to Eqs. (4) yield the eigenvalues ε_n as functions of the circular frequency ω, so that jointly solving (1) and (2) in view of (4), one can find the eigenfunctions (i.e., the configuration) of the mode $E_n(x, z)$ (in [7], this quantity is denoted as $U_n(z)$).

Let us exemplify the application of the method in the theory of lasers by evaluating a number of laser characteristics. Figure 2a demonstrates the simulated configuration of the mode of an active layer similar to that of an actual semiconductor laser. We assume that the length of the layer along the z axis is 1 mm, the thickness along the x axis is 20 μm, and the permittivity ε_1 inside the active medium is greater than the permittivity ε_2 of the surrounding medium ($\varepsilon_2 = 3.6$) by 0.02%. The amplitude reflection coefficient is 0.6 (accordingly, the intensity reflection coefficient is 0.36). On the vertical axis, we plot the envelope of the electric field distribution for the mode in relative units. It is seen that the area occupied by the radiation is about three times larger than the active layer; i.e., the width of the optical waveguide exceeds the width of the active area, which is typical of homojunction semiconductor lasers.

The field distribution along the x axis is determined from Eqs. (2). As for the field variation along the longitudinal z axis of the cavity, Fig. 2a shows only its envelope. Actually, the incident wave and the wave reflected from the mirror interfere, causing field oscillations with a spatial period that roughly equals half the radiation wavelength. Figure 2b shows the field distribution along the z axis at $x = 0$. Here, we consider the field of the same laser as in the previous plot, but the oscillation period is increased by a factor of 100 and the reflection coefficient of the mirror is decreased from 0.6 to 0.2 for more clarity. It is seen that the mean field increases and the oscillation amplitude decreases with distance from the totally reflecting mirror located at $z = 0$. Of interest is the case $\varepsilon_1 - \varepsilon_2 = 0$, which means the absence of total reflection and, hence, the unlimitedness of the radiation. In this case, the conventional frequency method does not allow one to introduce a mode. The field is limited due to amplification alone. Figures 2c and 2d

demonstrate field distributions in an optical waveguide 1 cm long and 20 μm thick for $\varepsilon_1 = \varepsilon_2 = 1$ and different amplifications. The results presented in Fig. 2c (2d) are obtained for a reflection coefficient of the mirror of 0.99 (0.2) and a logarithmic increment $\alpha = 0.005$ (0.8) cm^{-1}. When the gain is high, the propagation of the radiation along the transverse x axis is seen to be heavily restricted.

In the theory of lasers, the method of generalized eigenfunctions can also be used to solve dynamic problems. The generalization of the method for narrow-band nonstationary processes is described in detail in [2, 3]. In particular, using the technique of slowly varying amplitudes, we derived [3] a differential equation for the complex amplitudes $B_n(t)$ of lasing modes. Its form,

$$\frac{dB_n}{dt} + i(\omega_n - \omega)B_n = \frac{1}{\varepsilon - \varepsilon_n(k)}\frac{i(\omega - \omega_n)}{k^2}\int_{V^+} E_n(x, z)\, f\, dxdz, \quad (5)$$

is similar to the Lamb equations used in the theory of lasers [7].

The physical meaning of Eq. (5) readily follows from the semiclassical theory of lasers. The quantity B_n is virtually identical to the complex amplitude $E_n\exp(i\varphi_n)$ of the mode, and the cyclic frequency $\omega = kc$ of lasing is assumed to be close to the central frequency ω_p of the spectral line of the active medium. In the semiclassical theory, f corresponds to the term $\partial^2 P/\partial t^2$, which approximately equals $-\omega^2 P$, where P is the polarization of the medium. The volume V^+ is the volume of the active medium. This means that the integral in Eq. (5) represents the term $P_n(E_n)$, which enters into the amplitude and phase equations [7]. In contrast to the real circular frequency ω, ω_n are complex quantities, which are expressed through the eigenvalues ε_n: $(\omega_n/c)^2 = k^2\varepsilon_n$.

Separating the real and imaginary parts in Eq. (5), we come to the equations for the mode amplitudes and phases that were derived in [7].

To exemplify the analysis of dynamic processes, we numerically solved the set of differential equations (5) for the generation of one and two longitudinal modes in a laser with Doppler broadening of the amplification line. The parameters of the medium are taken to be close to the parameters of a helium–neon laser with a wavelength of 0.63 μm [7]. The linewidth is 1.5 GHz, and the homogeneous broadenings of the levels are $\gamma_a = \gamma_b = 50$ MHz and $\gamma_{ab} = 100$ MHz. We consider a plane-parallel laser cavity with a length $L = 20$ cm, width $2a = 2$ mm, and $\varepsilon_1 = \varepsilon_2 = 1.0$. The reflection coefficient of the mirror is $\Gamma = 0.99$. For these parameters of the cavity, the frequency separation of neighboring longitudinal modes (about 750 MHz) far exceeds γ_a, γ_b, and γ_{ab}. This fact allows one to determine the polarization of the medium using the approximate techniques of the semiclassical laser theory. It is known [7] that the equations

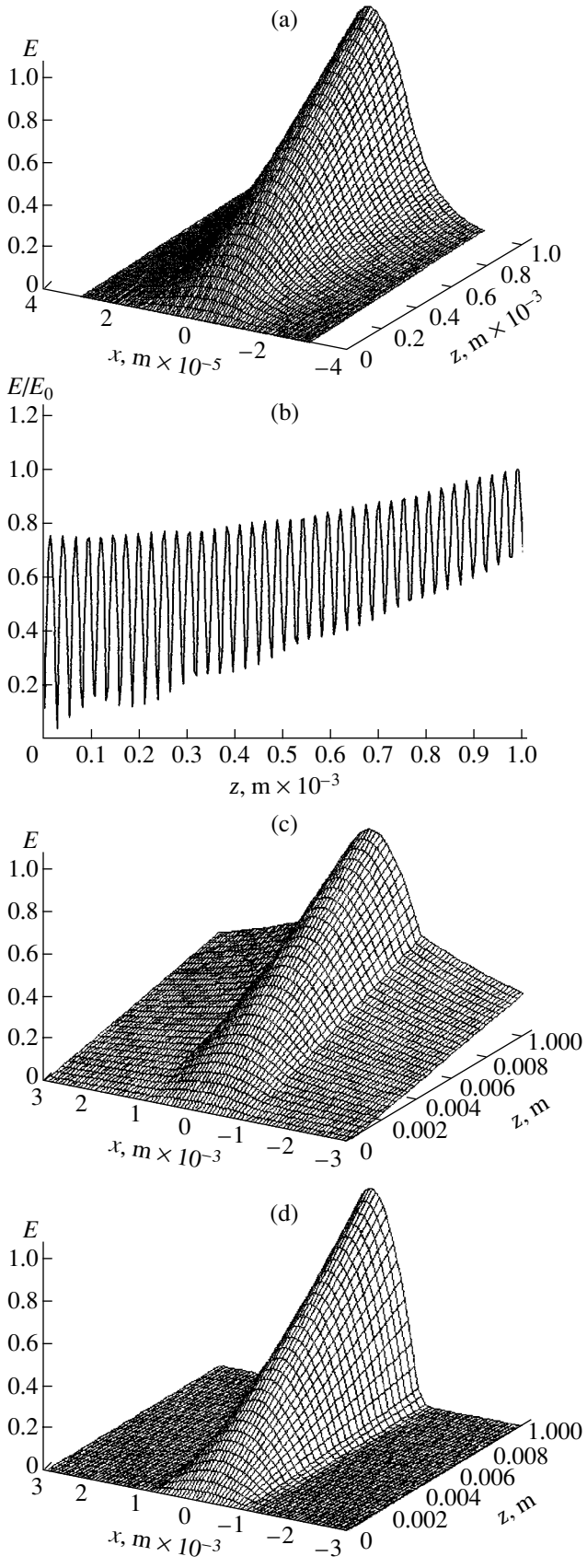

Fig. 2.

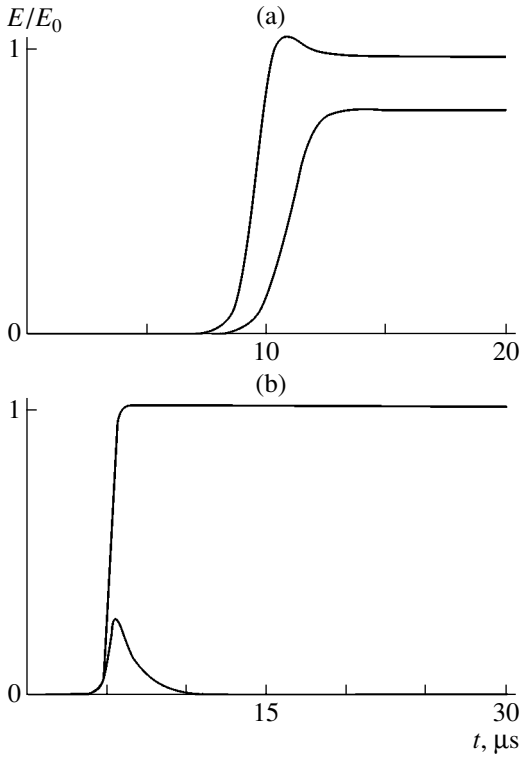

Fig. 3.

for the amplitudes of the modes E_1 and E_2 are reduced in this case to

$$\begin{aligned} dE_1/dt &= \alpha_1 E_1 - \beta_1 E_1^3 - \theta_{12} E_1 E_2^2, \\ dE_2/dt &= \alpha_2 E_2 - \beta_2 E_2^3 - \theta_{21} E_2 E_1^2. \end{aligned} \tag{6}$$

When calculating the coefficients α, β, and θ, we employed the formulas of the semiclassical theory [7]. It should be noted, however, that the configuration of the mode $E_n(x, z)$ that was derived from Eq. (2) and used in these formulas differs significantly from that used in [7]. Therein lies the difference between the method of generalized eigenfunctions and the conventional frequency method, in which the mode frequencies serve as eigenvalues.

Formulas (5) and (6) were used to calculate the mode buildup in an active medium where the gain is 1.3 times higher than the lasing threshold (Figs. 3a, 3b). Figure 3a shows the evolution of two-mode lasing in the case of weak mode coupling (the offset of the central mode from the center of the amplification line equals one-fourth of the mode separation):

$$\beta_1\beta_2 \approx 22\theta_{21}\theta_{12}.$$

Figure 3b shows the same process in the case of strong coupling:

$$\beta_1\beta_2 = \theta_{21}\theta_{12}.$$

When coupling is strong, one mode suppresses the other. This result is known from the theory of lasers; however, we considered a system with equal amplifications of the modes that are symmetric about the center of the line. The conventional semiclassical theory fails to predict which of the modes will be suppressed. In the case under consideration, the different configurations of the modes in the cavity lead to different losses and the mode with higher losses is suppressed. For clarity, the vertical axis in Figs. 3a and 3b is scaled up 100 times for the mode that is suppressed.

Thus, in analyzing dynamic processes in lasers with the method of generalized eigenfunctions, one may invoke the statements of the theory of lasers, for example, the Lamb approach [7]. However, the mode configurations will differ from the classical ones. The dependences of the fields on the coordinates *x* and *z* are closer to the real field distributions in the laser cavity, and the fields are limited at infinity.

Our analytical and numerical results indicate that the method of generalized eigenfunctions can be used for studying both stationary and slowly varying nonstationary processes in lasers. In comparison to the direct techniques of studying the time evolution of laser radiation, the method under consideration is simpler and does not require cumbersome computation. Using various parameters of the medium as eigenvalues, one can modify the method and tailor it to solve a variety of problems. Expansion in modes that are orthogonal to each other in the active medium makes it possible to avoid tedious integration and correctly eliminate an unlimited growth of the eigenfunctions at infinity.

REFERENCES

1. N. N. Voĭtovich, B. Z. Katsenelenbaum, and A. N. Sivov, *Generalized Method of Eigenmodes in the Theory of Diffraction* (Nauka, Moscow, 1977) [in Russian].
2. B. Lvov and V. Petrunkin, in *Proceedings of the International Conference on Electronics, Circuits and Systems (ICECS-95), Amman, 1995*, pp. 513–516.
3. V. Yu. Petrun'kin and B. V. L'vov, Zh. Tekh. Fiz. **67** (6), 46 (1997) [Tech. Phys. **42**, 628 (1997)].
4. B. V. Lvov and M. M. Suleiman, in *Proceedings of the International Wireless and Telecommunications Symposium (IWTS-97), Malaysia, 1997*, pp. 52–54.
5. B. Lvov and V. Petrunkin, in *Proceedings of the International Conference on Electronics, Circuits and Systems (ICECS-2001), Malta, 2001*, pp. 341–344.
6. B. Lvov, V. Petrunkin, and O. Ata, in *Proceedings of the World Multi Conference on Systemics, Cybernetics and Informatics (SCI-2002), Orlando, 2002.*
7. M. Sargent, M. Scully, and W. Lamb, in *Laser Physics Readings, New York, 1974*, pp. 96–114.
8. N. S. Kapany and J. J. Burke, *Optical Waveguides* (Academic, New York, 1972).

Translated by A. Chikishev

Technical Physics, Vol. 49, No. 5, 2004, pp. 613–618. Translated from Zhurnal Tekhnicheskoĭ Fiziki, Vol. 74, No. 5, 2004, pp. 94–100.

RADIOPHYSICS

Giant Magnetoresistance of Iron–Chromium Superlattices at Microwaves

V. V. Ustinov, A. B. Rinkevich, L. N. Romashev, and D. V. Perov

Institute of Metal Physics, Ural Division, Russian Academy of Sciences, ul. S. Kovalevskoĭ 18, Yekaterinburg, 620219 Russia

e-mail: rin@imp.uran.ru

Received July 21, 2003

Abstract—Interaction between an rf electromagnetic field and the Fe/Cr superlattice placed in a rectangular waveguide so that a high-frequency current passes in the plane of superlattice layers is considered. The transmission coefficient versus the magnetic field strength is found at centimeter waves, and a correlation between this dependence and the field dependence of the dc magnetoresistance is established. It is shown that a change in the transmission coefficient may greatly exceed the giant magnetoresistance of the superlattice. The frequency dependence of the microwave measurements has an oscillatory character. The oscillation frequencies are analyzed in terms of wavelet transformation. Two types of oscillation periods are found to exist, one of which corresponds to the resonance of waves traveling in the superlattice along the direction parallel to the narrow wall of the waveguide. © *2004 MAIK "Nauka/Interperiodica".*

INTRODUCTION

Magnetic metallic superlattices (film nanostructures consisting of alternate ferromagnetic and nonmagnetic metal layers) are viewed as promising materials for micro- and nanoelectronics, in particular, owing to the effect of giant magnetoresistance, i.e., a considerable increase (by several tens of a percent) in the resistance under a magnetic field. The physical basis for this effect is the dependence of the conduction electron scattering probability on the sense of the spin. The difference between the scattering probabilities is greatest when the magnetic moments of two adjacent ferromagnetic layers in a superlattice are arranged parallel and antiparallel to each other. If the magnetic moments are antiparallel to each other (the antiferromagnetic configuration) in the absence of a magnetic field, they become parallel to each other under the action of the field. The scattering probability for conduction electrons changes considerably, and the resistance drops significantly. This phenomenon was first observed in the Fe/Cr superlattice in 1988 and was named "the giant magnetoresistive (GMR) effect" [1].

A great stride forward in studying the magnetoresistive properties of metallic superlattices has been made with high-frequency (microwave) methods. Using these methods, researchers can variously orient an rf electric field with respect to the film plane and, accordingly, apply a current both along and across the films of the superlattices. In the latter configuration, the spin-dependent scattering of conduction electrons (hence, the GMR effect) shows up most vividly. It is important here that the current is applied with contactless techniques, which is of great value in studying metallic nanometer-sized objects.

High-frequency resonance methods were first applied to Fe/Cr/Fe sandwiches [2, 3]. Later, a strong correlation between the coefficient of penetration of an rf magnetic field into the Fe/Cr superlattice and its dc magnetoresistance was found [4] and a high-frequency analogue of the GMR effect was discovered in the "current-perpendicular-to-layer" geometry [5].

It should be noted that microwave investigation of multilayer nanostructures is also of interest because these structures may serve as a basis for producing electronic components and magnetic storages. Because of the need for improving the speed of these devices, their least necessary frequency spectrum constantly widens and has already reached several gigahertz and even several tens of gigahertz in a number of applications. Of special scientific interest is the fact that the electrodynamic properties of metallic superlattices differ substantially from those of thicker film structures, since the total thickness of a metal in metallic superlattices is much smaller than the skin depth. Therefore, the skin effect, typical of metals, is absent in them.

In this paper, we study the GMR effect in the Fe/Cr superlattice, using a high-frequency technique other than that used in previous works. A sample is placed in a rectangular waveguide in such a way that the longer side of the sample is parallel to the waveguide axis, while the plane of the layers is parallel to the shorter side of the waveguide. In this configuration, high-frequency currents pass in the plane of superlattice layers. Note that the same configuration of a dielectric or fer-

1063-7842/04/4905-0613$26.00 © 2004 MAIK "Nauka/Interperiodica"

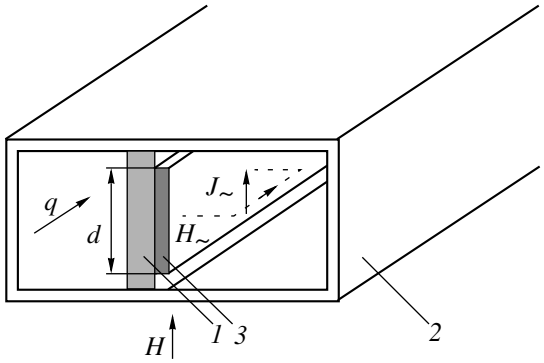

Fig. 1. Geometry of the experiment; *1*, substrate; *2*, waveguide, *3*, superlattice.

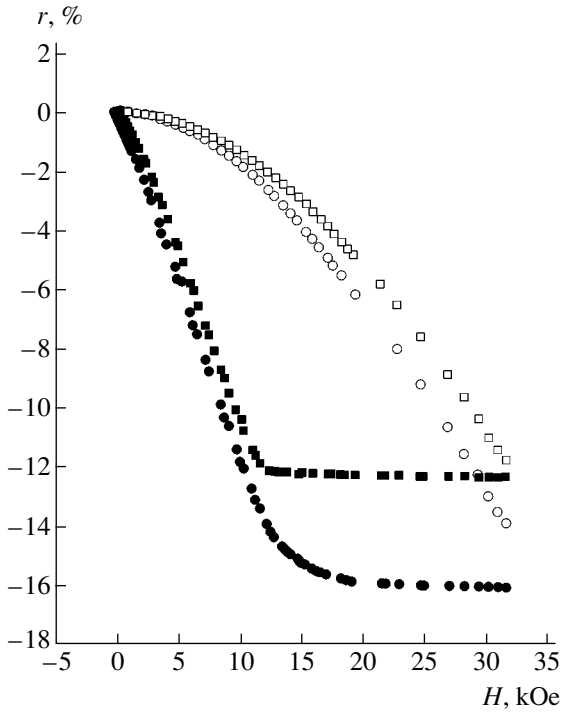

Fig. 2. Field dependence of the magnetoresistance of the Fe/Cr superlattice. (■) Sample 1, *H* parallel to the plane; (□) sample 1, *H* normal to the plane; (●) sample 2, *H* parallel to the plane; and (○) sample 2, *H* normal to the plane.

rite plate in a waveguide is used in attenuators and phase shifters.

EXPERIMENTAL

Fe/Cr superlattices used were grown by MBE in an ultrahigh vacuum on single-crystal MgO substrates measuring 30 × 30 × 0.5 mm. First, a ≈80-Å-thick buffer Cr layer was deposited. The role of this layer is to smooth out the substrate and provide relaxation of stresses due to a lattice mismatch between the substrate and superlattice. The buffer Cr layer was alternately covered by Fe and Cr layers with a deposition rate of 1.5 Å/min at a substrate temperature of 180°C. The top layer was a Cr layer, which prevented the underlying Fe layer from oxidation in air.

We studied systems of two compositions, $[Cr(13\ Å)/Fe(24\ Å)]_8/Cr(82\ Å)/MgO$ (sample 1) and $[Cr(12\ Å)/Fe(23\ Å)]_{16}/Cr(77\ Å)/MgO$ (sample 2), grown on the (001) plane of single-crystal MgO. The figures in the parentheses are the thicknesses of the layers in angstroms; the subscripts indicate the number of pairs of layers.

The static magnetoresistive parameters necessary to analyze rf measurements were determined from the field dependence of the relative magnetoresistance $r = [R(H) - R(0)]/R(0) \times 100\%$, where $R(H)$ is the magnetoresistance measured by the standard four-point probe technique in a magnetic field H.

Microwave measurements were made in the frequency range 5.7–12.0 GHz by using usual rectangular waveguides (Fig. 1). The wavevector q lay in the sample plane, and the microwave current $J_\sim$ passed along the layers. The magnitude of the transmission coefficient D of the waveguide with the sample was measured as a function of a permanent magnetic field H, which may be directed both parallel to the sample plane (as in Fig. 1) and normally to it, and the relative variation of the transmission coefficient in the magnetic field $r_m = [D(H) - D(0)]/D(0) \times 100\%$ was measured.

The superlattices used in the microwave measurements had the same length, 23 mm, but different widths: 11.5 and 2–6 mm, for sample1 and sample 2, respectively.

RESULTS

The field dependences of the relative dc magnetoresistance of the Fe/Cr superlattices that was measured in a permanent magnetic field are given in Fig. 2. For either of the samples, two curves $r(H)$ are shown: one for the magnetic field parallel to the plane of the superlattice; the other, for the field normal to the plane. The difference in the curves $r(H)$ that were obtained in the normal and parallel fields of the same value is due to the fact that demagnetizing fields in these film structures differ in these cases [6].

Note first of all that the variation of the transmission coefficient with permanent magnetic field is independent of its sense (the even effect) but depends noticeably on its orientation relative to the plane of the layers. The even effect is illustrated in Fig. 3a, where the results of measurements in the magnetic field normal to the plane at a frequency of 9.8 GHz are shown for sample 1. Figure 3b shows the field dependences of the transmission coefficient for the same sample at the same frequency in the field normal and parallel to the sample plane. Comparing these curves with the field dependences of the static magnetoresistance (Fig. 2), one can see their qualitative agreement. The magnetic field at which the curves saturate is also the same for the

microwave transmission coefficient and static magnetoresistance. These and our previous results [4, 5, 7] allow us to argue that the variations of the microwave transmission coefficient that are observed in this work are directly related to the magnetoresistive effect.

The frequency dependence of the microwave effect (the relative variation of the transmission coefficient) is complicated. First, unlike the static magnetoresistance of the superlattices, which has negative sign (Fig. 2), the change in the transmission coefficient at microwaves may be both negative and positive. In addition, it turned out that the magnitude of the microwave variation may be both greater and smaller than the static magnetoresistance according to the frequency (at certain frequencies, the variation exceeds the static magnetoresistance severalfold). The above-said is illustrated in Fig. 4, where the transmission coefficient is plotted against the parallel magnetic field for sample 1 at different frequencies.

Figure 5 demonstrates the frequency dependences of the relative variation of the transmission coefficient when sample 1 was exposed to a magnetic field of 23 kOe, which is the highest achievable in our experiments with the waveguide. The field was applied both parallel and perpendicularly to the plane of the sample. In the former case, the superlattice is magnetized to saturation, while in the latter case the magnetic field strength 23 kOe is insufficient for magnetic saturation (the superlattice saturates in a field of 32 kOe, Fig. 2). Hence, the dependences in Fig. 5 quantitatively disagree, being nearly identical in form. The likeness of the curves in Fig. 5 deserves special attention, since this means that the variations of the transmission coefficient and static magnetoresistance with magnetic field correlate with each other throughout the frequency range. Surprisingly, while the transmission coefficient remains positive and relatively low at frequencies to ≈9 GHz, at higher frequencies it oscillates more heavily, grows, and even may become negative (as was demonstrated above in Fig. 4).

The frequency dependence of the transmission coefficient for sample 2 is qualitatively similar to that for sample 1 with the only difference that the maximal variation of the coefficient for sample 2 is observed at higher frequencies.

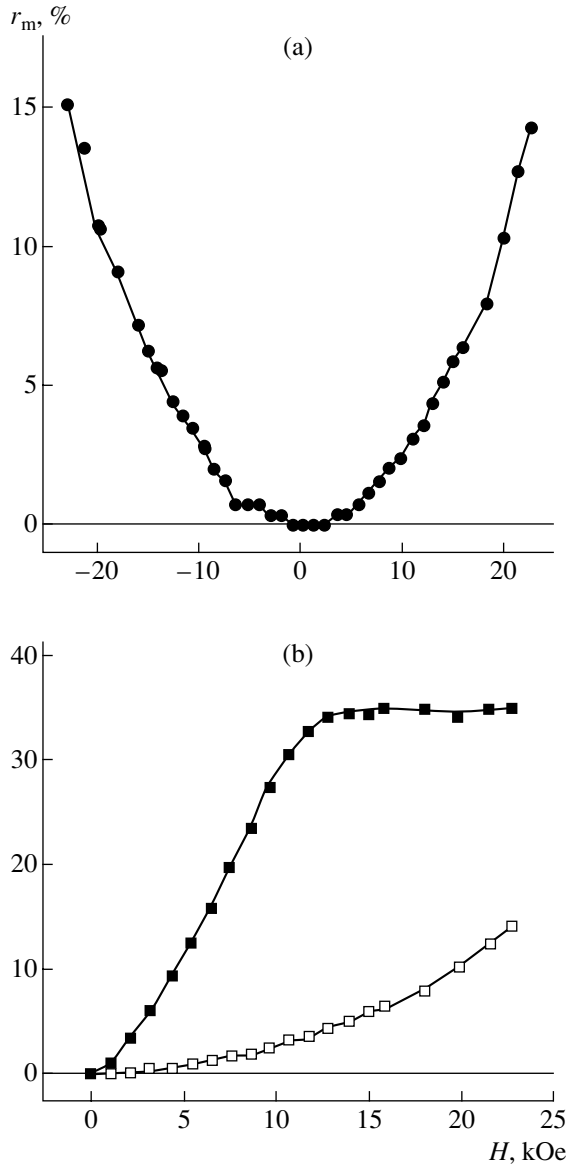

Fig. 3. Microwave magnetoresistive effect. (a) Evenness in magnetic field and (b) the transmission coefficient magnitude versus H (□) perpendicular and (■) parallel to the plane of the superlattice.

DISCUSSION

The experimental data obtained in this work clearly demonstrate the effect of the magnetoresistance of the superlattice on the transmission coefficient of microwaves. This means that the variation of the transmission coefficient with magnetic field is due to interaction of the rf field with the current passing through the superlattice. Specifically, Joule losses $Q = \int J_\sim E_\sim dV$ ($E_\sim$ is the rf electric field, and integration is over the sample volume) in the superlattice are directly related to the magnetoresistance value (the amount of the magnetoresistive effect).

To explain the experimentally found effect of the magnetoresistance on the travel of the rf electromagnetic wave, we note that the waveguide with the superlattice is cascaded in the microwave channel and so may exhibit resonance properties under certain conditions. Since the sample is arranged normally to the wider side of the waveguide (Fig. 1), the plane of the sample is parallel to the rf electric field vector; hence, high-frequency currents pass along the layers of the superlattice. An electrical contact between the superlattice and waveguide is absent; therefore, one may

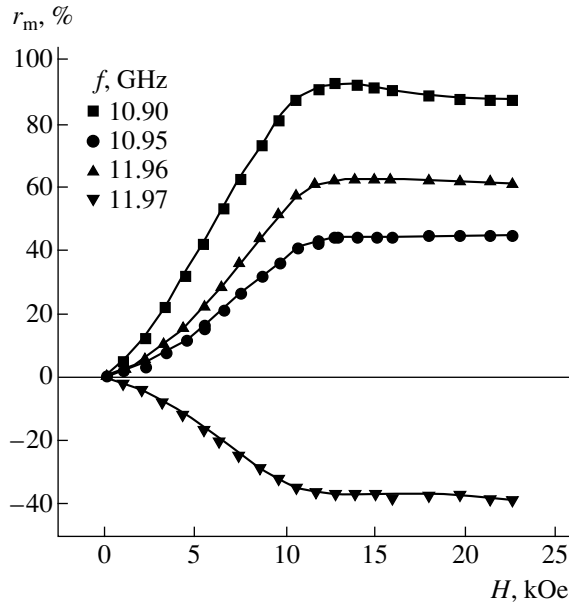

Fig. 4. Alternating-sign microwave magnetoresistive effect.

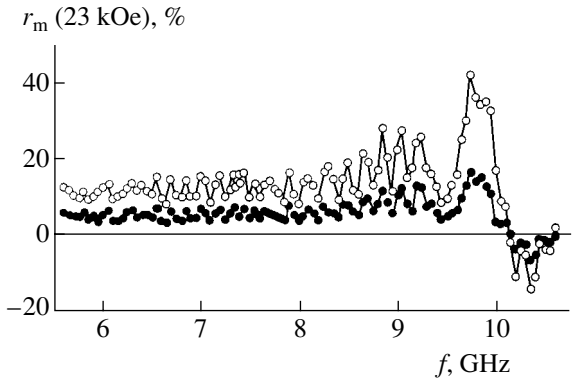

Fig. 5. Frequency dependence of the relative variation of the transmission coefficient magnitude in the field H = 23 kOe for sample 1 when the field is (●) perpendicular and (○) parallel to the plane of the superlattice.

assume that the waveguide with the sample has the resonant frequency of the fundamental mode near the frequency of half-wave resonance that corresponds to the sample thickness d. An offset from the half-wave resonant frequency is due to the presence of the insulating substrate and field distortion in the space between the sample and wider walls of the waveguide. The electrodynamics of similar systems was considered in [8], where the fields near the metallic film surface were expanded in LE and LM eigenmodes of an empty waveguide. It was shown that the resonant wavelength $l_0 = 2(l_e + \Delta)$ of the fundamental mode (where $l_e = d(\varepsilon_{eff})^{1/2}$ and ε_{eff} is the effective permittivity) depends on the permittivity of the substrate and its thickness. The correction Δ is due to the field distortion in the space between the superlattice and waveguide walls. The frequency spectrum of such a resonator, which was named the surface wave resonator, was calculated. This name implies that resonance generates a standing wave composed of counterpropagating waves traveling in the vertical direction (according to Fig. 1). It was found that the resonant frequency of the fundamental mode depends on the film extension along the waveguide only slightly but varies significantly at higher modes. The essential and practically important feature of this resonator is that the density of the current passing through the metal film in the vertical direction does not depend on the film length.

The difference between our experiments with the metallic superlattice and those carried out with superlattices consisting of thicker metallic and superconducting films [8] is that the total metal thickness in our superlattice is several tens of times smaller than the skin depth. This fact is insignificant when the resonant frequency is estimated, especially for the fundamental mode. However, the relationship between the tangential components of the electric and magnetic fields, which depends on the surface impedance, is of significance for calculating the Q factor of the resonator. Having regard for the high resistivity of the Fe/Cr superlattice, one may expect the Q factor of the resonator to be moderate. For example, the Q factor of the system near resonance at ≈9.7 GHz estimated from the data shown in Fig. 5 is less than 40. The frequency dependence of the microwave measurements for sample 1 exhibits resonance at 9.7 GHz and oscillations. Since the width of sample 2 is almost half as much as that of sample 1, the resonance condition for sample 2 is not met in the frequency range used in this work.

When analyzing the experimental data shown in Figs. 4–6, one should bear in mind that the transmission coefficient magnitude as a function of the magnetic field was measured for the resonator that was cascaded in the microwave channel. The application of an external magnetic field changes the conductivity of the sample. Accordingly, the Q factor of the resonator and the transmission coefficient of the entire system also change. The very fact of these changes and the dependence of the related parameters on the external magnetic field strength indicate that the microwave GMR effect takes place. This is confirmed by the results shown in Fig. 4 and also by comparing the dc (Fig. 2) and microwave (Fig. 3) magnetoresistance curves. The amount of resonance depends on the proximity of the frequency to any eigenfrequency of the surface wave resonator and also on the ratio between the sample length along the waveguide axis and the wavelength of the H_{10} mode in the waveguide. The same controls the sign of microwave variations.

The complex oscillatory dependence of the transmission coefficient on the frequency (Fig. 6) was treated in terms of wavelet analysis [9]. The coefficients of the wavelet transform (otherwise, the wavelet spec-

trum or the diagram of wavelet coefficients) of a function $f(t)$ are given by

$$W(s,\Theta) = W[f(t)] = \frac{1}{\sqrt{|s|}}\int_{-\infty}^{+\infty} f(t)\psi^*\left(\frac{t-\Theta}{s}\right)dt = \int_{-\infty}^{+\infty} f(t)\Psi^*_{s\Theta}(t)dt, \quad (1)$$

where

$$\Psi_{s\Theta}(t) = \frac{1}{\sqrt{|s|}}\psi\left(\frac{t-\Theta}{s}\right)$$

is the family of wavelets or basis functions of the wavelet transform with $\|\psi\| = 1$ (where $\|\psi\|$ is the norm of the function ψ), s is a scale factor, and Θ is the shift parameter. The factor $1/\sqrt{|s|}$ is introduced for all the wavelets of one family to have the unit norm at any t. The scale factor s shows how many times the width of the basis function $\psi(t/s)$ increases ($s > 1$) or decreases ($s < 1$) compared with the generating wavelet $\psi(t)$. Finally, the shift parameter Θ indicates how much the basis function is shifted relative to the zero time.

Thus, the basis of a wavelet transform is a set of wavelets, i.e., functions defined in a finite range of the argument t and differing from one another by scale of argument variation and shift parameter. The basic advantage of wavelet transformation over traditional Fourier transformation is a finite range of definition of the basis functions, which makes it possible to reveal and analyze local features of transient processes. Moreover, basis functions of wavelet transformation are mutually orthogonal at any value of the scale factor (i.e., at any width of a wavelet) unlike Fourier transformation in windows. Finally, wavelet transformation provides the possibility of analyzing both small-scale and regular features of functions in terms of a single mathematically rigorous procedure.

The diagram of the wavelet coefficients for the frequency dependence of the relative variation of the transmission coefficient magnitude when the external field is normal to the plane of the superlattice (Fig. 5) is shown in Fig. 6. As a generating wavelet, we used the MHAT wavelet, which is given by [10]

$$\psi(t) = \frac{-2}{\sqrt{3\sqrt{\pi}}}(t^2-1)\exp\left(-\frac{1}{2}t^2\right).$$

The abscissa in Fig. 6 is the shift parameter, which, in our case, can be identified with the frequency that serves as an argument in the frequency dependence of the relative variation of the transmission coefficient magnitude (Fig. 5). On the vertical axis, the oscillation frequency of the transmission coefficient magnitude is plotted. This frequency is calculated from the scale factor s by multiplying it by a constant [9] ($\sqrt{2}\pi$ for the MHAT wavelet). The loops in the diagram indicate the presence of several oscillation periods.

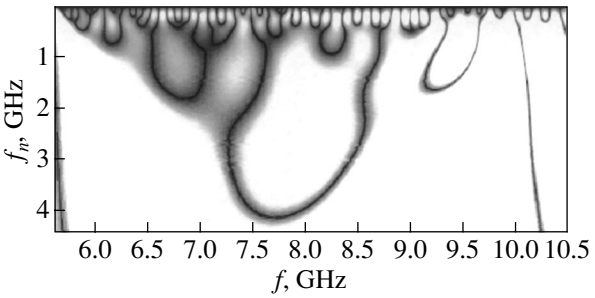

Fig. 6. Diagram of wavelet coefficients for the frequency dependence of the relative variation of the transmission coefficient magnitude for sample 1. f, frequency; f_n, oscillation frequency.

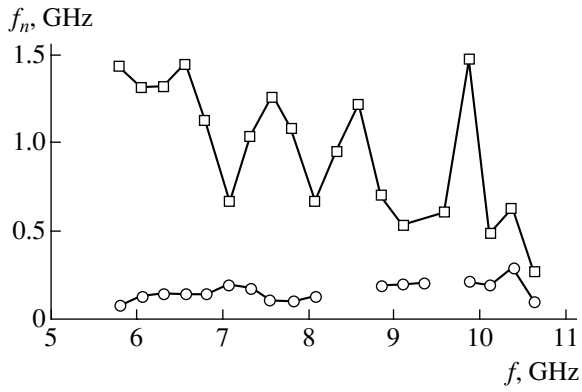

Fig. 7. Dominant oscillation frequencies in the variation of the transmission coefficient vs. wave frequency for sample 1.

Of great importance is the distribution of the energy of a signal being analyzed over scale factors, the scalogram of a wavelet transform, which can be written in the form

$$E_W(s) = \int_{-\infty}^{+\infty}\frac{|W(s,\Theta)|^2}{|s|}d\Theta. \quad (2)$$

It is known [9] that a scalogram represents the signal energy density $|W(s,\Theta)|^2$, which is normalized to the absolute value of the scale factor $|s|$ and is averaged over all possible values of the shift parameter Θ. Maxima in a scalogram correspond to characteristic scales on which a major part of the process energy is concentrated.

Scalogram (2) is defined throughout the length of a realization considered. However, the energy distribution over scale factors on the length of a realization is of special interest in transient analysis. To this end, one

may use a partial scalogram in the form

$$E_W^{\Delta}(s, \Theta_0) = \int_{\Theta_0 - \frac{\Delta\Theta}{2}}^{\Theta_0 + \frac{\Delta\Theta}{2}} \frac{|W(s, \Theta)|^2}{|s|} d\Theta, \quad (3)$$

where $\Delta\Theta$ is the range of the shift parameter that is reckoned from a certain fixed value Θ_0.

If the shift parameter varies in the interval Θ_{min}–Θ_{max}, this interval can be covered by varying Θ_0 from $\Theta_{min} + \Delta\Theta/2$ to $\Theta_{max} - \Delta\Theta/2$ and determining characteristic scales of a process being analyzed within a window of width $\Delta\Theta$ each time.

By applying formula (3) to the wavelet spectrum in Fig. 6, one can determine dominant oscillation frequencies for the relative variation of the transmission coefficient magnitude. Consider the curve obtained for sample 1 when the external field is oriented parallel to the plane (see Fig. 7). Here, as in Fig. 6, the vertical axis plots the oscillation frequency calculated from the scale factor s by multiplying it by $\sqrt{2}\pi$.

From Fig. 7, it follows that the realization being analyzed has two basic ranges of oscillation frequencies. In the diagram of wavelet coefficients (Fig. 6), these ranges correspond to the loops centered in these ranges of oscillation frequencies. One of the loops has a small dispersion and may be associated with the fundamental mode of the resonator; the other may be assigned to a higher mode of the resonator.

CONCLUSIONS

We studied interaction between an rf electromagnetic field and the Fe/Cr superlattice placed in a rectangular waveguide so that the longer side of the superlattice is parallel to the waveguide axis and the plane of the superlattice is parallel to the narrow wall of the waveguide. In this configuration, the high-frequency current passes in the plane of the superlattice. The transmission coefficient versus the magnetic field strength is found at centimeter waves, and a correlation between this dependence and the field dependence of the dc magnetoresistance is established. It is shown that the transmission coefficient and magnetoresistance depend on the magnetic field in a similar way and that a change in the transmission coefficient may several times exceed the dc giant magnetoresistance in magnitude. The frequency dependence of the microwave measurements has an oscillatory character. Analysis of this dependence in terms of wavelet transformation revealed two types of oscillation periods.

The results obtained in this work provide a basis for the development of magnetically controlled rf devices based on the microwave GMR effect. Such devices will be simple in design and offer a high performance, since the resistance of the superlattice placed in a magnetic field can be controlled even more effectively by applying resonant electrodynamic systems.

ACKNOWLEDGMENTS

This work was supported by the Russian Foundation for Basic Research (project no. 01-02-96429), the Ministry of Industry and Science of the Russian Federation, and the Presidium of the Russian Academy of Sciences (program “Quantum Macrophysics”).

REFERENCES

1. M. N. Baibich, J. M. Broto, A. Fert, *et al.*, Phys. Rev. Lett. **61**, 2472 (1988).
2. J. J. Krebs, P. Lubitz, A. Chaiken, and G. A. Prinz, J. Appl. Phys. **69**, 4795 (1991).
3. B. K. Kuanr, A. V. Kuanr, P. Grunberg, and G. Nimtz, Phys. Lett. A **221**, 245 (1996).
4. V. V. Ustinov, A. B. Rinkevich, L. N. Romashev, and V. I. Minin, J. Magn. Magn. Mater. **177–181**, 1205 (1998).
5. V. V. Ustinov, A. B. Rinkevich, and L. N. Romashev, J. Magn. Magn. Mater. **198–199** (6), 82 (1999).
6. V. V. Ustinov, L. N. Romashev, V. I. Minin, *et al.*, Fiz. Met. Metalloved. **80** (2), 71 (1995).
7. A. B. Rinkevich, L. N. Romashev, and V. V. Ustinov, Zh. Éksp. Teor. Fiz. **90**, 834 (2000) [JETP **90**, 834 (2000)].
8. G. A. Melkov, Y. V. Egorov, O. M. Ivanjuta, *et al.*, J. Supercond.: Incorporating Novel Magnetism **13**, 95 (2000).
9. N. M. Astaf’eva, Usp. Fiz. Nauk **166**, 1145 (1996) [Phys. Usp. **39**, 1085 (1996)].
10. L. R. Rabiner and B. Gold, *Theory and Application of Digital Signal Processing* (Prentice-Hall, Englewood Cliffs, 1975; Mir, Moscow, 1978).

Translated by V. Isaakyan

Technical Physics, Vol. 49, No. 5, 2004, pp. 619–622. Translated from Zhurnal Tekhnicheskoĭ Fiziki, Vol. 74, No. 5, 2004, pp. 101–104.

ELECTRON AND ION BEAMS, ACCELERATORS

Thin Carbon Films: II. Structure and Properties

A. P. Semyonov, A. F. Belyanin, I. A. Semyonova, P. V. Pashenko, and Y. A. Barnakov

Buryat Scientific Center, Siberian Division, Russian Academy of Sciences, Ulan-Ude, 670047 Buryat Republic, Russia

e-mail: semenov@pres.bsc.buryatia.ru

Received March 28, 2003; in final form, August 18, 2003

Abstract—The growth of thin carbon films of various modifications is studied. The films are applied by ion-beam sputtering of graphite, and the resulting carbon condensate is exposed to either ion or electron beams at low temperature and pressures. The phase composition, structure, surface morphology, and emissivity of the carbon films are examined by X-ray diffraction, Raman spectroscopy, and atomic-force microscopy. © *2004 MAIK "Nauka/Interperiodica".*

INTRODUCTION

At the current stage of thin carbon film growth technology, special emphasis is on diamond as a semiconducting material for solid-state microelectronics, acoustoelectronics, and emission electronics [1]. Also, the extremely high hardness of diamond makes it very promising for abrasive and cutting tools. Diamond offers a unique combination of properties, such as the highest thermal conductivity at 300 K on record (20–25 W/(cm K)), a carrier drift velocity of 2.7×10^7 cm/s, a breakdown field of 2×10^7 V/cm, and a Mohs' hardness of 10. In addition, it can withstand a fast-neutron fluence of 2×10^{14} cm^{-2} and an adsorbed dose of γ radiation of 5×10^5 Gy. Taken together, these properties render diamond an indispensable material for high-speed and radiation-resistant electronics, detectors of high-energy particle fluxes and ionizing electromagnetic radiation, field-emission cathodes, heat sinks, optical windows, X-ray diaphragms, and protective antireflection interference coatings for solar cells. Moreover, diamond features the highest velocity of propagation of surface acoustic waves (≈9 km/s) among all known materials; so, it can be used to advantage in acoustoelectronics. The feasibility of diamond-like materials as electron sources is based on their negative electron affinity, which allows one to decrease the emission threshold of nonincandescent cathodes in emissive electronic devices.

Much progress toward growing thin carbon films of various modifications (diamond, diamond-like carbon, and carbyne) has been achieved using low-temperature growth *in vacuo*. In this method, graphite is sputtered by ion beams and the resulting carbon condensate is then exposed to either ion or electron beams. Note that this is today a basic trend in using gas-discharge ion sources.

EXPERIMENTAL

Thin carbon films are usually grown using two basic methods: (i) ion beam sputtering of graphite followed by exposing the resulting carbon condensate to a high-energy electron beam and (ii) growth and subsequent irradiation of the films with one wide ion beam. At the first stage of process (i) [2], the films are grown on silicon substrates by sputtering 99.99% pure graphite using a mixed argon–hydrogen ion beam at a pressure of 6.6×10^{-3} Pa and a substrate temperature below 673 K. The ion beam current and energy are 5–10 mA and 4 keV, respectively. At the second stage, the amorphous (as indicated by X-ray diffraction data) thin carbon films are irradiated by a wide electron beam for 1 to 10 s to provide various heating conditions. The electron beam power ranges from 100 to 200 W. In case (ii), thin diamond-like carbon films are grown and irradiated with a wide argon–hydrogen ion beam at a substrate temperature of 293 K. The ion beam is obliquely incident on a graphite target (sputtering) and makes an angle of 85°–90° with the normal to the growth surface (irradiation under grazing incidence). In such a way, the necessary conditions for growing thin diamond films (such as a high supersaturation, hence, a high probability of nucleation; prevention of the graphite structure formation; and prevention of the diamond–graphite transition) are provided [3]. The growth conditions are such that scattering of incident ions by a growing film is an essential factor. Because of this, recoil atoms can create compressive stresses as high as ≈10 GPa at the growth surface, which favors the formation of the diamond phase. This process involves two atomic fluxes. One is the flux of carbon atoms knocked out from the target and impinging on the substrate, where they coalesce, forming the next layer and causing the growth surface to move with a certain flux-density-dependent rate. The other is the flux of recoil carbon atoms, which arise from scattering of ions in the bulk of a growing film and move toward its surface. This flux produces a

1063-7842/04/4905-0619$26.00

certain limiting concentration of interstitials, which induce stresses in a growing layer, making the diamond phase stable. The structure and surface morphology of the films, as well as phase nucleation, were examined by X-ray diffraction (Rigaku diffractometer, CuK_α radiation), Raman spectroscopy (Dilor-Jobin Y T6400TA spectrometer, the 488-nm line of an argon laser), and atomic-force microscopy (Digital Instruments Nanoscope 3 instrument operating in the contact mode, Si_3N_4 tip). The electron emissivity of the carbon films was studied by measuring the emission current versus the applied electric field. The electric field in the electrode gap was calculated as $E = V/d$, where V is the potential difference between the electrodes and d is the width of the electrode gap. The emission current was measured at a pressure of $\approx 1.33 \times 10^{-4}$ Pa by applying voltage pulses with a width of 30 μs and a repetition rate of 50 Hz. The film thickness was ≈50 nm; the emitting surface area, ≈0.25 cm^2. An electric field up to 5.6 kV was applied between the flat silicon substrate and flat anode electrode. The length of the vacuum gap between the film surface and anode was ≈160 μm.

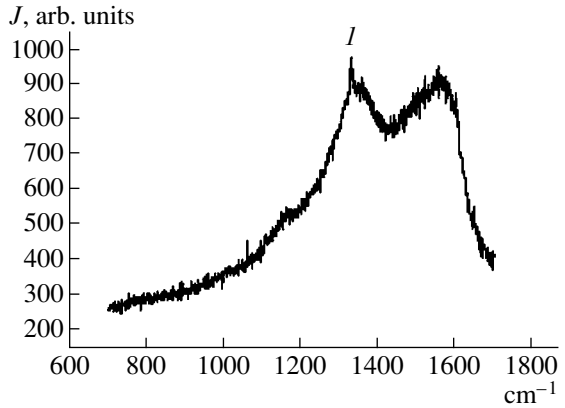

Fig. 1. Raman spectrum from a thin polycrystalline diamond-like carbon film (peak *1* at 1330 cm^{-1}).

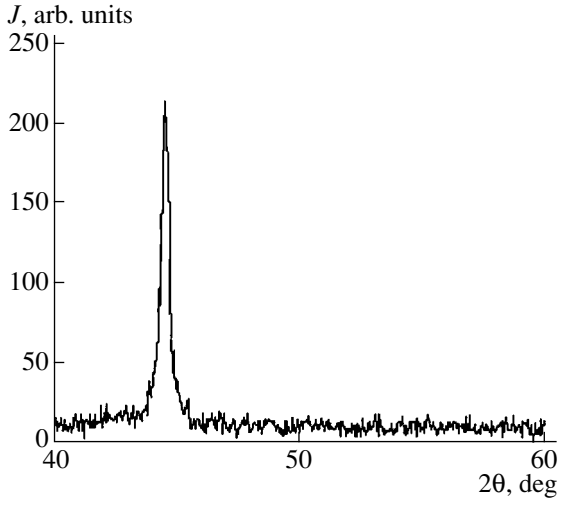

Fig. 2. X-ray diffraction pattern taken of a thin polycrystalline diamond-like carbon film.

RESULTS AND DISCUSSION

Thin carbon films obtained by sputtering the graphite target and then irradiated by the charge-particle beam were continuous and had a thickness from 50 nm to 6 μm. Under the two-stage growth conditions, electron irradiation causes the film to crystallize into the carbyne hexagonal structure. Carbyne is the linear carbon modification with *sp*-hybridized atoms, which possesses semiconducting properties (the band gap is ≈1 eV). Figure 1 shows the Raman spectrum from a 6-μm-thick polycrystalline carbon film grown by one-stage deposition. The intense narrow diamond peak at 1330 cm^{-1} indicates that diamond is the basic component of the film. The broad line at 1580 cm^{-1} is due to amorphous graphite. In the Raman spectra of the films grown under other conditions, the relative intensities, widths, and positions of the lines change, thus indicating changes in the phase composition, the crystallite sizes, and the degree of amorphization of the films [3]. The conclusions about the phase composition that were drawn based on the Raman data were supported by the X-ray diffraction and high-resolution electron microscopy data. The X-ray diffraction patterns have a diffraction peak at $2\theta = 44.452°$ ($d = 0.20364$ nm), which corresponds to the diamond structure (Fig. 2). The examination of the carbon film surface (Fig. 3) shows that the films pass through the globular growth stage, at which globules with a surface size of 50 nm and a height of 5 nm form. The average height of surface asperities is 6.425 nm. Diamond is known to grow in several stages: the formation of globules, the formation of {100} faces on globules, the stage of geometrical selection, the formation of the primary ⟨100⟩ axial texture, and the formation of the secondary ⟨110⟩ and ⟨111⟩ conic textures [4]. The occurrence of these stages depends on the growth temperature. In the low-temperature range, only the globular stage takes place. The thickness of a layer of globular diamond may vary from several tens of nanometers to several tens of micrometers according to growth conditions. Varying the ion sputtering parameters and growth conditions, one can control the content of carbon phases in the thin films.

Carbon films of various structural modifications are promising for efficient field-emission cathodes [5]. Field emission occurs without heating a cathode, which makes it possible to produce a flux of slow electrons and, hence, to simplify the design of solid-state vacuum devices. The possibility of applying diamond materials as electron sources is based on their negative electron affinity, which was predicted theoretically and found experimentally in both diamond single crystals and polycrystalline diamond films [6]. In particular, a negative electron affinity of an emitting surface allows for a significant decrease in a field-emission-initiating electric field from 10^3–10^4 V/μm (the values character-

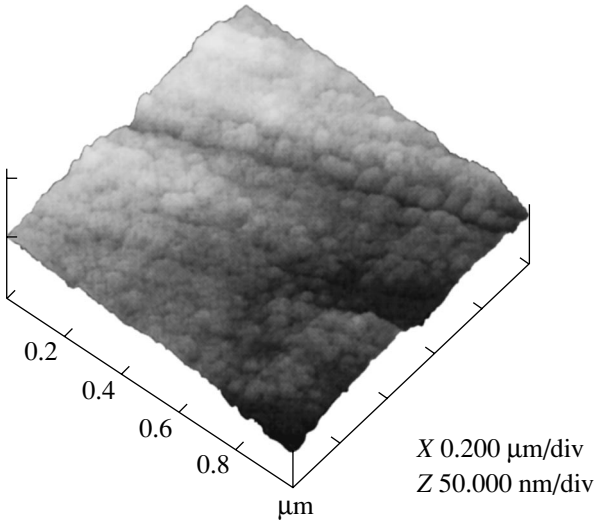

Fig. 3. Surface image of a carbon film.

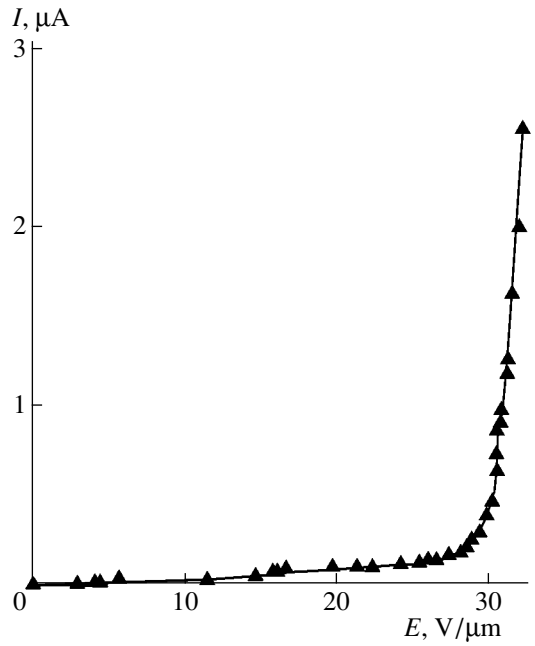

Fig. 4. *I–V* characteristic of a nonincandescent cathode.

istic of most metals and semiconductors) to 1–10 V/μm [7]. At the same time, the conductivity of polycrystalline diamond films depends on various structural defects, which produce extra levels in the band gap or extended regions of nondiamond carbon. The emissivity of diamond films is known to improve substantially as the density of defects rises up to amorphization. The characteristic sign of amorphization is the diamond-type hybridization of valence electron bonds in carbon atoms. For field-emission cathodes, the threshold electric field at which field electron emission occurs varies from 2 to 20 V/μm [8].

All carbon films grown under the conditions described above emitted electrons at a certain potential difference applied between the film cathode and anode. For the nanocrystalline diamond films, the threshold electric field of cold emission in the cathode–anode gap was found to be 30 V/μm. The emission current density was equal to 1.2×10^{-5} A/cm^2. Figure 4 shows the dependence of the field-emission current on the electric field. A sharp increase in the electron current (emission threshold) is observed at 3×10^5 V/cm, although emission becomes tangible even at $\approx 1.5 \times 10^5$ V/cm. Using the experimental emission characteristic, we calculated the work function φ by the Fowler–Nordheim theory, which relates the electron emission current density to the electric field by the expression [9]

$$J = 1.4 \times 10^{-6}(E^2/\varphi) \times 10^{4.39/\varphi^{1/2}} \times 10^{-2.82 \times 10^7(\varphi^{3/2}/E)}, \quad (1)$$

where φ is the work function, eV; j is the electron emission current density, A/cm^2; and E is the electric field strength, V/cm. Substituting $j = 1.2 \times 10^{-5}$ A/cm^2 and $E = 3 \times 10^5$ V/cm into Eq. (1), we have $\varphi \approx 0.332$ eV. Thus, the carbon films grown by charged particle beams offer a relatively high efficiency of field emission.

CONCLUSIONS

A method of growing thin carbon films of various modifications by ion-beam sputtering was proposed. It was shown that sputtering of graphite followed by irradiation of the carbon condensate by either an ion or electron beam provides necessary conditions for the formation of the diamond phase and can be used for growing thin films of diamond-like carbon or carbyne at low temperatures and pressures. The phase composition, structure, surface morphology, and field emissivity of the carbon films grown were considered. Exposure of the carbon condensate to an ion or electron beam is found to cause crystallization of the thin films. In the low-temperature stage, growth is limited by the globular stage and the films have a high content of the amorphous phase. Thin carbon films of various modifications (diamond and carbyne) grown under the conditions considered above may serve as efficient heat-removing, emissive, protective, or hardening coatings. Thin-film field-emission cathodes offering a relatively high efficiency of field emission at an electric field of $\approx 3 \times 10^5$ V/cm were made on ≈50-nm-thick carbon films with a work function of ≈0.33 eV that were grown by the method suggested.

A charge-particle source [10] proved to be highly efficient for growing thin carbon films with a high content of the diamond phase by ion and electron beams at low temperatures and pressures.

ACKNOWLEDGMENTS

This work was supported in part by the Lavrent'ev Young Scientists Competition at the Siberian Division, Russian Academy of Sciences (project no. 37).

REFERENCES

1. P. P. Vecherin, V. V. Zhuravlev, V. B. Kvaskov, Yu. A. Klyuev, A. V. Krasil'nikov, M. I. Samoĭlovich, and O. V. Sukhodol'skaya, *Natural Diamonds of Russia* (Polyaron, Moscow, 1997) [in Russian].
2. A. P. Semyonov, A. F. Belyanin, I. A. Semyonova, *et al.*, in *Proceedings of the 5th International Symposium "Diamond Films and Films of Diamond-Like Materials," Khar'kov, 2002*, pp. 79–82.
3. I. A. Semyonova, A. P. Semyonov, and A. F. Belyanin, in *Proceedings of the 1st International Congress on Radiation Physics, High Current Electronics, and Modification of Materials, Tomsk, 2000*, Vol. 3, pp. 411–415.
4. A. F. Belyanin, P. V. Pashenko, A. A. Blyablin, *et al.*, in *Proceedings of the 12th International Symposium "Thin Films in Electronics," Khar'kov, 2001*, pp. 96–105.
5. M. I. Elinson and G. F. Vasil'ev, *Field Emission* (GIFML, Moscow, 1958).
6. F. J. Himpsel, J. A. Knapp, J. A. van Vechten, and D. E. Eastman, Phys. Rev. B **20**, 624 (1979).
7. G. A. J. Armatunga and S. R. P. Silva, Appl. Phys. Lett. **68**, 2529 (1996).
8. A. N. Obraztsov, I. Yu. Pavlovskiĭ, and A. P. Volkov, Zh. Tekh. Fiz. **71** (11), 76 (2001) [Tech. Phys. **46**, 1437 (2001)].
9. G. A. Mesyats, *Ectons* (Nauka, Yekaterinburg, 1993), Part 1.
10. A. P. Semyonov and I. A. Semyonova, Zh. Tekh. Fiz. **74** (4), 102 (2004) [Tech. Phys. **49**, 479 (2004)].

Translated by K. Shakhlevich

Technical Physics, Vol. 49, No. 5, 2004, pp. 623–629. Translated from Zhurnal Tekhnicheskoĭ Fiziki, Vol. 74, No. 5, 2004, pp. 105–112.

SURFACES, ELECTRON AND ION EMISSION

Energy Distributions of Electrons Emitted from Tungsten Tips Covered by Diamond-Like Films

S. A. Pshenichnyuk* and Yu. M. Yumaguzin**

** Institute of Physics of Molecules and Crystals, Ufa Scientific Center, Russian Academy of Sciences, pr. Oktyabrya 151, Ufa, 450075 Bashkortostan, Russia*

*** Bashkortostan State University, ul. Frunze 32, Ufa, 450074 Bashkortostan, Russia*

e-mail: sapsh@anrb.ru

Received March 5, 2003; in final form, August 29, 2003

Abstract—The energy distribution of electrons emitted from the surface of diamond-like pointed cathodes under the action of a high electric field is reported. Diamond-like coatings are applied on thin tungsten tips by ion-beam evaporation in an ultrahigh vacuum. The structure of the carboniferous films covering the tungsten tips is examined by field-emission microscopy. The stability of the field-emission cathode current is considered, and the Fowler–Nordheim *I–V* characteristics are presented. Based on the results obtained, a model of field-emission cathode covered by a thin diamond-like coating that explains the energy distributions is suggested. © *2004 MAIK "Nauka/Interperiodica"*.

INTRODUCTION

Carboniferous films with the diamond structure are a promising material for cathodes (tips) of field-emission vacuum devices [1]. The basic obstacle to the wide application of cathodic tips is their unstable characteristics due mostly to fast contamination of the emitting surface by residual gas molecules in a medium vacuum. Diamond eliminates this problem, since its surface is chemically inert and weakly sensitive to adsorption [2]. Another important property of diamond is the negative electron affinity of the (111) face of Group IIb natural semiconducting diamond [3], which makes it possible to substantially reduce (down to 10^5 V/cm) field strengths used for cold emission of electrons [4]. Today, the emissivity of diamond coatings on both flat surfaces [5, 6] and very thin metallic and semiconducting tips [7, 8] is the subject of extensive research. There exist a number of theoretical works concerned with field emission from diamond-based structures [9–11]. Experiments on field emission from diamond-like films usually boil down to taking the Fowler–Nordheim characteristic and estimating the work function. Data on the stability of the field-emission current from diamond cathodes are also available. Energy distributions of electrons emitted under an ultrahigh vacuum that are taken with high-resolution analyzers are almost nil. However, these distributions would provide valuable information about the emission process. Moreover, at this point in the research, it is necessary to compare these distributions with the *I–V* characteristics and field-emission images of the tips coated by diamond-like films. Comparative analysis could support or rule out the present-day model notions of the thin tip–diamond-like film system.

In this work, we examine diamond-like films on tungsten tips by field-emission spectroscopy. The energy distributions of electrons versus the electric field strength at the cathode are obtained. Also, the *I–V* characteristics of the films, field-emission microscopy data on their structure, and the evolution of the field-emission current with time are reported. Based on this data, a model of an emitting tungsten tip coated by a thin diamond film is developed.

EXPERIMENTAL

(i) Diamond-like film evaporation. Diamond-like films were applied on tungsten tips by ion-beam evaporation. Positive carbon ions of energy 10–100 eV and current 1–25 μA were directed on the tip surface by a beam-forming system consisting of an electrostatic lens and deflecting plates. The process was carried out at a pressure of 10^{-7} Torr provided by an oil-free pump. Prior to evaporation, the tip surface was cleaned by heating to high temperatures (≈1500°C) and bombarding with 500-eV argon ions. The source of positive carbon ions and the design of the ion-beam evaporator were detailed in [12].

(ii) Field-emission characteristics. Tips on which diamond-like films were deposited were made of polycrystalline tungsten wires 0.08 mm in diameter with grains oriented largely in the [011] drawing direction. The same wires were used to prepare an ear on which the tips were mounted when heated by applying a current. The wires were sharpened by electrochemically etching in a saturated water solution of KOH. The radius of the tips obtained was no greater than 1 μm. The tips were then rinsed in distilled water and placed in a high-vacuum deposition chamber. Immediately

1063-7842/04/4905-0623$26.00

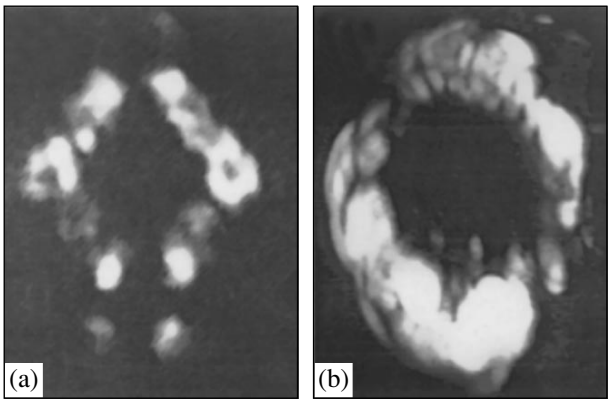

Fig. 1. Typical field-emission images of the tungsten tip coated by the (a) thin and (b) thick diamond-like film.

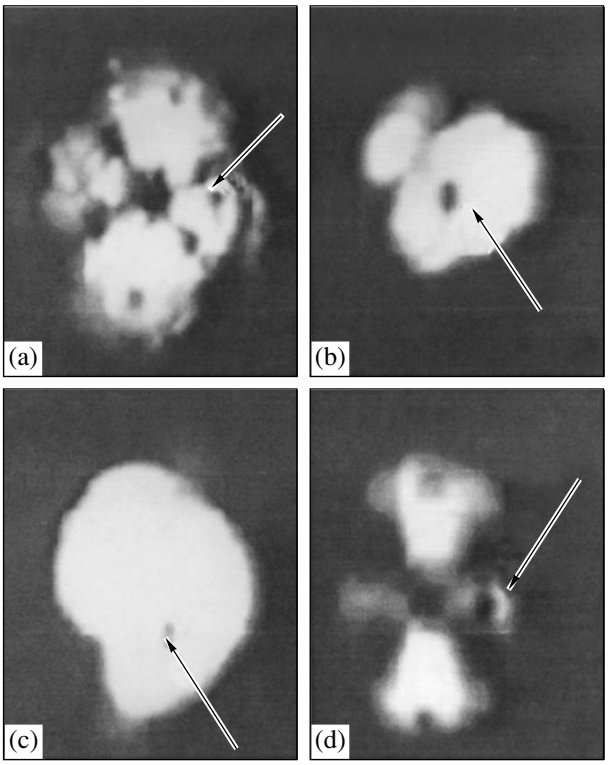

Fig. 2. Field-emission images of sample 3: (a) as-prepared (pure) tungsten tip, (b, c) diamond-like cluster on the (111) face of the tungsten tip, and (d) the same tip after the removal of the diamond-like cluster by heating. The corresponding emission voltages are (a) 3.4, (b) 1.5, (c) 1.9, and (d) 4.0 kV.

before deposition, the tips were heated to ≈800°C by passing a continuous current and then to ≈1500°C by passing a pulsed current through the ear to remove contamination. Then, the emitter was bombarded with ≈500-eV Ar^+ ions to provide the atomically clean surface. We studied three types of diamond samples (in all experiments, the ion energy during deposition was 65–70 eV and the current of positive carbon ions at the substrate was 1 μA): a thick film (deposition time 2 h), a thin film (deposition time 1 h), and a carbon cluster on the (111) face of the tungsten tip (deposition time 1 h).

The thickness of the layers deposited could not be measured directly. Estimated from the deposition time, it did not exceed several tens of carbon monolayers when a continuous film formed.

The system for studying field emission from cathodic tips is described in detail elsewhere [13]. The residual pressure provided by oil-free magnetic-discharge pumping was no higher than 10^{-10} Torr. Data processing and control of the operation of the setup were accomplished with a PC with the KAMAK standard interface. The ultrahigh-vacuum chamber of the spectrometer is provided with a rotation-and-displacement system, which makes it possible to display desired areas of the tip on a fluorescent screen with a magnification of 10^6. The distribution of the emitted electron total energy was taken with a dispersion energy analyzer consisting of seven electrostatic lenses. The diameters of the entrance and exit diaphragms were 0.50 and 0.17 mm, respectively; the resolution of the analyzer, 20 meV; and the range of measurement, 2.5 eV. The electrons passing through the exit diaphragm fell on the input of a VÉU-6 secondary emission electron multiplier operating as an electronic counter. The high amplification of the VÉU (on the order of 10^7) allowed us to display weakly emitting areas of the tip surface.

RESULTS

(a) Field-emission microscopy. A typical field-emission image of the diamond-like film on the tungsten tip surface is shown in Fig. 1. The image is typical in that emission from the central part of the film (i.e., from the (011) face of the tip) is absent (in all test samples). When the coating is thin (Fig. 1a), the image is symmetric, which means that the diamond-like film has a regular crystal structure at the initial stage of growth. As the deposition time increases (Fig. 1b), the structure becomes irregular with carbon clusters at the edges of the (011) central face of the substrate (tip). These clusters form microprotrusions, from which emission takes place when the film is sufficiently thick. The clusters decay when the temperature reaches 1000°C [14]. It seems that the arrangement of the clusters is related to the crystal structure of the as-prepared tip, since the field-emission image has certain symmetry; namely, electrons are emitted largely from the circumference of the (011) central face of the tungsten tip.

The diamond-like film on the tip sometimes consists of carbon atom clusters. Figure 2 shows the sequence of field-emission images taken (Fig. 2a) from the as-prepared tungsten tip, (Figs. 2b, 2c) after the deposition of a diamond-like cluster, and (Fig. 2d) after the evaporation of the cluster by heating the tip to 1500°C. The arrows indicate the position of the entrance diaphragm of the energy analyzer. It is seen that the final image closely copies the initial pattern of emission.

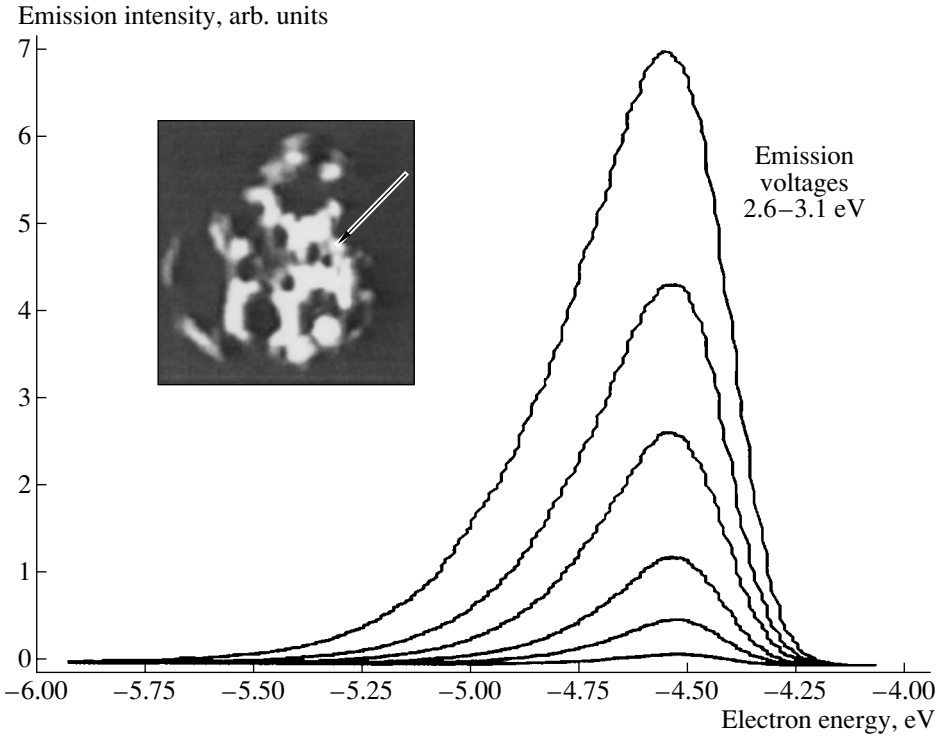

Fig. 3. Energy distributions of electrons emitted from the as-prepared tungsten tip at different emission voltages and corresponding image of the tip (the inset) obtained by field-emission microscopy.

(ii) Electron energy distribution. The energy distributions of emitted electrons for different emission voltages (a series of distributions) were taken in a single program cycle. During the series, the field-emission image of the tip remained unchanged. The insets demonstrate the related field-emission images, where the arrows indicate the position of the entrance diaphragm of the energy analyzer, i.e., the areas of the tip from which the distributions were taken.

Figure 3 shows the electron energy distributions taken from the as-prepared tungsten tip. The related field-emission image is characteristic of a tip that is not smoothed out by heating (a so-called ribbed tungsten tip [15]). The position of the peak (at –4.51 eV) is almost independent of the emission voltage. The FWHM of the curves is small (≈0.28 eV), which is typical of emission from metal surface. The smooth rise in the emission intensity with increasing emission voltage is noteworthy.

Typical spectra obtained from the tungsten tip coated by the thick diamond-like film (sample 1) is shown in Fig. 4. The emitting area (the inset) is the microprotrusion (mentioned above) produced by carbon clusters. The sharp rise in the emission intensity with increasing emission voltage is distinctly seen, which is typical of many diamond-like tips studied. Possibly, this is associated with the transition to region II in the *I–V* characteristic. The position of the peaks in these curves (–4.9 eV for the most intense curve) differs from that observed in the spectra from the uncovered tungsten tip. The considerable shift in the position of the peak with increasing voltage for three lowest curves manifests a voltage drop across the diamond-coated tip, i.e., the transition to region II in the *I–V* characteristic. Such behavior is typical of field emission from semiconductor surfaces. The curves taken at low emission voltages have the second maximum, whose position is nearly coincident with the position of the single peak in the spectra for the uncovered tungsten tip. This peak is attributed to the electrons that tunnel through the thin diamond-like film from the Fermi level of tungsten. This follows from the fact that its position depends on the emission voltage insignificantly.

The supposition that the electrons tunnel through the diamond-like film is also supported by the form of the energy distributions taken when the tungsten tip is coated by the thin film (sample 2, Fig. 5a). The intense peak (–4.51 eV) of the electrons tunneling from the Fermi level of tungsten is clearly seen. The wider part of the spectrum, which has the fine structure, is related to the diamond-like film. The position of the basic maximum here varies from –5.8 to –6.2 eV. This broad peak can be explained by the emission from the conduction band of the film. This is possible only if the energy bands are heavily inclined throughout the length of the carbon layer, which may take place when the emission voltage is very high. It also counts in favor of such a supposition that the peak of the electrons emitted from the tungsten substrate is fairly intense, which may be observed if the semiconducting coating in the area from

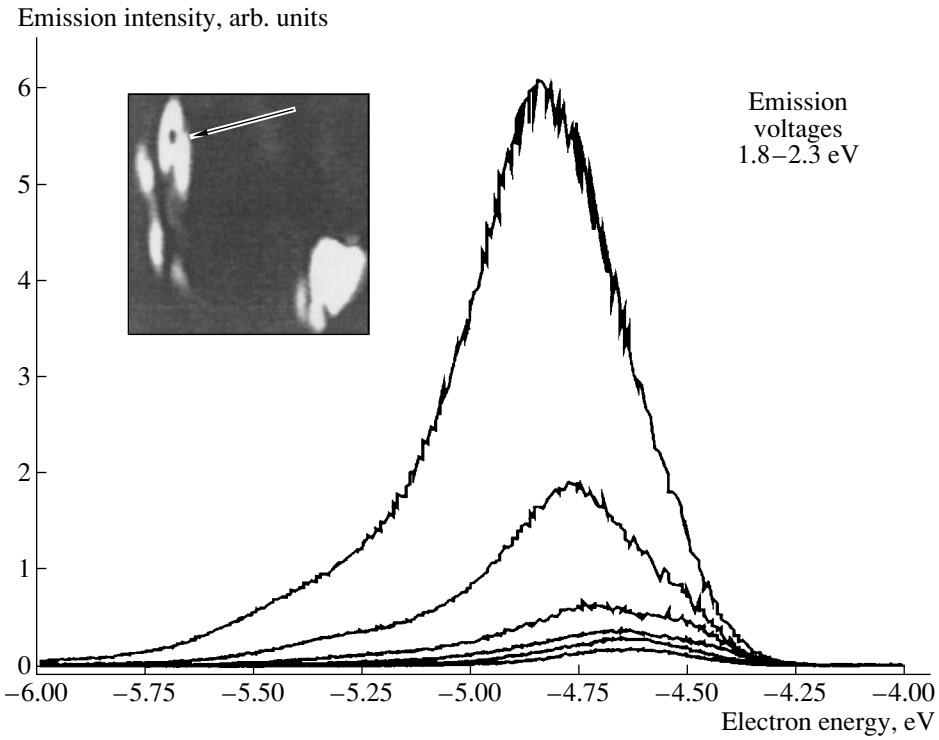

Fig. 4. Energy distributions of electrons emitted from the tungsten tip coated by the thick diamond-like film (sample 1) at different emission voltages.

which the energy distributions are taken is thin. This, in turn, favors a high inclination of the energy bands and, accordingly, a broadening of the energy distribution.

Sample 2 was heated to a high temperature (≈1500°C) in order to remove the carbon layer. The results for this series of experiments are shown in Fig. 5b. The field-emission image (the inset) suggests that the tip acquired a ribbed shape, which is typical of tungsten. The peak is now at –4.51 eV; i.e., it corresponds to an uncovered tungsten tip. It is known that a small amount of carbon atoms on the tip surface suppresses tungsten atom migration [15], which was the case in the experiments: the field-emission image and the form of the energy distribution remained unchanged upon heating to a higher temperature (≈2000°C) for a long time.

(iii) Emission current stability and Fowler–Nordheim *I–V* characteristics. The field emission microscopy data in Fig. 2 suggest that the emission intensity for sample 3 grows upon depositing the carbon cluster. This is clearly evident from Fig. 2b, where the image contrast is high while the emission voltage is relatively low. The Fowler–Nordheim *I–V* characteristics for the atomically clean tungsten tip and for the tip covered by the diamond-like film are presented in Fig. 6. These curves correspond to the field-emission images in Figs. 2a (pure W) and 2b (W/C composition). As a rule, Fowler–Nordheim characteristics are used for estimating the change in the work function upon film-thin deposition. Such an approach is valid if the electric field at the surface before and after deposition is the same. In our case, however, the curvature of the tip at the place of the carbon cluster changes significantly, as follows from the images in Figs. 2a and 2b, causing a related change in the local field strength. This makes direct estimation of the work function for the surface covered by the film impossible.

Below we report experimental data indicating that the diamond-like film improves the long-term stability of the field-emission current from the tip. Figure 7a shows the time variation of the total emission current normalized to its maximum value for the tip with and without the film. The pressure in the vacuum chamber was no higher than 10^{-8} Torr. For the uncovered tungsten tip, the total current irreversibly declines unlike the film-coated tip. The decrease in the total emission current for the pure tungsten tip is explained by severe contamination of the metal surface exposed to residual gas ions when a high voltage is applied to the tip. This is confirmed by the emission images of the tip that were taken before and after the measurements (Fig. 7b). It is clearly seen that a stable adatom layer forms on the surface. This layer can be removed only by heating. The field-emission image of the tip during the measurements remained unchanged (as in Fig. 2b), suggesting that the surface of the film is fairly stable against residual gas ion bombardment. The high fluctuation of the emission current (Fig. 7a) decays with time.

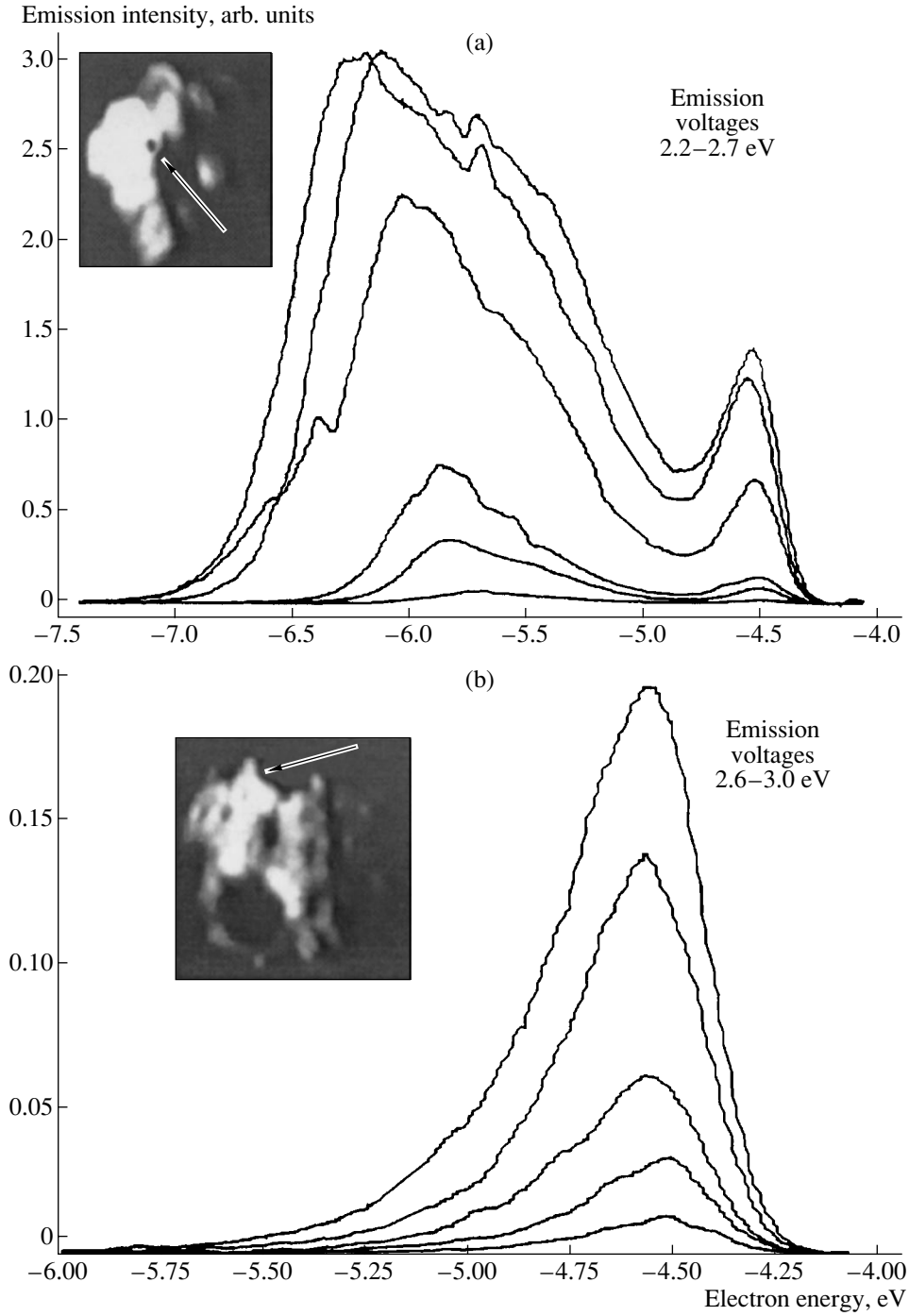

Fig. 5. Energy distributions of electrons emitted from the surface of sample 2: (a) the tungsten tip coated by the thin diamond-like film and (b) the tungsten tip after the removal of the film by heating at different emission voltages.

DISCUSSION

If the diamond-like surface has a small positive (or negative) affinity χ for electrons, the inequality

$$\frac{E_g}{2} + \chi < \varphi, \quad (1)$$

where φ is the work function of tungsten, is valid in a wide range of energy gaps E_g.

On the side of the film at the interface, a depleted region, or a potential barrier for electrons injected from the metal, forms. The conduction band bottom in the semiconducting layer lies above the Fermi level except for the case of high degeneracy, when the film contains a high concentration of donors. The band structure for this case in the absence of the emission voltage and tip current is represented in Fig. 8a. The extent L of the

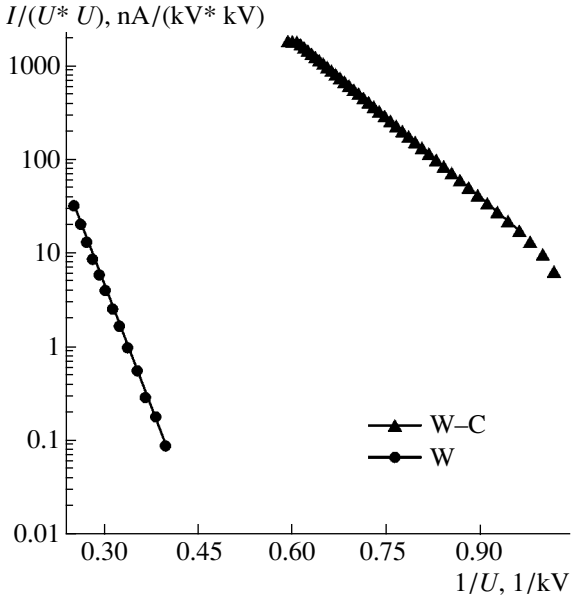

Fig. 6. Fowler–Nordheim *I–V* characteristics for the diamond-like cluster (W–C) and as-prepared tungsten tip (W). The corresponding field-emission images are presented in Figs. 2b and 2a, respectively.

depleted region at room temperature is estimated as 100 nm; that is, this region extends throughout the thickness of the diamond-like film in our case. With regard to the Schottky effect, this means the presence of a potential barrier, not a threshold, even in the absence of an external field. Probably, low-field emission is due to this fact.

In the case of thick films ($L < d$), injection of electrons from the Fermi level to the conduction band of the film is impossible until a high penetrating external field causes an additional bend of the energy bands in the film. In this case, a potential threshold turns into a barrier (even if the electrons thermally excited above the Fermi level of the system are taken into consideration). This explains the limitation sometimes imposed to the maximal thickness of a diamond-like film covering the tip [16, 17]; namely, if the penetration depth δ of an external field is $\delta < d - L$, electron injection to the conduction band is impossible and other mechanisms that explain stable delivery of charge carriers to the emitter surface must be invoked: the formation of conductive channels, conduction through defect-related energy bands, grain-boundary conduction, etc.

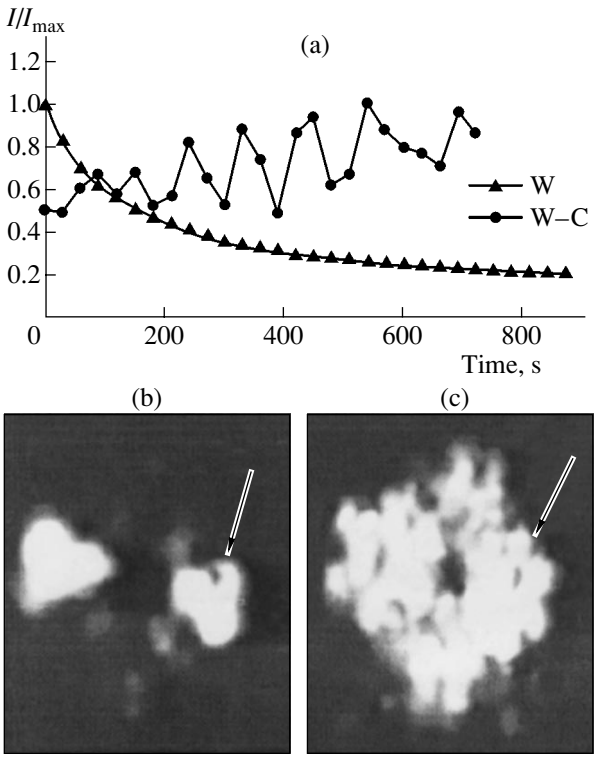

Fig. 7. (a) Time dependences of the emission current for the tungsten tip coated by the diamond-like film (W–C) and for the as-prepared tungsten emitter (W) and field-emission images of the tungsten emitter (b) before and (c) after taking this dependence.

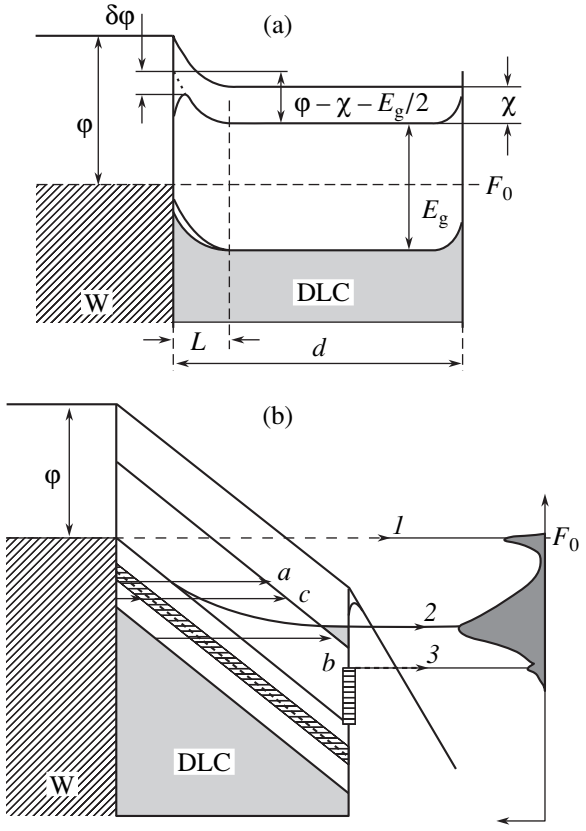

Fig. 8. Energy band diagram of a tungsten tip coated by a thin diamond-like film: (a) in the absence of an applied voltage and (b) in the presence of a high applied voltage and emission current. W, tungsten substrate; DLC, diamond-like coating.

The application of an external field and its penetration into a thin semiconducting carbon film on the tip causes a bend of the energy bands throughout the film. In our case of extremely thin films and high fields, the situation is such that the conduction band bottom in the subsurface layer is below the Fermi level of the system; i.e., a highly degenerate region forms. Then, the following electrons make a major contribution to the field-emission current (Fig. 8b).

(i) The electrons that ballistically (without an energy loss) tunnel through the thin semiconducting film from the Fermi level of the tungsten tip. If the electron affinity of the film is low, they pass through the barrier at the film–vacuum interface (the effective negative electron affinity).

(ii) The electrons that escape into a vacuum from the conduction band. The greater the bend of the bands, the wider the peak in the energy distribution that corresponds to this component of the total emission current. Charge carriers that fall into the conduction band of the film from the metal may be (a) the electrons of group (i) that are scattered by phonons or structural defects when traveling through the conduction band, (b) valence band electrons passing into the conduction band due to the Zener effect when the bend of the bands is high, and (c) the electrons that fall into the conduction band via local states or defect-induced energy bands both by the Zener mechanism and from the tungsten substrate.

CONCLUSIONS

We studied thin tungsten tips that are covered by diamond-like films grown by ion-beam evaporation. Diamond-coated field-emission cathodes are examined by the methods of field emission spectroscopy and field emission microscopy. The *I–V* characteristics of the emission show that a diamond-like coating tip makes the emitting surface of the tungsten tip less sensitive to residual gas adsorption, thereby extending the long-term stability of the tip's emissivity. A band diagram for the tip–film system that explains qualitatively experimental energy distributions of emitted electrons is constructed. Exact quantitative consideration requires that various electron scattering mechanisms in the film and also mechanisms of their escape into a vacuum be taken into account.

REFERENCES

1. W. Zhu, G. P. Kochanski, and S. Jin, Science **282**, 1471 (1998).
2. G. Davis, *The Properties and Growth of Diamond* (JEE, London, 1994).
3. F. J. Himpsel, J. A. Knapp, J. A. van Vechten, *et al.*, Phys. Rev. B **20**, 624 (1979).
4. W. Zhu, G. P. Kochanski, S. Jin, *et al.*, J. Vac. Sci. Technol. B **14**, 2011 (1996).
5. N. S. Xu, Y. Tzeng, and R. V. Latham, J. Phys. D **27**, 1988 (1994).
6. M. W. Geis, J. S. Twichell, J. Macaulay, *et al.*, Appl. Phys. Lett. **67**, 1328 (1995).
7. F. Y. Chuang, C. Y. Sun, H. F. Cheng, *et al.*, Appl. Phys. Lett. **68**, 1666 (1996).
8. A. F. Myers, S. M. Camphausen, J. J. Cuomo, *et al.*, J. Vac. Sci. Technol. B **14**, 2024 (1996).
9. P. H. Cutler, Z.-H. Huang, N. M. Miskovscy, *et al.*, J. Vac. Sci. Technol. B **14**, 2020 (1996).
10. N. M. Miskovscy, P. H. Cutler, and Z.-H. Huang, J. Vac. Sci. Technol. B **14**, 2037 (1996).
11. P. H. Cutler, N. M. Miskovscy, and P. B. Lerner, in *Proceedings of the 2nd International Vacuum Electron Source Conference, Tsukuba, 1998*, pp. 275–276.
12. S. A. Pshenichnyuk, Yu. M. Yumaguzin, and R. Z. Bakhtizin, Prib. Tekh. Éksp., No. 6, 143 (1998).
13. R. Z. Bakhtizin, V. M. Lobanov, and Yu. M. Yumaguzin, Prib. Tekh. Éksp., No. 4, 246 (1987).
14. E. W. Muller, Ergeb. Exakten. Naturwiss. **27**, 290 (1953).
15. A. P. Komar and Yu. N. Talanin, Izv. Akad. Nauk SSSR, Ser. Fiz. **10**, 1137 (1956).
16. W. B. Choi, M. Q. Ding, V. V. Zhirnov, *et al.*, in *Proceedings of the 10th International Vacuum Microelectronics Conference, Kyongju, 1997*, pp. 527–529.
17. G. J. Wojak, V. V. Zhirnov, W. B. Choi, *et al.*, in *Proceedings of the 10th International Vacuum Microelectronics Conference, Kyongju, 1997*, pp. 146–148.

Translated by V. Isaakyan

Technical Physics, Vol. 49, No. 5, 2004, pp. 630–634. From Zhurnal Tekhnicheskoĭ Fiziki, Vol. 74, No. 5, 2004, pp. 113–117.

SURFACES, ELECTRON AND ION EMISSION

Unoccupied Electronic States and the Interface Formation between Oligo(Phenylene-Vinylene) Films and a Ge(111) Surface[1]

A. S. Komolov

Fock Institute of Physics, St. Petersburg State University, Ulyanovskaya ul. 1, St. Petersburg, 198504 Russia
Department of Chemistry, University of Copenhagen, Universitetsparken 5, DK-2100, Copenhagen, Denmark
e-mail: akomolov@kiku.dk

Received June 25, 2003

Abstract—Thin films of tri-oligo(phenylene-vinylene) end-terminated by di-butyl-thiole (tOPV) were thermally deposited in UHV on Ge(111) substrates. The surface potential and the structure of unoccupied electron states (DOUS) located 5–20 eV above the Fermi level (E_F) were monitored during the film deposition using an incident beam of low-energy electrons according to the total current electron spectroscopy (TCS) method. The electronic work function of the surface changed during the film deposition until it reached a stable value of 4.3 ± 0.1 eV at a tOPV film thickness of 8–10 nm. Deposition of the tOPV under 3 nm led to the formation of intermediate DOUS structures that were replaced by another DOUS structure along with an increase in the tOPV deposit thickness up to 8–10 nm. The occurrence of the intermediate DOUS structure is indicative of a substantial reconfiguration of the electronic structure of the tOPV molecules due to the interaction with the Ge(111) surface. Analysis of the TCS data allowed us to assign the unoccupied electronic bands in tOPV located at 5.5–6.5 and 7.5–9.5 eV above the E_F as π* bands and at 11–14 and 16–19 eV above E_F as σ* bands. © *2004 MAIK "Nauka/Interperiodica".*

INTRODUCTION

Thin films of phenylene-vinylene oligomers (OPV) have shown promising electronic properties that can be used in light-emitting diodes and other device applications [1, 2]. The electronic structure of the film–electrode interfaces is crucial for the device performance, and electron spectroscopy techniques have been applied to study the interface formation [2–5]. Like for other types of aromatic molecular films [6, 7], electronic charge transfer may affect the formation of OPV interfaces with metals and semiconductors [3, 5] and this would lead to a discontinuity of the vacuum level (E_{vac}) at the interface. Chemical interaction leading to electronic and geometrical reconfiguration of both OPV films and the electrode material has been reported for a number of interfaces [4, 5]. Inorganic semiconductors as contact materials to organic films provide larger possibilities for interfacial chemistry [8, 9]. The performance of the photovoltaic device we studied earlier [10] was mostly related to the properties of the Si/organic film interface. Si(111) and Ge(111) surfaces could be of special interest for device fabrication as one can deposit similar types of organic films on them in air and in vacuo using wet chemistry methods and vacuum sublimation, respectively [9].

Studies of unoccupied electronic states can provide information about the interface formation complementary to the information on valence electronic states [2, 6, 7] traditionally obtained by photoelectron spectroscopy. Unoccupied electron states are more sensitive to modifications of the films because they have larger spatial delocalization. The electronic structure of the unoccupied states can be obtained by monitoring secondary electrons backscattered from the sample surface using very low-energy electron diffraction (VLEED) or total (target) current spectroscopy (TCS) [11, 12]. Information on band bending in a semiconductor substrate, the formation of an interface charge transfer layer, and the evolution of the work function has been obtained as a result of the TCS studies of organic films interfacing with solid substrates [13]. Side- and end-substitution of OPV affects the aromatic electronic structure of the molecule [14]. Thiole-based substituents in the tOPV molecule under study (Fig. 1) may also be relevant for intermolecular and film-substrate interactions. The Ge(111) surface was chosen as a chemically reactive substrate surface with respect to the tOPV films [9]. In this paper, we report the results of our TCS studies of the tOPV/Ge(111) interfaces and of the unoccupied electronic states of thin tOPV films.

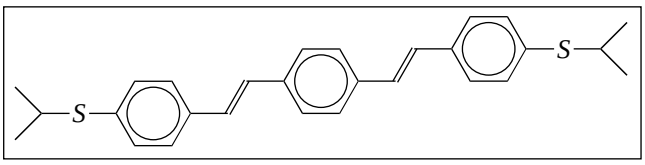

Fig. 1. Molecular structure of tri-oligo(phenylene-vinylene) end-terminated by di-butyl-thiole (tOPV).

[1] This article was submitted by the author in English.

EXPERIMENTAL

The experiment was performed in a UHV system (base pressure 5×10^{-8} Pa) in which an Auger electron spectroscopy (AES) unit and a low-energy electron diffraction (LEED) unit were installed. The LEED unit was also used as the main instrumentation in the TCS technique, which we discussed in detail in previous papers [11–13]. In our TCS experiment, a probing beam of electrons with typical energies of 0–25 eV, forming an electrical current of about 10 nA, was directed normally to the surface under study and the derivative of the total current in the sample circuit J(E) was measured: $S(E) = dJ(E)/dE$, the total current spectrum. The total current spectrum consists of a primary peak and a fine structure. The energy position of the primary peak corresponds to the condition of the equal vacuum levels of the cathode and the sample surface. One can therefore determine the work function of the surface under study using TCS and taking into account calibration of the TCS instrument on a known reference surface, such as a freshly deposited surface of Au at 10^{-8} Pa with a work function of 5.2 eV [15]. The fine structure of a total current spectrum is located in the energy interval 0–25 eV above the vacuum level and is determined by the energy dependence of the elastic scattering of the incident electrons from the sample surface, which is closely related to the density of the unoccupied electron states (DOUS) of the sample surface [16]. In a forbidden energy region at the surface, the electron reflection is high and the total current J reaches a minimum, and, when the DOUS is high, the total current J reaches a maximum. DOUS analysis is usually carried out using the negative second derivative $-d^2J(E)/dE^2 = -dS(E)/dE$, and its peaks are assumed to represent the DOUS peaks [11, 12, 16, 17].

The Ge(111) surface was pretreated with an $HF/HNO_3/AgNO_3$ mixture prior to the substrate being placed into the UHV chamber. After the base pressure was achieved, the substrate surface was subjected to an externally focused beam from a high-pressure xenon lamp. The atomic composition of the substrate was tested by AES and LEED, and a $c(2 \times 8)$ reconstruction typical of the Ge(111) surface was determined [9, 15]. Tri-oligo(phenylene-vinylene) end-terminated by dibutyl-thiole (tOPV) (Fig. 1) have been recently synthesized as described in [18]. Thin films of these molecules were thermally deposited at the rate 0.1 nm/min *in situ* from a Rnudsen cell spaced 10 cm from the substrate with the deposition beam oriented approximately 45° to the substrate surface. The films were simultaneously deposited onto the surface of a quartz microbalance with the aim of controlling the deposit thickness, to which we assign a typical uncertainty of 0.1 nm. The AES spectrum of the tOPV films had main peaks corresponding to C (275 eV) and S (153 eV), and their relative intensities were in good agreement with the atomic composition of tOPV molecules ($C_{26}S_2H_{28}$). The LEED patterns of the Ge(111)-c 2×8 surface was attenuated during the tOPV deposition, and no new pattern appeared manifesting the formation of a disordered organic film.

RESULTS AND DISCUSSION

The structures of the unoccupied electronic states and the surface potential were monitored by measuring a series of TCS spectra during the tOPV film deposition process. The TCS spectrum of the Ge(111) substrate (0 nm coverage) is represented by the primary TCS peak and the TCS fine structure in the range 5–25 eV (Fig. 2a). The position of the primary TCS peak indicates the work function value of the Ge(111) substrate 4.8 eV, which corresponds well to the literature data [17]. The shape of the primary TCS peak did not substantially change during the film deposition, which indicates a uniform distribution of the tOPV molecules on the substrate. On the other hand, the energy position of the primary TCS peak changed gradually during the film deposition, which will be discussed later in this section together with the discussion on the interface

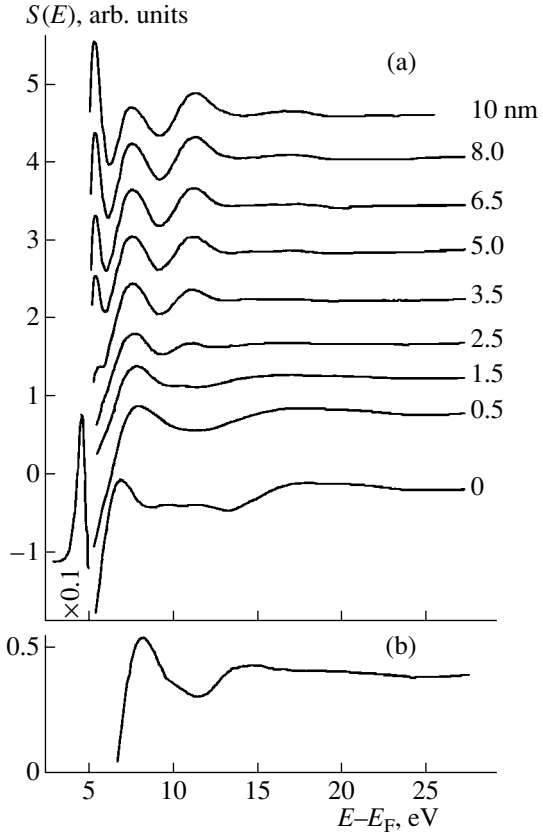

Fig. 2. (a) TCS fine structure illustrating the process of the tOPV film deposition on the Ge(111) surface. The primary peak scaled 0.1 is shown for the case of a zero deposit thickness. Numbers to the right of each curve indicate the corresponding thickness (nm)of the tOPV film. (b) Intermediate TCS fine structure corresponding to the modified electronic structure of the tOPV films of up to 3 nm on the Ge(111) surface.

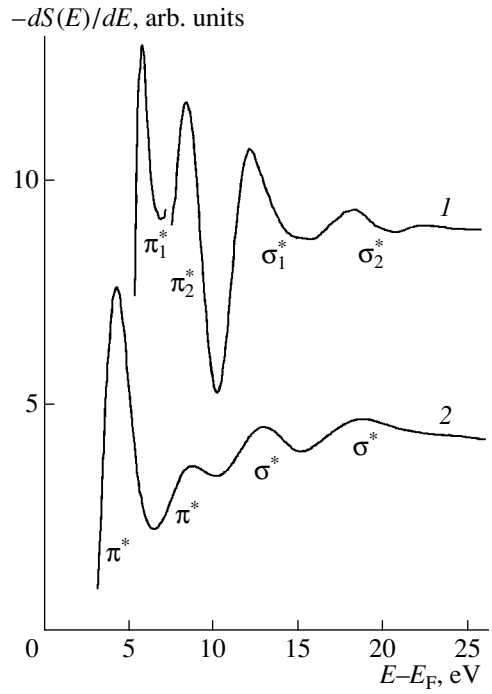

Fig. 3. (*1*) $-dS(E)/dE$ spectrum of the DOUS peaks of the tOPV films. (*2*) DOUS of the condensed benzene molecules obtained on the basis of the NEXAFS data [22]. π* and σ* bands are numerated in (*1*) along with the increase in energy *E*.

formation. During the tOPV film deposition, the TCS fine structure of the Ge (111) substrate attenuated and the new TCS fine structure appeared (Fig. 2a). At about 10 nm of film coverage, there was a stable TCS fine structure with main peaks at 5.5, 7.5, 12, and 17.5 eV and no changes in the TCS fine structure on further deposition were observed until charging of the sample at about 15 nm of the tOPV deposit occurred.

In order to study the appearance of the TCS fine structure of the molecular deposits, we analyzed the differential curves between the TCS fine structures measured before and after the deposition of each adlayer. The partial contribution of the TCS fine structure from the substrate and from the underlaying film to the differential curves was subtracted according to its exponential attenuation [12, 13]. The evolution of the TCS fine structure of the tOPV deposit had two main stages. When the deposit thickness was in the range 3–10 nm, and the TCS fine structure with peaks at 5.5, 7.5, 12, and 17.5 eV appeared from each adlayer of the tOPV deposit, although the relative intensities of the peaks varied to some extent within the thickness range. This TCS fine structure corresponds well to the final TCS fine structure of a 10- to -12-nm-thick tOPV film (Fig. 2a). At the earlier stages of the tOPV deposition, when the film thickness was under 3 nm, the intermediate TCS fine structure was observed (Fig. 3b), which had a typical peak at 8.5 eV and a shoulder at 14 eV.

According to the literature data, a decrease in the degree of conjugation in a molecule under study would lead to vanishing of the corresponding DOUS bands [19]. Studies of the interfaces of perylene derivatives [20] and phthalocyanines [13] with Si single crystals have shown that the π electronic structure of the aromatic molecules becomes substantially reconfigured, so dissociation of the molecules was assumed. Dissociation of a thiophene oligomer onto monomers (which in turn could be considered as a decrease in conjugation) due to interaction with Si(100) was reported in [21]. As for the tOPV/Ge(l 11) interface under study, we suggest that the observation of the less pronounced features in Fig. 2b as compared to Fig. 2a indicates a lower conjugation within the 0- to -3-nm-thick tOPV deposit as compared to the rest of the tOPV film (3–10 nm). Interestingly, the width of the intermediate tOPV layer, 3 nm, is larger than the size of a tOPV molecule in any direction, which indicates that the modification of the electronic structure of the tOPV molecules occurred within a film area broader than one monolayer.

Direct assignment of the DOUS peaks of the tOPV films turns out to be rather complicated because of the lack of theoretical studies devoted to calculations of the electronic structure of these molecules in the energy region of interest. It is worth comparing our experimental results on the DOUS of tOPV films with the results of the DOUS studies of condensed benzene and its derivatives [22, 23], as the aromatic component of tOPV (Fig. 1) makes a substantial contribution to the electronic spectrum of the whole molecule. The $-dS(E)/dE$ spectrum of the tOPV films is shown by curve *1* in Fig. 3. We suggest assigning the DOUS peak of the tOPV films as follows: the peaks in the regions 5.5–6.5 eV and 7.5–9.5 eV correspond to electronic bands π_1^* and π_2^*, and the peaks in the regions 11–14 and 16–19 eV correspond to σ_1^* (C–C) and σ_2^* (C=C) bands. The π_1^*, σ_1^*, and σ_2^* bands (curve *1*, Fig. 3) correspond well to the analogous DOUS bands of condensed benzene (curve *2*, Fig. 3) [22] determined by means of near edge X-ray absorption spectroscopy (NEXAFS).

We note that one should not expect a complete identity between the TCS and NEXAFS spectra because NEXAFS measurements may introduce error to the DOUS spectrum obtained due to the site-on dependence of the core electron excitation energy [23]. The π_1^* electronic band (curve *1*, Fig. 3) is situated close to the edge of the energy region in which we can register the DOUS by means of TCS. The DOUS of the tOPV in the region of the π_1^* band differs from the DOUS of benzene (Fig. 3), and we relate this difference to the contribution of the vinylene component to the electronic spectrum of the tOPV molecules.

Let us consider the TCS data (Fig. 2a) on the subject of revealing the formation of an interface dipole at the

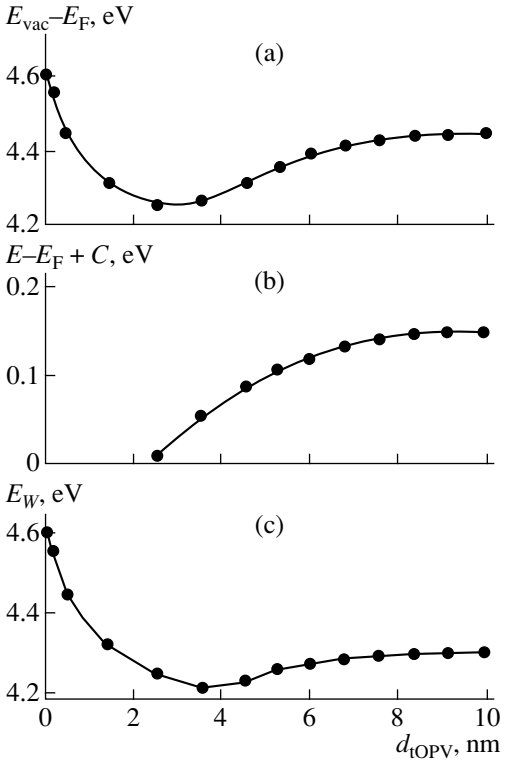

Fig. 4. Analysis of the tOPV deposition on the Ge(111) surface, (a) changes in the surface potential, (b) energy shifts of the TCS fine structure from the tOPV film, and (c) changes of the tOPV film work function derived from subtracting the curve in (b) from the curve in (a).

tOPV/Ge(111) boarder. Changes in the surface potential during the tOPV deposition observed as changes of the primary TCS peak position are shown in Fig. 4a. The surface potential decreases until the tOPV film thickness reaches about 3 nm and then increases to a final value of 4.4 ± 4.5 eV. One can see that the surface potential of the 2- to -3-nm-thick tOPV is lower than the surface potential of the finally formed 10-nm-thick tOPV films and that this difference corresponds well to the difference of the TCS fine structures from the thicker and the thinner tOPV films (Fig. 2). A similar result was reported for side-substituted phenylene-vinylene oligomers on polycrystalline Au in [5]. A gradual shift of the tOPV film TCS fine structure was observed starting from an approximately 3-nm-thick deposit (Fig. 4b). This shift of the fine structure corresponds to a transfer of the positive charge from the films outside the intermediate region (3–10 nm) towards the film–substrate interface. The charge transfer may be related to the polarization of the tOPV molecules, so the polarization becomes weaker with the film thickness according to the model of an extended interface dipole suggested by us earlier [13, 24]. A specific feature of the polarization layer in the tOPV film is that it extends approximately 10 nm away from the geometrical interface with the Ge(l 11) substrate. Subtracting the interface effect (Fig. 4b) from the changes in the surface potential (Fig. 4a) reveals the evolution of the work function during the tOPV film deposition (Fig. 4c), which achieves a final value of 4.3 ± 0.1 eV. Electronic charge transfer has been observed for a large number of interfaces between organic films and metal surfaces [6, 7], and the formation of abrupt interface dipoles within one molecular layer of the deposit was attributed to this type of interfaces with some exceptions [5, 25]. With respect to organic film–inorganic semiconductor interfaces, we have observed here and earlier [13] rather extended interface dipoles.

CONCLUSIONS

The TCS technique is used in an experimental approach to study the density of the unoccupied electronic states of the tOPV organic films and to describe the formation of the electronic structure at the interface between the tOPV films and Ge(111) substrate. A substantial reconfiguration of the electronic structure of the unoccupied electronic states of the tOPV films within a 3-nm deposit layer due to the interaction with the substrate was deduced. π* unoccupied electronic bands in tOPV are located at 5.5–6.5 and 7.5–9.5 eV above the Fermi level, and the CT* bands are located at 11–14 and 16–19 eV above the Fermi level. Electronic charge transfer of the positive charge from the tOPV film to the tOPV/Ge(111) interface region has been observed and related to the polarization of the tOPV molecules in a tOPV film layer up to 10 nm thick.

ACKNOWLEDGMENTS

This work was supported by the Danish Research Agency (STVF-26-02-0223), the Russian Foundation for Basic Research (02-03-32751), and the Russian state program “Surface Atomic Structures.”

REFERENCES

1. J. H. Burroughes, D. D. C. Bradley, A. R. Brown, *et al.*, Nature **347**, 539 (1990).
2. M. Fahlman and W. R. Salaneck, Surf. Sci. **500**, 904 (2002).
3. W. R. Salaneck, M. Lögdlund, M. Fahlman, *et al.*, Mater. Sci. Eng. **R34**, 121 (2001).
4. G. Greczynski, T. Kugler, and W. R. Salaneck, Curr. Appl. Phys. **1**, 98 (2001).
5. A. Siokou, V. Papaefthimiou, and S. Kennou, Surf. Sci. **482–485**, 1186 (2001).
6. K. Seki, N. Hayashi, H. Oji, *et al.*, Thin Solid Films **393**, 298 (2001).
7. I. Hill, D. Milliron, J. Schwartz, and A. Kahn, Appl. Surf. Sci. **166**, 354 (2000).
8. J. O. McCaldin, Prog. Solid State Chem. **26**, 241 (1998).
9. S. F. Bent, Surf. Sci. **500**, 879 (2002).
10. A. S. Komolov, Fiz. Tverd. Tela (St. Petersburg) **43**, 379 (2001) [Phys. Solid State **43**, 397 (2001)].

11. V. N. Strocov and H. I. Starnberg, Phys. Rev. B **52**, 8759 (1995).
12. S. A. Komolov, *Total Current Spectroscopy of Surfaces* (Gordon and Breach, Philadelphia, 1992).
13. A. S. Komolov and P. J. Möller, Synth. Met. **128**, 205 (2002).
14. Y. Tao, A. Donat-Bouillud, M. D'Iorio, *et al.*, Thin Solid Films **363**, 298 (2000).
15. J. C. Riviére, *Solid State Surface Science*, Ed. by M. Green (Dekker, New York, 1969), Vol. 1, pp. 180–303.
16. I. Barlos, Prog. Surf. Sci. **59**, 197 (1998).
17. A. M. Schäfer, M. Schlüter, and M. Skibowski, Phys. Rev. B **35/14**, 7663 (1987).
18. N. Stuhr-Hansen, J. B. Christensen, N. Harrit, and T. Bjornholm, J. Org. Chem. **68** (4), 1275 (2003).
19. A. P. Hitchcock, D. C. Newbury, I. Ishii, *et al.*, J. Chem. Phys. **85**, 4849 (1986).
20. J. Taborski, P. Vaterlein, U. Zimmermann, and E. Umbach, J. Electron Spectrosc. Relat. Phenom. **75**, 129 (1995).
21. R. Lin, M. Galili, U. J. Quaade, *et al.*, J. Chem. Phys. **117**, 321 (2002).
22. J. Stöhr, *NEXAFS Spectroscopy* (Springer, Berlin, 1996).
23. H. Oji, R. Mitsumoto, E. Ilo, *et al.*, J. Chem. Phys. **109**, 10409 (1998).
24. A. S. Komolov and P. J. Möller, Synth. Met. **138**, 119 (2003).
25. I. G. Hill, J. Schwartz, and A. Kahn, Organic Electronics **1**, 5 (2000).

Technical Physics, Vol. 49, No. 5, 2004, pp. 635–637. Translated from Zhurnal Tekhnicheskoĭ Fiziki, Vol. 74, No. 5, 2004, pp. 118–120.

SHORT COMMUNICATIONS

Orientation Relaxation in H8 Nematic and Its Solution in a Nonmesogenic Solvent under a Magnetic Field

D. L. Bogdanov, E. V. Gevorkian, A. A. Romanov, and M. V. Shevchuk

Moscow State Regional University, ul. Radio 10a, Moscow, 105005 Russia

e-mail: shevchukmv@rambler.ru

Received April 24, 2003; in final form, October 21, 2003

Abstract—The time dependences of the ultrasound absorption coefficient in the H8 nematic and its solution in a nonmesogenic solvent (benzene) under a pulsating magnetic field and varying thermodynamic parameters of state (p, T) are studied. The ratio of the rotational viscosity to the diamagnetic susceptibility ($\gamma_1/\Delta\chi$), the activation energy for different pressures, and the activation volume are found. © *2004 MAIK "Nauka/Interperiodica".*

The dissipative properties of liquid crystals (LCs) and their solutions in the range of existence of the mesophase are of both scientific and applied interest. While the molecular–kinetic, thermodynamic, hydrodynamic, and other physical properties of many LCs have received much study, those of LC solutions are poorly known.

Objects of investigation in this work are the H8 nematic, consisting of *n*-methoxybenzylidene-*n*-*p*-butylaniline (MBBA) and *n*-ethoxybenzylidene-*n*-*p*-butylaniline (EBBA) (for their structural formulas, see Fig. 1), and a solution of H8 in a nonmesogenic solvent benzene (H8 : C_6H_6 = 7 : 1 by weight). In this LC, the temperature interval of existence of the mesophase is rather wide, which makes it possible to study its dissipative properties in the regular range. With a nonmesogenic solvent added to an LC, one can study not only the LC properties but also their disappearance upon the nematic–isotropic liquid transition.

It is known that the addition of a nonmesogenic solvent (i.e., a solvent free of the LC phase) to H8 decreases the isotropic transition temperature T_{tr}. In H8 the isotropic transition temperature is T_{tr} = 325 K, while in the solution studied T_{tr} = 306 K.

The properties of an LC as such must be studied when the orienting effect of the wall does not disturb parameters to be measured. In view of this requirement, the sample volume was sufficiently large. Knowing the parameters of a bulk LC, one can estimate those of related thin films used in displays and other devices.

Measurements were carried out in fields of 0.1–0.2 T. The application of a magnetic field to a nonoriented nematic in the mesophase range renders the ultrasound absorption coefficient anisotropic. In this case, an LC may be viewed as a single crystal, whereas in the absence of the field it is akin to a polycrystal. At the isotropic transition temperature, anisotropy disappears. Accordingly, the transition temperature may be determined for different pressures from the point at which the absorption coefficient becomes isotropic.

In the pressure range studied in this work, the pressure dependence of the transition temperature $T_{tr}(p)$ is linear both for pure H8 and for its solution:

$$T_{tr}(p) = T_{tr} + \frac{dT}{dp}p, \qquad (1)$$

where $dT/dp \approx 0.29$ K/MPa for H8 and 0.3 K/MPa for the solution.

In the range where the mesophase exists, the application of a magnetic field retards the response of the nematic physical properties, including the ultrasound absorption coefficient. This process has a finite relaxation time, which depends on the rotational viscosity. Figure 2 shows the time dependence of the ultrasound absorption coefficient divided by the frequency squared, $\alpha^{\parallel}(t)/f^2$, in a pulsating magnetic field when the magnetic induction is parallel to the wavevector. At the time $t_1 = 0$, the magnetic field is switched on and the parameter $\alpha^{\parallel}(t)/f^2$ increases from α_0/f^2 (α_0 is the absorption without the field) to $\alpha_m^{\parallel}/f^2$ at $t_2 \approx 100$ s.

Below are the time dependences [1] of the ultrasound absorption coefficient in a pulsating magnetic field parallel to the wavevector; these dependences include the

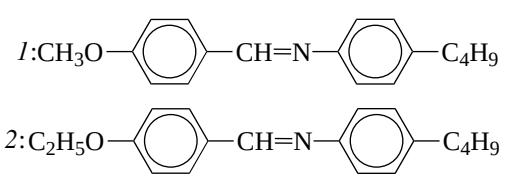

Fig. 1. Structural formulas for (*1*) MBBA and (*2*) EBBA.

1063-7842/04/4905-0635$26.00 © 2004 MAIK "Nauka/Interperiodica"

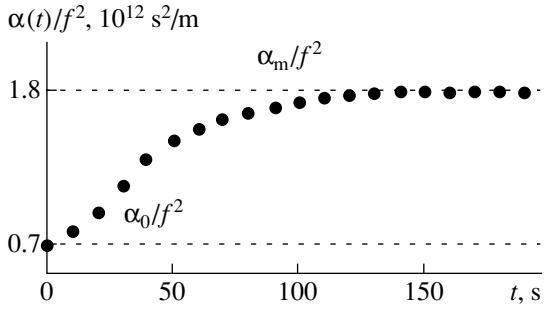

Fig. 2. Time dependence of $\alpha^{\parallel}(t)/f^2$ for H8 at $B = 0.052$ T, $p = 0.1$ MPa, $T = 315$ K, and $f = 6.5$ MHz.

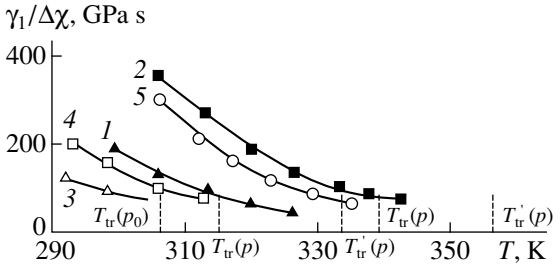

Fig. 3. $\gamma_1/\Delta\chi$ vs. temperature for H8 at p = (*1*) 30 and (*2*) 110 MPa and for the solution at (*3*) 0.1, (*4*) 30, and (*5*) 110 MPa.

switching duration τ_{mag} of an electromagnet [1]:

$$f^{-2}\alpha(t) = c^* + a\frac{1-\left(\frac{e^-}{1-e^-}\right)^{1/2}\arccos\left((e^-)^{1/2}\right)}{1-e^-} + b\frac{1+\frac{e^-}{2}-\frac{3}{2}\left(\frac{e^-}{1-e^-}\right)^{1/2}\arccos\left((e^-)^{1/2}\right)}{(1-e^-)^2}, \quad (2)$$

where the time variation of the parameter e^- is given by

$$e^- = \exp\left[-\frac{1}{\tau_n}\left(2t - 3\tau_{mag} + 4\tau_{mag}\exp\left(-\frac{t}{\tau_{mag}}\right) - \tau_{mag}\exp\left(-\frac{2t}{\tau_{mag}}\right)\right)\right]. \quad (3)$$

Here, τ_n is the relaxation time of the ultrasound absorption coefficient. The switching duration of an electromagnet τ_{mag} is expressed as

$$e(t) = \left[1 - \exp\left(-\frac{t}{\tau_{mag}}\right)\right]B_m. \quad (4)$$

The time τ_n is found by the least squares method from expression (2) when the analytical curve fits experimental data most closely. The parameters of a and b, which define the slope of the absorption coefficient for pure H8 and H8 in the solution, were taken from [2].

The pressure and temperature dependences of the time τ_n for pure H8 and its solution are given in Tables 1 and 2.

From the relaxation time τ_n of the ultrasound absorption coefficient, we determined the ratio $\gamma_1/\Delta\chi = \tau_n B^2/\mu_0$ of the rotational viscosity to the diamagnetic susceptibility.

Figure 3 plots $\gamma_1/\Delta\chi$ versus temperature for pure H8 at pressures of 30 and 110 MPa and for its solution at 0.1, 30, 110 MPa. These dependences have the exponential form

$$\frac{\gamma_1}{\Delta\chi} = Ae^{\frac{E}{RT}}. \quad (5)$$

Here, A is a factor that is almost independent of the temperature and pressure and characterizes a particular nematic (for H8 and its solution, $A = 7.5$ and 2.8 Pa s, respectively), E is the molar energy of activation, and R is the universal gas constant.

The energies of activation for H8 and the solution for different pressures are listed in Table 3.

The energy of activation can be approximated by the linear formula $E = E^* + (dE/dp)p$, where E^* is the energy of activation at $p = 0$. The quantity dE/dp has the dimension of the molar volume. Its values at different pressures are listed in Table 3.

From the data mentioned above, it follows that the parameter dE/dp decreases with increasing pressure. This corresponds to a decrease in the slope of isochores in Fig. 4. For H8, $dE/dp = 41 \times 10^{-6}$ m^3/mol (14% of the

Table 1. Pressure dependence of the time τ_n at 306 K

B, T	p, MPa						
	0.1	30	70	110	30	70	110
	H8				Solution		
0.070	17	28	49	71	21	38	66
0.060	28	46	69	114	29	52	90
0.050	40	62	115	155	48	79	141

Table 2. Temperature dependence of τ_n at 30 MPa

B, T	H8				Solution			
	T = 298 K	T = 306 K	T = 312 K	T = 320 K	T = 293 K	T = 298 K	T = 306 K	T = 312 K
0.070	43	28	19	12	45	31	21	19
0.060	58	46	30	20	68	46	29	30
0.050	87	62	47	33	96	70	48	47

Table 3. Values of E and dE/dp at different pressures for H8 and its solution

	p, MPa	E, kJ/mol	dE/dp, 10^{-6} m^3/mol
H8	0.1	35.8	41
	30	36.8	37
	50	37.4	34
	70	38.1	32
	90	38.8	31
	110	39.4	30
Solution	0.1	37.4	44
	30	38.6	38
	50	39.3	33
	70	40	30
	90	40.5	29
	110	41	29

Table 4. Values of $d(\ln(\gamma_1/\Delta\chi))/dp$ calculated by expression (6) and obtained from experimental dependences

T, K	dQ/dp, GPa^{-1}	$d(\ln(\gamma_1/\Delta\chi))/dp$, MPa	
		calculation by (6)	experiment
300	1.78	0.014	0.0132
305	2	0.0121	0.0129
310	2.33	0.0109	0.0127
315	2.91	0.0107	0.0125
320	4.36	0.0123	0.0123
T, K		$d(\ln(\gamma_1/\Delta\chi))/dp$, MPa^{-1}	
		calculation by (6)	experiment
300		0.0171	0.0132
305		0.0133	0.0129
310		0.0106	0.0127
315		0.0097	0.0125
320		0.0090	0.0123

volume) under atmospheric pressure; at 110 MPa, this value is lower by roughly one-third. Hence, as the pressure rises, the free volume between molecules shrinks and their transition from one equilibrium state to another becomes difficult.

The Diogo–Martins semi-phenomenological theory of rotational viscosity [3], which is based on the Maier–Saupe mean field approximation, yields

$$\gamma_1 = qQ^2 \exp\left[\frac{\varepsilon Q}{kT} + \frac{\theta Q^2}{T - T^*}\right], \qquad (6)$$

where q and θ are constants and T^* is the temperature at which the director stops rotating.

In the temperature interval $T_{tr} < T < T^*$, the behavior of γ_1 depends largely on the probability of molecules passing from the excited to the ground state because of a change in the free volume:

$$\gamma_1(T_{tr} < T < T^*) \approx qQ^2 \exp\left[\frac{\theta Q^2}{T - T^*}\right]. \qquad (7)$$

The pressure has an effect on two parameters: Q and T^*. The order parameter for the first place depends on the difference $T_{tr} - T$. For $T_{tr} - T$ = const, the orientational order parameter Q is almost pressure independent. Thus, the pressure dependence of the orientational order parameter is reduced to its dependence on $T_{tr}(p)$:

$$\frac{dQ}{dp} = \frac{dQ\,dT_{tr}}{dT_{tr}\,dp}. \qquad (8)$$

The calculated values of $d(\ln(\gamma_1/\Delta\chi))/dp$ for H8 at $dT^*/dp \approx 0.14$ K/MPa are listed in Table 4.

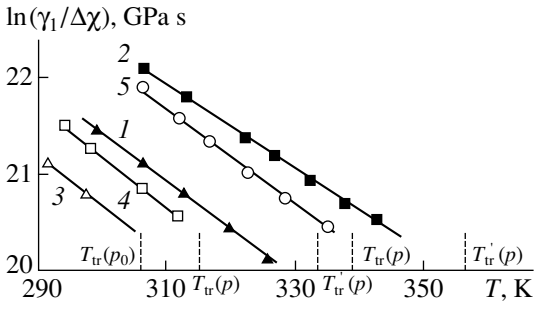

Fig. 4. $\ln(\gamma_1/\Delta\chi)$ vs. temperature for H8 at p = (*1*) 30 and (*2*) 110 MPa and for the solution at (*3*) 0.1, (*4*) 30, and (*5*) 110 MPa.

REFERENCES

1. P. K. Khabibullaev, É. V. Gevorkyan, and A. S. Lagunov, *Rheology of Liquid Crystals* (Fan, Tashkent, 1992) [in Russian].
2. M. P. Vekovishchev, Candidate's Dissertation (Moscow Pedagogical University, Moscow, 1997).
3. A. Diogo and A. F. Martins, Mol. Cryst. Liq. Cryst. **66**, 133 (1981).

Translated by V. Isaakyan

Technical Physics, Vol. 49, No. 5, 2004, pp. 638–641. Translated from Zhurnal Tekhnicheskoĭ Fiziki, Vol. 74, No. 5, 2004, pp. 121–124.

SHORT COMMUNICATIONS

Wide-Aperture Cathodoluminescent Light Source Based on an Open Discharge

E. A. Muratov, A. T. Rakhimov, and N. V. Suetin

Skobel'tsyn Research Institute of Nuclear Physics, Moscow State University, Vorob'evy Gory, Moscow, 119899 Russia

e-mail: muratov@dnph.phys.msu.su

Received June 17, 2003

Abstract—The feasibility of an effective high-luminance light source based on an open discharge is considered. Experimental data for the light characteristics of different cathodoluminescent screens are presented. Phosphor coatings are excited by an electron beam initiated by a planar cathode–grid injector in an inert gas atmosphere. The feasibility of maintaining an open discharge using continuous or pulsed–periodic excitation of the gas medium in the light emitter is discussed. The use of the specular method to excite the phosphor coating of the screen makes it possible to achieve a higher luminance and a higher luminous efficacy in comparison with these characteristics for cathodophosphors. The design of the cathode–grid unit allows for a large surface area of the electron injector, making it promising for wide-aperture light sources. © *2004 MAIK "Nauka/Interperiodica".*

INTRODUCTION

The creation of effective, simple, inexpensive, and stable light sources for different applications is the mainstream in contemporary lighting engineering. It is evident that users place various requirements upon light source characteristics (such as luminance, color scale, luminous efficacy, service life, dimensions, directivity diagram, etc.). These requirements are frequently mutually contradictory and cannot be satisfied with available light sources.

The authors suggested [1] a new gas-discharge light source based on the so-called open discharge (OD) [2]. The basic feature of this source is the direct excitation of a phosphor screen by an electron beam the formation of which accounts for more than 80% of the total energy introduced into the discharge [3]. Owing to this feature, an open discharge was repeatedly advantageously used for the excitation of the lasing medium in gas lasers [4].

DESIGN OF THE LIGHT SOURCE

The light source proposed has a glass or cermet body and a transparent phosphor-coated screen. The chemical composition of the phosphor is responsible for the color scale (red, green, blue, yellow, etc.). The electrode system of the emitter is rather simple and consists of a plane (continuous or grid) metallic cathode and a grid (anode) with a narrow gap in between. The light source is a gas-filled device. It should be emphasized that only noble gases free of mercury vapors or other elements usually used in gas-discharge light sources may be applied as a working medium. The parameters of the system are selected such that most of the electrons in the discharge form a high-energy beam, which, passing through the grid (anode), excites the phosphor.

To measure the chief characteristics of the light source (of which the electrical-to-light energy conversion efficiency is of primary importance), we prepared several prototypes differing mainly in design parameters of the electrode units and in overall dimensions. The design of an OD-based light source is schematically shown in Fig. 1.

A voltage is applied to cathode *3* from high-voltage power supply *1*, which can operate in both the continuous and pulsed–periodic regimes. The cathode–grid unit then serves as an injector of electrons with an energy equal to the cathode voltage. These electrons pass through the grid into the drift space (between the grid and screen), where a part of their energy is spent on

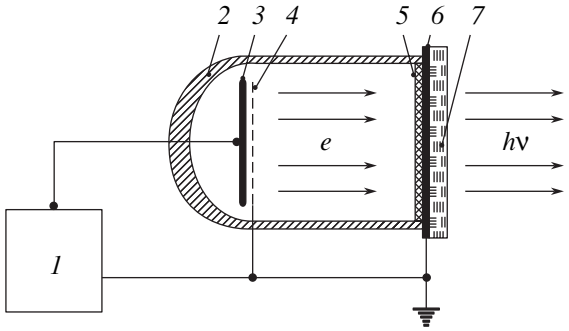

Fig. 1. Light source based on an open discharge: (*1*) power supply, (*2*) body (glass or cermet), (*3*) cathode, (*4*) grid (anode), (*5*) phosphor, (*6*) ITO conducting layer, and (*7*) screen (glass).

1063-7842/04/4905-0638$26.00 © 2004 MAIK "Nauka/Interperiodica"

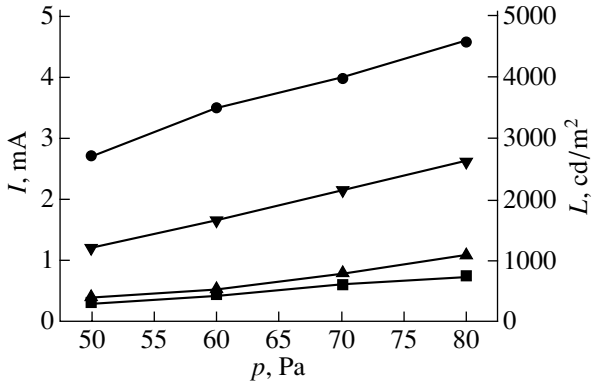

Fig. 2. (■, ●) Luminance L and (▲, ▼) current I toward the screen vs. the gas pressure. The screen surface area is 20 cm^2. Hydrogen, ZnS : Cu phosphor. The cathode voltage is (▲, ■) 3 and (▼, ●) 4 kV.

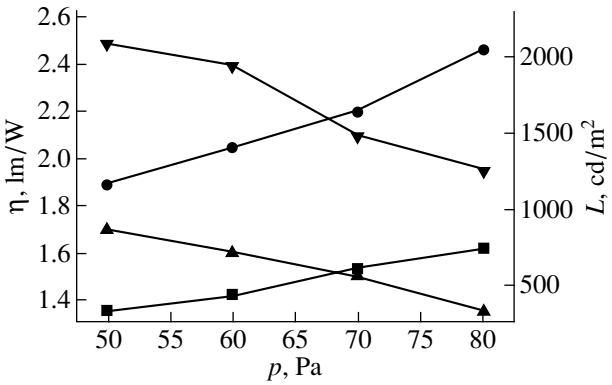

Fig. 3. (■, ●) Luminance L and (▲, ▼) luminous efficacy η vs. the working gas pressure. Hydrogen, ZnS : Cu phosphor. The cathode voltage is (▲, ■) 3.0 and (▼, ●) 3.5 kV.

the ionization of the gas. Positive ions and photons produced in the drift space pass back through the grid and cause secondary electron emission directly from the cathode surface, thereby maintaining the open discharge. In this discharge, a major part of the electrons are involved in a high-energy beam, which excites the phosphor coating of the screen.

ENERGY CHARACTERISTICS AND OPERATING MODES OF THE LIGHT SOURCE

As was noted, the electron beam is generated when a negative voltage is applied to the cathode. The minimum voltage initiating an open discharge depends on the discharge ignition threshold, and the maximal value is limited by the stability range of the discharge.

We investigated continuous and pulsed–periodic regimes of discharge maintenance.

In experiments with the continuous generation of the electron beam, high levels of luminance were reached (several thousand of cd/m^2). Such high levels of luminance are now achieved only in mercury-vapor, sodium-vapor, and sulfur-vapor lamps.

Figure 2 shows the luminance measured as a function of the gas pressure and discharge voltage. The luminance of the source is seen to correlate with the density of the current toward the phosphor screen and rises linearly with increasing gas pressure. However, the increase in the gas pressure leads to the undesirable reduction of the luminous efficacy of the source (Fig. 3), since the electron energy losses in the gas grow. In addition, a rise in the gas pressure renders the discharge unstable.

Figure 4 shows that the luminance may also be raised by increasing the electron energy (electron beam power). In this case, the quasi-continuous regime of electron beam generation may stabilize the discharge when an elevated voltage is applied to the cathode.

Indeed, the application of the quasi-continuous regime for OD maintenance (exciting pulse duration ≈10 μs, repetition rate 1–10 kHz) provided stable operation of the device under elevated gas pressures and at low beam energies. However, here we again observe the reduction of the luminous efficacy of the source as the gas density grows (Fig. 5).

Figures 6 and 7 show experimental data obtained under the conditions of the pulsed–periodic regime of electron beam generation. They clearly demonstrate the dependence of the luminance on the gaseous medium density and on the voltage applied to the cathode. Obviously, the luminance will be improved if faster electron beams are applied, especially in view of the fact that the efficiency of the source drops sharply as the gas pressure increases and rises with increasing the electron energy.

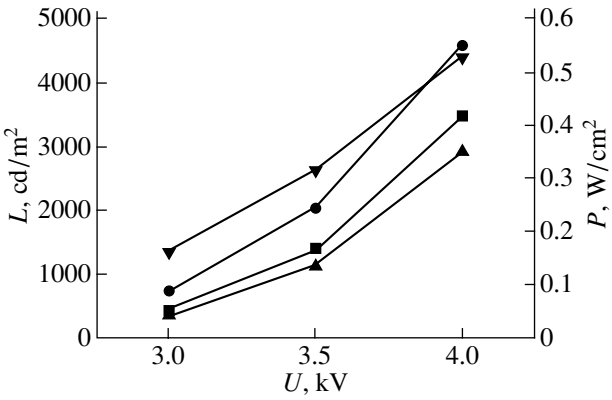

Fig. 4. (■, ●) Luminance and (▲, ▼) electron beam power vs. the cathode voltage. Hydrogen, ZnS : Cu phosphor. The gas pressure is (▲, ■) 60 and (▼, ●) 80 Pa.

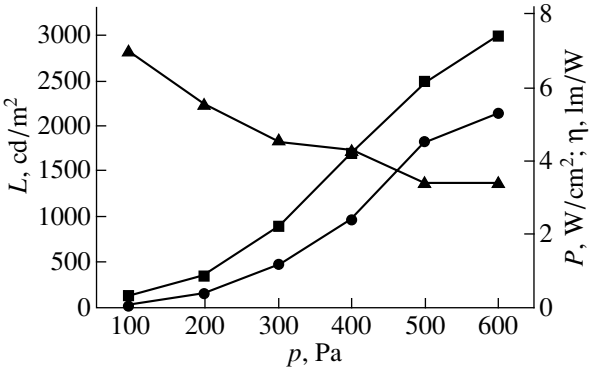

Fig. 5. (■) Luminance L, (●) electron beam power P, and (▲) luminous efficacy η of the device vs. gas pressure p. The screen surface area is 20 cm^2. Helium, ZnS : Cu phosphor. U = 1.5 kV.

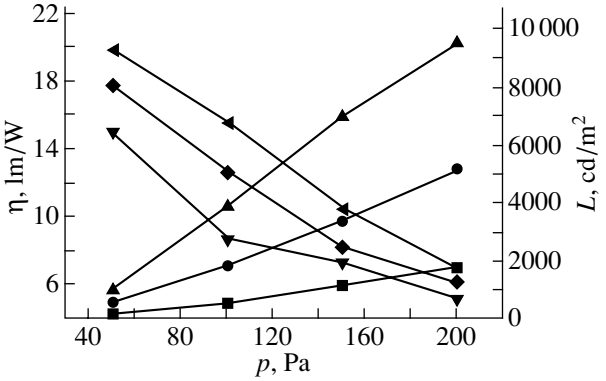

Fig. 6. (■, ●, ▲) Luminance L and (▼, ◆, ◀) luminous efficacy η of the emitter vs. the gas pressure. Helium, ZnS : Cu phosphor. The cathode voltage is (▼, ■) 2.0, (◆, ●) 2.5, and (◀, ▲) 3.0 kV.

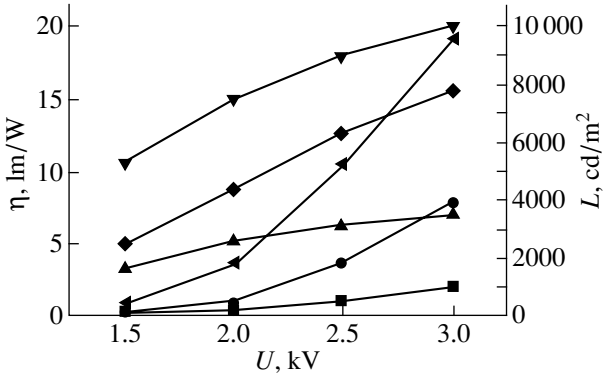

Fig. 7. (■, ●, ◀) Luminance L and (▼, ◆, ▲) luminous efficacy η of the light source vs. the cathode voltage U for the gas pressure (▼, ■) 50, (◆, ●) 100, and (▲, ◀) 200 Pa. Helium, ZnS : Cu phosphor.

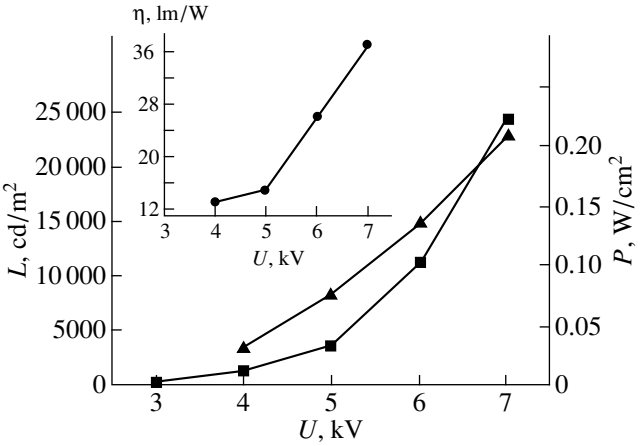

Fig. 8. (■) Luminance L and the luminous efficacy η (the inset) of the light source, as well as (▲) the electron beam power P vs. the cathode voltage. KB-3 phosphor is coated by the reflecting Al film. The gaseous medium is argon.

In practice, the efficiency of the source is improved by making the most use of the light-emitting surface of the phosphor. For this purpose, the phosphor layer is, in turn, coated by a thin Al film (on the side exposed to the incident electron beam). In this case, the light from the phosphor layer excited, which is emitted toward the drift space, reflects from the Al layer and, passing through the thin (8–10 μm) phosphor layer, makes an additional contribution to the emission of the screen. Here, the phosphor is excited by electrons with an energy exceeding the energy transparency threshold of the Al coating.

Experimental data in Fig. 8 clearly demonstrate that the phosphor starts luminescing at a cathode voltage exceeding 3 kV (the luminescence threshold depends on the Al film thickness).

The use of the specular effect described above allowed us to achieve considerably high luminance levels (≈25 000 cd/m^2) at a relatively high luminous efficacy (≈35 lm/W).

CONCLUSIONS

The experimental data presented in this work let us devise a high-power light source based on an open discharge in an inert gas. The simple design of the source and the cheapness of its components make it competitive on the market. The light-emitting area of an OD-based source may be easily extended, which makes it possible to develop intense wide-aperture emitters.

Moreover, these sources gradually lose luminance with time (because of a finite cathode service time and degradation of the gas medium) rather than burn out instantly.

Finally, the gaseous medium of this light emitter is environmentally safe (unlike that in mercury-vapor luminescent lamps).

Possible applications of OD-based light sources are the following: traffic lights, road signs, information boards, billboards, runway markers, aircraft and car display panels, etc.

ACKNOWLEDGMENTS

We thank D.V. Lopaev for the assistance in the experiments and valuable discussions.

REFERENCES

1. E. A. Muratov, A. T. Rakhimov, and N. V. Suetin, RF Patent No. 2155416 (2002); US Patent No. 6005343 (1999).
2. P. A. Bokhan and A. R. Sorokin, Zh. Tekh. Fiz. **55**, 88 (1985) [Sov. Phys. Tech. Phys. **30**, 50 (1985)].
3. A. S. Kovalev, Yu. A. Mankelevich, E. A. Muratov, *et al.*, J. Vac. Sci. Technol. A **10**, 1086 (1992).
4. V. M. Butenin, *Lasers on Self-Constrained Transitions in Metal Atoms* (RFFI, Moscow, 1998), Chap. 9, pp. 510–540 [in Russian].

Translated by Yu. Vishnyakov

Technical Physics, Vol. 49, No. 5, 2004, pp. 642–646. Translated from Zhurnal Tekhnicheskoĭ Fiziki, Vol. 74, No. 5, 2004, pp. 125–129.

SHORT COMMUNICATIONS

Vircator with Ballistic Focusing of an Electron Beam

V. D. Selemir, A. E. Dubinov, B. G. Ptitsyn, A. A. Evseenko, I. A. Efimova, V. A. Letyagin, R. K. Nurgaliev, N. V. Stepanov, K. S. Shilin, and A. V. Yachnyĭ

All-Russia Research Institute of Experimental Physics (VNIIEF), Russian Federal Nuclear Center, Sarov, Nizhni Novgorod Oblast, 607190 Russia

e-mail: dubinov@ntc.vniief.ru

Received June 17, 2003

Abstract—A high-power microwave oscillator (vircator) is built around an ironless induction linac. The feature of this device is ballistic focusing of an electron beam in a diode-type system with a concentric spherical cathode and anode. The possibility of the vircator to generate high-power microwave pulses is demonstrated.

INTRODUCTION

Microwave oscillators with a virtual cathode (vircators) form a basic class of oscillators in ultra-high-power relativistic high-current electronics (for the current status of developments in this field, see review [1]).

To date, vircators have been built around high-voltage nanosecond oscillators that are based on single and dual pulse-forming lines [2, 3], inductive storage devices with plasma current interrupters [4, 5], or magnetic explosion generators [6, 7]. Recently [8], we have designed and studied a vircator based on the Korvet ironless linear induction accelerator (LIA), which has a conventional plane-parallel diode system.

In a diode with plane parallel electrodes, the beam usually expands in the radial direction, which causes electron losses in the region of interaction and decreases the charge of a virtual cathode (VC). One way to minimize the losses is the application of a magnetic field in the longitudinal direction [9]. This, however, generates the need for much auxiliary equipment (solenoids, feed circuits, and synchronization systems). Another way is beam pinching [3], which is frequently difficult to do, because high currents must be generated in this case.

In view of the aforesaid, it is of interest to have diodes with a configuration other than plane-parallel (for example, spherical or cylindrical) where the beam radially converges, since ballistic focusing of electrons toward the center, to a certain extent, decreases electron losses.

Microwave oscillators with cylindrical diodes have been well studied [1, 10, 11], but spherical-diode vircators have not been studied at all, except for [12], where the potential of a spherical-diode vircator for collective acceleration of ions (not electrons) have been considered theoretically.

Thus, it seems topical to see whether ballistic focusing of electrons toward the center of the spherical diode of a vircator is possible and whether such a vircator may generate high-power microwave radiation. The aim of this work was to design and tentatively investigate a spherical-diode vircator. Also, we measured the spatial distribution of electrons in the drift space, parameters of the microwave radiation, and diode current.

SPHERICAL-DIODE VIRCATOR

A vircator with ballistic focusing of electrons was designed based on the Korvet LIA, which can accelerate an electron beam to an energy of 900 keV at a current pulse duration of 40 ns.

The design of the vircator is depicted in Fig. 1. It consists of a diode unit, which incorporates a concentric anode and cathode; the drift space; and a horn-type antenna for extracting radiation.

The cathode (Fig. 2b) is hollow metallic tube *1* to which steel support *2* is welded. Electrons are emitted from the concave spherical end face (63 mm in radius) of graphite cylinder *3* (70 mm in radius). The central

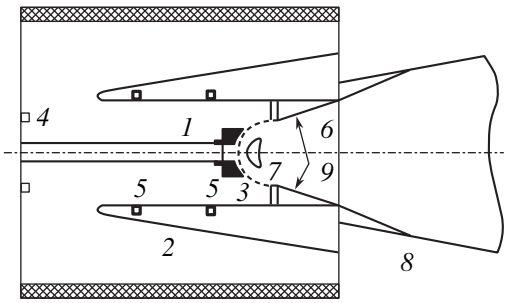

Fig. 1. Design of a relativistic spherical-diode vircator based on the Korvet induction linac: (*1*) cathode, (*2*) anode, (*3*) grid, (*4*) cathodic Rogowski loop, (*5*) anodic Rogowski loops, (*6*) drift space, (*7*) virtual cathode, (*8*) horn antenna, and (*9*) mating cone.

1063-7842/04/4905-0642$26.00 © 2004 MAIK "Nauka/Interperiodica"

part of the graphite cylinder is hollow. Its diameter was made equal to 30 mm in order to provide good ballistic focusing of the beam and increase the electron flux density, which forms a VC in the drift space.

The anode is a hollow metallic cylinder 380 mm long and 160 mm in diameter. It has a grid (Fig. 2a) made of crossing wires 0.8 mm in diameter, which form a semispherical surface of radius 50 mm. The mesh size (spacing between the wires) is *5* mm.

The anode terminates in a horn-type antenna with an opening angle of the horn of 10°. The diameter of the exit window (organic glass), which separates the evacuated space of the vircator from the environment, is 700 mm. The residual pressure in the vircator is kept at $(3–5) \times 10^{-5}$ Torr.

Depending on the aims of the experiment, grid *3* (Fig. 1) was moved along the axis of anode cylinder *2*. The position of the cathode unit was appropriately adjusted by varying the length of tubular holder *1* (Fig. 2b) so that the cathode was at a desired distance from the grid. The grid and the end face of the cathode were concentric when 13 mm distant.

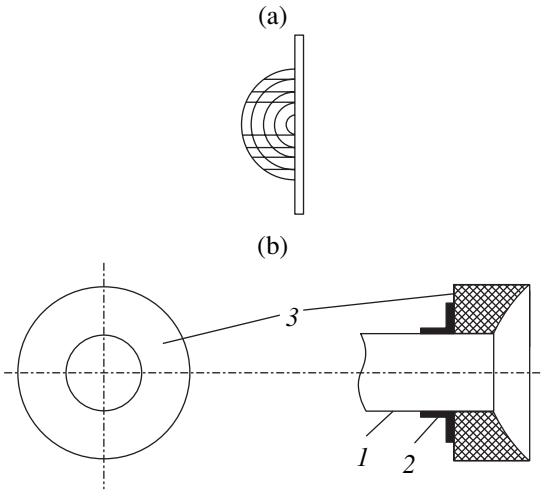

Fig. 2. Design of the (a) grid and (b) cathode: (*1*) tube, (*2*) support, and (*3*) graphite cylinder.

NUMERICAL SIMULATION OF THE VIRCATOR

The computer simulation of the ballistic focusing vircator was performed with the KARAT PIC-code [13]. We simulated the beam dynamics and microwave radiation mechanisms, as well as compared the simulation results and experimental data.

The geometry of the area simulated is shown in Fig. 3. It covers the cathode, anode, and grid of the vircator depicted in Fig. 1. The cathode is a cylinder with a spherical working (electron-emitting) surface 63 mm in diameter. The diameter of the cathode end face equals 70 mm. The cathode is placed on a 270-mm-long tubular holder. The anode is a cylinder 380 mm in diameter with a grid (semisphere with a diameter of 100 mm). The cathode–grid spacing is varied from 10 to 15 mm in 1 mm steps. The end face of the cathode and the grid are concentric when 13 mm apart.

A 900-kV 40-ns-long pulse was applied across the diode gap (the pulse waveform was similar to the actual waveform observed on the oscilloscope). The pulsed current of the diode was as high as 40 kA and had the same duration.

The results of numerical simulation indicate ballistic focusing of the electron beam (Fig. 4). At the time the current reaches a certain value (by this time, an appreciable amount of charge has been accumulated in the gap), a VC forms. For each of the diode gaps considered, its formation was observed within the early 10 ns. A typical phase portrait of the electron beam after the VC has formed is shown in Fig. 5.

The time of VC formation (10 to 12 ns from the beginning) corresponds to the onset of microwave generation; the time of VC collapse (37 ns from the beginning), with the termination of microwave generation and a decrease in the density of the electron cloud, which is responsible for the occurrence of a VC.

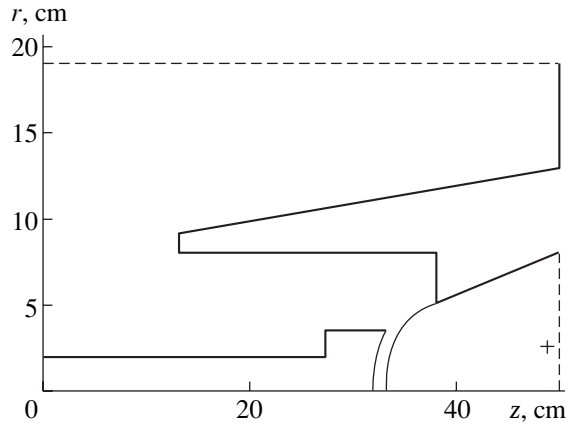

Fig. 3. Geometry of the vircator simulated.

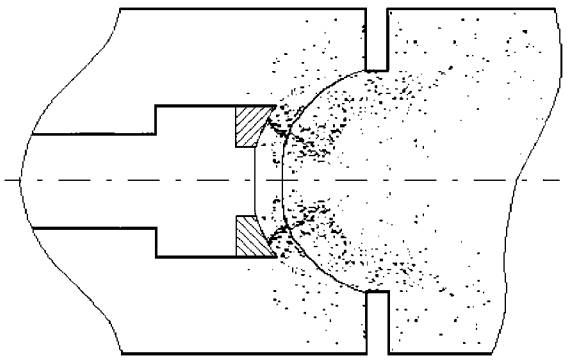

Fig. 4. Electron density simulated.

We calculated the time dependence of the microwave power in the section $z = 50$ cm for a cathode–grid

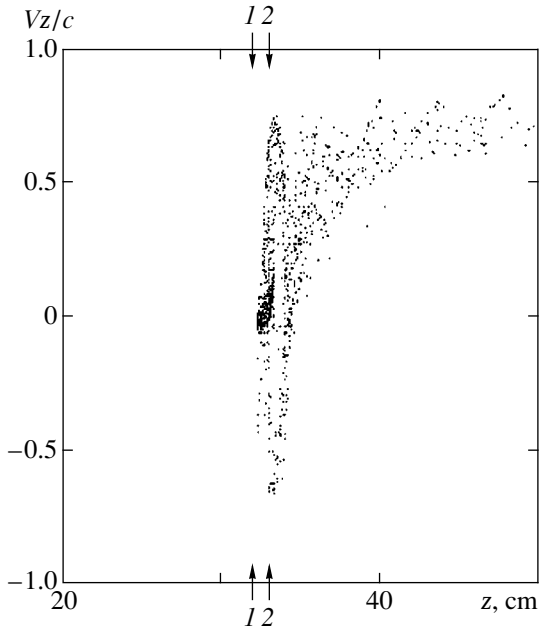

Fig. 5. Formation of a virtual cathode (phase portrait): (*1*) cathode and (*2*) grid.

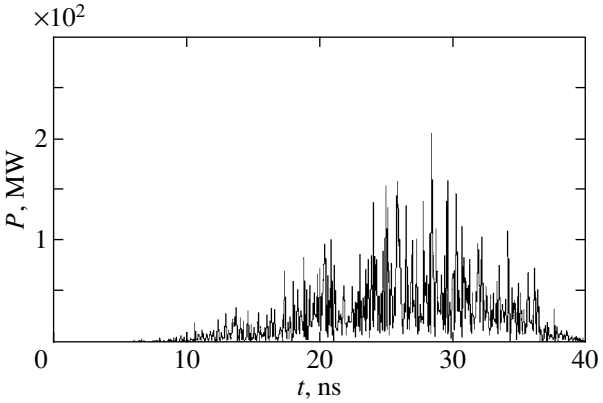

Fig. 6. Radiation power waveform simulated by the KARAT PIC-code.

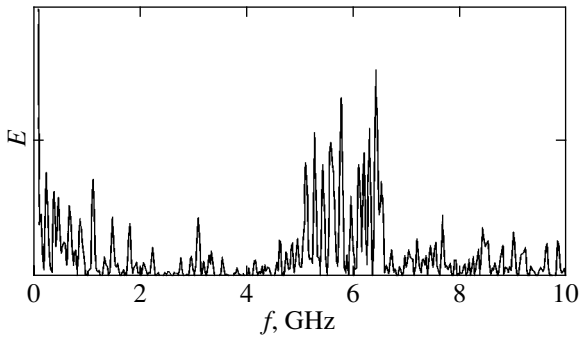

Fig. 7. Spectrum of microwave output.

spacing of 13 mm (Fig. 6). The peak power is maximal (≈220 MW) when the cathode–grid spacing is 10 and 13 mm. The radiation power spectrum is demonstrated in Fig. 7, from which it follows that the maximal microwave output is observed in the frequency range 5.0–6.5 GHz.

By means of detectors, whose positions were coincident with those of anodic Rogowski loops *5* (Fig. 1) in the vircator, we determined the transit-time current in the drift space. To this end, the diode unit was displaced to the left. The maximal calculated value of this current was 5 and 2 kA for the first and second detectors, respectively.

EXPERIMENTAL STUDY OF GENERATION CHARACTERISTICS OF THE VIRCATOR VERSUS THE DIODE UNIT GEOMETRY

The experimental study of the energy characteristics of the spherical vircator was carried out for the diode geometry shown in Fig. 1. This geometry, which features the proximity of the diode unit to the entrance window of the horn antenna and the presence of additional mating cone *9*, makes it possible to attain high values of the cathode current.

The microwave radiation parameters were measured as a function of the cathode–grid spacing. The spacing was varied between 11 and 16 mm. The microwave energy was detected with a calorimeter and measured by hot-carrier cryogenic detectors [14], which were arranged ≈2 m from the horn in the free space.

The signal from the cryogenic detector for the case when the end face of the cathode and the grid are concentric (the cathode–grid spacing is 13 mm) is shown in Fig. 8. The energy detected by the calorimeter is 0.8 J. The duration of the pulse base is 30 ns. Then, the mean power of the microwave generator is $\bar{P} = W/t = 26$ MW. The peak (maximal) power of the microwave signal is $P_m = 65$ MW. For other gap widths (in the absence of concentricity), this value was lower.

The peak power in the vircator of the given configuration is lower than in the vircator with the plane-parallel electrode configuration studied in [8]. The decrease is associated with a longer duration of the microwave signal. In addition, we did not optimize the design of the diode because of the intricate shape of the electrodes: our primary goal was to elucidate whether ballistic focusing of electrons is a possibility. Optimization of the design to improve the peak power of microwave radiation will be made later.

To determine the current value initiating microwave oscillation, the signals from the cathodic loop and cryogenic detector were synchronized with an accuracy of ≈1 ns (Fig. 9). The initiating current was found to be $I = 6.2$ kA. For the plane-parallel configuration of the diode electrodes, this value was 19 kA [8]. Thus, ballistic focusing favors the formation of a VC.

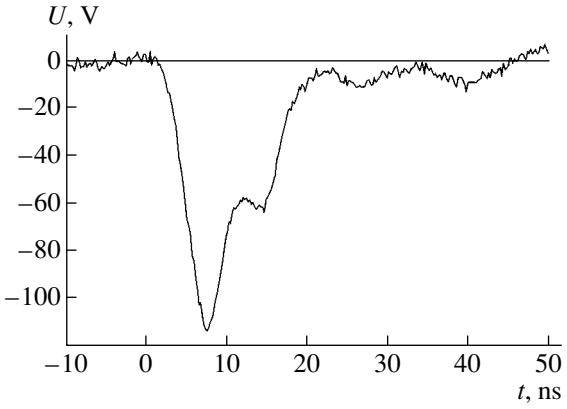

Fig. 8. Waveform of the signal from the hot-carrier cryogenic detector (cathode–grid spacing is 13 mm).

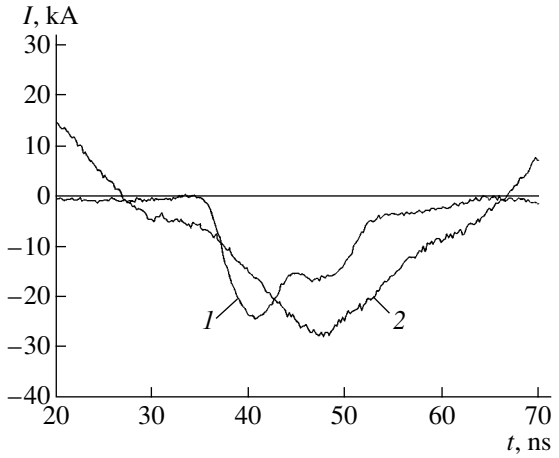

Fig. 9. Waveforms of the signals from the (*1*) cryogenic detector and (*2*) cathodic loop.

The transit-time current in the drift space was measured by using anodic Rogowski loops *5* (Fig. 1). To improve their efficiency, the diode unit was displaced toward the left edge of the anode. The maximal values of the transit-time current detected by the first and second loops were found to be 5.2 and 1.3 kA, respectively (cf. 5.0 and 2.5 kA obtained by calculation).

Analytical formulas for the frequency range of microwave oscillation in a vircator are known only for the plane-parallel diode configuration [3]. To a first approximation, they may be applied to spherical electrodes. Given a cathode–grid spacing of 13 mm and a voltage across the spacing of 900 kV, we find a microwave frequency of 10 GHz. Estimated by the KARAT PIC-code, this frequency lies in the range 5.0–6.5 GHz (Fig. 7).

BALLISTIC FOCUSING OF ELECTRONS: ANALYSIS OF THE BEAM AUTOGRAPH

Additional information on the behavior of the electron beam in the vicinity of the VC may be extracted from its autograph. A glass plate of special configuration (copying the geometry of the space behind the grid) was placed in the drift space on the LIA axis. The shape of the plate and its position in the drift space of the electrodynamic system are shown in Fig. 10a.

Beam-induced darkening on the plate indicates areas where the electron density and energy are the highest. The scanned image of the plate is shown in Fig. 10b.

In Fig. 11, the electron beam autograph obtained with the glass plate is imposed on the electron beam image simulated on a computer.

More intense darkening on the glass is observed almost in the same place where the electron density calculated by the KARAT PIC-code is the highest. Thus, the feasibility of electron focusing by using spherical electrodes has been demonstrated experimentally.

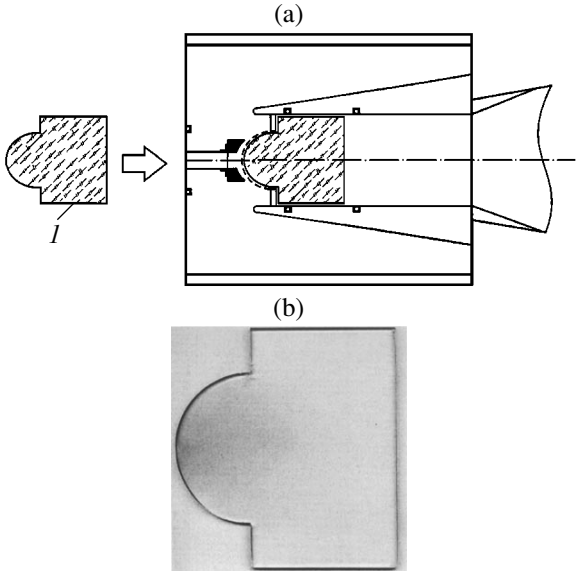

Fig. 10. (a) Beam autograph on glass plate *1* placed in the drift space and (b) scanned image of the plate.

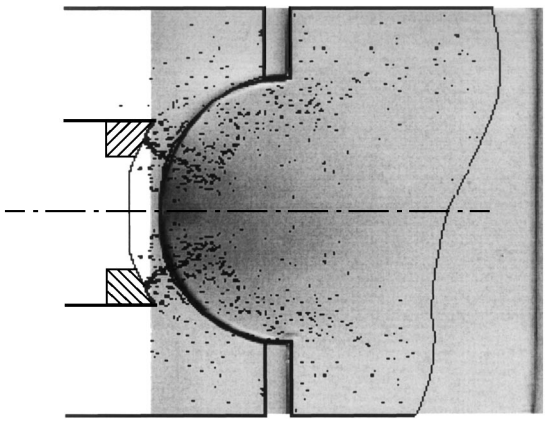

Fig. 11. Simulated electron cloud density imposed on the beam autograph.

CONCLUSIONS

A vircator built around the Korvet ironless LIA and having diode electrodes of spherical shape is designed for the first time. It is proved experimentally that the spherical electrodes decrease electron losses in the region of interaction and favors the formation of an VC. The parameters of the vircator are the following: the peak power is ≈65 MW; the duration of the microwave pulse base, 30 ns; the transit-time currents measured by anodic Rogowski loops, 5.2 and 1.3 kA; and the microwave frequency, 10 GHz.

REFERENCES

1. V. D. Selemir and A. E. Dubinov, Radiotekh. Élektron. (Moscow) **47**, 645 (2002).
2. R. D. Scarpetti and S. C. Burkhart, IEEE Trans. Plasma Sci. **13**, 506 (1985).
3. V. D. Selemir, B. V. Alekhin, V. E. Vatrunin, *et al.*, Fiz. Plazmy **20**, 689 (1994) [Plasma Phys. Rep. **20**, 621 (1994)].
4. A. G. Zherlitsyn, V. S. Lopatin, and O. V. Luk'yanov, Pis'ma Zh. Tekh. Fiz. **16** (11), 69 (1990) [Sov. Tech. Phys. Lett. **16**, 431 (1990)].
5. V. S. Zhdanov, A. L. Babkin, S. M. Galkin, *et al.*, in *Proceedings of the 25th Zvenigorod Conference on Plasma Physics and Controlled Fusion, Zvenigorod, 1998*, p. 169.
6. E. I. Azarkevich, A. N. Didenko, P. V. Dolgopolov, *et al.*, Dokl. Akad. Nauk SSSR **319**, 352 (1991) [Sov. Phys. Dokl. **36**, 539 (1991)].
7. E. I. Azarkevich, A. N. Didenko, A. G. Zherlitsyn, *et al.*, Teplofiz. Vys. Temp. **32**, 127 (1994).
8. V. D. Selemir, A. E. Dubinov, B. G. Ptitsyn, *et al.*, Zh. Tekh. Fiz. **71** (11), 68 (2001) [Tech. Phys. **46**, 1415 (2001)].
9. W. Jiang, H. Kitano, L. Huang, *et al.*, IEEE Trans. Plasma Sci. **24**, 187 (1996).
10. W. Jiang, K. Woolverton, J. Dickens, and M. Kristiansen, IEEE Trans. Plasma Sci. **27**, 1538 (1999).
11. A. G. Zherlitsyn, Pis'ma Zh. Tekh. Fiz. **16** (22), 78 (1990) [Sov. Tech. Phys. Lett. **16**, 879 (1990)].
12. Sh. Kawata, T. Abe, K. Kasuya, and K. Niu, J. Phys. Soc. Jpn. **47**, 1651 (1979).
13. V. P. Tarakanov, *User's Manual for Code Karat* (Berkley, Springfield, 1992).
14. M. D. Raĭzer and L. É. Tsopp, Radiotekh. Élektron. (Moscow) **20**, 1691 (1975).

Translated by V. Isaakyan

Technical Physics, Vol. 49, No. 5, 2004, pp. 647–650. Translated from Zhurnal Tekhnicheskoĭ Fiziki, Vol. 74, No. 5, 2004, pp. 130–133.

SHORT COMMUNICATIONS

Longitudinal rf Discharge in Xe/Cl_2 Mixtures

A. K. Shuaibov, A. I. Dashchenko, and I. V. Shevera

Uzhhorod National University, Uzhhorod, 88000 Ukraine

e-mail: ishev@univ.uzhgorod.ua

Received June 19, 2003

Abstract—Results are presented from the studies of the electrical and emission characteristics of the low-temperature plasma of a longitudinal rf (f_0 = 1.76 MHz) discharge in Xe/Cl_2 mixtures at pressures of 100–800 Pa. The discharge was ignited in a cylindrical quartz tube with an inner diameter of 1.4 cm and interelectrode distance of 3.0 cm. The discharge emission within the spectral range of 190–670 nm is studied. The dynamics of the discharge current and discharge emission at different pressures and compositions of a Xe/Cl_2 mixture are investigated. It is shown that a discharge in a Xe/Cl_2 mixture acts as a wideband excimer–halogen lamp with a cylindrical output aperture emitting in the spectral range of 220–320 nm. The broad plasma emission spectrum is formed due to the overlap of the XeCl(*D*, *B*–*X*; *B*, *C*–*A*) bands that are broadened at low working-gas pressures. The composition of the working mixture is optimized to achieve the maximum power of the wideband UV plasma emission. Longitudinal rf discharges in low-pressure Xe/Cl_2 mixtures are of interest for developing small-size wideband ($\Delta\lambda$ = 220–450 nm) cylindrical-aperture lamps, whose efficiency can, on average, exceed the efficiency of conventional hydrogen lamps by more than one order of magnitude. © *2004 MAIK "Nauka/Interperiodica".*

INTRODUCTION

At present, efficient high-power sources of spontaneous UV and VUV emission operating on the vibronic bands of argon, krypton, and xenon monohalogenides are widely used in microelectronics, high-energy physics, ecology, biotechnology, and medicine [1, 2]. Glow, capacitive, or barrier discharges [3–7] are usually used to pump low- and moderate-pressure lamps. The maximum repetition rate of the emission pulses from transitions in the monochlorides and monobromides of heavy noble gases does not exceed 100–200 kHz. This limitation is mainly imposed by power supply units, whose key elements are thyratrons and tasitrons. To improve the discharge stability and increase the repetition rate of UV emission pulses in electronegative gases, it seems promising to use rf sources to feed low-pressure excimer halogen lamps. A xenon-chloride lamp pumped by a low-current rf barrier discharge was described in [8]. To increase the output power of a low-size lamp with a cylindrical output aperture, it is expedient to use a high-current longitudinal electrode rf discharge in a Xe/Cl_2 mixture.

EXPERIMENTAL SETUP

A schematic of an excimer–halogen lamp with a cylindrical output aperture is shown in Fig. 1. A high-current γ-type rf discharge was ignited in a cylindrical quartz discharge tube with an inner diameter of 1.4 cm. The distance between 1.5-cm-long and 1.4-cm-diameter hollow cylindrical nickel electrodes was 3.0 cm. A longitudinal rf discharge was supplied from an amplitude-modulated ($f \le 50$ Hz) ÉN-57M rf source with an operating frequency of f_0 = 1.76 MHz and average power of no higher than 250 W. Voltage pulses with an amplitude of 5–6 kV were applied to the lamp electrodes via a 200-pF KVI-2 blocking capacitor. The Xe/Cl_2 mixture circulated through the discharge tube with a flow rate of 0.1 l/min. The technique for recording the characteristics of a longitudinal rf discharge was described in our earlier papers [9–11]. The power of spontaneous emission was measured by a Kvarts-01 power meter equipped with a UFS-5 light filter, which cuts off visible and IR radiation. The pulses of the total plasma emission were recorded using a Foton photomultiplier (equipped with a UFS-5 filter) and a S1-99 oscilloscope.

The plasma emission was observed in the axial direction through one of the hollow electrodes. Hence,

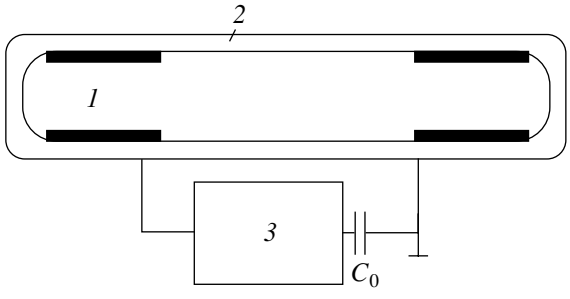

Fig. 1. Schematic of an excimer–halogen lamp pumped by a low-pressure longitudinal rf discharge: (*1*) electrodes, (*2*) discharge tube, (*3*) source of the modulated rf voltage, and (C_0) blocking capacitor.

1063-7842/04/4905-0647$26.00 © 2004 MAIK "Nauka/Interperiodica"

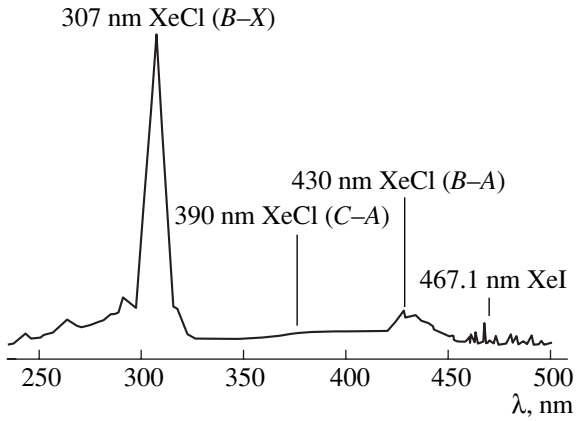

Fig. 2. Emission spectrum from a discharge in a Xe/Cl_2 mixture at pressures of 100–500 Pa.

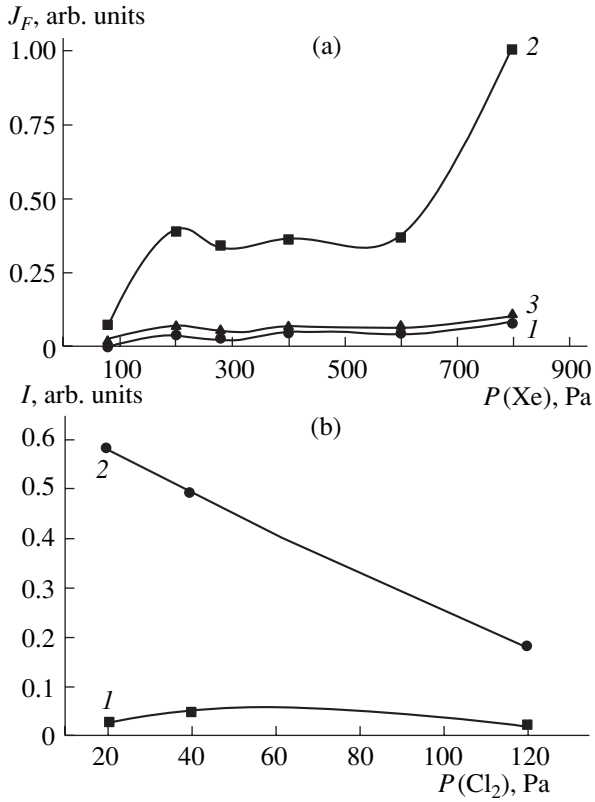

Fig. 3. Emission intensity of the (*1*) XeCl(*D–X*) 236-nm, (*2*) XeCl(*B–X*) 307-nm, and (*3*) XeCl(*B–A*) 430-nm bands vs. (a) xenon partial pressure at $P(Cl_2)$ = 80 Pa and (b) chlorine partial pressure at $P(Xe)$ = 280 Pa.

the emission from both the electrode regions and the positive column was recorded by the photomultiplier.

DISCHARGE PLASMA EMISSION

A major fraction of the emission from a longitudinal rf discharge in a Xe/Cl_2 mixture corresponds to the XeCl(*B–X*) and XeCl(*D–X*) bands with maxima at 307 and 236 nm, respectively (Fig. 2). At low working-gas pressures, the process of vibrational relaxation within the *D* and *B* states of xenon chloride is incomplete [12]. The XeCl(*B–X*) and XeCl(*D–X*) bands are greatly broadened; the overlap between them and the Cl_2(*D'–A'*) band with a maximum at 257 nm results in the formation of an emission continuum in the spectral range of 220–320 nm. As compared to atmospheric-pressure lamps [13–15], the main maxima of XeCl(*B–X*) emission were shifted to the shorter wavelength range and were observed at λ = 307 and 289 nm. The decrease in the xenon partial pressure from 500 to 50 Pa leads to a decrease in the UV emission intensity from the plasma. In the spectral range of 320–450 nm, there are two less intense broad emission bands with maxima at λ = 390 and 430 nm, corresponding to the *C–A* and *B–A* transitions of XeCl molecules, respectively. The width of the XeCl(*C–A*) band is approximately two to three times the width of the XeCl(*B–X*) band. The overlap of all the main emission bands of XeCl molecules leads to the formation of an emission continuum in the spectral range of 220–450 nm. In the visible region, the plasma emission consists mainly of the most intense lines of Xe atoms, the most intense of which is the XeI (6*s*–7*p*) 467.1-nm line (Fig. 2).

Figure 3 illustrates the results of optimization of the emission intensities of the XeCl(*D, B–X*; *B–A*) bands in terms of the pressure and partial composition of the Xe/Cl_2 mixture. The optimum partial pressure of xenon is $P(Xe)$ = 600–800 Pa (at $P(Cl_2)$ = 80 Pa), and the optimum chlorine partial pressure is $P(Cl_2)$ = 20–40 Pa (at a fixed moderate xenon pressure of $P(Xe)$ = 280 Pa).

Figures 4 and 5 show waveforms of the discharge current (I) and the total emission intensity (J_F) from longitudinal rf discharges in Xe/Cl_2 mixtures. In each figure, the upper two curves illustrate the waveforms of the rf current and the total emission intensity in the submicrosecond range, whereas the lower curves show the envelopes of I and J_F, whose variations are related to the low-frequency amplitude modulation of the rf voltage supplied from the ÉN-57M power source. In Figs. 4 and 5, only the envelopes corresponding to the high-current stage of the rf discharge are presented. During the low-current stage of the discharge (within the time intervals t = 0–2 and 7–9 ms), the current was too low to be recorded. The amplitude of the rf current half-wave reached 1 A, and its duration was 300 ns. The plasma emission consisted mainly of the zero-frequency component. The emission intensity was modulated in amplitude with a frequency twice as high as the frequency of the pumping rf current. The percentage of the pulsating component in the plasma emission increased with the partial pressure of chlorine in a Xe/Cl_2 mixture. The maxima of the plasma emission intensity (see Figs. 4 and 5) corresponded to the descending and ascending segments of the waveform of the rf component of the discharge current.

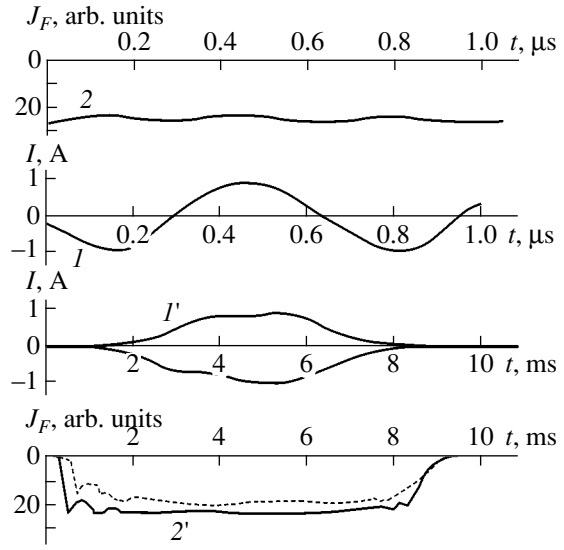

Fig. 4. Waveforms of (*1*, *1*') the rf current and (*2*, *2*') the total emission intensity of a longitudinal rf discharge in a $P(Xe)/P(Cl_2)$ = 400/20-Pa mixture: (*1*, *2*) the rf structure and (*1'*, *2'*) the envelopes of the current and the emission intensity. The dashed line refers to the constant component of radiation.

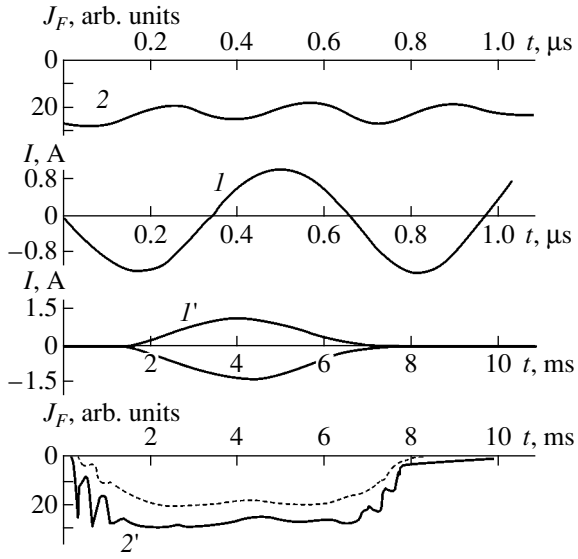

Fig. 5. Waveforms of (*1*, *1*') the current and (*2*, *2*') the emission intensity of a discharge in a $P(Xe)/P(Cl_2)$ = 400/80-Pa mixture. The dashed line shows a zero-frequency component of the emission intensity.

For glow, capacitive, and rf discharges in low-pressure Xe/Cl_2 mixtures, one of the main reactions is the "harpoon" reaction of XeCl* molecules [7, 16, 17]. Within the electrode sheaths of an rf discharge, positive and negative ions are also efficiently produced [18]. As a result of recombination of these ions, XeCl* and Cl_2^* molecules are produced, whose spontaneous decay is responsible for the formation of the emission continuum in the spectral range of 220–450 nm.

The harpoon reaction is of most importance for enabling continuous operation of these channels for the production of emitting molecules. For this reaction to proceed, it is necessary to maintain a steady-state density of Xe and Cl metastable atoms. Such a situation can occur in a longitudinal rf discharge, in which the density of metastable atoms is maintained at a certain nonzero level (rather than decreasing to zero) when the rf current changes its sign.

It can be seen from Figs. 4 and 5 that there are two or three clearly pronounced short-duration maxima at the leading and trailing edges of the emission envelopes. The maximum duration of the emission pulses decreases from 7 to 6 ms as the chlorine partial pressure increases from 20 to 80 Pa. The spiking structure at the edges of the emission envelope becomes even more pronounced as $P(Cl_2)$ increases.

The maximum power of broadband UV emission from the entire side aperture of the lamp reached 15–20 W, whereas the lamp efficiency was no higher than 10%. The lamp lifetime in a static-gas regime was no longer than 30–40 min. It significantly increased when the working mixture circulated with a flow rate of ≤0.1 l/min. Under forced air cooling of the discharge tube and "hot" passivation with high-purity chlorine, the lamp lifetime can be increased to several hundred hours, which is equal to the lifetime of $XeCl^*/Cl_2^*$ lamps pumped by a dc glow discharge.

CONCLUSIONS

The results of the study of the characteristics of a longitudinal rf discharge in Xe/Cl_2 mixtures can be summarized as follows:

(i) The discharge acts as a source of broadband emission in the spectral range of 220–450 nm.

(ii) The main component of the emission spectrum corresponds to the XeCl(*B*–*X*) 307-nm band.

(iii) The main physical process shifting the maximum of UV emission to the shorter wavelength range is vibrational relaxation.

(iv) The plasma emission mainly consists of the zero-frequency component, whereas the contribution of the alternating component is insignificant and increases with the partial pressure of chlorine in the mixture.

(v) Short-duration peaks of the total plasma emission are generated within the time intervals in which the discharge current is close to its threshold value.

(vi) Optimum mixtures for achieving the maximum UV emission power are gas mixtures with $P(Xe)/P(Cl_2)$ = (600–800)/(20–40) Pa.

REFERENCES

1. U. Kogelschatz, B. Eliasson, and W. Egli, Pure Appl. Chem. **71**, 1819 (1999).
2. E. A. Sosnin, V. N. Batalova, and G. B. Slepchenko, Proc. SPIE **4747**, 352 (2001).
3. A. P. Golovitskiĭ, Pis'ma Zh. Tekh. Fiz. **18** (8), 73 (1992) [Sov. Tech. Phys. Lett. **18**, 269 (1992)].
4. A. N. Panchenko, V. S. Skakun, É. A. Sosnin, *et al.*, Pis'ma Zh. Tekh. Fiz. **21** (20), 77 (1995) [Tech. Phys. Lett. **21**, 851 (1995)].
5. A. K. Shuaibov, A. I. Dashchenko, and I. V. Shevera, Kvantovaya Élektron. (Moscow) **31**, 371 (2001).
6. A. K. Shuaibov, Zh. Tekh. Fiz. **72** (10), 138 (2002) [Tech. Phys. **47**, 1341 (2002)].
7. M. I. Lomaev, V. S. Skakun, É. A. Sosnin, *et al.*, Usp. Fiz. Nauk **173**, 201 (2003).
8. A. P. Golovitskiĭ, Pis'ma Zh. Tekh. Fiz. **24** (6), 63 (1998) [Tech. Phys. Lett. **24**, 233 (1998)].
9. A. K. Shuaibov, L. L. Shimon, A. I. Dashchenko, and I. V. Shevera, Prib. Tekh. Éksp., No. 1, 104 (2002).
10. A. K. Shuaibov, L. L. Shimon, A. I. Dashchenko, and I. V. Shevera, J. Phys. Stud. **5**, 131 (2001).
11. A. Shuaibov, L. Shimon, A. Dashchenko, and I. Shevera, Proc. SPIE **4747**, 409 (2001).
12. V. V. Datsyuk, I. A. Izmaĭlov, and V. A. Kochelap, Usp. Fiz. Nauk **168**, 439 (1998) [Phys. Usp. **41**, 379 (1998)].
13. A. K. Shuaibov, Zh. Tekh. Fiz. **68** (12), 64 (1998) [Tech. Phys. **43**, 1459 (1998)].
14. A. K. Shuaibov, Teplofiz. Vys. Temp. **37**, 188 (1999).
15. A. K. Shuaibov, Opt. Spektrosk. **88**, 875 (2000) [Opt. Spectrosc. **88**, 796 (2000)].
16. A. P. Golovitskiĭ and V. F. Kan, Opt. Spektrosk. **75**, 604 (1993) [Opt. Spectrosc. **75**, 357 (1993)].
17. A. P. Golovitskiĭ and S. V. Lebedev, Opt. Spektrosk. **82**, 251 (1997) [Opt. Spectrosc. **82**, 227 (1997)].
18. I. D. Kaganovich, Fiz. Plazmy **21**, 431 (1995) [Plasma Phys. Rep. **21**, 410 (1995)].

Translated by N. Ustinovskiĭ

Technical Physics, Vol. 49, No. 5, 2004, pp. 651–652. Translated from Zhurnal Tekhnicheskoĭ Fiziki, Vol. 74, No. 5, 2004, pp. 134–135.

SHORT COMMUNICATIONS

Interpretation of Acceleration Measurements in Inertial Navigation

A. S. Devyatisilny

Institute of Automatics and Control, Far-East Division, Russian Academy of Sciences, Vladivostok, 690041 Russia

e-mail: devyatis@iacp.dvo.ru

Received September 5, 2003

Abstract—It is shown that, when the absolute and apparent accelerations are measured simultaneously, the problem of autonomous inertial navigation is reduced to the solvable inverse problem. Physical and geometrical (kinematic) conditions for solvability are formulated. *© 2004 MAIK "Nauka/Interperiodica".*

(1) Modern technology makes optical meters of absolute acceleration feasible [1]. It would be therefore of interest to test them in various applications, such as inertial navigation, where use of apparent-acceleration meters is common practice [2]. In this case, application of the inertial navigation method is essentially reduced to the solution of the direct problem using two (dynamic and kinematic) sets of equations. A solution to the direct problem thus stated is unstable, and straightforward use of the method faces certain difficulties [3].

The situation will change qualitatively if the absolute and apparent accelerations are measured simultaneously. Then, one can identify the inertial navigation method with the inverse problem provided that a model of gravitational field is known.

In this work, we state and discuss the inverse problem.

(2) While on the subject of *f*, *gf*, and *g* meters (measurements) of nongravitational specific forces (apparent acceleration), total specific forces (absolute acceleration), and gravitational specific forces or gravitational field strength (free-fall acceleration), we will consider 3D devices, bearing in mind that a *g* meter is a combination of *f* and *gf* meters [4]. It is reasonable to call these three devices *f*, *gf*, and *g* newtonmeters.

Let $oy = oy_1y_2y_3$ be an orthogonal coordinate rectangle uniquely related to a measuring platform whose constant (in the ideal case) orientation relative to the inertial frame of reference ($o\xi = o\xi_1\xi_2\xi_3$) is maintained by gyros.

Let oy physically simulate $o\xi$ (within a kinematic error) by a β vector of a small angular perturbation of the platform orientation, so that $y = (E + \hat{\beta})\xi$, where E is the unit matrix and $\hat{\beta}\xi = \beta \times \xi$.

Note that the case at hand differs substantially from that considered in [4], where oy physically simulated an attending geographically oriented coordinate trihedron. In essence, oy is an instrumental trihedron; that is, all vector measurements (including measurements by newtonmeters) are made relative to its coordinates. In view of the aforesaid, newtonmeter readings are representable in the form

$$\begin{aligned} J_f &= (E + \hat{\beta})f + \Delta_f, \\ J_{gf} &= (E + \hat{\beta})(g + f) + \Delta_{gf}, \end{aligned} \tag{1}$$

where g and f are the vectors of the gravitational field strengths and nongravitational specific forces projected onto the axes of the $o\xi$ coordinate system and Δ_f and Δ_{gf} are the instrumental errors of measurement.

In view of (1), the measurements of a *g* newtonmeter obviously take the form

$$J_g = g + \hat{\beta}g + \Delta_g, \tag{2}$$

where $\Delta_g = \Delta_{gf} - \Delta_f$.

Above all, the gravimetric character of measurements (2) receives attention; however, no consideration will be given to this point, since it goes beyond the scope of this work.

(3) Integration of *gf* measurements on the axes of the trihedron oy makes it possible to determine the current values of the velocity, v, and position, r, of an object. However, these values involve errors arising from erroneous initial conditions of integration and the instrumental error of a *gf* newtonmeter.

Later on, we will proceed from the following assumptions (which do not limit the applied value of our considerations): (i) the form of the gravitational potential $U(r)$ is known: $g(r) = \partial U/\partial r = U'(r)$; (ii) gyros and newtonmeters do not introduce instrumental errors; that is, errors in input ($t = 0$) data are the only source of perturbations of the platform spatial orientation and at the integrator output. Then, $\beta = \text{const}$, $\delta v = \delta v_0$, $\delta r = \delta r_0 + \delta v_0 t$, where $\delta v_0 = \delta v(0)$ and $\delta r_0 = \delta r(0)$.

1063-7842/04/4905-0651$26.00

In view of assumption (i), the inverse problem mentioned above is stated in general form (2); in view of both assumptions, in the form

$$J_g = g(r) - \hat{g}(r)\beta = g(r) - G(r)\hat{\beta}, \quad (3)$$

where $G(r) = \hat{g}(r)$.

Our aim is to find a phase vector $s = (\beta^T, r^T, v^T)^T$ for both (kinematic and dynamic) sets of equations that constitute the inertial navigation method. Accordingly, we must answer the question as to whether the problem is solvable for the vector s.

(4) Let us return to integration of *gf* measurements, i.e., to the solution of the direct problem. Taking into account the results of integration, we may localize the initially nonlinear problem by constructing a residual vector and passing to the problem in the small according to the following linear model:

$$\delta J_g = g'(r)\delta r + G(r)\beta, \quad (4)$$

where δJ_g is the residual vector of measurements and $g'(r) = U''(r)$.

Before proceeding further, we will consider a hypothetical case that is similar to the case under discussion and is of independent interest (as will be seen from the following). Let $g(r) = \text{const}$ or $g'(r) = 0$. Then, from (4), we have

$$\delta\tilde{J}_g = G(r)|g|^{-1}\beta = \hat{\tau}\beta = \hat{\tau}\beta^+, \quad (5)$$

where $\tau = g/|g|$, $\delta\tilde{J}_g = \delta J_g/|g|$, and β^+ is the component of the vector β that is orthogonal to the unit vector τ or, which is the same, to the field line.

As follows from (5), a *g* newtonmeter shows the properties of a "telescope"; that is, it locates the platform up to rotation about the unit vector τ of the "sighting" of a specific "star."

It is known that, in the case of real telescopes, this problem is completely solved by sighting two or more stars or by sighting one fixed (at $\tau \neq \text{const}$) object whose angular coordinates are known.

In the case of a *g* newtonmeter as a telescope, sighting of several stars is impossible because field lines outside sources do not intersect. However, the case $\tau \neq \text{const}$ seems quite realistic but requires that model (4) be invoked.

In the general case of an arbitrary field, when $g'(r) = U''(r) \neq 0$, model (4) is representable (with regard to assumption (ii)) in the form

$$\delta J_g = W\delta s_0, \quad (6)$$

where $\delta s_0 = (\beta^T, \delta r_0^T, \delta v_0^T)^T$ and $W = \|G \vdots U'' \vdots U''t\|$.

In the final interval of measurements, the set of equations that is generated by model (6) can be solved for the constant vector δs_0. This statement follows from the fact that the columns of the matrix W as functions of time (paths) are generally linearly independent unless the Hessian $U''(r)$ of the field is nondegenerate. Exceptions are cases when paths for which $\tau = g/|g| = \text{const}$ ($G = \text{const}$) are realized in the time intervals of measurements. In this case, the vector β is a "weak point," since its component $\beta^- = (\tau^T\beta)\tau$ becomes nonidentifiable.

If, by way of example, we pass from the general case to the specific case of a central field, by which the exterior field of terrestrial gravitation is frequently simulated, the Hessian $U''(r)$ of such a field is nondegenerate (its singular numbers relate as 2 : 1 : 1 [5]) and singular (for the matrix W) trajectories (on which $\tau = \text{const}$) are realized on central straight lines.

Thus, the inverse problem is solvable if two conditions are fulfilled simultaneously. The first one, $\det U''(r) \neq 0$, has the purely physical meaning; the other, $\tau(r) \neq \text{const}$, is of geometric or kinematic (if it is kept in mind that "kinematics is the geometry of motion" [2]) character. The former condition is universal; the latter leaves room for selection.

(5) To conclude, the basic result of this study and its applied value are as follows. Combined use of *f* and *gf* newtonmeters allows one to reduce the inertial navigation method to the inverse problem, which is fundamentally solvable for the phase vector of a set of dynamic and kinematic equations that simulate the evolution of the trajectory and the frame of reference. This offers scope for designing autonomous asymptotically stable operating inertial navigation systems (unlike conventional systems [3]).

REFERENCES

1. Yu. I. Kolyada, S. V. Sokolov, and S. A. Olenev, Izmer. Tekh., No. 4, 33 (2001).
2. A. Yu. Ishlinskiĭ, *Classical Mechanics and Inertial Forces* (Nauka, Moscow, 1987) [in Russian].
3. V. D. Andreev, *Theory of Inertial Navigation: Autonomous Systems* (Nauka, Moscow, 1966) [in Russian].
4. A. S. Devyatisilny, Zh. Tekh. Fiz. **73** (12), 99 (2003) [Tech. Phys. **48**, 1598 (2003)].
5. A. S. Devyatisilny, Zh. Tekh. Fiz. **73** (9), 130 (2003) [Tech. Phys. **48**, 1209 (2003)].

Translated by V. Isaakyan

Technical Physics, Vol. 49, No. 5, 2004, pp. 653–657. Translated from Zhurnal Tekhnicheskoĭ Fiziki, Vol. 74, No. 5, 2004, pp. 136–140.

SHORT COMMUNICATIONS

Duration of Transients Versus Initial Conditions in Zaslavsky Mapping

A. A. Koronovskii and A. E. Khramova

Kolledzh State Scientific–Educational Center, Chernyshevsky State University, Saratov, 410026 Russia

e-mail: alkor@cas.ssu.runnet.ru

Received September 25, 2003

Abstract—Mechanisms are considered that complicate the dependence of the duration of transients on initial conditions in a 2D dynamic discrete-time system (Zaslavsky mapping) when control parameters are changed with the dynamic regime remaining unchanged. For a stable cycle, the form of this dependence is governed by multipliers and their associated manifolds. Reasons why this dependence becomes qualitatively more complicated are discussed. Results obtained may be generalized for a wide class of dynamic systems with both discrete and continuous time. © *2004 MAIK "Nauka/Interperiodica".*

Transients in dynamic systems have recently attracted much attention [1–4]. These investigations are of both fundamental [5–7] and applied [8–10] interest. As subjects of investigation, the researchers usually take various mappings [11–13], since they are simple to study, on the one hand, and demonstrate basic nonlinear phenomena typical of lumped and distributed systems, on the other.

Earlier [11, 12], it was demonstrated with Hénon mapping that the dependence of the duration of transients on initial conditions when control parameters change with the dynamic regime remaining invariable may become more complicated following two scenarios. The former is realized when the multipliers of a periodic cycle become complex conjugate; the latter, when the multipliers are equal in magnitude and opposite in sign, remain real quantities. The aim of this work is to extend the results obtained for the Hénon mapping [11, 12] to a wider class of 2D dynamic systems in an effort to prove their general character.

As an object of study, we take a 2D dynamic system with discrete time known as the Zaslavsky mapping [14–18]:

$$\begin{aligned} x_{n+1} &= x_n + \Omega + \frac{k}{2\pi}\sin(2\pi x_n) + dy_n, \quad \mod 1, \\ y_{n+1} &= dy_n + \frac{k}{2\pi}\sin(2\pi x_n). \end{aligned} \tag{1}$$

In the case of Zaslavsky mapping (1), the dependence of the duration of a transient on given initial conditions $T_\varepsilon(x_0, y_0)$ was determined as in [11, 19–21].

Here, we consider various dynamic regimes of Zaslavsky mapping (1): stable cycles with periods of 1 and 2. From bifurcational analysis of mapping (1), it follows that, if the values of control parameters meet the conditions $0 < d < 1$, $\Omega > 0$, and $\Omega\sqrt{1-2d+d^2} < k < \sqrt{4+\Omega^2+8d-2\Omega^2 d+4d^2+\Omega^2 d^2}$, there are only one unstable, (x^0, y^0), and one stable, (x^1, y^1), point on the plane (x, y):

$$\begin{aligned} x^0 &= \arcsin\frac{\Omega(-1+d)}{k} + 2\pi, \\ y^0 &= -\Omega, \\ x^1 &= -\arcsin\frac{\Omega(-1+d)}{k} + \pi, \\ y^1 &= -\Omega. \end{aligned} \tag{2}$$

The stable point (x^1, y^1) is characterized by the multipliers

$$\begin{aligned} \mu_1 &= 0.5\left(1 - k\sqrt{1-\frac{\Omega^2(-1+d)^2}{k^2}}\right. \\ &\left. - \sqrt{\left(-1 - k\sqrt{1-\frac{\Omega^2(-1+d)^2}{k^2}} - d\right)^2 - 4d} + d\right), \\ \mu_2 &= 0.5\left(1 - k\sqrt{1-\frac{\Omega^2(-1+d)^2}{k^2}}\right. \\ &\left. + \sqrt{\left(-1 - k\sqrt{1-\frac{\Omega^2(-1+d)^2}{k^2}} - d\right)^2 - 4d} + d\right). \end{aligned} \tag{3}$$

For the unstable point (x^0, y^0), the multipliers are

$$\mu^1 = 0.5\left(1 + k\sqrt{1-\frac{\Omega^2(-1+d)^2}{k^2}}\right.$$

$$-\sqrt{\left(-1+k\sqrt{1-\frac{\Omega^2(-1+d)^2}{k^2}}-d\right)^2-4d}+d\Bigg),$$

$$\mu^2 = 0.5\Bigg(1+k\sqrt{1-\frac{\Omega^2(-1+d)^2}{k^2}} \tag{4}$$

$$+\sqrt{\left(-1+k\sqrt{1-\frac{\Omega^2(-1+d)^2}{k^2}}-d\right)^2-4d}+d\Bigg).$$

Figure 1a shows the dependences of the multipliers μ_1 and μ_2 on the control parameter k for $\Omega = 0.9$ and $d = 0.3$, which correspond to the stable cycle with a period of 1, (x^1, y^1). It is seen that the multiplies are in the complex domain at $0.66237 < k < 2.4769$, where they experience a discontinuity. At the extremes of the discontinuity range, $k = 0.66237$ and 2.4769, the values of the multipliers μ_1 and μ_2 coincide. At $k < 0.66237$, the multipliers μ_1 and μ_2 take on positive values with $\mu_1 < \mu_2$. Thus, as the control parameter grows from 0.63 to 0.66237 (i.e., before the multipliers become complex), the multiplier μ_1 gradually increases, while μ_2 decreases. At the boundary of the domain where the cycle with a period of 1 is stable, the multipliers take the values $\mu_2 = 1$ and $\mu_1 = 0.25$, and at the boundary of the discontinuity range, they tend to the same value 0.48. At the other boundary of the discontinuity range ($k = 2.4769$), both multipliers equal –0.48. At $k > 2.4769$, they are negative, with the multiplier μ_2 being smaller in magnitude. As k varies from 2.4769 to 2.67524, μ_1 tends to –1. In the range $0.66237 < k < 2.4769$, the multipliers μ_1 and μ_2 are complex conjugate and $|\mu_1| = |\mu_2|$.

Comparing the projections of the surface $T_\varepsilon(x_0, y_0)$ onto the plane of the initial conditions (x_0, y_0) (Figs. 1b, 1c) with the positions of stable manifolds (Figs. 1d, 1e) for the stable cycle of period 1 (see (2)), one may notice a distinctive feature: the minima of the durations of transients coincide with the manifold corresponding to the smaller modulus multiplier (the bright lines in Figs. 1b, 1c). The maxima of the durations coincide with the stable manifold for the unstable point (x^0, y^0) (the dark lines in Figs. 1b, 1c). It should be noted that, after the discontinuity range ($2.4769 < k < 2.6752$), the dependence of the transient process duration on the initial conditions $T_\varepsilon(x_0, y_0)$ becomes more complicated: an infinite number of minima appear that accumulate at the line of transient duration maxima.

To explain this observation, let us consider in detail the behavior of the stable manifolds for the fixed stable point and of the stable and unstable manifolds for the fixed unstable point. For the control parameter values $\Omega = 0.9$, $d = 0.3$, and $k < 0.66237$, the fastest divergence to the fixed stable point is observed over the manifold where the multiplier μ_1 is the smallest. Obviously, any point of the initial conditions (x_0, y_0) that lies in the neighborhood of the unstable point (x^0, y^0) will tend to the attractor over the unstable manifold μ^2 (see (4)) of the unstable point (x^0, y^0). The behavior of the unstable manifold of the unstable point in the vicinity of (x^1, y^1) at $k < 0.66237$ will depend on the behavior of the stable manifold of the stable point (x^1, y^1) that corresponds to the larger magnitude multiplier μ_2 (Fig. 1d). After the range of complex values of the multipliers for the fixed stable point (x^1, y^1) (at $\Omega = 0.9$, $d = 0.3$, and $k > 2.4769$), the behavior of the unstable manifold of the unstable point (x^0, y^0) near the stable point (x^1, y^1) depends on the behavior of the stable manifold corresponding to the larger magnitude multiplier μ_1 (Fig. 1e). Since the multiplier μ_1 is negative at $k > 2.4769$, the unstable manifold of the point (x^0, y^0) crosses the stable manifolds of the point (x^1, y^1) an infinite number of times. This generates an infinite number of minima of the transient process durations at $k > 2.4769$.

Similar analysis can be carried out for the more complex dynamic regime, the cycle with a period of 2. In the case of Zaslavsky mapping, exact analytical expressions for the elements (x_{2c}^1, y_{2c}^1) and (x_{2c}^2, y_{2c}^2) of the cycle with a period of 2 is impossible to derive. Therefore, expressions for the stable elements of this cycle were obtained numerically. The elements (x_{2c}^1, y_{2c}^1) and (x_{2c}^2, y_{2c}^2) of this cycle are characterized by the multipliers

$$\mu_1^{2c} = 0.5(1 + d^2 + k\cos x_{2c}^1 + k\cos x_{2c}^2 + k^2\cos x_{2c}^1\cos x_{2c}^2)$$

$$-0.5\sqrt{-4(d^2 + kd^2\cos x_{2c}^1 + kd^2\cos x_{2c}^2) + (-1 - d^2 - k\cos x_{2c}^1 - k\cos x_{2c}^2 - k^2\cos x_{2c}^1\cos x_{2c}^2)^2}, \tag{5}$$

$$\mu_2^{2c} = 0.5(1 + d^2 + k\cos x_{2c}^1 + k\cos x_{2c}^2 + k^2\cos x_{2c}^1\cos x_{2c}^2)$$

$$+0.5\sqrt{-4(d^2 + kd^2\cos x_{2c}^1 + kd^2\cos x_{2c}^2) + (-1 - d^2 - k\cos x_{2c}^1 - k\cos x_{2c}^2 - k^2\cos x_{2c}^1\cos x_{2c}^2)^2}.$$

Figure 2a plots the multipliers μ_1^{2c} and μ_2^{2c} against the control parameter k at fixed $\Omega = 0.9$ and $d = 0.3$, which correspond to the stable cycle of period 2. As in the case of the fixed stable point, the multiplies here also fall into the complex domain in the range $2.7723 < k < 3.0641$ (the discontinuity range). At the boundaries

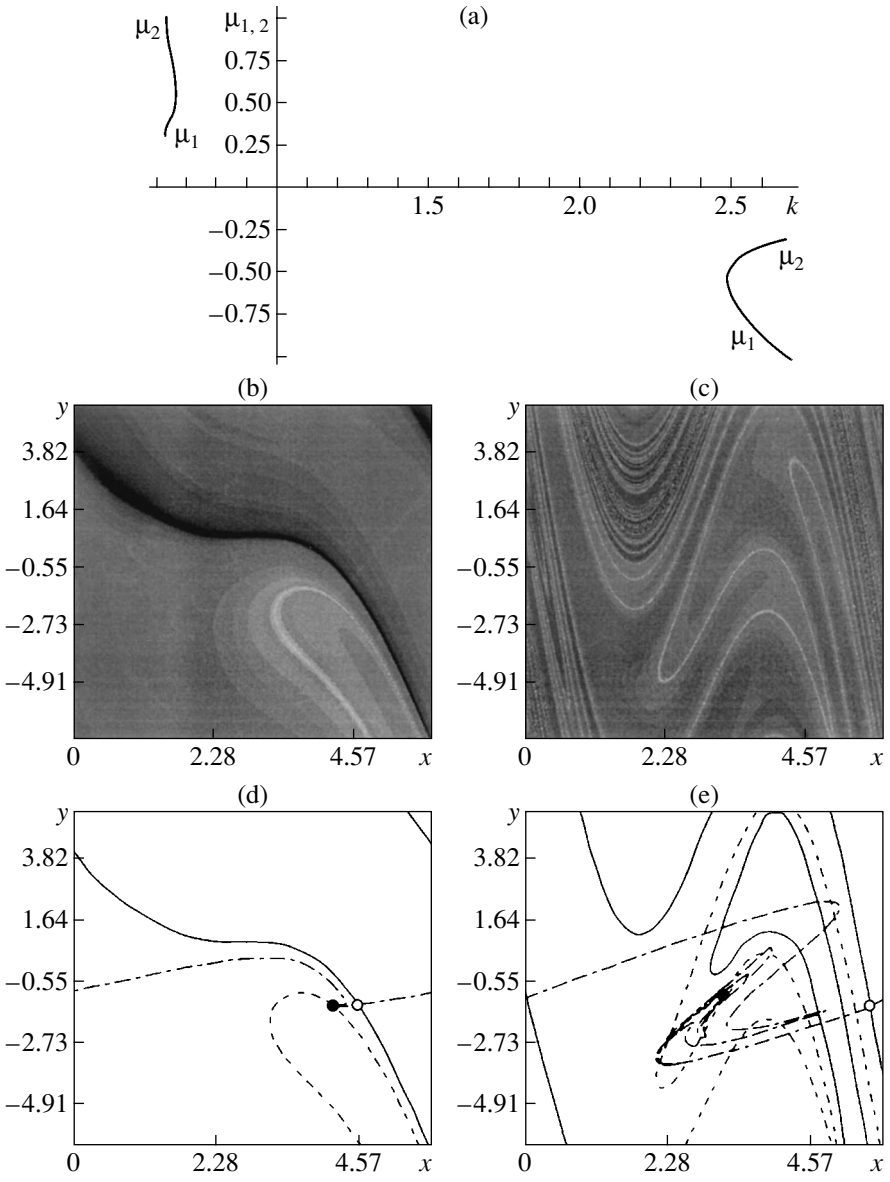

Fig. 1. (a) Multipliers μ_1 and μ_2 for the fixed stable point vs. the control parameter k at $\Omega = 0.9$ and $d = 0.3$. The discontinuity range corresponds to the complex values of the multipliers. (b) Projection of the surface of the dependence of the transient process duration on the initial conditions $T_\varepsilon(x_0, y_0)$ onto the plane (x, y) of possible states in Zaslavsky mapping at $\Omega = 0.9$, $k = 0.65$, and $d = 0.3$. Gray gradations indicate the duration of transients: white color, zero duration; black color, 70 units of discrete time. (c) The same projection as above for $\Omega = 0.9$, $k = 2.5755$, and $d = 0.3$. Gray gradations indicate the duration of transients: white color, zero duration; black color, 100 units of discrete time. (d) Schematic view of the manifolds for the unstable, (x^0, y^0), and stable, (x^1, y^2), points at the fixed control parameters $\Omega = 0.9$, $k = 0.65$, and $d = 0.3$. For these values of the parameters, the multipliers of the fixed stable point are $\mu_1 = 0.4122$ and $\mu_2 = 0.7278$. The continuous curve, the stable manifold of the fixed unstable point (x^0, y^0); the dash-and-dot curve, the unstable manifold of the same point; and the dashed line, the stable manifold of the attractor, which is characterized by the smaller magnitude multiplier μ_1. Dark circle, point of attraction; open circle, the fixed unstable point. (e) Manifolds of the unstable, (x^0, y^0), and stable, (x^1, y^1), points at the fixed control parameters $\Omega = 0.9$, $k = 2.5755$, and $d = 0.3$. For these values of the parameters, the multipliers of the fixed stable point are $\mu_1 = -0.8402$ and $\mu_2 = -0.3571$. The continuous curve, the stable manifold of the fixed unstable point (x^0, y^0); the dash-and-dot curve, the unstable manifold of the same point; and the dashed line, the stable manifold of the attractor, which is characterized by the smaller magnitude multiplier μ_2. Dark circle, point of attraction; open circle, the fixed unstable point.

of the discontinuity range, the values of the multipliers μ_1^{2c} and μ_2^{2c} coincide. At $2.67524 < k < 2.7723$, the multipliers μ_1^{2c} and μ_2^{2c} are positive with $\mu_1^{2c} < \mu_2^{2c}$. At the boundaries of the discontinuity range, the multipliers tend to the same value 0.29. Outside the discontinuity range, at $k = 3.0641$, they equal 0.29. At $3.0641 < k < 3.2039$, both multipliers are negative, with the multiplier μ_2^{2c} being smaller in magnitude: $|\mu_1^{2c}| > |\mu_2^{2c}|$.

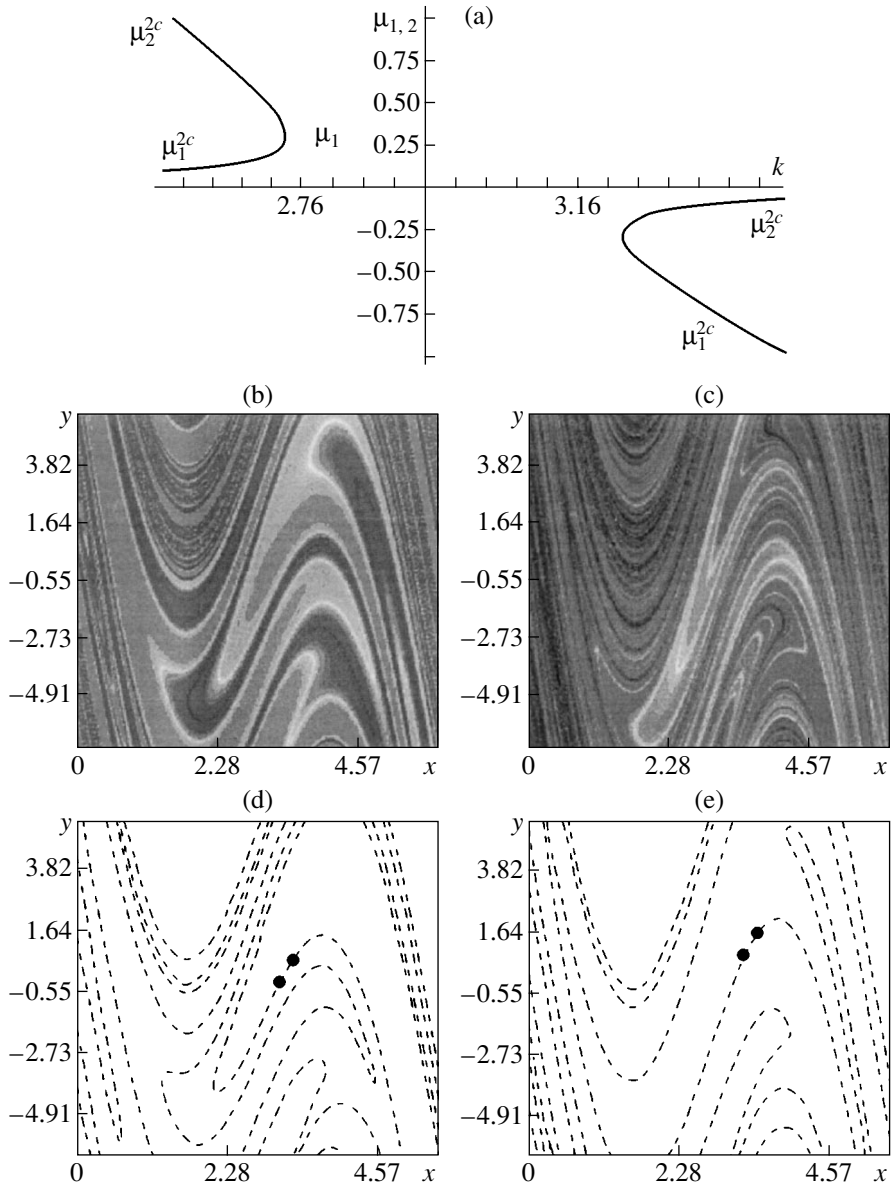

Fig. 2. (a) Multipliers μ_1^{2c} and μ_2^{2c} vs. the control parameter k at $\Omega = 0.9$ and $d = 0.3$. The discontinuity range corresponds to the complex values of the multipliers. (b) Projection of the surface of the dependence of the transient process duration on the initial conditions $T_\varepsilon(x_0, y_0)$ onto the plane (x, y) of possible states in Zaslavsky mapping at $\Omega = 0.9$, $k = 2.70$, and $d = 0.3$. Gray gradations indicate the duration of transients: white color, zero duration; black color, 80 units of discrete time. (c) The same projection as above for $\Omega = 0.9$, $k = 3.10$, and $d = 0.3$. White color, zero duration; black color, 110 units of discrete time. (d) Schematic view of the manifolds for the stable elements (x_{2c}^1, x_{2c}^2) of the cycle of period 2 at the fixed control parameters $\Omega = 0.9$, $k = 2.70$, and $d = 0.3$. For these values of the parameters, the multipliers of the stable 2-period cycle are $\mu_1^{2c} = 0.1054$ and $\mu_2^{2c} = 0.8536$. The dashed lines depict the stable manifold of the attractor, which is characterized by the smaller magnitude multiplier μ_1^{2c}. Dark circles, elements of the 2-period stable cycle. (e) Schematic view of the manifolds for the stable elements (x_{2c}^1, x_{2c}^2) of the 2-period stable cycle at the fixed control parameters $\Omega = 0.9$, $k = 3.10$, and $d = 0.3$. For these values of the parameters, the multipliers of the 2-period stable cycle are $\mu_1^{2c} = -0.5720$ and $\mu_2^{2c} = -0.1573$. The dashed lines depict the stable manifold of the attractor, which is characterized by the smaller magnitude multiplier μ_2^{2c}. Dark circles, the elements of the period-2 stable cycle.

Similarly, comparing the projections of the surface $T_\varepsilon(x_0, y_0)$ onto the plane (x_0, y_0) of the initial conditions (Figs. 2b, 2c) with the positions of stable manifolds (Figs. 2d, 2e) for the stable cycle of period 2, we see that the change in the dependence of the transient process duration on the initial conditions $T_\varepsilon(x_0, y_0)$ that was found for the fixed stable point is also observed in the more complex dynamic regime, i.e., for the stable cycle of period 2. The more complicated form of the dependence of the transient process duration on the initial conditions $T_\varepsilon(x_0, y_0)$ is explained by the fact that the multipliers μ_1^{2c} and μ_2^{2c} change sign when crossing the complex plane. A similar complication of this dependence is also observed for cycles of period 4, 8, etc., in Zaslavsky mapping.

Thus, one scenario of complication of the dependence of the transient process duration on the initial conditions [11, 12] is also valid for Zaslavsky mapping. Hence, the earlier analytical results are universal. It should be noted that the results of our study for discrete-time systems may be extended to data-flow systems, since they may be reduced to mappings by applying the Poincaré cross-section technique.

ACKNOWLEDGMENTS

This work was supported by the Russian Foundation for Basic Research (grant no. 02-02-16351), the program in support of leading scientific schools of Russia, and CRDF (grant no. REC-006).

REFERENCES

1. A. V. Astakhov *et al.*, Radiotekh. Élektron. (Moscow) **38**, 291 (1993).
2. É. V. Kal'yanov, Pis'ma Zh. Tekh. Fiz. **26** (16), 26 (2000) [Tech. Phys. Lett. **26**, 656 (2000)].
3. B. P. Bezruchko, T. V. Dikanev, and D. A. Smirnov, Phys. Rev. E **64**, 036210 (2001).
4. A. A. Koronovskiĭ, D. I. Trubetskov, A. E. Khramov, and A. E. Khramova, Dokl. Akad. Nauk **383**, 322 (2002) [Dokl. Phys. **47**, 181 (2002)].
5. P. J. Aston and P. K. Marriot, Phys. Rev. E **57**, 1181 (1998).
6. M. Dhamala *et al.*, Phys. Rev. E **64**, 056207 (2001).
7. P. Woafo and R. A. Kraenkel, Phys. Rev. E **65**, 036225 (2002).
8. R. Meucci *et al.*, Phys. Rev. E **52**, 4676 (1995).
9. M. I. Yalandin, V. G. Shpak, S. A. Shunaĭlov, and M. R. Ul'maskulov, Pis'ma Zh. Tekh. Fiz. **25** (10), 19 (1998) [Tech. Phys. Lett. **25**, 388 (1998)].
10. L. Zhu *et al.*, Phys. Rev. Lett. **86**, 4017 (2001).
11. A. A. Koronovskiĭ and A. E. Khramov, Pis'ma Zh. Tekh. Fiz. **28** (15), 61 (2002) [Tech. Phys. Lett. **28**, 648 (2002)].
12. A. A. Koronovskiĭ and A. E. Khramova, Pis'ma Zh. Tekh. Fiz. **29** (13), 10 (2003) [Tech. Phys. Lett. **29**, 533 (2003)].
13. G. B. Astaf'ev, A. A. Koronovskiĭ, A. E. Khramov, *et al.*, Izv. Vyssh. Uchebn. Zaved. Prikl. Nelineĭnaya Din. **11** (4) (2003).
14. M. Henon, in *Strange Attractors*, Ed. by Ya. G. Sinaĭ and L. P. Shil'nikov (Mir, Moscow, 1981), p. 152.
15. G. M. Zaslavsky, *Stochasticity of Dynamic Systems* (Nauka, Moscow, 1984) [in Russian].
16. G. M. Zaslavsky, *Stochastic Irreversibility in Nonlinear Systems* (Nauka, Moscow, 1970) [in Russian].
17. G. M. Zaslavsky and R. Z. Sagdeev, *Introduction to Nonlinear Physics* (Nauka, Moscow, 1988) [in Russian]; R. Z. Sagdeev, D. A. Usikov, and G. M. Zaslavsky, *Nonlinear Physics: From a Pendulum to Turbulence and Chaos* (Harwood Academic, New York, 1988).
18. S. P. Kuznetsov, *Dynamic Chaos* (Fizmatlit, Moscow, 2001) [in Russian].
19. A. A. Koronovskiĭ, A. E. Khramov, and A. V. Starodubov, Izv. Vyssh. Uchebn. Zaved. Prikl. Nelineinaya Din. **10** (5), 25 (2002).
20. A. A. Koronovskiĭ, D. I. Trubetskov, A. E. Khramov, and A. E. Khramova, Izv. Vyssh. Uchebn. Zaved. Radiofiz. **45**, 880 (2002).
21. A. A. Koronovskiĭ, A. E. Khramov, and I. A. Khromova, Izv. Vyssh. Uchebn. Zaved. Prikl. Nelineinaya Din. **11** (1), 36 (2003).

Translated by V. Isaakyan

Technical Physics, Vol. 49, No. 5, 2004, pp. 658–659. Translated from Zhurnal Tekhnicheskoĭ Fiziki, Vol. 74, No. 5, 2004, pp. 141–142.

SHORT COMMUNICATIONS

On the Mechanism of Current Passage in Metal/*p*-$CuInSe_2$ Structures

P. N. Gorleĭ*, Z. D. Kovalyuk, V. B. Orletskiĭ**, O. N. Sydor**, V. V. Netyaga**, and V. V. Khomyak***

** Fed'kovich National University, Chernovtsy, 58012 Ukraine*
e-mail: semicon@chnu.cv.ua
*** Institute of Problems of Materials Science, Chernovtsy Branch, National Academy of Sciences of Ukraine, Chernovtsy, 58001 Ukraine*
e-mail: chimsp@unicom.cv.ua
Received October 21, 2003

Abstract—Mechanisms of current passage and the temperature dependence of the current–voltage characteristics in Schottky diodes produced by vacuum evaporation of indium on *p*-$CuInSe_2$ single crystals are discussed. High values of the open-circuit voltage and short-circuit current in these surface-barrier diodes, as well as a high reproducibility of these parameters, suggest that such an inexpensive and rather simple technology is promising for efficient conversion of solar radiation. © *2004 MAIK "Nauka/Interperiodica".*

INTRODUCTION

$CuInSe_2$ and its quaternary compounds $CuIn_xGa_{1-x}Se_2$ are viewed as promising materials for radiation-hard solar cells with a conversion efficiency above 15% [1, 2]. Copper indium diselenide is a direct-gap material ($E_g \approx 1$ eV) with a high absorption factor ($\alpha \geq 10^5$ cm^{-1}). Many publications are concerned with $CuInSe_2$-based homo- and heterojunctions; however, $CuInSe_2$-based Schottky barriers have received little attention [3, 4].

In this study, we consider the electrical and photoelectric properties of the In/*p*-$CuInSe_2$ metal–semiconductor contact.

RESULTS AND DISCUSSION

Copper indium diselenide crystals were grown by the Bridgman method. The carrier concentration and mobility determined from Hall measurements at room temperature ranged from 1.0×10^{17} to 3.0×10^{17} cm^{-3} and from 20 to 50 cm^2/(V s), respectively. The wafers were scribed into dices measuring $5 \times 5 \times 0.3$ mm on average, which were mechanically polished and etched. An indium layer ≤0.5 μm thick was deposited on the semiconductor surface by vacuum evaporation. An ohmic contact was produced by the deposition of gold.

The illumination of the indium surface causes the photovoltaic effect. For a photon flux with an energy density of $P = 100$ mW/cm^2, the open-circuit voltage of the barriers reached $V_1 \approx 0.33$ V; the short-circuit current $J_{sc} \approx 15$ mA/cm^2; and the fill factor *FF*, 0.5 or more. Note that the built-in potential derived from the *I–V* characteristics is in good agreement with the value of V_1.

For temperatures between 240 and 324 K, the Schottky barriers exhibited pronounced diode properties. At room temperature and a bias voltage of 1.3 V, the rectification factor varied between 200 and 500.

For direct biases in the range $0 < V < 0.2$ V (Fig. 1a), the slope of the *I–V* curve roughly equals unity. This situation corresponds to charge carrier tunneling and also is typical of the space-charge-limited current in the velocity-saturation mode. This current is given by [4, 5]

$$J = \frac{2\varepsilon\varepsilon_0 v_{sat} A}{L^2} V, \quad (1)$$

where ε is the permittivity, ε_0 is the permittivity of free space, v_{sat} is the saturation velocity, *A* is the diode surface area, and *L* is the thickness of a semiconductor.

The portion of the *I–V* curve in the range $0.2 < V < 0.5$ V increases as $J \cong J_{sat}\exp(qV/nkT)$, where the saturation current density J_{sat} varies between 5.3×10^{-6} and 9.9×10^{-5} A/cm^2 depending on the temperature and the diode factor *n* lies in the range 1.8–3.0. At low temperatures, the diode factor is the highest and charge carrier transport obeys the tunneling–recombination mechanism. At $T > 300$ K, the current has the recombination character ($n \sim 2$) and becomes overbarrier at still higher temperatures.

At voltages in the range $0.5 < V < 1$ V, the current varies by the square law (Fig. 1a), which means that we are dealing with the space-charge-limited current in the mobility mode (the so-called trap-free quadratic dependence) [4, 5]:

$$J = \frac{9\varepsilon\varepsilon_0\mu A}{8L^3} V^2, \quad (2)$$

where μ is the mobility of holes.

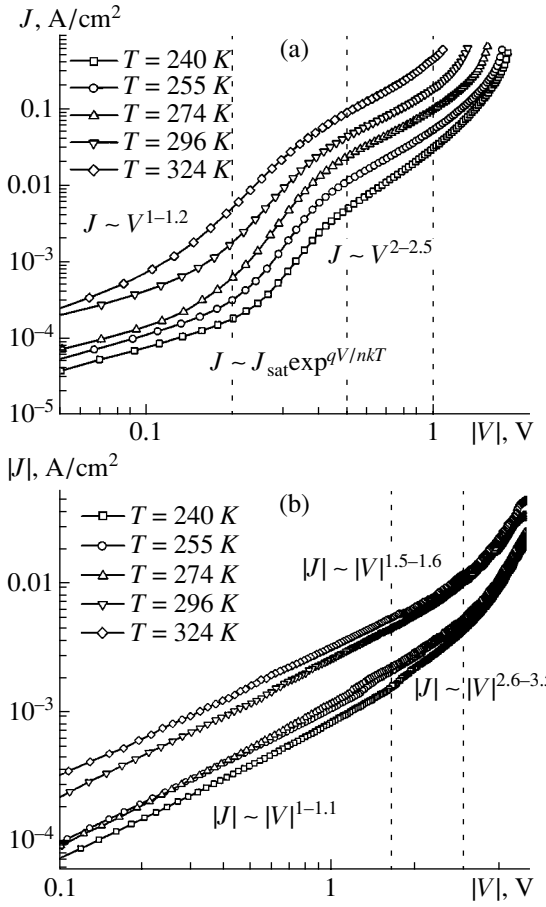

Fig. 1. (a) Direct and (b) inverse *I–V* characteristics of the In/*p*-$CuInSe_2$ Schottky barriers at different temperatures in the log–log coordinates.

As follows from Fig. 1b, the inverse current grows as $J \sim V^m$ throughout the voltage range under study. For $-1.5 < V < 0$ V, the *I–V* characteristic is linear in the temperature range of interest. Therefore, the current either is due to tunneling or is described by formula (1).

In the interval $-3.0 < V < -1.5$ V, the *I–V* curve plotted in the log–log coordinates is described by the power function $J \sim V^{1.48–1.6}$; i.e., it follows the Child–Langmuir law (the space-charge-limited current in the ballistic mode) [4, 5]

$$J = \frac{4\varepsilon}{9L^2}\left(\frac{2q}{m^*}\right)^{1/2} V^{3/2}. \quad (3)$$

At high inverse biases, the exponent m falls into the range $2.6 < m < 3.5$. In this case, the current–voltage dependence can be described under the assumption of continuous (exponential) trap energy distribution [5]:

$$J \approx q\mu N_v \left(\frac{\varepsilon}{qN_0 kT_t}\right)^m \frac{1}{L^{2m+1}} V^{m+1}, \quad (4)$$

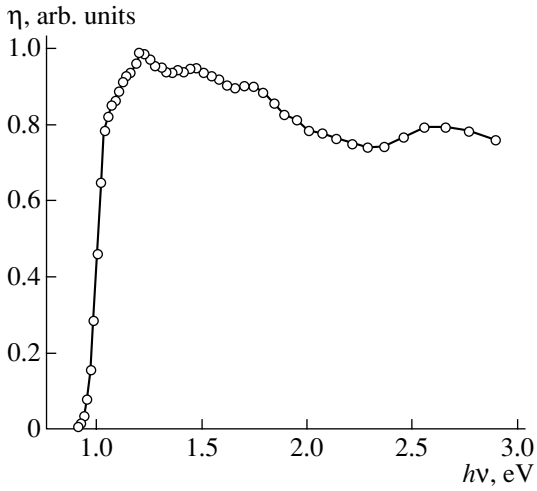

Fig. 2. Spectral dependence of the relative quantum efficiency of photovoltaic conversion η in the In/*p*-$CuInSe_2$ Schottky barrier structures.

where N_v is the effective density of states in the valence band, $N_0 = N_t(E)/\exp[-E/kT_t]$, $N_t(E)$ is the concentration of traps per unit energy, and T_t is a temperature parameter.

It should be noted that our diode structures show the wide-range photovoltaic effect (Fig. 2). The FWHM $\delta_{1/2}$ of the conversion quantum efficiency spectrum (η) exceeds 2 eV.

CONCLUSIONS

Experimental results obtained for In/*p*-$CuInSe_2$ Schottky barriers indicate that these structures are promising for energy converters. Optimization of the process and electrophysical parameters may improve substantially the key photoelectric properties, such as V_1, J_{sc}, and *FF* [6].

REFERENCES

1. H. W. Schock, Sol. Energy Mater. Sol. Cells **34**, 19 (1994).
2. C. F. Gay, R. R. Potter, D. P. Tanner, *et al.*, in *Proceedings of the 17th IEEE Photovoltaics Specialists Conference, Kissimmee, 1984* (IEEE, New York, 1984), pp. 151–152.
3. M. A. Magomedov, V. D. Prochukhan, and Yu. V. Rud', Fiz. Tekh. Poluprovodn. (St. Petersburg) **26**, 1997 (1992) [Sov. Phys. Semicond. **26**, 1123 (1992)].
4. E. Hernandez, Cryst. Res. Technol. **33**, 285 (1998).
5. M. Lampert and P. Mark, *Current Injection in Solids* (Academic, New York, 1970; Mir, Moscow, 1973).
6. S. I. Drapak, Z. D. Kovalyuk, V. V. Netyaga, *et al.*, in *Proceedings of the International Conference "Science for Materials in the Frontier of Centuries: Advantages and Challenges," Ukraine, 2002*, pp. 129–130.

Translated by A. Sidorova